UNIVERSITY OF OKLAHOMA

GRADUATE COLLEGE

LABORATORY DEVELOPMENT AND MOLECULAR-SCALE SIMULATION OF SENSOR-ENABLED GEOGRIDS

A DISSERTATION

SUBMITTED TO THE GRADUATE FACULTY

in partial fulfillment of the requirements for the

Degree of

DOCTOR OF PHILOSOPHY

By

HESSAM YAZDANI
Norman, Oklahoma
2015

Downloaded from SHAREOK. Persistent Handle URL: https://hdl.handle.net/11244/23312

LABORATORY DEVELOPMENT AND MOLECULAR-SCALE SIMULATION OF SENSOR-ENABLED GEOGRIDS

A DISSERTATION APPROVED FOR THE
SCHOOL OF CIVIL ENGINEERING AND ENVIRONMENTAL SCIENCE

BY

Dr. Kianoosh Hatami, Chair

Dr. Gerald A. Miller

Dr. Brian P. Grady

Dr. Amy B. Cerato

Dr. Benjamin E. Smith

© Copyright by HESSAM YAZDANI 2015
All Rights Reserved.

to

Sama

Acknowledgements

"A Finnish proverb goes, strong sisu (guts) will help get a person even through a gray rock. Now I chant "sis-u, sis-u," inside my head as I lug myself up those weary hills toward the end of a long run."

Richard Rogin, in *The Runner Magazine*

I would like to thank and commend everyone who has contributed to this dissertation. Though this only bears my name, a major factor leading to its completion comes from the dedicated work of other people. I wish to express my appreciation to them.

To my advisor, Dr. Kianoosh Hatami, for your confidence in me and giving me the opportunity to work with you, for your unwavering support all throughout my PhD study, for your continuous patience when I was going off on a tangent, for your guidance and motivation that greatly inspired me to do my best, for instilling a strong sense of academic ethics and never compromising thoroughness in favor of a longer list of papers or a quick turnaround to publication, for indulging my curiosity and letting me dispel it with your encouraging remarks and for your positive attitude when I felt on the verge of a nervous breakdown. May you be as proud to have been my mentor as I am to be your mentee.

To my committee members for your willingness to serve and for your insightful and articulate comments which widened my research perspectives. To Professor Gerald Miller for your contagious passion for geotechnical engineering and for conveying the core concepts of "Unsaturated Soil Mechanics" in an efficient and easily-understood manner that I will always remember as a precedent for teaching. To Professor Brian Grady for your valuable comments on our joint publications and for your generosity in providing the facilities in your lab. To Dr. Amy Cerato for counseling me with respect to the program and

degree requirements, and to Dr. Benjamin Smith for your keen interest in my research and sharing with me your intellect and immense microscopy skills.

To the staff, Mrs. Susan Williams, Mrs. Brenda Clouse, Ms. Molly Smith, Mrs. Audre Carter, Mr. Michael Schmitz and Mr. Ronald Conlon of CEES and Mr. Alan Miles of CBME, for all the assistance you gave which made many things during the course of my studies so much easier.

To Dr. Preston Larson and Mr. Gregory Strout of the OU Samuel Roberts Noble Microscopy Laboratory for your generous assistance with the transmission and scanning electron microscopy of my samples. To Dr. Donald Ward of the Sandia National Laboratory, Dr. Mehdi Eftekhari of Azad University, Iran, Dr. Takumi Hawa, former assistant professor in the AME at OU, and Mr. Nuwan Dewapriya of Simon Fraser University for your invaluable input and comments on my molecular dynamics simulations. To Dr. Henry Neeman and his associates at the OU supercomputing center for education and research (OSCER) for providing the computational resources for the simulations.

To my office colleagues, past and present, whom it has been my fortune to have befriended: Yewei Zheng, Theresa Ngo, Fabien Pariot, Dr. Tahsina Mahmood, Luis Pena and Juan Pereira. To my friends Mr. Ali Parvizinia, Dr. Ebrahim Fathi, Dr. Shaya Karimkashi and Dr. Shahrokh Saeidi. Thank you for making the OU years fun ones.

To the undergraduate students, Kendall Harper, Michelle Basham, Hiep Chuong, Ellyson Uldrich and Katherine Ngo, for your tireless efforts in helping me with the laboratory works and data analysis and reduction.

To our caring host family, Kevin and Becca Bradford and their children, for your support and help over the past four years. I feel very lucky to be associated with you.

My sincerest and deepest gratitude to my family for your unfaltering love and support all throughout the different stages I have gone through in my life. I want you to know that the distance and time you have endured is worth every drop of sweat and blood I poured into this journey. You are the reason for my being and you make everything worthwhile. To my family-in-law for your unflagging support and encouragement.

I most especially thank my wife, Sama, the only person who worked harder on my PhD than I did, to whom I owe my degree and sanity, for your resilient spirit and your strong orientation toward keeping our life tightknit, for spending a few months in the lab assiduously helping me with my tests, for spending countless nights alone while I was in my office glued to my computer, for doing everything to save me from dissertation-caused neuroses and for doing it all without a single complaint, ever.

Thank you so much everyone and my apologies to anyone inadvertently overlooked.

Table of Contents

Acknowledgements iv

List of Tables xi

List of Figures xiii

Abstract xxv

CHAPTER 1. Introduction 1

1.1. Geosynthetics and performance monitoring of geosynthetic structures 1

1.2. Nanotechnology 1

1.3. Electrically-conductive polymer composites 3

1.3.1. Common conductive fillers 4

1.3.2. Filler dispersion 11

1.3.3. Percolation threshold 13

1.3.4. Strain-sensitive electrical conductivity of filled composites 16

1.4. Molecular-scale simulations in nanotechnology 18

1.4.1. Monte Carlo simulations 19

1.4.2. Molecular dynamics simulations 20

1.5. Sensor-enabled geosynthetics 31

1.6. Scope and outline of the dissertation 33

1.6.1. Contribution toward SEG development 33

1.6.2. Outline 34

CHAPTER 2. Literature Survey 36

2.1. Performance monitoring in geosynthetics engineering 36

2.1.1. Significance 36

2.1.2. Existing technology for measuring strains in geosynthetics 37

2.2. Selected experimental studies on electrical conductivity of filled composites...43

2.2.1. Experimental studies.....44

2.2.2. Numerical studies on the mechanical and electrical properties of filled composites49

CHAPTER 3. Laboratory Tests on Carbon black-filled PVC Composites 58

3.1. Development of a tensoresistive PVC coating for sensor-enabled geogrids.....59

3.1.1. Introduction 59

3.1.2. Study approach 64

3.1.3. Results and discussion 84

3.1.4. Conclusions 101

3.2. Strain-sensitive electrical conductivity of CB-filled PVC composites subjected to cyclic loading..... 102

3.2.1. Introduction 102

3.2.2. Experimental program..... 104

3.2.3. Results and discussion 110

3.2.4. Conclusions 128

3.3. In-soil tensoresistivity of sensor-enabled geogrids 129

3.3.1. Introduction 129

3.3.2. Laboratory tests 130

3.3.3. Results and discussion 136

3.3.4. Conclusions 139

CHAPTER 4. Laboratory Tests on Carbon Nanotube-filled PVC Composites..... 141

4.1. Introduction..... 141

4.2. Experimental program 145

4.2.1. Materials 145

4.2.2. Assessment of filler dispersion 151

4.2.3. Tensile-conductivity tests 163

4.3. Results and discussion 164

4.3.1. LSCM analysis 164

4.3.2. Electrical conductivity 174

4.3.3. Mechanical properties 185

4.3.4. Tensoresistivity response of the coating composite 198

4.4. Conclusions 202

CHAPTER 5. Monte Carlo Simulation of the Percolation Behavior of Filled Composites 204

5.1. Introduction 204

5.2. Mathematical models 205

5.2.1. CB model 205

5.2.2. CNT model 205

5.2.3. Connection criteria 207

5.3. Simulation procedure 210

5.4. Results and discussion 214

5.5. Conclusions 220

CHAPTER 6. Molecular Dynamics Simulation of Nanocarbons and Filled Polymer Composites 222

6.1. Failure criterion for graphene in biaxial loading 223

6.1.1. Introduction 223

6.1.2. Molecular dynamics simulations 226

6.1.3. Results and discussions 234

6.1.4. Conclusions 244

6.2. Atomistic insight into the mechanical properties of single-walled carbon nanotubes 245

6.2.1. Introduction 245

6.2.2. Molecular dynamics simulations 246

6.2.2.1. Simulation 246

6.2.3. Results and discussions 250

6.2.4. Conclusions 264

6.3. MD simulation of pristine and SWCNT-filled polyethylene composites 265

6.3.1. Introduction 265

6.3.2. Approximate models for polymer chains 266

6.3.3. MD simulation of PE and CNT-filled PE composites using UA approximation 272

6.3.4. Results and discussion 279

6.4. MD simulation of polyvinyl chloride 288

6.4.1. Simulation models 289

6.4.2. Results and discussion 294

CHAPTER 7. Conclusions 302

7.1. Summary and conclusions 302

7.2. Suggestions for further research 307

REFERENCES 309

Appendix A: Publlications and presentations from this study 355

List of Tables

Table 1-1. Mechanical properties of CNT vs. A36 steel and PAN carbon fiber 7

Table 1-2. Transport properties of CNT vs. copper and PAN carbon fiber (at 298 K) 8

Table 2-1. Summary of experimental studies on the electrical conductivity of selected CNT-filled polymer composites 48

Table 3-1. Properties of the CB particles used in the study (as measured, or provided by the supplier) 67

Table 3-2. Information related to the CB-filled samples prepared and tested in this study.75

Table 3-3. Information of the cyclic load tests 110

Table 3-4. Gauge factors[1] of the coating composite at large strains 121

Table 3-5. Key findings of the cyclic load tests..... 127

Table 4-1. Properties of the MWCNT used in this study (as measured, or provided by the supplier) 147

Table 4-2. Information related to the specimens prepared and tested in this study. Note: three specimens were used for all electrical conductivity tests listed in the table. Only a subset of cases were also subjected to mechanical testing as indicated..... 153

Table 4-3. Mean and standard deviations of MWCNT volume log-normal distributions in different filled specimens. Note: The values indicate the Shapiro-Wilk test results and the mean values of three independent experiments..... 168

Table 4-4. Summary of the percolation threshold of some common amorphous polymers filled with MWCNT..... 183

Table 4-5. Changes in mechanical properties of selected common polymers filled with MWCNT..... 196

Table 4-6. Gauge factors reported for selected filled polymer composites 200

Table 5-1. Probability density function and corresponding parameters and values for the CNT model variables 207

Table 6-1. Strain-rate dependent failure properties of graphene under equi-biaxial loading (Régime III) 242

Table 6-2. Information of the MD models made for compressive numerical experiments 247

Table 6-3. Information of the MD models made for tensile numerical experiments (aspect ratio = 10) 248

Table 6-4. Information germane to the PE models studied. Temperatures studied: 100 and 300 K. 274

Table 6-5. Information germane to the CNT-filled PE models studied. Temperatures studied: 100 and 300 K. 275

Table 6-6. Dreiding force field parameters and corresponding values used for the MD simulations of PE (Mayo et al. 1990) 276

Table 6-7. Information germane to the PVC models studied 290

Table 6-8. Poisson's ratio of the PVC models at different temperatures 300

List of Figures

Figure 1.1. Different variety of nanocarbons 3

Figure 1.2. Graphite's structure (after Medcoat (2015)) 6

Figure 1.3. Types of carbon nanotube (Physicsworld 2015) 9

Figure 1.4. a) Schema of CNT formation by rolling a graphene sheet and b) models of zigzag, armchair and chiral CNTs (after Kis and Zettl (2008)) 11

Figure 1.5. Filler dispersion vs. electrical conductivity (After Peters (2009)) 13

Figure 1.6. Percolation process in CFP-filled composites (After Alamusi *et al.* (2011)) 14

Figure 1.7. Filler concentration vs. electrical conductivity ((After Alamusi *et al.* (2011)) 15

Figure 1.8. Schematic illustration of the rupture causing tensoresistivity (After Fathi (2011)) 17

Figure 1.9. Bond stretching: (a) natural length and (b) stretched length 23

Figure 1.10. Bond angle bending 25

Figure 1.11. Torsion interactions 26

Figure 1.12. Functional form of the collective interatomic interaction potential between two non-ionic atoms 28

Figure 1.13. Periodic boundary conditions in two dimensions. The events in the primary cell are duplicated in each image cell. 30

Figure 1.14. Outline of the SEG project 32

Figure 2.1. Bonded strain gauge: (a) construction, (b) bonding on the surface, (c) schematic placement, and (d) actual placement (a–c, after Ghosh (2009) and d, after Fathi (2011)) 38

Figure 2.2. Schematic diagram of placement of a transducer: (a) target and coil at right angles, (b) coaxial target and coil, and (c) measuring arrangement (after Ghosh (2009)) 39

Figure 2.3. LVDTs: (a) basics (after Ghosh (2009)) and (b) actual view (after Fathi (2011)) 39

Figure 2.4. Wire potentiometer (Musikding 2015).....40

Figure 2.5. Schematic representation of the concentric spherical model (after Wang and Ogale (1993)).....52

Figure 3.1. The setup used to measure the water absorbed by CB.....66

Figure 3.2. Combinations of rotational speed and spindle number examined to measure the viscosity of an industrial geogrid coating material. Notes: The concentrations of CB and primary plasticizer in the coating were unreported; T = 23 ± 1 °C; one sample was tested for each rotational speed and spindle number combination.....69

Figure 3.3. Viscosity of the PL/PR/CB composite with different PR/CB ratios. Notes: T= 23 ± 1 °C; spindle #5; rotational speed= 5 rpm; one sample was tested for each PR/CB ratio.....70

Figure 3.4. Coating sample used for electrical conductivity tests (mean thickness = 0.8 mm) 76

Figure 3.5. Sample fabrication stages: 1) filler is poured into the plasticizer and 2) the resulting blend is mixed and 3) added to PVC plastisol. 4) the composite is poured into a mold and 5) compression-molded to obtain 6) a sample which is tested in 7) a tensile testing machine or an electrometer 78

Figure 3.6. Laboratory setup for measuring flexural rigidity of polymer specimens in overall conformance with the ASTM D1388 (2014) test standard.....82

Figure 3.7. Setup to measure the tensoresistivity response of filled polymers.....84

Figure 3.8. Comparison of electrical conductivity values of different ingredients in the composite. Notes: three samples were tested for each case; BS: bath sonication, MS: mechanical stirring.....85

Figure 3.9. Volume conductivity results for electrically conductive composite specimens filled with a) 3% CB1, b) 5% CB1, and produced using different mixing techniques. Notes:

three samples were tested for each mixing case shown; specimen thickness, t = 0.8 mm; time periods on the horizontal axis refer to the stirring or sonication durations (as applicable).....87

Figure 3.10. Volume conductivity results for electrically conductive composite specimens filled with a) 3% CB2, b) 5% CB2, and produced using different mixing techniques. Notes: three samples were tested for each mixing case shown; specimen thickness, t = 0.8 mm; time periods on the horizontal axis refer to the stirring or sonication durations (as applicable).....88

Figure 3.11. SEM images for a) pure plastisol, b) 3 wt.% CB1-filled composite mixed with the PS method (550 W, 2 hrs), c) 3 wt.% CB1-filled composite mixed with the MS method (750 rpm, 10 minutes), and d) 3 wt.% CB1-filled composite mixed with the MS method (1500 rpm, 10 minutes). Note: black circles show areas where CB particles were not adequately separated in the blending process.....90

Figure 3.12. SEM images for a) pure plastisol, b) 5 wt.% CB2-filled composite mixed with the PS method (550 W, 1hr), c) 5 wt.% CB2-filled composite mixed with the MS method (375 rpm, 10 minutes), and d) 5 wt.% CB2-filled composite mixed with the MS method (750 rpm, 10 minutes). Note: black circles show areas where CB particles were not adequately separated in the blending process.....90

Figure 3.13. Influence of the sample thickness on its measured volume conductivity. Notes: results are the mean values of three tests for each case; the time periods shown in the legend are the stirring or sonication durations (as applicable).....92

Figure 3.14. Volume conductivity of PVC/plastisol as a function of CB concentration. Note: thickness of specimens = 0.8 mm.....93

Figure 3.15. Flexural stiffness (rigidity) of the coating material.....95

Figure 3.16. Strain-sensitive electrical conductivity response of 1.5 wt.% CB1-filled coating material.....96

Figure 3.17. Strain-sensitivity electrical conductivity of 5 wt.% CB2-filled coating material 97

Figure 3.18. Influence of specimen width on the strain-sensitivity response of the CB-filled coating material....98

Figure 3.19. Influence of strain rate on the strain-sensitivity response of the CB-filled coating material....99

Figure 3.20. Influence of strain rate on the tensile properties of the CB-filled coating material. Note: the insets show the full-range stress-strain behavior of the material.... 100

Figure 3.21. Hysteretic behavior of electrical conductivity 107

Figure 3.22. Loading-unloading régime for a) Type I, b) Type II, c) Type III, d) Type IV, and e) Type V 108

Figure 3.23. Tensoresistivity of CB1-filled coating composite subjected to loading Type I, a) $\dot{\varepsilon}=0.15\%/\text{min}$, b) $\dot{\varepsilon}=2\%/\text{min}$, and c) $\dot{\varepsilon}=10\%/\text{min}$.... 112

Figure 3.24. Tensoresistivity of CB2-filled coating composite subjected to loading Type I at a) $\dot{\varepsilon}=0.15\%/\text{min}$, b) $\dot{\varepsilon}=2\%/\text{min}$, and c) $\dot{\varepsilon}=10\%/\text{min}$. 113

Figure 3.25. NDI vs. number of cycles for a) CB1- and b) CB2-filled coating composite subjected to loading Type I.... 114

Figure 3.26. Tensoresistive response of a CB-1 filled coating composite subjected to load Type II. Note: $\dot{\varepsilon}=2\%/\text{min}$. The encircled area is magnified in the inset. 116

Figure 3.27. Tensoresistive response of a CB-1 filled coating composite subjected to load Type II. Note: $\dot{\varepsilon}=2\%/\text{min}$. The encircled area is magnified in the inset. 118

Figure 3.28. Tensoresistive of a) CB1- and b) CB2-filled coating at large strains. Note: The encircled area is magnified in the inset.... 120

Figure 3.29. Tensoresistive responses of a) CB1- and b) CB2-filled coating specimens subjected to low-strain cyclic loading at OER = $\varepsilon_p/\varepsilon_c$ = 1, variations of c) the NDI and d) *GF* with low-strain (5%) cyclic load for CB1- and CB2-filled coating specimens.... 124

Figure 3.30. Influence of prestraining on the tensoresistivity of a CB1-filled coating specimen with a) OER = 3.3, b) OER = 2, and c) OER = 1.4.... 125

Figure 3.31. Influence of prestraining on the tensoresistivity of a CB2-filled coating specimen with a) OER = 3.3, b) OER = 2, and c) OER = 1.4 126

Figure 3.32. Influence prestraining on the damage experienced by the conductive network. Note: The error bars indicate the max/min NDIs observed during a full test. 127

Figure 3.33. Fabrication of SEGG specimens: a) virgin PET yarns, b) brushing the coating composite on PET yarns, c) coated yarns, d) compression molding the coated yarns, e) SEGG specimens, f) a SEGG rib 131

Figure 3.34. Exploded view of the DST apparatus modified for in-soil tests 132

Figure 3.35. A SEGG specimen clamped in the DST test cell with electric terminals attached 25 mm apart 133

Figure 3.36. Comparison of the strains observed using the digital imagery approach with those measured from the crosshead movements in three independent experiments ... 134

Figure 3.37. Evaluation of the clamps performance 134

Figure 3.38. In-isolation (strain rates = 0.15, 2 and 10 %/min) and confined (confining pressures = 10, 30 and 50 kPa) normalized resistance of SEGG specimens as a function of strain. Note: The data shown correspond to three independent experiments. 137

Figure 3.39. Tensile response of SEGG specimens at different strain rates. Note: The data shown correspond to three independent experiments..... 139

Figure 4.1. LSCM 3D Imaging of CNT bundles in composite samples prepared using PS/55/120. (a, d, g) Orthogonal sections from 3D images of PVC autofluorescence in three separate samples. The white lines show where the corresponding orthogonal sections are located in each image. These images were then deconvolved (b, e, h) and then rendered with an isosurface (c, f, i), revealing the shape and position of each CNT bundle within the 3D image. Arrowheads point to a CNT bundle within the sample. Scale bars = 50 μm..... 159

Figure 4.2. LSCM 3D imaging of CNT bundles in BS/70/120. (a) Orthogonal sections from a 3D image of PVC autofluorescence in a CNT composite sample. The white lines show where the corresponding orthogonal sections are located in each image. (b) Image (a)

post-deconvolution. (c) Orthogonal views of the entire 3D image with an isosurface rendering around each bundle. Note: Scale bars = 50 μm. 160

Figure 4.3. Experimental setup used to image the subsurface failure mechanics in CNT composite samples under tensile strain. The composite sample is mounted directly under the objective. 163

Figure 4.4. CNT bundles are optically translucent with PVC impregnation into CNT bundles (a) A single optical section of a CNT bundle (white). PVC (black) is clearly visible within the bundle itself. Scale bar = 20 μm. (b) A TEM micrograph of a CNT bundle showing that the bundles are a loosely entangled cluster of CNTs impregnated with PVC. Scale bar = 1 μm. (c) A magnified view from b. Scale bar = 200 nm. 166

Figure 4.5. Distribution of CNT bundle volume within three different PVC composite samples composite samples prepared using PS/55/120. (a-c) Histograms of the distribution of CNT bundle volumes across three separate CNT composite samples. The red line shows the corresponding log-normal distribution of the same mean and standard deviation. (d-f) Probability plots comparing the bundle volume distributions to the corresponding log-normal distributions. Dashed lines = 95% confidence interval. 167

Figure 4.6. (a) Histogram of the distribution of the CNT bundle volumes in the BS/70/120 specimens, with the superimposed curve showing the corresponding log-normal distribution. (b) Corresponding probability plot showing the distribution of bundle volumes relative to a log-normal distribution 168

Figure 4.7. (a) A schema showing how the total 3D image was divided into 5 bins along each axis in a, with the side of the image that was closest to the objective facing up. Distribution of CNT bundles in PVC. (b) Plots showing the distribution of individual bundle volumes (box plots) as well as the bulk distribution of CNTs (dashed line) along the X, Y and Z axes of the image in Figure 4.1. 170

Figure 4.8. 3D distribution of CNT bundles in BS/70/120 specimens from LSCM images. (a) Isosurface rendering of CNT bundles from a 3D confocal image series. (b) The corresponding color coded Z-position of each bundle in image (a). (c) An overlay of

images (a) and (b) showing the three-dimensional position of each bundle within the image stack. Scale bar in each image = 50 μm. 171

Figure 4.9. Hierarchical clustering of CNT dispersion methods in filled PVC composites based on the CNT aggregate volume distributions 172

Figure 4.10. Correlation between quantitative metrics of CNT dispersion and resistivity. Note: the dashed lines represent correlations that are statistically significant ($p < 0.05$). 173

Figure 4.11. Volume conductivity of composite specimens filled with 0.5 wt.% MWCNT and produced using different mixing techniques. Note: three specimens were tested for each mixing case shown. 175

Figure 4.12. SEM images for (a) pure PL, (b) PS/55/60, (c) PS/55/120, (d) PS/55/180, (e) BS/70/120, and (f) BM/150/100/20 176

Figure 4.13. Influence of curing time in compression molding on the conductivity of PS/55/120 180

Figure 4.14. Volume conductivity of PVC/plastisol as a function of CNT concentration for PS/55/120. The inset is the scaling law of $\log \sigma \propto \log (\varphi - \varphi_c)$ (Equation (4-3)) to determine σ_0 and t. 182

Figure 4.15. Failure mechanics of the composite material under tensile strain. (a) Maximum intensity projections of test samples with and without CNTs under increasing strain. Arrowheads show where new fractures have formed within the CNT bundles. Scale bar = 200 μm. Arrows show direction of tensile loading. (b) A 3D grayscale image and colorimetric surface profile of a large tear forming in a composite sample under tensile load, with a fractured CNT bundle clearly visible at the base of the tear (arrowhead). (c) A single optical section and 3D rendering of a fractured CNT bundle after tensile loading. Scale bar = 20 μm. Scale bar = 200 μm. 187

Figure 4.16. Influence of dispersion technique on the mechanical properties of the PVC composite. Note: manual refers to the pristine matrix. 188

Figure 4.17. Typical stress-strain behavior of the composite filled with 0.5 wt.% MWCNT 192

Figure 4.18. Influence of plasticizer and the CNT concentration on a) the tensile strength and ultimate strain and b) the elastic modulus and Poisson's ratio of the PVC composite (four samples were tested at each concentration shown) 193

Figure 4.19. Influence of loading rate on the ultimate strength and strain of the composite (MWCNT = 0.5 wt.%) 198

Figure 4.20. Strain-sensitivity response of the coating composite at the strain rates: a) 0.15%/min, b) 2%/min, and c) 10 %/min. Note: Data shown are for three specimens per strain rate. 199

Figure 4.21. Strain sensitivity of a sample conductivity during imaging..... 199

Figure 5.1. Configuration of the ith CNT 207

Figure 5.2. Schematic representation of the hard-core soft-shell continuum model 208

Figure 5.3. Fiber contact mechanisms: a) body-to-body, b) end-to-end and c) end-to-body (after Ma and Gao (2008))..... 210

Figure 5.4. Graphical representation of percolation simulated by the MC algorithm..... 212

Figure 5.5. Clusters' information matrix before the insertion of Particle #16 in Figure 5.4 212

Figure 5.6. Clusters' information matrix just after the insertion of Particle #16 in Figure 5.4 213

Figure 5.7. Clusters' information matrix at percolation (after the insertion of Particle #20 in Figure 5.4)..... 213

Figure 5.8. Mean, standard deviation and COV of the percolation threshold of a model as a function of simulation runs. Note: the model contains CNTs with a diameter of 0.01Lx, r/δ of 100 and mean values of 100 and 120° for aspect ratio and φ..... 214

Figure 5.9. Sample graphical representation of the percolation of CB-filled frames. Note: CBs' diameter = 0.05Lx and r/δ = 2..... 215

Figure 5.10. Percolation threshold prediction for CB-filled composites with different CB radii and shell thicknesses. Note: a mean COV of 25% was observed for 500 simulations that were carried out for each combination of L/r and r/δ. 216

Figure 5.11. Sample graphical representation of the percolation of CNT-filled frames. Note: CNTs' diameter = $0.01L_x$, r/δ = 5, and mean values of 40 and 120° for aspect ratio and φ. 218

Figure 5.12. Percolation threshold prediction for CNTs with r/δ = a) 5, b) 7, c) 9, d) 11, e) 13 and f) 15. Note: a range of 26% to 52% and a mean value of 41% were observed for the COV of 500 simulations that were carried out for each combination of aspect ratio and r/δ. 220

Figure 6.1. Straightforward evaluation of the macroscopic stress (after van Dommelen (2003)) 230

Figure 6.2. Averaging in the y-direction (after van Dommelen (2003)) 230

Figure 6.3. The cross-over problem in the virial stress calculation (after van Dommelen (2003)) 231

Figure 6.4. Variations of predicted ultimate strength of graphene in zigzag (ZZ) and armchair (AC) directions with temperature subjected to uniaxial loading (strain rate = 0.001/ps). The inset shows a schematic nonlinear behavior expected for graphene based on MD simulations. The data points at each temperature represent the mean values over three independent numerical experiments. 235

Figure 6.5. Typical stress–strain behavior of bulk graphene in a) staged (Régimes I and II) and b) equi- (Régime III) biaxial loading 236

Figure 6.6. Combinations of biaxial stresses resulting in failure in graphene at different temperatures and loading régimes (strain rate = 0.001/ps) 239

Figure 6.7. Failure modes of graphene at 0 K under Loading Régimes a) I, b) II and c) III 241

Figure 6.8. Biaxial failure envelopes for graphene subjected to different loading régimes 243

Figure 6.9. SWCNT model 249

Figure 6.10. Compressive stress-strain behavior and buckling modes of SWCNT (0,17) with an slenderness ratio of a) 5, b) 10, c) 15 and d) 20 253

Figure 6.11. Influence of slenderness ratio and chirality on the buckling strength of SWCNTs at T = a) 100 K, b) 300 K and c) 500 K 255

Figure 6.12. Influence of slenderness ratio and chirality on the initial buckling strain of SWCNTs at T = a) 100 K, b) 300 K and c) 500 K 256

Figure 6.13. Influence of slenderness ratio and chirality on the elastic modulus of SWCNTs at T = a) 100 K, b) 300 K and c) 500 K 257

Figure 6.14. Tensile stress-strain behavior and failure modes of selected SWCNTs with similar diameters (~13.5 Å) at T = a) 100 K, b) 300 K and c) 500 K. Note: aspect ratio = 10. 259

Figure 6.15. Equilibrium of carbon atoms in a) zigzag and b) armchair CNTs subjected to tension 259

Figure 6.16. Influence of chirality and temperature on the a) tensile strength, b) ultimate strain and c) elastic modulus of SWCNTs 261

Figure 6.17. Influence of diameter on the a) tensile strength, b) ultimate strain and c) elastic modulus of zigzag SWCNTs 262

Figure 6.18. Influence of diameter on the a) tensile strength, b) ultimate strain and c) elastic modulus of armchair SWCNTs 263

Figure 6.19. The united atom model 267

Figure 6.20. 2D lattice model for polymer chains with a) linear polymer, b) star polymer, c) comb polymer and d) copolymer chain topologies (after Kawakatsu (2004)) 269

Figure 6.21. Polymer chains with identical configuration but different conformations (after Kawakatsu (2004)) 270

Figure 6.22. Self-avoiding random walk on a 2D square lattice 272

Figure 6.23. Physical meaning of excluded volume where hard cores severely hamper local atomic rearrangements (after Kawakatsu (2004)) 272

Figure 6.24. A CNT-filled PE model construction. a) polymer chains are generated according to a given set of density, chain length and number of chains, b) an indent is made at the center of the box along the z-axis, and c) a CNT is inserted in the hole. 274

Figure 6.25. Volume change of the model LDPE-20-1000 in pristine form as a function of temperature 277

Figure 6.26. Stress-strain response of the LDPE models at 100 K. Strain rate = 0.01/ps. 282

Figure 6.27. Stress-strain response of the HDPE models at 100 K. Strain rate = 0.01/ps. 282

Figure 6.28. Stress-strain response of the LDPE models at 300 K. Strain rate = 0.01/ps. 283

Figure 6.29. Stress-strain response of the HDPE models at 300 K. Strain rate = 0.01/ps. 283

Figure 6.30. Stress-strain response of the model CNT09LDPE20k at 300 K. Strain rate = 0.01/ps. 286

Figure 6.31. Influence of CNT concentration on the strength of CNT-filled a) LDPE and b) HDPE composites. Strain rate = 0.01/ps. 287

Figure 6.32. Influence of CNT chirality on the strength of CNT-filled PE composites. Strain rate = 0.01/ps. 288

Figure 6.33. Single chain (left) and amorphous box (right) of a) isotactic (substituents on the same side of the chain), b) syndiotactic (substituents on alternating sides of the chain) and c) atactic (substituents placed randomly along the chain) PVC. Note: each box contains 30 PVC chains each having 33 monomers. 290

Figure 6.34. Volume change of the model Iso-10-100 as a function of temperature 293

Figure 6.35. Evolution of the energy of the model Iso-10-100 during relaxation 293

Figure 6.36. Stress-strain response of the model Iso-10-100 at 300 K in uniaxial tension 295

Figure 6.37. Microstructural evolution of the model Iso-10-100 at a) 0%, b) 50%, c) 100% and d) 200% strain. T = 300 K. 295

Figure 6.38. Stress-strain response of the isotactic PVC models at 100 K and 300 K 297

Figure 6.39. Stress-strain response of the syndiotactic PVC models at 100 K and 300 K 297

Figure 6.40. Stress-strain response of the atactic PVC models at 100 K and 300 K..... 298

Figure 6.41. Evolutions of potential energy and its constituents for Iso-10-100 at 300 K 301

Abstract

Structural health monitoring (SHM) and performance assessment are increasingly integrated to modern civil engineering projects in order to prevent and mitigate their catastrophic premature failures. Significant advancements in sensor and communication technologies during the last decades have boosted research on SHM and revolutionized its traditional and low-tech techniques.

Inherent variability and uncertainties in soils arising from different sources (e.g. data insufficiency) pose significant challenges to the design of geosystems (e.g. geosynthetically-modified structures), but the increasing trend in using SHM and performance evaluation techniques could offer substantial help in counterbalancing the design uncertainties and to identify the impending failure of high-risk geosystems.

Strain gauges, optical fibers and extensometers are current technologies to measure strains in geosynthetics where the sensing is achieved by attaching these devices to a geosynthetic layer in desirable positions. However, these devices require complex and expensive data acquisition systems to collect information. Also, strain gauges attached to a reinforcement material need to be calibrated against global strains from crosshead displacements in in-isolation tensile tests. However, the resulting calibration factors are typically not accurate when the reinforcement layer is embedded in soil due to the local stiffening effect of the bonding assembly, difference in the in-soil mechanical properties and other complications such as soil arching.

During the last few years, a novel technique has been under development at the University of Oklahoma based on the strain sensitivity of polymer nanocomposites to measure the

tensile strain in modified geosynthetics without the need for conventional instrumentation. In this technique, electrically-conductive fillers are used to induce conductivity in geosynthetics in order to produce sensor-enabled geosynthetics (SEG). The electrical conductivity of a SEG product with a prescribed concentration of a conductive filler is highly sensitive to the applied strain, affording the product the self-sensing function.

As part of this long-term study to develop SEG materials, an interdisciplinary study was carried out as described in this dissertation to develop sensor-enabled geogrids (SEGG) through laboratory experiments and molecular-scale simulations. The study yielded several formulations and production processes in the laboratory to fabricate nanocomposites that would exhibit adequate mechanical and strain-sensitive electrical properties for SEGG applications. Molecular dynamics and Monte Carlo simulations were used to gain insight into the laboratory results on a more fundamental level. The molecular dynamics simulations were carried out to study the mechanical properties of the composites whereas Monte Carlo simulations were used to examine their electrical conductivity (i.e. percolation) behavior. Results showed that, contingent upon further development and addressing practical issues such as durability and protective measures for field installation, the SEGG technology holds promise to offer a practical and cost-effective alternative to the existing technologies for performance-monitoring of a wide range of geotechnical structures during and after construction.

CHAPTER 1. INTRODUCTION

1.1. Geosynthetics and performance monitoring of geosynthetic structures

Geosynthetics are products made mostly from synthetic polymers of polypropylene (PP), polyvinyl chloride (PVC), polyester (PET) or polyethylene (PE) that are extensively used with soil and rock in a wide range of applications such as separation, reinforcement, filtration, containment, drainage and combinations thereof (Koerner and Hsuan 2001; Kay *et al.* 2004). Since their introduction in the late 1960s, the application of geosynthetics has rapidly expanded in many aspects of civil, geotechnical, geoenvironmental, hydraulic and transportation engineering practice and is currently a multi-billion dollar industry (Holtz 2001).

As increasing numbers of structures and facilities are constructed using geosynthetics, it becomes more important to monitor them to ensure their safety and serviceability. In situ monitoring of these structures can help to prevent costly repairs due to inadequate structural performance and possibly, catastrophic failures.

1.2. Nanotechnology

The word "nano" is a scientific prefix that denotes a factor of 10^{-9}. There is, however, no clear consensus about the definition of nanotechnology. A survey on its definition that was conducted for the inaugural issue of the journal *Nature Nanotechnology* yielded a variety of

perspectives. Most responses revolved around studying, understanding and manipulating matter at the scale of nanometers. This inconceivably-small dimension is 100,000 times thinner than a strand of human hair. Controlled arrangement of atoms at this scale has enabled the creation and utilization of custom-designed, ultra-precise structures, devices and systems that exhibit novel properties and functions at larger scales (Nat Nano 2006). Single-atom transistors (Fuechsle *et al.* 2012), artificial muscles (Haines *et al.* 2014) and molecule printers (Li *et al.* 2015) are only a few examples that owe their existence to nanotechnology.

Envisioned as early as 1959 by the renowned physicist Richard Feynman, nanotechnology, in its traditional sense, means the bottom-up formation of materials and structures with atomic precision (Feynman 1992; CRN 2015):

> *"I want to build a billion tiny factories, models of each other, which are manufacturing simultaneously… The principles of physics, as far as I can see, do not speak against the possibility of maneuvering things atom by atom. It is not an attempt to violate any laws; it is something, in principle, that can be done; but in practice, it has not been done because we are too big."*
>
> Richard Feynman, 1965 Nobel Prize Laureate in Physics

Research at nanoscale gained momentum after the advent of scanning tunneling microscopy (STM) in 1982 (Binnig *et al.* 1982) and atomic force microscopy (AFM) in 1986 (Binnig *et al.* 1986) by the IBM's Zürich research group led by Gerd Binnig. The invention of STM awarded him and Heinrich Rohrer the 1986 Nobel Prize in Physics, shared with Ernst Ruska for the design of the first electron microscope in 1933. The features offered by these imaging techniques provided researchers with an unprecedented ability to observe and manipulate individual atoms and discover exceptional materials and atomic structures, particularly three allotropes of carbon namely buckminsterfullerene, carbon nanotube (CNT) and graphene.

Buckminsterfullerene (buckyball) is a hollow, spherical fullerene molecule consisting of 60 carbon atoms arranged in the shape of a soccer ball (Figure 1.1). Its discovery in 1985 awarded the 1996 Nobel Prize in Chemistry to Robert Curl and Richard Smalley of Rice University and Harold Kroto of the University of Sussex. Later, the characterization of CNT by Sumio Iijima in 1991 (Iijima 1991) spawned tremendous research activities that have led to outstanding breakthroughs in many fields. More recently, the discovery (or more accurately, isolation) of graphene in 2004 (Novoselov *et al.* 2004), which laureled two scientists of the University of Manchester the 2010 Nobel Prize in Physics, opened a new window and a prospect of endless possibilities for improved devices, structures and materials.

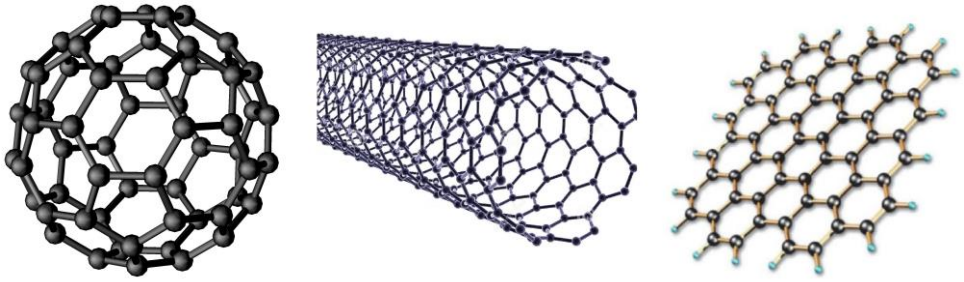

Figure 1.1. Different variety of nanocarbons

1.3. Electrically-conductive polymer composites

Nanotechnology has held promise to bring a wave of radical innovation to various areas. One of the areas where nanotechnology has sparked a revolution is polymer composites filled with conductive fillers. Incorporating conductive fillers into a polymer matrix results in a nanocomposite that typically offers a combination of properties and a diversity of applications that would otherwise be impossible to obtain using its constituents alone.

Particularly, the electrical properties of these fillers are a strong function of their atomic structure, and dispersing a sufficient quantity of them in a dielectric polymer results in a conductive polymer composite. Conductivity, when paired with other desirable characteristics (e.g. flexibility, affordability and durability), makes the composite technologically and economically attractive in a legion of applications. Example applications of conductive polymer composites include electromagnetic interference (EMI) shielding (the ability to block electromagnetic radiation, particularly that in the radio frequency régime – Luo and Chung (1999); Geetha *et al.* (2009)) and stimulus-response or self-sensing materials (Yang *et al.* 2012).

1.3.1. Common conductive fillers

Metal nanopowders and nanocarbons are the popular conducive fillers used in composites research and industry. Silver (Ag), nickel (Ni), gold (Au) and copper (Cu) are examples of highly-conductive metal nanopowders. Among them, silver has the highest room temperature electrical and thermal conductivity. Although metals are superior conductors (typical conductivity in the order of 10^{6} S/cm in contrast to typical conductivity values in the range 10^{-14} to 10^{-17} S/cm for polymers – Clingerman *et al.* (2003)), their application is limited due to their increasing effect on the weight of the composite as well as their poor conductivity after aging and oxidation/corrosion, especially at elevated temperatures and humid environments (Li *et al.* 2010).

Compared to metals, nanocarbons or carbonaceous fillers have a lower conductivity in the range of 10^{-1}–10^{+2} S/cm (Probst 1993; King *et al.* 2009a). However, this property has been exploited in an extensive range of applications in electronic components, cables, electrodes

and highly-sensitive strain sensors (Sánchez-González *et al.* 2005). Besides CNTs, graphene and fullerene, carbon blacks (CBs) and carbon fibers are other examples for nanocarbons.

1.3.1.1. Carbon blacks

Carbon black (CB) is an amorphous form of carbon with a structure resembling disordered graphite (Huang 2002). Its structure can be categorized as one between crystalline and amorphous materials (Biscoe and Warren 1942). CB is formed when aromatic hydrocarbons are subjected to incomplete combustion at high temperatures. Under these conditions, rupture occurs at the C-H bounds resulting in dissociation of the hydrocarbon molecules into carbon atoms and aromatic radicals. Subsequently, carbon atoms and aromatic radicals react to form layer structures composed of hexagonal carbon rings. Three to four hexagonal layers are combined in crystallites or bundles that join to form prime particles of CB, which further fuse into primary aggregates. van der Waals forces cause these aggregates to unify into more loosely-assembled agglomerates (Medalia 1986; Donnet 1994; Accorsi and Romero 1995; Huang 2002).

The structure of CB has been the subject of numerous studies. Based on the X-ray diffraction patterns of CB, Warren (1934) showed the existence of single graphite layers in the CB structure resulting in a heterogeneous mixture of particles which range from a few graphene layers up to several-layers-thick graphite crystals. Franklin (1951) studied the structure of carbons of different origin and showed that the majority of carbons correspond to one of two well-defined and markedly-different types of non-graphitizing and graphitizing carbons. The non-graphitizing carbons are formed from substances containing little hydrogen or much oxygen and have a strong system of crosslinking, which immobilizes the structure and

unites the crystallites in a rigid mass. The graphitizing carbons, in contrast, are made of substances containing a significant amount of hydrogen and have a low degree of crosslinking, resulting in a relatively-softer and less-porous structure. Franklin (1951) showed that the dominant types of carbon can be distinguished according to their deviation from graphite. Therefore, the properties of CB can be predicted from the properties of the graphite crystal.

The graphite crystal consists of stacks of multi layers 0.335 nm apart (Figure 1.2). Each layer consists of monatomic thick sheet of sp^2-hybridized carbon atoms 0.142 nm apart arranged in a honeycomb lattice and linked by covalent bonds, having a bond stretch potential energy of 400 kJ/mol. These strong bonds are responsible for the extremely strong and stiff nature of the in-plane graphite structure (*a*-axis). However, the strength in the perpendicular direction (*c*-axis) is relatively low due to the weak van der Waals bonds between the layers (Fitzer and Manocha 1998).

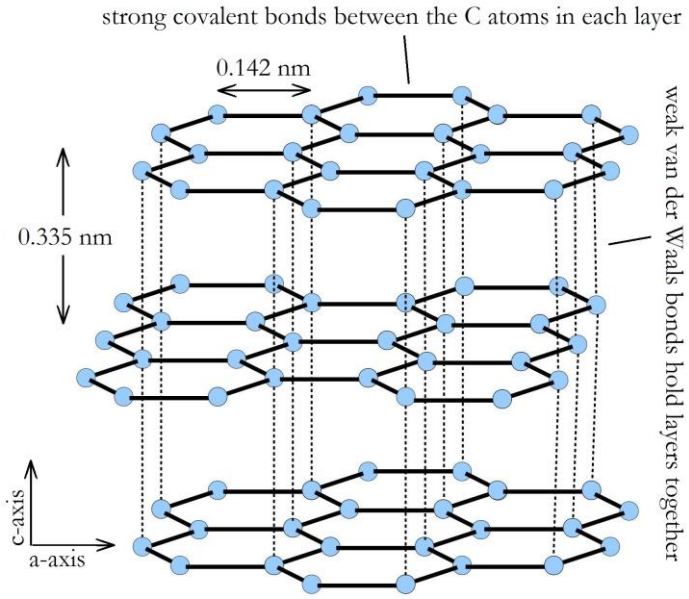

Figure 1.2. Graphite's structure (after Medcoat (2015))

The structure of CB is determined according to the particle size, aggregate size and shape of its primary particles. Smaller primary particles have higher interaggregate attractive forces, resulting in a CB with higher structure and larger agglomerate size. A low-structure CB, in contrast, is formed when the aggregates are composed of few primary particles (Medalia 1986). A quantitative characterization of the CB structure is provided by the oil absorption number (AON – also known as DBPA – Laube *et al.* (2001)), which is the amount of oil absorbed by 100 grams of CB particles. AON is determined according to ASTM D2414 (2013).

1.3.1.2. Carbon nanotubes

Among different types of fillers used in polymer nanocomposites, carbon nanotubes (CNTs) provide outstanding characteristics such as high flexibility (Cooper *et al.* 2001), low mass density (Gao *et al.* 1998) and large aspect ratio (length-to-diameter ratio – Guo *et al.* (2014)) together with their exceptional mechanical and electrical properties. A comparison of the mechanical and transport properties between CNT, A36 steel, copper and polyacrylonitrile-based (PAN) carbon fiber is given in Tables 1-1 and 1-2.

Table 1-1. Mechanical properties of CNT vs. A36 steel and PAN carbon fiber

Material	**Specific density**	**Young's modulus (TPa)**	**Tensile strength (GPa)**	**Ultimate strain (%)**	**Source**
CNT	1.3–2	0.2–5	10–60	10–15	Koziol *et al.* (2007)
A36 steel	7.8	0.2	0.4–0.55	20.0	
PAN carbon fiber	1.7–2	0.2–0.6	1.7–5	0.3–2.4	Liu *et al.* (2008)

Table 1-2. Transport properties of CNT vs. copper and PAN carbon fiber (at 298 K)

Material	Thermal conductivity (W/(m·K)	Electrical conductivity (S/m)	Source
CNT	2e3–6e3	10e6–10e7	(Li *et al.* 2007c); Han and Fina (2011)
Copper	385	6e7	
PAN carbon fiber	8e5	1e7	Wang *et al.* (2014)

CNTs can be produced in several ways. Small quantities of high-quality CNTs can be produced by cooling the carbon plasma generated either during an arc discharge between two graphitic electrodes in an inert atmosphere (Iijima 1991) or by laser ablation of a graphitic target (Thess *et al.* 1996). Today, almost all CNTs in industrial quantities are produced using catalytic chemical vapor deposition (CVD). CVD, which is practiced in a variety of formats, basically involves the decomposition of various hydrocarbons (e.g. methane or acetylene mixed with nitrogen or hydrogen) by passing them over catalytic metal particles (Li *et al.* 1996). Although CVD offers the possibility of controlling the growth of CNTs by patterning the catalyst (Kong *et al.* 1998), it introduces a higher concentration of defects to CNTs that will in turn diminish their stiffness (Salvetat *et al.* 1999) and tensile strength (Barber *et al.* 2005; Kis and Zettl 2008). Enhanced manufacturing and large-scale production have led to a significant drop in the price of CVD-produced CNTs, from around $1,500,000 per kilogram in 1999 to retail prices in the range of $50–$300 per kilogram today (Cheaptubes 2015).

With respect to their structure, CNTs are categorized into three types (Figure 1.3): 1) single-walled CNTs (SWCNTs), which can be conceptualized as a one-atom-thick layer of graphite (i.e. graphene – Figure 1.1) rolled into a seamless cylinder with a diameter ranging between 0.7 and 50 nm and with a tube length that can be many millions of times longer and possibly capped with a hemi-fullerene at the ends, 2) double-walled CNTs (DWCNTs), consisting of

two concentric cylinders and 3) multi-walled CNTs (MWCNTs), which are comprised of 3 to 30 concentrically-nested tubes having an outside diameter generally between 1 and 100 nm and a typical shell separation of 0.34 nm, which is equivalent to the distance between graphene layers in graphite (Muster *et al.* 1998; Mir *et al.* 2008; Grady 2011).

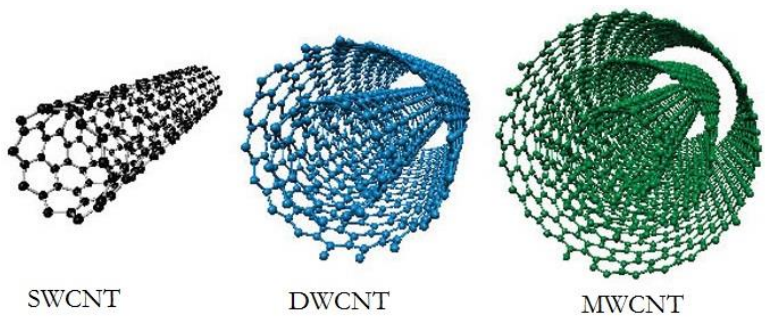

Figure 1.3. Types of carbon nanotube (Physicsworld 2015)

Besides the number of walls, the properties of CNTs are significantly influenced by their geometry, which can be reproduced by rolling a graphite/graphene sheet at a specific direction. This direction that imparts a characteristic twist known as "chirality" to the structure of CNTs is represented by the chiral vector $\mathbf{C}_h$ expressed as (Saito *et al.* 1992):

$$\mathbf{C}_h = n\mathbf{a}_1 + m\mathbf{a}_2 \tag{1-1}$$

where $\mathbf{a}_1$ and $\mathbf{a}_2$ denote the unit vectors 60° apart shown in Figure 1.4a, and (n,m) is a pair of integer indices (chiral indices) that collectively determine the direction and length of $\mathbf{C}_h$ which respectively correspond to the angle of twist and the diameter of a CNT. With the definition given in Figure 1.4, $\mathbf{a}_1$ and $\mathbf{a}_2$ can be expressed using the standard (x,y) Cartesian coordinate system in the plane as:

$$\mathbf{a}_1 = (\frac{3}{2}a_{cc}, \frac{\sqrt{3}}{2}a_{cc}) \tag{1-2}$$

$$\mathbf{a}_2 = (\frac{3}{2}a_{cc}, -\frac{\sqrt{3}}{2}a_{cc}) \tag{1-3}$$

where a_{cc} is the bond length of carbon atoms and, neglecting the curvature of the CNT, is approximately equal to that for graphite (i.e. 1.42 Å – Figure 1.2). Therefore, the unit lengths of $\mathbf{a}_1$ and $\mathbf{a}_2$ are the same and equal to $\sqrt{3}\ a_{cc}$. The circumferential length of the CNT, L, is then given by:

$$L = |\mathbf{C}_h| = \sqrt{\mathbf{C}_h.\mathbf{C}_h} = \sqrt{3}a\sqrt{n^2 + nm + m^2} \tag{1-4}$$

which gives the diameter of nanotube as:

$$d = \frac{L}{\pi} = \frac{\sqrt{3}a\sqrt{n^2 + nm + m^2}}{\pi} \tag{1-5}$$

Also, the chiral angle θ (angle between the chiral vector and the zigzag direction) is defined as:

$$\theta = \tan^{-1}\left[\sqrt{3}m/(m + 2n)\right] \tag{1-6}$$

If $m = 0$ ($\theta = 0°$), the CNT is called zigzag, and if $n = m$ ($\theta = 30°$), the CNT is called armchair, and it is chiral ($0° < \theta < 30°$) otherwise (see the models shown in Figure 1.4b).

As mentioned earlier, chirality has a strong impact on the properties of CNTs. For instance, armchair CNTs exhibit metallic characteristics, and the CNTs for which $|n - m| = 3i$ (i is an integer) are semiconductive (Blase *et al.* 1994; Wilder *et al.* 1998). From the mechanical point of view, strength and Poisson's ratio are strongly affected by chirality, while Young's modulus is practically independent of chirality for CNTs greater than 0.7 nm in diameter (Hernández *et al.* 1998).

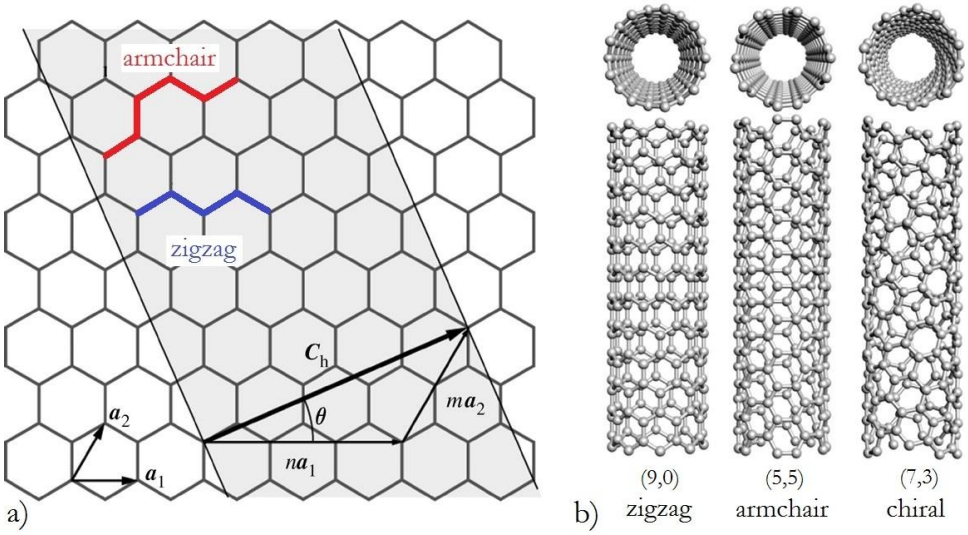

Figure 1.4. a) Schema of CNT formation by rolling a graphene sheet and b) models of zigzag, armchair and chiral CNTs (after Kis and Zettl (2008))

1.3.2. Filler dispersion

As stated earlier, dispersing a sufficient concentration of conductive particles such as CB, carbon fiber, CNT or synthetic graphite in an insulating polymer matrix can develop a continuous conducting network that provides comparatively low-resistance electrical paths for the free movement of electrons (Bigg 1984; Simon 1985; Du *et al.* 2004). This is partly because electrons can flow across the polymer barrier when the distances between conductive particles/aggregates become less than some critical value (e.g. 10 nm).

Proper dispersion of filler particles in a host polymer is crucial in order to produce conducting polymer composites that would exhibit a desired level of accuracy and consistency in their electrical and mechanical response. Generally, conductive fillers are dispersed in a polymer by applying shear force to the polymer/filler mixture. When the shearing forces acting on the filler agglomerates during the mixing process overcome the weak van der Waals forces between the filler aggregates, the agglomerates are broken up into

primary aggregates (Huang 2002). The processing temperature, duration and pressure influence the arrangement of filler particles in the resulting composite. For example, Chan *et al.* (1997) showed that the effects of temperature and processing duration on the resistivity of CB-filled composites are significantly greater than the effect of pressure. Furthermore, they stated that using a greater amount of filler increases the viscosity of the mix, and longer processing durations and higher temperatures result in a more-resistive composite. Moreover, it was shown by Bigg (1984) that composites with highly-structured CB are more sensitive to the processing duration.

During the very first stages of mixing, the conductivity of filled composites increases rapidly mainly due to the distribution of particulate fillers in the polymer matrix (dispersion) as well as the establishment of conductive pathways among the particles and agglomerates (Stage I in Figure 1.5). After an optimum mixing duration (Stage II), the conductivity gradually decreases primarily due to the breakage in the continuous conductive network, resulting in the formation of gaps between individual aggregates (Stage III). Beyond a certain time, the breakdown in the conductive network is ceased and a shearing resistant structure is established (Dannenberg 1952; Das *et al.* 2002).

The mixing effort also influences the mechanical properties of a filled composite. For instance, by compounding styrene-butadiene rubber with two types of CB with different structures, Cembrola (1982) concluded that prolonged mixing duration would reduce the dynamic modulus of the blends.

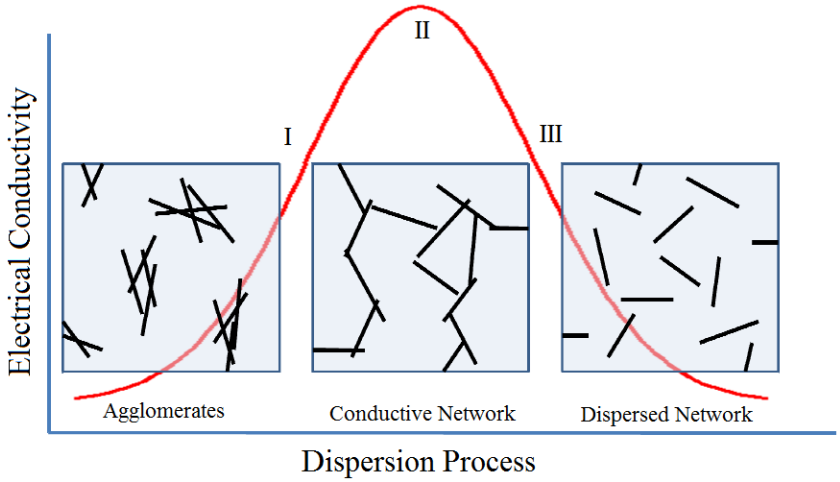

Figure 1.5. Filler dispersion vs. electrical conductivity (After Peters (2009))

1.3.3. Percolation threshold

The term *percolation* was coined by Broadbent and Hammersley (1957) who studied the fluid seepage through a porous medium with randomly-blocked channels. Besides transport properties of porous media, the percolation phenomena arise in many other applications, including mechanical properties of composites and porous media, fracture process in heterogeneous rock formations, spread of diseases and fires and even star formation in galaxies, just to name a few (Torquato 2001). For the insulator-conductor transition in a polymer composite, the percolation threshold is the lowest concentration of conductive fillers at which a sample-spanning cluster first appears within the composite (Bunde and Dieterich 2000). Here, a cluster is simply a connected group of elements, and what constitutes a cluster depends on the definition of connection.

Figure 1.6 shows the formation stages of spanning clusters each corresponding to a specific filler concentration shown in Figure 1.7. During the first stage, the electrical conductivity of the composite is close to that of the electrically-insulating polymer matrix simply because the

conductive filler particles (CFPs) are not sufficient to establish a conductive network. As the number of CFPs increases, the filler fraction exceeds the lower bound, ϕ_L, of a region called the *percolation region*, across which the conductive network is developed. The electrical conductivity of the composite in this stage (Stage II) is slightly higher than that in Stage I which can be attributed to the *tunneling (hopping) conduction* through the thin layers of polymer sandwiched by CFPs (Sarychev and Brouers 1994; Alamusi *et al.* 2011). By loading the composite with more CFPs, an excess energy caused due to the formation of carbon-polymer interfaces reaches a universal value independent of polymer type, and then the CFPs begin to coagulate to form conductive networks in the composite, from Stage II to Stage III (Miyasaka *et al.* 1982). As the level of doping is increased to a concentration called *percolation threshold*, ϕ_P, the trends in conductivity imply that there is a transition in the nature of charge transport from tunneling to partial metallic diffusive transport (Stage III – Du *et al.* (2004)).

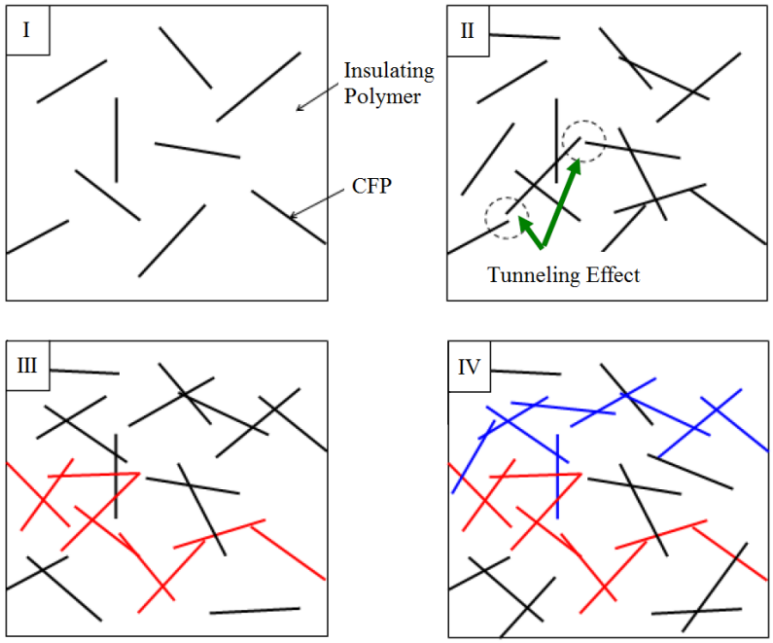

Figure 1.6. Percolation process in CFP-filled composites (After Alamusi *et al.* (2011))

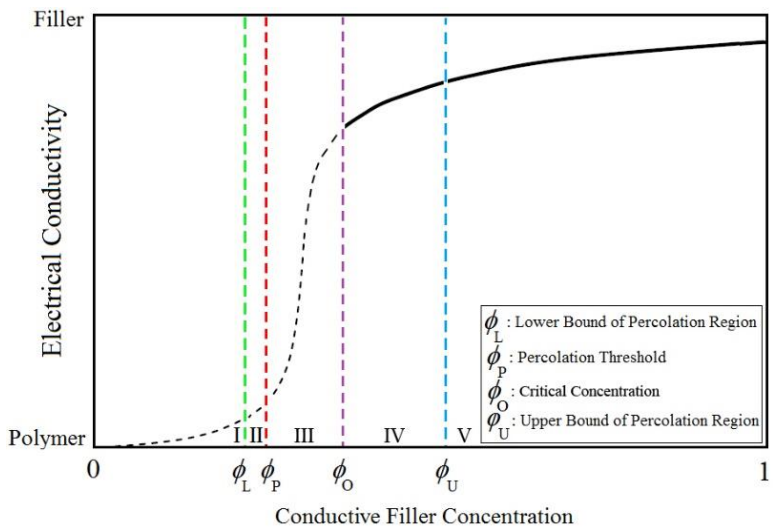

Figure 1.7. Filler concentration vs. electrical conductivity ((After Alamusi *et al.* (2011))

Both the percolation threshold and the conductivity of the filled composites are influenced by the type, size, shape and structure, orientation, porosity and surface chemistry of the filler, the chemical structure, surface properties and crystallinity of the polymer as well as the processing methods and conditions employed (Narkis *et al.* 1981; Wu 1982; Sumita *et al.* 1986a; Sumita *et al.* 1986b; Tchoudakov *et al.* 1996; Breuer *et al.* 1997). For CB as the conductive filler, smaller particles lower the percolation threshold (Jing *et al.* 2000). Also, in case of using carbon fibers or CNTs, larger aspect ratios (length-to-diameter ratios) and a broader range of aspect ratios decrease the percolation threshold (Göktürk *et al.* 1993; Yi and Choi 1999). The difference between the surface energies (usually measured with the Washburn adsorption method – Washburn (1921)) of the filler and polymer is a determining factor in terms of the materials surface properties. The smaller the difference, the better wetting of the filler, the larger amount of polymer coating the filler, the more uniform filler dispersion and, consequently, the higher percolation threshold and electrical conductivity (Mamunya *et al.* 1996; Clingerman *et al.* 2003).

Adding more CFP to the composite would slightly increase its conductivity due to the evolution of the existing or formation of new conductive paths (Stage IV). Beyond a certain concentration, ϕ_U, the upper bound of the percolation region, the conductivity levels off to a value lower than that of the conductive filler (Stage V).

The filler concentration at which the electrical conductivity of a composite would drastically change due to strain is called the *critical (target) concentration*, which is defined according to the type of the strain (tensile or compressive). If the composite is subjected to a tensile strain, the upper bound of the percolation region (transition from Stage III to Stage IV) is the critical concentration. In contrast, the critical concentration would be the lower bound (transition from Stage II to Stage II) in case of compressive strains.

It is noteworthy that the electrical conductivity of semi-conductive materials (including CB-filled polymers) is also influenced by temperature. In fact, temperature-induced insulator–conductor transition is another important mechanism beside percolation that can change the conductivity of filled polymers, especially semi-crystalline polymer composites such as PVC. However, this mechanism is only effective when the polymer matrix is close to its melting point (e.g. > 115 °C for PE, PP and PVC) where a sudden expansion in the matrix due to melting results in the breakage of the conducting network, reducing the electrical conductivity (Huang *et al.* 1999).

1.3.4. Strain-sensitive electrical conductivity of filled composites

Tensoresistivity refers to the change in the electrical resistance of a material due to a tensile stress as opposed to *piezoresistivity* which denotes the pressure-induced increase of the

mobility of electrons. The tensoresistivity mechanism is schematically depicted in Figure 1.8. The rupture occurring in the conductive network due to tensile loading results in a drop in the conductivity of the composite. Composites filled at the critical concentration (see Section 1.3.3) show the highest level of sensitivity to strain.

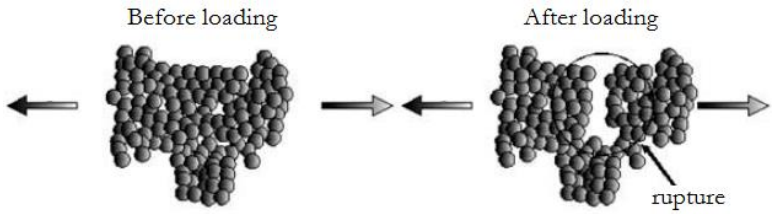

Figure 1.8. Schematic illustration of the rupture causing tensoresistivity (After Fathi (2011))

The tensoresistivity of CB- and CNT-filled composites has been shown by measuring the change in the electrical resistance of the composites when subjected to tensile strain (Calvert *et al.* 2007; Knite *et al.* 2007; Hatami *et al.* 2009; Wichmann *et al.* 2009; Fathi *et al.* 2012; Tang *et al.* 2012; Yang *et al.* 2012). Some of the different methods used to manufacture strain-dependent materials are as follows:

- integrating a textile substrate with several layers of the filled composite; the textile substrate is coated with the blend, left to dry, and finally protected using a latex film (Koncar *et al.* 2009; Lynch *et al.* 2009),
- bonding a layer of filled composite to a specimen using strain gauge adhesives (Park *et al.* 2008), and
- extrusion of the host polymer with CB or CNT fillers to fabricate a conductive composite.

1.4. Molecular-scale simulations in nanotechnology

As a crucial factor to the continued vitality of countless industries, design and development of engineered materials have significantly benefited from modeling and simulation techniques. Substantial advances in computational resources have facilitated the use of experimentally-validated modeling and simulation techniques in understanding and predicting materials behavior from their fine structures (i.e. chemical constitutions, macromolecular arrangements and physical interactions) at scales spanning nanoscopic to macroscopic. The crucial advantage of these techniques is the ability to address a wider range of factors and parametric values that would otherwise be difficult or unfeasible to investigate in the laboratory. Several computational modeling techniques have thus far been proposed for the simulation of materials (e.g. see a review by Steinhauser and Hiermaier (2009)). However, due to the enormous spread of length and time scales associated with different materials, no single technique has proven to accurately describe the behavior of all materials, and hierarchical multi-scale approaches are often needed to do so (Uhlherr and Theodorou 1998).

Among other computational techniques, molecular dynamics (MD) and Monte Carlo (MC) simulations have been extensively used in materials science and engineering. MD simulations have primarily been used to study the mechanical properties of polymers and filled polymer composites, whereas their electrical properties have mostly been the subject of MC simulations.

1.4.1. Monte Carlo simulations

Monte Carlo (MC) method is a powerful class of computational algorithms in which random sampling is used to estimate definite results (Dunn and Shultis 2011). MC simulations are commonly used wherever a problem is too complicated to solve analytically. Systems with large number of coupled degrees of freedom, numerical problems with complicated boundary conditions and any phenomena with significant uncertainty in inputs are a few examples of the areas that benefit from MC simulations (Jain 1992). MC method is essentially underlain by two statistical theorems: the *law of large numbers* and the *central limit theorem*. The law of large numbers denotes that estimation for an expected value eventually approaches the expected value by increasing the number of iterations. The central limit theorem indicates that besides the estimated value itself, its uncertainty can also be calculated. Therefore, an MC simulation not only provides an estimated answer for a definite value, but also evaluates the accuracy of the estimated answer.

Essential for MC simulations is a reliable source of random numbers. A myriad of random number generators have been proposed in the literature. Marsaglia *et al.* (1990) summarized the following desirable characteristics for a random number generator:

- *Randomness*. The generator should provide a sequence of independent, uniformly-distributed random numbers, suitable for all reasonable applications. In particular, the generator should pass stringent tests for randomness and independence.

- *Long period*. Without repeating the initial sequence, the generator should be able to produce all of the random variables of a huge sample that are accessible by current computer speeds.

- *Computational efficiency*. The execution should be rapid, with modest memory requirements.

- *Repeatability*. Initial conditions (seed values) completely determine the resulting sequence of random variables.

- *Portability*. Identical sequence of random variables may be produced on a wide variety of computers, for given seed values.

- *Homogeneity*. All subsets of bits of the numbers are random, from most- to least-significant bits.

1.4.2. Molecular dynamics simulations

Molecular dynamics (MD) simulation is a simple yet powerful tool in computational statistical mechanics to study the temporal evolution (fluctuations and conformational changes) of a system over short length and time scales. In fact, MD simulation is a modern realization of an old idea in science which asserts that the equilibrium and motion of a classical, interacting N-body system can be computed if the initial conditions and forces of interaction are known. This is the simplicity of MD simulations yet their capability in handling a broad range of problems from simple to intricate at any required level of detail that distinguishes them from alternative approaches and makes them indispensable in both pure and applied research (Haile 1997; Rapaport 2004).

The key idea in MD is motion (dynamic properties), which describes how position, velocities and orientations change over time. In a simulation, the positions and momenta of N bodies

(atoms) are mapped into a 6*N*-dimensional hyperspace, called *phase space*. Phase space is comprised of a 3*N*-dimensional *configurational space*, where the coordinates of atoms are defined, and a 3*N*-dimensional *momentum space* in which the atoms' momenta are specified. At one instant, the positions and momenta of the entire *N*-atom system are represented by a point in the phase space. Atoms are allowed to interact for a period of time. These interactions result in a change in the positions and momenta of the atoms as they dart back and forth, twisting, turning and colliding with one another and the container. As a result, a trajectory (motion picture) is constituted that follows interacting particles (i.e. molecules or atoms). This trajectory is obtained by numerically solving the Newton's equation of motion, or equivalently Hamilton's equations. The overall simulation framework is controlled by the ensemble(s) (Section 1.4.2.2) of choice (Haile 1997).

An efficient MD algorithm provides an accurate answer with as few operations as possible (Griebel *et al.* 2010). The minimum number of operations required to achieve a given accuracy ε is called ε–complexity. Algorithm 1-1 shows a basic algorithm for the computation of the trajectories of *N* particles.

```
{
t = t_start;
for i = 1, …, N
      set initial conditions x_i (positions) and v_i (velocities);
while (t < t_end) {
      compute for i = 1, …, N the new positions x_i and velocities v_i at time t
      + delta_t by an integration procedure from the positions x_i, velocities v_i
      and force F_i on the particle at earlier times;
      t = t + delta_t
}
```

Algorithm 1-1. Basic algorithm for computation of trajectories of *N* particles (After Griebel *et al.* (2010)).

1.4.2.1. Force fields

Force fields define the energy of a system through identifying and evaluating the interactions among the particles in the system. Numerous force fields have been proposed in the literature, ranging from relatively simple to more complicated ones. Dreiding, for instance, is a generic force field designed for predicting the structures and dynamics of organic, biological and main-group inorganic molecules containing a variety of atoms (Mayo *et al.* 1990). CHARMM (Chemistry at HARvard Molecular Mechanics), AMBER (Assisted Model Building and Energy Refinement), CFF, PCFF, OPLS and CVFF are just some of the other frequently-used force fields. Here, Dreiding force field is briefly explained due to its simplicity and enough confidence in dealing with polymer systems.

1.4.2.1.1. Dreiding force field

The potential energy E of a generic force field for an arbitrary geometry of molecules is typically the sum of bonded E_{VAL} (covalent; pairs of electrons shared between atoms) and non-bonded E_{NB} (non-covalent) interactions:

$$E = E_{\mathrm{VAL}} + E_{\mathrm{NB}} \tag{1-7}$$

where

$$E_{\mathrm{VAL}} = E_{\mathrm{B}} + E_{\mathrm{A}} + E_{\mathrm{T}} + E_{\mathrm{I}} \tag{1-8}$$

$$E_{\mathrm{NB}} = E_{\mathrm{C}} + E_{\mathrm{VDW}} + E_{\mathrm{HB}} \tag{1-9}$$

in which E_B is the energy due to bond stretching (two-body); E_A is the energy due to angle bending (three-body); E_T is the energy due to torsion (four-body); E_I is the energy due to

out-of-plane configuration (four-body); E_C is the energy due to Columbic interaction; E_{VDW} is the energy due to van der Waals interactions; and E_{HB} is the energy due to hydrogen bonding. It is worth noting that while the above terms are common to all force fields and often able to determine structures in a satisfactory manner. However, other terms such as cross and improper terms are occasionally present in force fields to account for effects not accounted for by the terms above. Also, it is possible to include terms describing electronegativity or conjugative effects.

- Bonded interactions
    - Bond stretching interactions

Investigating how the energy of a bond changes with its length is helpful to find a functional form for bond stretching interactions. The minimum energy of a bond takes place at the *equilibrium* bond length. If the bond undergoes compression, the electron clouds of the two atoms forming it will gradually overlap, leading to a rapid increase in the energy. Similarly, stretching the bond beyond equilibrium results in an increase in the energy. The bond eventually disassociates if stretched above a certain level. Figure 1.9 shows a schematic view of the bond stretching interaction.

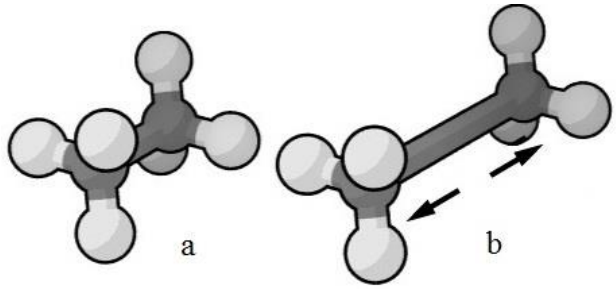

Figure 1.9. Bond stretching: (a) natural length and (b) stretched length

The default form for bond-stretching function in Dreiding is *harmonic*. For small deviations from the equilibrium length r_0, the bond energy of two atoms can be can be expressed as a Taylor series about r_0 as (Cheung 2002):

$$E(r) = E(r_0) + \left.\frac{dE}{dr}\right|_{r=r_0}(r - r_0) + \frac{1}{2}\left.\frac{d^2E}{dr^2}\right|_{r=r_0}(r - r_0)^2 + \frac{1}{6}\left.\frac{d^3E}{dr^3}\right|_{r=r_0}(r - r_0)^3 + \ldots \tag{1-10}$$

where r represents the distance between the atoms. Terminating the expression at the $(r - r_0)^2$ term reduces it to its simplest form, which is known as the harmonic approximation. Assuming $E(r_0) = 0$ and noting that at $r = r_0$ the force and hence the first derivative of the energy is zero, the bond stretching function in harmonic form can be written as:

$$E_B(r) = \frac{1}{2}k_r(r - r_0)^2 \tag{1-11}$$

where k_r is the harmonic force constant given by:

$$k_r = \left.\frac{d^2E}{dr^2}\right|_{r=r_0} \tag{1-12}$$

An analogy being made between a bond and a spring, Equation (1-11) is based on the Hook's law where k_r controls the stiffness of the bond spring. Accurate calculation of molecular structures and vibrational frequencies for situations with bond length deviating far from r_0 requires going beyond the harmonic approximation and including higher order terms usually up to $(r - r_0)^4$.

- Bond angle bending interactions

The energy associated with the change in a bond angle can also be expressed based on the Hook's law. For an angle θ formed by the atoms *IJK* (Figure 1.10), two frequently-used forms are harmonic cosine and harmonic angle forms defined as:

- Harmonic cosine form

$$E_{IJK} = \frac{1}{2} k_{IJK} \left[\cos\theta_{IJK} - \cos\theta_J^0 \right]^2 \tag{1-13}$$

- Harmonic angle form

$$E_{IJK} = \frac{1}{2} k_{IJK} \left[\theta_{IJK} - \theta_J^0 \right]^2 \tag{1-14}$$

where k_{IJK} is the stiffness of the spring. The equilibrium angle θ^0_J is assumed to be independent of atoms *I* and *K* and hence is only denoted by *J*. Harmonic cosine is a default functional form in Dreiding because its slope does not approach zero when θ is close to 180°.

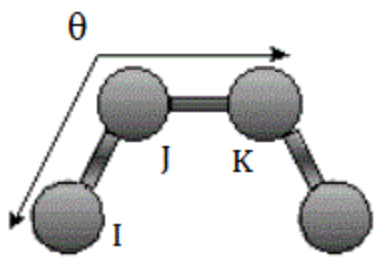

Figure 1.10. Bond angle bending

- Torsion (dihedral) interactions

Torsional deformation of a bond assembly is shown in Figure 1.11 where the dotted path is the locus of atom *L*. The interaction energy arising from the torsional deformation between the two bonds *IJ* and *KL* connected through *JK* is described as:

$$E_{IJK} = \frac{1}{2} k_{JK} \left\{ 1 - \cos\left[n_{JK} (\psi - \psi_{JK}^0 \right] \right\} \tag{1-15}$$

where ψ is the dihedral or torsional angle, defined as the angle between *IJK* and *JKL* planes. ψ^0_{JK} is the equilibrium angle; n_{JK} is periodicity; and k_{JK} is the stiffness to rotation.

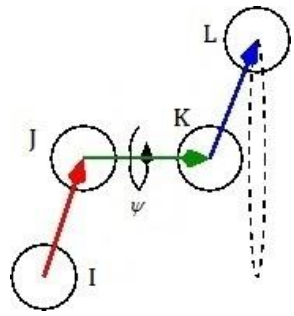

Figure 1.11. Torsion interactions

- Non-bonded interactions
    - Electrostatic interactions

The electrostatic interactions arise due to the unequal distribution of charge in a molecule and can be described using the Coulomb's law. According to the Coulomb's law, the force acting between two electric charges is radial, inverse-square and proportional to the product of the charges as:

$$E_C = \frac{1}{4\pi\varepsilon_0}\frac{q_i q_j}{r_{ij}^2} \tag{1-16}$$

where ε_0 is the permittivity of free space; q_i and q_j are atomic charges; and $r_{i,j}$ is the distance between the atoms *i* and *j* (Stone 1996).

    - van der Waals interactions

The van der Waals interaction, named after Dutch scientist Johannes Diderik van der Waals, includes all types of interactions between atoms (or molecules) that are not represented by electrostatic interactions (Burkert and Allinger 1982). Such interactions are comprised of four contributions: repulsion, attraction, induction and dispersion. When two atoms (or molecules) approach each other quite closely, their electron orbitals start to overlap, causing

a strong repulsion. At farther interatomic distances, an attractive interaction takes place between the electric dipoles of the two atoms where one of the dipoles generated by an instantaneous deformation of the electron cloud of one atom induces a dipole in the other atom. Induction interactions arise from the distortion of the charge distribution of a particle in the electric field of its neighbors. Finally, dispersion includes non-polar atoms arising from the interactions of instantaneous multipoles (Stone 1996).

The functional form of the collective interatomic interaction potential between a pair of non-ionic (neutral) atoms is shown in Figure 1.12. This interaction potential is commonly approximated using a simple mathematical model known as the Lennard–Jones (usually abbreviated as the L–J) potential and defined as (Jones 1924):

$$E_{VDW} = 4\varepsilon\left[\left(\frac{\sigma}{r}\right)^{12} - \left(\frac{\sigma}{r}\right)^{6}\right] \tag{1-17}$$

where r is the interparticle distance; σ is the finite distance at which the interparticle potential is zero (Figure 1.12); and ε is the depth of the potential well, which is the region surrounding a local minimum of potential energy (Figure 1.12).

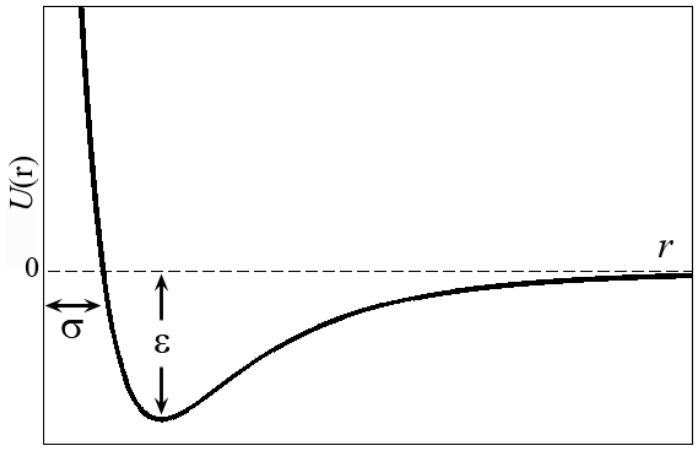

Figure 1.12. Functional form of the collective interatomic interaction potential between two non-ionic atoms

Calculation of non-bonded interactions is computationally expensive and contributes significantly to the overall simulation time. As these interactions occur between any two atoms, the associated computational time is in the order of N^2, where N is the number of atoms in the system. The electrostatic interactions are also long-range interactions that decay with distance. The rate of decay is proportional to the inverse square of distance, r^2, hence contributing even for large values of r. In MD simulations, a spherical vicinity with a radius called the *cutoff distance* is usually defined around each atom beyond which the long-range interactions are considered insignificant and truncated.

1.4.2.2. Ensembles

An ensemble formalizes the notion that a range of outcomes might be observed and different microscopic details might be produced from repeating an experiment under certain macroscopic conditions (i.e. temperature, volume and pressure) on a system. There are mainly four kinds of ensembles in statistical mechanics, namely micro-canonical (NVE), canonical (NVT), grand canonical ($TV\mu$) and isothermal-isobaric (NPT), where N, V, E, T,

μ, and P denote the number of particles or moles, volume of the system, energy, temperature, chemical potential and pressure, respectively. The macroscopic conditions for each ensemble (e.g. the number of particles, volume and temperature in NVT) are conserved during (part of) a simulation and other properties (e.g. pressure in NVT) are calculated.

1.4.2.3. Periodic boundary conditions

The boundary of a system of finite size must be properly treated in order to either compensate for the limited size of the system or model an infinite system (see Haile (1997) p. 4 for the difference between model and simulation). Periodic boundary conditions (PBC) are a type of boundary conditions that are usually used to simulate a cluster of particles in both periodic and non-periodic systems (Figure 1.13). It is natural to impose PBC on the boundaries of periodic systems, e.g. amorphous polymers. PBC are also applied to non-periodic systems to compensate for the limited size of a model. In PBC, the simulation box is replicated along a desired direction in space to form an infinite lattice. In the course of a simulation on system with PBC, when a particle moves in the central box, its periodic image in every one of the other boxes moves in exactly the same way (same orientation and speed). Although all these image particles move together, in fact only one of them is represented in the model. Also, the particles located close to opposite sides of the model interact with each other. It should be noted that there are no walls at the boundaries of the central box, nor does the system have any surface. The central box simply forms a convenient coordinate system to measure the trajectories of the particles (Griebel *et al.* 2010).

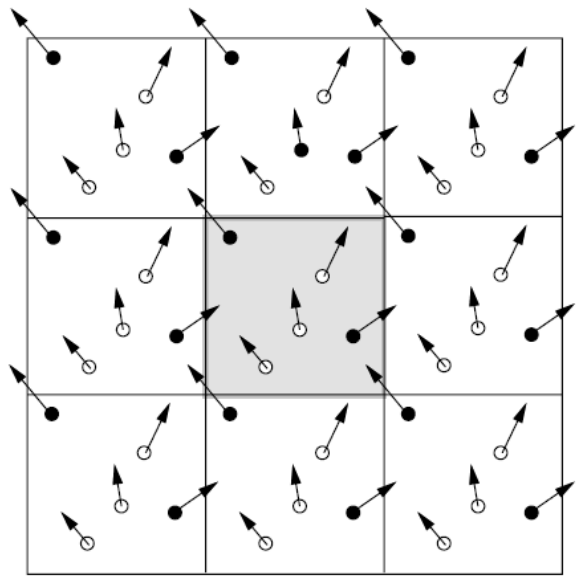

Figure 1.13. Periodic boundary conditions in two dimensions. The events in the primary cell are duplicated in each image cell.

1.4.2.4. Trajectories of particles

In MD, a trajectory (configurations as a function of time) of a molecular system consisting of N particles with masses [m_1, …, m_N] characterized by the positions [$\boldsymbol{r}_1$, …, $\boldsymbol{r}_N$] and the associated velocities [$\boldsymbol{v}_1$, …, $\boldsymbol{v}_N$] (respective momenta $\mathbf{p}_i = m_i\mathbf{v}_i$) is tracked by the simultaneous integration of Newton's equations of motion for all the atoms in the system. The force applied on the particle i is denoted by F_i:

$$m_i \ddot{r}_i = F_i, \quad i = 1,...,N \tag{1-18}$$

where the over-dot ˙ denotes the partial derivative with respect to time and:

$$F_i = -\nabla_{x_i} E(r_i,...,r_N) \tag{1-19}$$

By convention, attractive forces are negative while repulsive forces are positive. Given the initial conditions of a system (i.e. the positions and velocities of the particles), the evolution

of the MD simulation in time depends only on the gradient of the potential energy governing the interactions between the particle, which must be a differentiable function of the particle coordinates. The integration of Equation (1-19) is performed in small time steps Δt, typically 1–10 fs (femtosecond = 10^{-15} s) for molecular systems.

Time step is an important consideration in MD simulations. Ideally the time step in a simulation should be such that it can capture the fastest motion in the system which is typically the vibration mode of the lightest atom. In other words, the approximation of a physical system is satisfactory as long as the energy difference between adjacent vibrational energy levels, $h\nu$, is less than $k_B T$, where h is the Planck constant ($6.626\ 069\ 57 \times 10^{-34}$ J.s), ν is the vibrational frequency of an atom (1/s), k_B is the Boltzmann constant ($1.380\ 648\ 8 \times 10^{-23}$ J/K) and T is the temperature (K). For instance, a typical system at room temperature can be accurately approximated if $\nu < 0.6 \times 10^{13}$ Hz, i.e. for motions of time periods of about $t > 1.6 \times 10^{-13}$ sec or 0.16 ps (Harmandaris and Mavrantzas 2004).

1.5. Sensor-enabled geosynthetics

Strain gauges (Warren *et al.* 2010), optical fibers (Nishio *et al.* 2010; Lostumbo and Artieres 2011; Peters 2011) and extensometers (Watts *et al.* 1998) are the current technologies employed to measure strains in geosynthetics where the sensing is achieved by attaching the devices to a geosynthetic layer in key structural positions.

During the last few years, a novel technique has been developed based on the strain sensitivity (see Section 1.3.4) of polymer nanocomposites to measure the tensile strain in modified geosynthetics without the need for conventional instrumentation and ongoing

sensor calibration. In this technique, electrically-conductive fillers are used to impart electrical conductivity to a class of geosynthetics (e.g. geogrids) in order to produce sensor-enabled geosynthetics (SEG). The electrical conductivity of a SEG product with a prescribed concentration of conductive filler is highly sensitive to the applied strain (see Section 1.3.4).

Figure 1.14 shows a flowchart of the SEG development plan summarizing different phases of the study in the long run. So far, the proof-of-concept of the SEG technology has been established through laboratory tests on CB-filled PE and PP composites to measure the change in their conductivity when subjected to tensile strain (Hatami *et al.* 2009; Fathi 2011; Hatami *et al.* 2011; Fathi *et al.* 2012). Focusing on Phases 1 and 2, the primary objective of this dissertation is to develop strain-sensitive coated geogrids using laboratory tests and molecular-scale simulations.

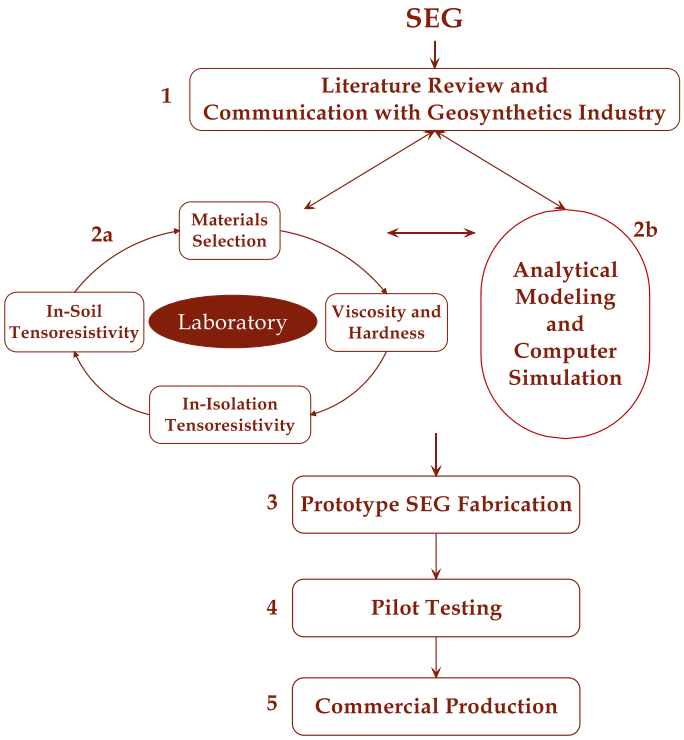

Figure 1.14. Outline of the SEG project

1.6. Scope and outline of the dissertation

1.6.1. Contribution toward SEG development

This dissertation revolves around three main research questions (RQs):

RQ 1: Can we induce tensoresistivity in coated geosynthetics (e.g. PVC-coated woven polyester geogrids) by adjusting the concentration of the conductive filler currently used in their chemical formulation without adversely impacting their primary functions (e.g. reinforcement)?

Significance: A small adjustment in the formulation of a geosynthetic product is expected to have little impact on its production cost, rendering the technology viable and cost-effective.

RQ 2: What are the alternative conductive and ancillary filler materials that could replace, or be used in conjunction with, the materials currently used in the formulations of geosynthetics, and how effective are they in developing self-sensing capability in the existing products?

Significance: Potential for better and more accurate performance, reduced costs and more sustainable sources of materials.

RQ 3: Can modified (i.e. sensor-enabled) geosynthetics (SEG) maintain their strain-sensing capability in the field?

Significance: Soil pressure and loading régime (e.g. cyclic loading in bridge abutments) could irreversibly damage the microstructure of conductive composites and, consequently, impair

their effectiveness in measuring the deformation of geosynthetic products. Study of these effects could lead to SEG formulations that could better withstand environmental influences on their field behavior.

1.6.2. Outline

The tasks carried out in this dissertation are based on the RQs outlined in the previous section and the literature survey provided in CHAPTER 2.

CHAPTER 3 addresses RQ 1. The functions of the materials in the chemical formulation of conventional coated geogrids are characterized. Details of laboratory tests are reported that were carried out to investigate the influence of the commonly-used CB fillers on the in-isolation mechanical and electrical properties and strain sensitivity of modified (i.e. sensor-enabled) geogrids (SEGG). The ability of SEGG to preserve their in-isolation strain sensitivity under cyclic loading is also studied. In addition, this chapter provides details and results of the laboratory experiments carried out to examine the in-soil strain sensitivity of SEGG (RQ 3).

CHAPTER 4 reports the laboratory tests that were carried out to investigate the in-isolation mechanical, electrical and strain-sensitive performance of SEGG filled with MWCNT as an alternative filler. The development and use of a microscopic imaging technique to characterize the depth profile of inclusions (including their size, orientation and dispersion) in MWCNT-filled PVC composites are discussed in detail.

CHAPTER 5 describes a series of MC simulations that were carried out to investigate the percolation behavior of polymer composites with CB and CNT fillers.

CHAPTER 6 includes the MD simulations that were carried out to study the mechanical properties of pristine polyethylene and PVC matrices and CNT-filled polyethylene composites. It also reports additional MD simulations that were carried out to investigate the influence of temperature, size, aspect ratio and chirality on the mechanical properties of SWCNTs under tension and compression. Furthermore, it describes the development of a failure criterion for graphene as an increasingly-popular filler used in nanocomposites.

CHAPTER 7 presents the summary and conclusions of the present work and recommendations for future work in the continuation of this study.

CHAPTER 2. LITERATURE SURVEY

This chapter reviews the state of the art or state of the practice in different subjects related to this multidisciplinary dissertation. Although the bibliography is lengthy, this survey is not intended to be comprehensive, and only the most salient studies are summarized, evaluated and compared.

2.1. Performance monitoring in geosynthetics engineering

2.1.1. Significance

Structural health monitoring (SHM) and performance assessment are increasingly integrated into modern civil engineering projects in order to assess their damage level and predict their future courses of safety and serviceability (Huston 2010; Bonessio *et al.* 2012). Performance monitoring of structures also helps engineers assess the accuracy and validity of the existing design approaches and improve them based on the actual field data and observations. Significant advancements in sensor and communication technologies during the last decades have boosted research on SHM and transformed its traditional and low-tech techniques (Aktan *et al.* 1997; Feng *et al.* 1998; Hera and Hou 2004; Ghanem and Ferro 2006).

In light of the inevitable aging and deterioration resulting from operational environments, *damage* in SHM is broadly defined as the changes introduced to the material

and/or geometric properties of a structure that adversely affect its intended function (Farrar and Worden 2008). Damage in a structure is evaluated by periodically collecting sampled responses of measurands by means of an array of sensors installed at critical locations. Measurands are physical object quantities directly measurable with sensing instruments. There is a wide variety of measurands used in SHM of which the information is measured and transduced into an easily-measured property (e.g. voltage or optical intensity). Depending on the application, these measurands can range from geometric (e.g. displacement and tilt) to acceleration, stress, strain, temperature and chemical state (Huston 2010).

SHM can play a major role in preventing and mitigating economically and environmentally catastrophic premature structural failures. For non-safety-critical applications, SHM can provide information for structural performance assessment, improved scheduling of maintenance, increasing asset availability and predicting and extending lifetime. Other benefits of SHM include the drastic reduction of manual inspection costs and the use of collected data to improve current design guidelines and regulations and facilitate structural certification and quality assurance (Shukla 2002; Marr 2008; Hatami *et al.* 2009; Huston 2010; Metis Design 2015).

2.1.2. Existing technology for measuring strains in geosynthetics

Inherent variability and uncertainties in soils arising from different sources (e.g. data insufficiency, simplified models and incompetence in design and construction – Bulleit (2008)) pose significant challenges to the design of geosystems. However, the increasing trend in using SHM and performance evaluation techniques could offer substantial help in

counterbalancing the uncertainties (e.g. associated with data insufficiency) in the design and identify the impending failure of high-risk geosystems.

A methodology to plan and carry out a monitoring program in geotechnical engineering can be found in Dunnicliff (1993). Among a great number of measurands used in the SHM and performance assessment of geosystems, strain is more common for GMS, especially retaining walls, soil slopes and bridge/railway abutments reinforced with geogrids and geotextiles. Koerner (1996) provides a summary of the methods and devices that are used to monitor and evaluate geosynthetics performance in practice. The following three methods are primarily used to measure strains in different materials:

- electrical resistance (foil) strain gauges for gauge lengths within the range 0.25–150 mm (Figure 2.1),

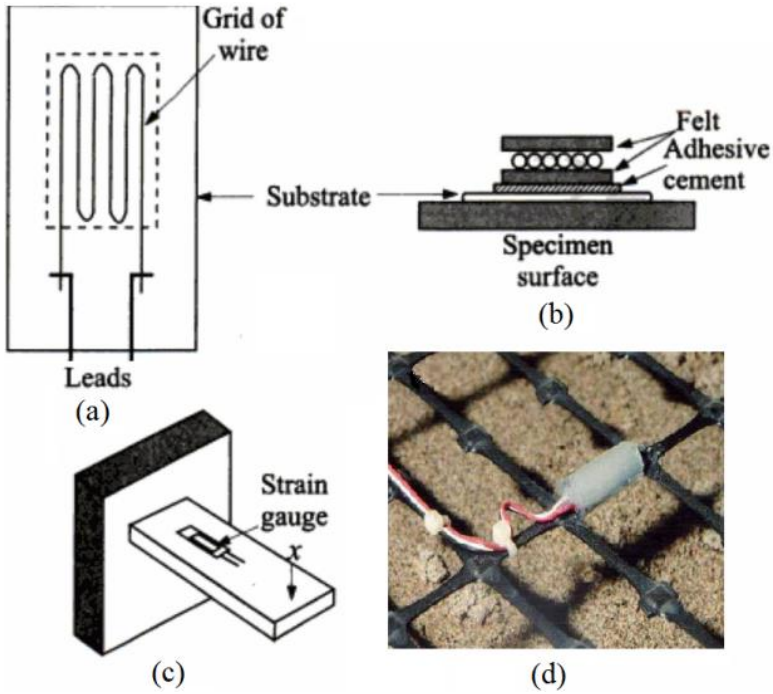

Figure 2.1. Bonded strain gauge: (a) construction, (b) bonding on the surface, (c) schematic placement, and (d) actual placement (a–c, after Ghosh (2009) and d, after Fathi (2011))

- inductance gauges (coils) to measure the movement between two embedded coils up to 1000 mm apart (Figure 2.2),

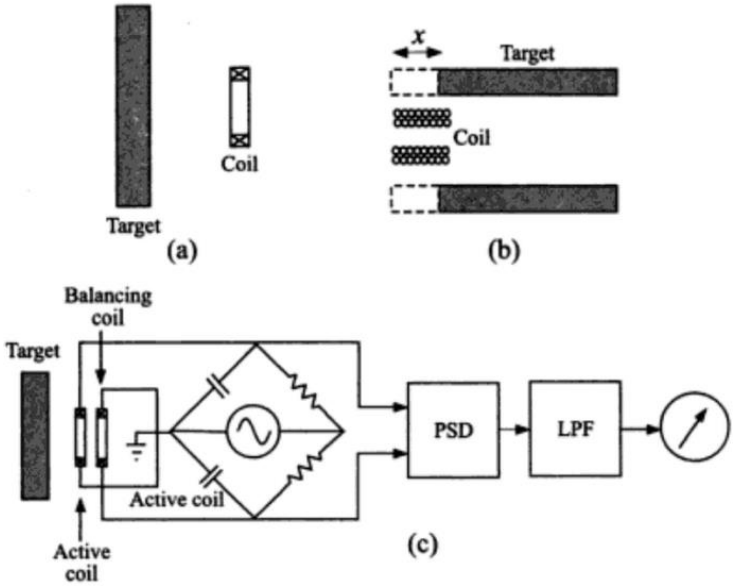

Figure 2.2. Schematic diagram of placement of a transducer: (a) target and coil at right angles, (b) coaxial target and coil, and (c) measuring arrangement (after Ghosh (2009))

- LVDT (linear variable differential transformer) gauges that are used to measure the movement between two fixed points 100–200 mm apart (Figure 2.3), and

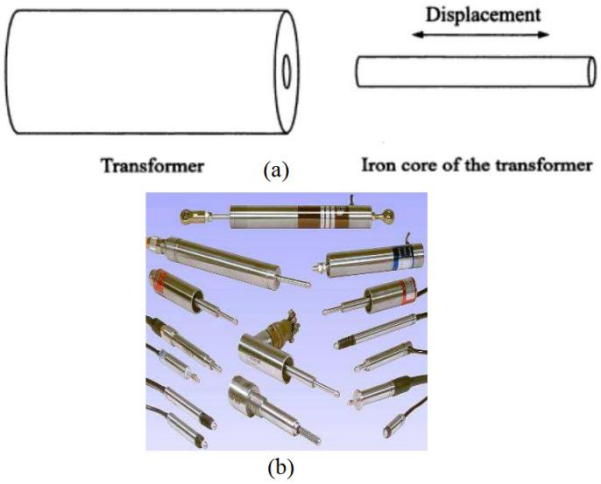

Figure 2.3. LVDTs: (a) basics (after Ghosh (2009)) and (b) actual view (after Fathi (2011))

- wire potentiometers or "wire pots" that used to measure large displacements (Figure 2.4).

Figure 2.4. Wire potentiometer (Musikding 2015)

In practice, properly-selected strain sensing devices are attached at key structural positions to a geosynthetic material to monitor its deformations. When selecting an instrumentation device, one must consider different factors including range of strains/deformations, accuracy, long-term stability, cyclic endurance, range of operational temperature, ease of installation, tolerable amounts of elongation and stability in harsh environments (Liu 2011).

In situ monitoring of geotextile and geogrids systems for reinforcement applications has been the subject of numerous studies. Sluimer and Risseeuw (1982), Risseeuw (1984) and Risseeuw and Voskamp (1984) pioneered using strain gauges for the strain measurement of geotextiles used for reinforcement. They installed waterproofed, 100-mm-long strain gauges directly on geotextiles with wire leads extended to a monitoring station. This technique was later adopted in its original and modified forms by other researchers for a wide range of reinforcement applications.

Haji Ali and Tee (1988) instrumented and monitored a 7-m-high, geogrid-reinforced slope using strain gauges, inclinometers, pressure cells, piezometers and settlement stations. Simac *et al.* (1990) reported a successful application of 42 strain gauges protected and waterproofed with a highly elastic, asphaltic emulsion to evaluate the deformations, pull-out behavior and the tensile load distribution in the reinforcement of a 6-m-high geogrid wall. Hadj-Hamou *et*

al. (1990) built, instrumented and monitored the performance of a full-scale model of a geogrid-reinforced levee underlain by a soft clay. The back-analyses of the measurement of horizontal movements, vertical settlements, pore pressures and strains in geogrids indicated (at the time) excessively conservative estimates for the volume of reinforcement required to guarantee satisfactory long-term levee performance. The results were then allowed the use of smaller stabilizing berms in the final design, resulting in appreciable savings. Also, Farrag *et al.* (1994) reported a successful application of strain gauges to monitor deformations of a geogrid-reinforced wall up to 10% strain. Similar reports were made later by Rowe and Mylleville (1996), Carrubba *et al.* (1999), Carrubba *et al.* (2000), Bathurst *et al.* (2000), Gnanendran and Selvadurai (2001), Bathurst *et al.* (2002), Farrag *et al.* (2004), Viswanadham and König (2004) and Ling *et al.* (2005).

Bathurst *et al.* (2006) reported the results of two instrumented full-scale geogrid-reinforced walls (among a series of 11 full-scale test walls; Bathurst and Hatami (2006)), one with a stiff face and the other with a flexible wrapped face. More than 300 instruments were used including displacement-type potentiometers, vertical settlement plates, soil strain inductance coils, load cells together with wire-line extensometers and strain gauges directly attached to the reinforcement layers. The results demonstrated that using a stiff facing in a reinforced soil wall significantly attenuates the reinforcement loads and wall deformations compared to using flexible facing systems.

In an attempt toward making geotextile-reinforced retaining walls more feasible and common practice, Benjamim *et al.* (2007) constructed and analyzed the behavior of eight prototype geotextile-reinforced soil structures instrumented with extensometers. The results showed that strains were larger behind the facing at mid-height of the prototype wall.

In addition to the instruments described above, other technologies have emerged for the continuous deformation monitoring of geosynthetic structures. Among them are optical-fiber strain gauges that, compared to their metal-wire counterpart, offer significant weight reduction, greater versatility and improved multi-parameter test capabilities (Yee 2001). Embedding optical fibers into geotextiles led to a technology known as GeoDetect® that allows sensitive and precise measurement of strains due to strong bonding at the geotextile-optical fiber interface (Briançon *et al.* 2004; Nancey *et al.* 2004; Nancey *et al.* 2005; Lostumbo and Artieres 2011). Interested readers are referred to a review by Pei *et al.* (2014) for the application of optical-fiber sensors in the health monitoring of geosystems.

The methods and devices mentioned above require complex and expensive data acquisition systems to collect the information needed to analyze the safety of structures. Also, strain gauges attached to a reinforcement material need to be calibrated against global strains from crosshead displacements in in-isolation tensile tests. However, the resulting calibration factors are typically not accurate when the reinforcement layer is embedded in soil due to at least the following important reasons (Hatami *et al.* 2009):

- local stiffening effect of the bonding assembly. Strain gauges bonded to a reinforcement layer (Figure 2.1d) typically generate a local "hard spot" that causes under-registration of global tensile strains (Bathurst *et al.* 2002; Bathurst *et al.* 2005),
- different in-soil mechanical properties (e.g. tensile modulus) of geosynthetics compared to their in-isolation values due to confining pressure and interlocking effects, and

- complications such as soil arching due to the mechanical interference and interaction of strain gauges and their bonding assembly (e.g. adhesive and protective sleeve) with the local soil.

These factors can introduce significant errors in measured strains in geosynthetics in field applications. Applying in-isolation calibration factors to in-soil readout data could lead to significant under-registration of reinforcement strain and axial load with potential consequences with respect to the stability and performance of the monitored structure.

Rapid technological advances in sensing, networking and information processing are driving the field of SHM and structural prognosis (Huston 2010). Continued developments in the closely-related areas of nanotechnology and nano- and microelectromechanical systems (NEMS and MEMS) are leading to smaller, less expensive, yet better-performing integrated sensor systems (Varadan 2003). For instance, ShapeAccelArray (Dasenbrock *et al.* 2011) is a MEMS-based, in-place inclinometer that has recently been developed and used to monitor landslides. The following sections provide further details on the recent progress in developing these types of sensors.

2.2. Selected experimental studies on electrical conductivity of filled composites

As described earlier in Section 1.3.3, composites containing a critical filler concentration exhibit strain sensitivity in their electrical conductivity response. This behavior is essentially attributed to the piezoresistive/tensoresistive properties of the conductive network in the host matrix. On a micro/nano level, deformation in the composite material alters the number and spatial distribution of the contacts and the tunneling distance between the filler particles,

leading to changes in the electrical conductivity of the network (Wang *et al.* 2009a). The following sections provide a survey of salient studies on carbon-based piezoresistive polymer composites. Interested readers are referred to a review by Cravanzola *et al.* (2013) for further details.

2.2.1. Experimental studies

2.2.1.1. Carbon black-filled composites

Carbon black (CB) is widely used as a conductive filler in polymer composites. The effectiveness of CB in inducing conductivity in an insulating host polymer is characterized by three primary properties: particle size or surface area, structure and surface chemistry (Sichel *et al.* 1982; Donnet 1994). The surface area of a particular CB is usually determined using the BET theory (Brunauer *et al.* 1938; ASTM D6556 2014) and is inversely proportional to its percolation threshold. Nanocarbons, including CB, possess an inherent thermodynamic drive to create physical entanglement with neighboring particles via van der Waals forces and form aggregates (Bourrat 1993). High electrical conductivity is achieved when the gap distance between aggregates is less than some critical distance (10 to 28 nm), enabling electrons to flow across the polymer barrier. The critical distance is independent of the CB particle size. Increasing the surface area of CB would reduce the interaggregate gaps, consequently lowering the percolation threshold (Polley and Boonstra 1957).

Percolation threshold of a particular CB in a polymer matrix also depends on its dispersion capability, which is a function of the crystallinity, surface tension and melt viscosity of the polymer and its interaction with CB particles. CB particles in crystalline polymers are ejected

from the crystalline regions during crystallization and concentrate in the amorphous regions. Therefore, the CB particles dispersed in amorphous polymers percolate at a higher concentration than in crystalline polymers everything being equal (Huang 2002). Miyasaka *et al.* (1982) investigated the influence of surface tension on the percolation threshold of CB-filled composites. Polymers with different surface tensions were used, and the results showed a reduction in the percolation threshold as the surface tension decreased. Similarly, reducing the molecular weight and melt viscosity of the polymer matrix (e.g. by means of plasticizers) decreases the percolation threshold due to the improved spreading capability of polymer chains on CB particles/aggregates that in turn promotes the formation of conducting networks (Huang *et al.* 1999). Polymer-filler interactions are also important. If fillers possess strong interactions with one another, aggregates and agglomerates are formed that are difficult to disperse. Strong filler-polymer interactions help to better separate the fillers, impeding the formation of a conductive network in the composite (Tchoudakov *et al.* 1996).

The electrical and tensoresistive properties of the CB-filled polymers have been the subject of extensive research. A significant part of these studies has been on polyethylene (PE), polypropylene (PP) and polyvinyl chloride (PVC), which are also commonly used in the geosynthetics industry. Narkis *et al.* (1981), Calleja *et al.* (1988), Mather and Thomas (1997), Hindermann-Bischoff and Ehrburger-Dolle (2001), Mironi-Harpaz and Narkis (2001) and Zheng *et al.* (2014) investigated the conductivity and strain sensitivity of CB-filled PE composites. Their results indicated that the composite has the potential for sensor applications. Similar observations were made for CB-filled PP composites where CB has been reported to significantly influence the morphology and crystallinity of the polymer matrix (Petrović *et al.* 1993; Tchoudakov *et al.* 1996; Yui *et al.* 2006; Huang *et al.* 2011). PVC-

based composites filled with CB have also been shown to exhibit high electrical conductivity and strain sensitivity (Sichel *et al.* 1978; Chung 1982; Sumita *et al.* 1986a). The percolation threshold reported in the studies cited above is in the range of 1–10 wt.%. Since higher concentrations of CB particles in the host polymer promote their agglomeration, special consideration should be given to their proper dispersion and the preparation and fabrication of composites with a goal to reduce the filler concentration in the final product as much as possible. Agglomeration of CB particles in polymer composites results in the formation of stress concentration zones and deteriorated mechanical properties.

Other studies on strain sensitivity of electrical conductivity in CB-filled polymer composites include those on rubber (Ding *et al.* 2007; Mahmoud *et al.* 2007; Luheng *et al.* 2009; Nanni *et al.* 2011) and cement-based composites (Xiao *et al.* 2010).

2.2.1.2. Carbon nanotube-filled composites

Among different types of fillers used in polymer nanocomposites, CNTs provide outstanding characteristics such as high flexibility (Cooper *et al.* 2001), low mass density (Gao *et al.* 1998) and large aspect ratio (length-to-diameter ratio), together with exceptional mechanical and electrical properties (Hilding *et al.* 2003). By now, percolation-dominated electrical conductivity has been observed in a wide range of CNT-filled polymer composites. The most relevant of these studies (i.e. those on polymers which are also used in the geosynthetics industry) are summarized in Table 2-1. Interested readers are referred to works by Li *et al.* (2008), Bauhofer and Kovacs (2009) Demarchi and Tagliaferro (2015) for further details. Table 2-1 shows that the percolation threshold of the CNT-filled composites largely depends on the processing and fabrication methods employed as well as the CNT type and

aspect ratio. A carefully-designed and fabricated composite can have a percolation threshold as low as 0.04 wt.%, which is considerably lower than the percolation threshold of comparable CB-filled polymers. However, the needle-shaped geometry of CNTs together with the their inherent thermodynamic drive to create physical entanglement with neighboring tubules via van der Waals forces promote the formation of aggregated morphologies termed bundles (Grady 2011). Therefore, particular attention should be paid to the proper dispersion of CNTs in a composite, which necessitates an experimental effort to determine the optimum input of shear force/energy required to overcome the van der Waals forces between bundles.

Improving the quality of CNT dispersion in a composite is a trade-off between mechanical and electrical properties. On the one hand, near-perfect dispersion results in smaller and less bundle-induced stress concentration zones that could otherwise compromise the weight, mechanical properties and manufacturability of the composite (Ajayan *et al.* 2000). On the other hand, a higher percolation threshold filler can have significantly better dispersion than a lower percolation threshold filler as bundling can reduce the percolation threshold (Grady 2010).

Table 2-1. Summary of experimental studies on the electrical conductivity of selected CNT-filled polymer composites

Matrix	Filler	*l*/*d*	Dispersion	Percolation threshold (wt.%)	σ_{max} (S/m)	Source
HDPE	MWCNT	100	Sonicated, dry mixed, hot pressed	0.045	5E+1 @ 1 wt.%	Mierczynska *et al.* (2007)
		> 100	Stirred, hot pressed	0.07	1E-2 @ 0.7 wt.%	Mierczynska *et al.* (2007)
		-	Stirred	0.14	1E-1 @ 0.7 wt.%	Mierczynska *et al.* (2007)
		5000	Dry mixed, hot pressed	0.28	1E+1 @ 1 wt.%	Mierczynska *et al.* (2007)
	SWCNT	-	Sonicated, dry mixed, hot pressed	0.09	5E-2 @ 2 wt.%	Mierczynska *et al.* (2007)
		-	Dry mixed, hot pressed	0.6–1.1	5E-2 @ 3 wt.% – 5E-1 @ 3 wt.%	Mierczynska *et al.* (2007)
		-	Sonicated, centrifuged, sprayed, extruded	4	5E-1 @ 6 wt.%	Zhang *et al.* (2006)
LDPE	MWCNT	100	Sonicated, melt mixed	15	5E-6 @ 30 wt.%	Zhao *et al.* (2006)
		< 100	Melt mixed, hot pressed	0.081	5E-4 @ 0.1 wt.%	Song *et al.* (2010)
PP	MWCNT	-	Sonicated, extruded	0.4	1E-1 @ 0.07 wt.%	Kharchenko *et al.* (2004)
		-	Extruded (high shear), hot pressed	0.44	2E+0 @ 9 wt.%	Tjong *et al.* (2007)
		700	Sonicated, hot pressed	0.11	7E+1 @ 2 wt.%	Grossiord *et al.* (2010)
		1000	Extruded, hot pressed	1.5	2E-1 @ 5 wt.%	Seo and Park (2004)
		-	Extruded, hot pressed	2	5E-1 @ 10 wt.%	Gorrasi *et al.* (2007)
	SWCNT	700	Sonicated, hot pressed	0.04	7E+0 @ 2 wt.%	Grossiord *et al.* (2010)
PVC	MWCNT	1000	Stirred, grinded, hot pressed	0.094	1E-2 @ 1.4 wt.%	Mamunya *et al.* (2008)

Developing composites filled with a combination of CB and CNT has recently gained momentum due to the synergic effect of the fillers in enhancing the electrical conductivity

of composites while balancing their mechanical properties. For instance, Ma *et al.* (2009) achieved a low percolation threshold with 0.2 wt.% CNT and 0.2 wt.% CB in an epoxy-based nanocomposite. The CB particles were aimed to enhance the ductility and fracture toughness of the nanocomposites, while CNTs were used to improve the strength and lower the percolation threshold by bridging the CB particles.

2.2.2. Numerical studies on the mechanical and electrical properties of filled composites

A synopsis on the application of MD and MC simulation techniques for filled composites is given in the following sections.

2.2.2.1. Monte Carlo (MC) simulations

Percolation is one of the simplest models for spatial disorder in probability theory to predict a phase transition. Phase transition is a significant change in the macrostate that occurs at a rigorously-specified value of a control parameter known as percolation threshold (see Section 1.3.3).

MC simulations have been widely used to describe the phase transition of disordered systems. Scher and Zallen (1970) used MC simulations to estimate the percolation threshold of identical, conducting spheres located in predefined lattice models with different coordination numbers. Their findings were later examined by Pike and Seager (1974) and Seager and Pike (1974) who were the first to study percolation in many random-lattice percolation models in two and three dimensions. The models covered different particle geometries including circles, squares, sticks, spheres and hemispheres. The percolation threshold of the models was approximated using MC simulations. It was concluded that the

application of the Scher and Zallen (1970)'s findings is appropriate only in rather limited circumstances, and a general knowledge of the topological properties of the fillers would be needed in order to find the percolation threshold. However, Pike and Seager (1974) and Seager and Pike (1974) only considered the percolation of isotropic systems of identical, randomly-oriented objects and did not take into account the influence of object size distribution on percolation behavior.

Similarly, Powell (1979) investigated the percolation behavior of identical, randomly-packed hard spheres in a 3D lattice using MC simulations and reported a site-percolation threshold of 0.310 ($\pm$0.005). Also, Gawlinski and Stanley (1981) reported estimated values for the threshold parameter of the connectivity properties of a system of identical discs that were uniformly and randomly distributed within a square. Their results were in close agreement with the findings of Last and Thouless (1971) who measured the conductivity of a randomly-punched sheet made of conducting paper.

Extending the work of Pike and Seager (1974) and Seager and Pike (1974), Balberg and Binenbaum (1983) studied the percolation threshold in two-dimensional systems of conducting sticks using MC simulations. They investigated the dependence of percolation on the anisotropic systems with preferred orientation of the sticks ensemble as well as on the stick length distribution. Their results showed that the percolation threshold increased with the degree of anisotropy in the system. The results also indicated that a broader stick-length distribution results in a lower stick concentration for the onset of percolation. The last observation was in contradiction to the experimental findings of Nicodemo *et al.* (1978) and Berger and McCullough (1985) who reported an increase in the percolation threshold by widening the object size distribution. Balberg and Binenbaum (1983)'s study was limited

to samples with not more than 1000 sticks. Balberg *et al.* (1984) extended the work of Balberg and Binenbaum (1983) and reported similar results for 3D systems.

The model proposed by Pike and Seager (1974) and Seager and Pike (1974) was also adopted by Ueda and Taya (1986) to obtain a critical fiber length at which a network of short fibers would percolate as well as to investigate the influence of geometric anisotropy and fiber aspect ratio (length-to-diameter-ratio) on the percolation threshold. Xia and Thorpe (1988) investigated the percolation properties of a system containing randomly-oriented, identical ellipses with an aspect ratio of b/a ($b > a$) that were allowed to overlap one another and occupy the same space in the model (fully penetrable). They interpolated a general equation for the percolation threshold of such a model as $P_c = (1+4y)/(19+4y)$, where $y = b/a + a/b$. Kortschot and Woodhams (1988) used MC simulations to determine the percolation threshold of rectangular particles in two dimensions. The aspect ratio and orientation of particles were considered as random variables. A similar study was carried out by Munson-McGee (1991) for cylindrical particles. All these studies reported that the lowest percolation thresholds correspond to high-aspect-ratio and randomly-oriented objects.

Criticizing the flexibility of the lattice models for modeling the microstructure of composites as well as the capability of the fully penetrable models to adequately represent the real inclusions, Wang and Ogale (1993) proposed a semi-penetrable, three-dimensional continuum model of particles consisting of an impermeable hard core of diameter (d - 2δ) and a permeable, soft shell of thickness δ (Figure 2.5). Each spheres consisted of an impenetrable hard core representing the actual physical inclusion and a permeable soft shell representing the effective range for electron transfer in fillers. MC simulations were followed to determine the mean percolation thresholds in finite systems, and the finite size scaling

theory (Fisher and Essam 1961; Stauffer 1987) was used to predict the threshold in the infinite systems. A reduction in threshold was observed by increasing the ratio between the shell thickness and core diameter (δ/d). Also, the correlation length exponent calculated was in good agreement with that proposed by Stauffer (1987). This study, however, did not report the influence of diameter on percolation behavior.

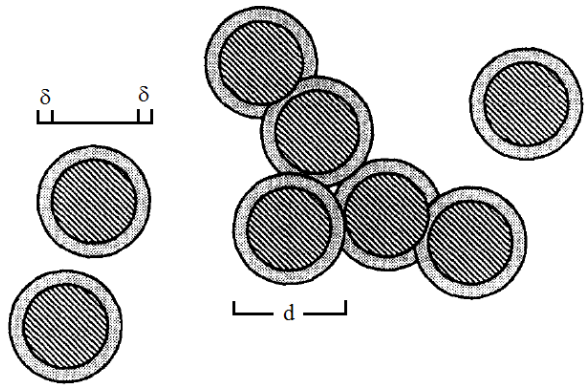

Figure 2.5. Schematic representation of the concentric spherical model (after Wang and Ogale (1993))

Ogale and Wang (1993) adopted the continuum model developed by Wang and Ogale (1993) study the influence of δ/d and aspect ratio on the threshold volume fraction of randomly-oriented fibers. They showed that increasing the aspect ratio would monotonically decrease the percolation threshold. This study was limited to models with aspect ratios ranging from 12 and 50, making it barely applicable to CNT-filled composites.

Dani and Ogale (1996) studied the capability of the core-shell morphology, proposed by Wang and Ogale (1993), to predict the percolation threshold of injection-molded, carbon fiber-filled composites. An image analysis was first carried out in order to measure the three-dimensional orientation and the length distribution of the fibers. Results indicated that the core-shell morphology could be used to determine the percolation threshold of carbon

fibers. MC simulations showed that considering the tunneling conduction in the formulations would result in good agreement between the numerically-predicted and experimentally-measured values for the percolation threshold.

Celzard *et al.* (1996) and Néda *et al.* (1999) investigated the percolation behavior of short-fiber composites in two- and three-dimensional continuum systems. It was concluded that the systems with distributed fiber lengths percolate at lower fiber concentrations. This observation could be due to the bridging act of shorter fibers between the longer fibers that would help to form clusters. These studies were limited to short-fiber systems.

Grujicic *et al.* (2004) carried out numerical simulations to determine the percolation threshold and electrical conductivity of SWCNT-filled polymer composites considering the bundling tendency of CNTs. Individual CNTs and bundles of three, seven and nineteen CNTs were created. Such bundles were assumed to be spherocylinders with the same length as that of the individual CNTs and increased radii for simplification. According to their results, bundling increases the percolation threshold of CNT composites.

Ma and Gao (2008) used MC simulations to predict the percolation threshold and electrical conductivity of three-dimensional conductive curved fibers. The arm length, aspect ratio and arm angle of the fiber were considered as the controlling parameters. The results showed higher percolation thresholds for more curved fibers, especially for low-aspect-ratio fibers. With the percolation threshold obtained from the Monte Carlo model, the effective electrical conductivity of the composite can be determined by applying the theory of percolation. Although these results are in general agreement with experimental results (e.g. Guo *et al.*

(2014)), this study did not consider distribution of fiber length and aspect ratio and arm length on percolation behavior.

More recently, Lu *et al.* (2010), Bao *et al.* (2011) and Yu *et al.* (2013) adopted the CNT curviness concept in the work of Ma and Gao (2008) and extended it to the MC simulation of the percolation of CNTs with multiple segments considering tunneling effects. The results of these studies, which were in a quantitative agreement with existing experimental observations, consistently showed that curved CNTs would percolate at lower concentrations when they are partially aligned as compared to when their alignment is completely random. These studies, however, did not consider the variations in influential parameters (e.g. CNT aspect ratio), except Bao *et al.* (2011) who assumed a Weibull distribution for CNT length.

The models developed or used in the majority of the surveyed studies did not consider the tunneling effect in inducing conductivity in nanocomposites. Such omission significantly alters the predicted values of percolation threshold using MC simulations, rendering them inaccurate relative to the experimental observations. In addition, although some recent studies have considered uncertainty in the CNTs aspect ratio, no study was found to address uncertainties in the curvature of CNTs and the size of CB particles. These knowledge gaps are discussed in CHAPTER 5.

2.2.2.2. Molecular dynamics simulations

Polymer systems in MD simulation are generally modeled in two different forms, explicit-atom (EA) and united-atom (UA). EA models (also known as all-atom models) are relatively

intricate and take into account all the atoms in a polymer chain. UA models, in contrast, are idealized versions of EA models where pendent atoms (e.g. hydrogens in PE) are collapsed into the backbone carbon to form single, spherically symmetric force centers (see Section 6.3.2). UA models, which belong to a wide class of computational techniques known as coarse-grained techniques, provide increased computational efficiency and enable long-time simulations of macromolecules such as synthetic polymers or CNTs (Flory 1953; de Gennes 1979; Fukunaga *et al.* 2002).

Sorensen *et al.* (1988) and Kavassalis and Sundararajan (1993) used an EA model to predict the crystal structure and properties of linear PE. Pant *et al.* (1993) and Paul *et al.* (1995) developed UA models for PE, and Yoon *et al.* (1993) compared the results of MD simulations on UA models of PE against those on EA models and raised caution in making simplifications such as UA approximation in the simulation of real polymer systems.

Hossain *et al.* (2010) used MD simulations to study the deformation mechanisms and stress-strain behavior of amorphous PE in uniaxial tension. Results revealed elastic, yield, strain softening and strain hardening regions in the stress-strain response, which is qualitatively in agreement with previous simulations and experimental results (Capaldi *et al.* 2002, 2004). It was also shown that the elastic and yield regions were mainly dominated by interchain, nonbonded interactions whereas strain hardening regions were primarily governed by intrachain dihedral motions of PE.

Frankland *et al.* (2003) used MD to study the stress–strain curve of SWCNT-filled PE composites. The report lacks information on the CNT concentration in the models. However, the results showed a 30-fold increase in the tensile strength of PE, which is

comparable to the findings of Zhu *et al.* (2007) who used MD simulation and reported a 50-fold improvement in the strength of epoxy Epon 862 matrix after mixing it with SWCNT. Griebel and Hamaekers (2005) used a similar MD simulation study on the stress-strain response of CNT-filled PE. Compared to the findings reported by Frankland *et al.* (2003), Griebel and Hamaekers (2005) obtained an only 2-fold increase in the PE strength upon mixing with CNTs. The large discrepancy observed among these findings and their significant departure from laboratory results (e.g. Xiao *et al.* (2007)) could be attributed to the imperfect CNT-PE interface in laboratory experiments. Also, due to constraints imposed by computational power, MD simulations have been limited to models with only one or two CNTs, whereas CNTs make bundles in actual laboratory specimens which creates significantly sophisticated stress transfer and failure mechanisms, contributing to the discrepancy between experimental and numerical results. Therefore, more realistic interface characteristics are required in order to exploit the advantages of MD simulations in understanding composites behavior.

Compared to PE systems and composites, PP, PVC and their composites have not so far benefited from MD simulations to understand their mechanical properties. Mandal and Singh (2011) carried out an MD study on the pull-out strength of SWCNT-reinforced PP composites. Their results showed that non-bond van der Waals interactions between the polymer and CNT were responsible for the adsorption and orientation of polymer chains. It was also shown that the chirality of CNTs has a significant influence on their pull-out strength. In a more recent study, Haghighatpanah *et al.* (2014) carried out MD and molecular mechanics (MM) simulations to investigate the influence of functionalization on the interfacial properties in SWCNT-PP and SWCNT-polyacrylonitrile composites. Results

indicated that functionalizing SWCNTs with carboxylic acid groups would lead to an increase in both interfacial shear strength and bonding energy, with greater increases in the polyacrylonitrile composites.

CHAPTER 3. LABORATORY TESTS ON CARBON BLACK-FILLED PVC COMPOSITES

This chapter reports the laboratory studies that were carried out in order to develop and examine the performance of a tensoresistive coating composite for sensor-enabled geogrids (SEGG). This chapter is comprised of three main sections and deals only with the composites filled with carbon black (CB).

Section 3.1 presents the laboratory development of a strain-sensitive coating composite for SEGG. An adaptation of a paper previously published in the *ASCE Journal of Nanomechanics and Micromechanics* in 2014 (Hatami *et al.* 2014), this section describes the chemical formulation, fabrication procedure, viscosity, stiffness and electrical properties of the coating composite along with its tensoresistivity and mechanical properties under monotonic loading.

Section 3.2 is a slightly different version of a paper published in the journal *Carbon* (Yazdani *et al.* 2014) and describes the cyclic loading tests that were carried out on the composites developed in Section 3.1 so as to evaluate their in-isolation tensoresistive properties under time-dependent loading.

The coating composite exhibiting favorable in-isolation tensoresistive properties was studied in a modified direct shear test apparatus in order to investigate its in-soil performance. This

is the subject of Section 3.3, which has recently been accepted for publication in the *ASTM Journal of Testing and Evaluation* (Yazdani *et al.* 2016).

3.1. Development of a tensoresistive PVC coating for sensor-enabled geogrids

3.1.1. Introduction

Carbon black-filled polyvinyl chloride (PVC/CB) is a polymer composite that is commonly used as the coating of woven and knitted geogrids. The primary function of the CB fillers in the coating (or in the bulk of the polymer in extruded geogrids) is to protect the geogrid against the degrading effects of ultraviolet (UV) rays (e.g. Koerner (2012)). Adjusting the CB concentration could result in geogrids that exhibit tensoresistive properties (tensoresistivity refers to an increase in the electrical resistivity of a material when subjected to tensile strain; see Section 1.3.4).

There are several advantages in using CB to develop tensoresistive geogrid products: (1) tensoresistivity adds a novel and practically-significant characteristic to the geogrid by allowing its tensile strain to be measured at virtually any location without the need for conventional instrumentation (e.g. strain gauges). As a result, the CB filler at a specific concentration not only serves as a UV-protecting agent, but also results in a sensor-enabled geogrid (SEGG). This could help circumvent current shortcomings and challenges in using strain gauges and other instrumentation techniques for geogrids related to their attachment techniques, durability and cost (see p. 42); (2) since the cost of CB is only a minute fraction of the total cost of producing geogrids, a small adjustment in its concentration in the formulation of geogrids (e.g. 2%-5%) is not expected to add any significant amount to their

production cost; (3) since CB is already used in the production of geogrids and the amount of adjustment in its concentration in SEGG would be fairly small, little modification would be required in the existing production processes employed by the geogrid manufacturers to produce SEGG materials; and (4) in PVC-coated polyester yarn geogrids, any change in the tensile strength of the coating as a result of increased CB concentration will not adversely impact the mechanical properties of the geogrid as a reinforcement material.

Dispersing sufficient concentration of conductive particles such as CB in an insulating polymer matrix can develop a continuous conducting network that provides comparatively low-resistance electrical paths for free movement of electrons (Huang 2002; Hatami *et al.* 2009). This is partly because electrons can flow across the polymer barrier when the distances between conductive particles/aggregates become less than some critical value (e.g. 10 nm). Polley and Boonstra (1957) stated that the electrical conductivity of a filled composite increases exponentially with the reduction in the distance between the CB particles irrespective of their size. Both the percolation threshold (Section 1.3.3) and the conductivity at high concentrations of CB-filled composites depend on the properties of the carbon black (i.e. particle size, structure, porosity and surface chemistry) and polymer (i.e. chemical structure and crystallinity), and on the processing methods and conditions employed (Narkis *et al.* 1981; Wu 1982; Sumita *et al.* 1986a; Sumita *et al.* 1986b; Tchoudakov *et al.* 1996; Breuer *et al.* 1997).

The surface of CB is generally comprised of chemisorbed anionic oxygen groups (mainly carboxylic, quinonic, phenolic or lactonic groups). When mixed with a cationic polymer matrix, strong interactions are established between cationic polymer chains and the anionic CB surface which reduce the contact between the CB particles. In addition, the functional

groups tend to act as electron traps and thus reduce the electrical conductivity of the polymer composite (Zhang *et al.* 2007b). The dispersion quality of CB in polymers can be improved by using CBs with smaller particle size (i.e. larger surface area), lower particle density (i.e. higher particle porosity), higher structure (i.e. significantly branched configuration) and low volatility (i.e. fewer chemisorbed oxygen groups). These properties allow the composite to exhibit greater electrical conductivity at lower filler concentrations (Narkis and Vaxman 1984; Flandin *et al.* 2000). However, the melt viscosity of a polymer matrix containing high-structure CB (see Sections 1.3.1.1 and 3.1.2.1 for the definition of CB structure) can become too high for processing purposes before a desired conductivity can be achieved (King *et al.* 2006). Therefore, it may be preferable to use a moderate-structure CB in order to achieve the desired conductivity at slightly higher concentrations (Huang 2002).

Polyvinyl chloride (PVC) is a thermoplastic insulating polymer (conductivity on the order of 10^{-12} S/cm – Maruthamuthu *et al.* (1993)) with a relatively low degree of crystallinity (approximately 10% – Balberg and Bozowski (1982); Titow (1984); Gilbert (1994)). Adding CB even at low concentrations to a thermoplastic polymer (e.g. PVC or polypropylene) could result in the deterioration of the mechanical properties (e.g. strength, elastic modulus and ductility) of the composite (Narkis *et al.* 1981; Fathi *et al.* 2012). Therefore, the CB concentration in PVC composites should be kept at a minimum. At the same time, the conductivity properties of a CB-filled polymer composite can be significantly influenced by the blending method used to disperse the conductive particles in the polymer host.

In this endeavor, a primary objective toward developing SEGG materials was to determine a blending procedure that would result in a coating material with adequate and consistent tensoresistive and tensile properties at the lowest possible CB concentration.

The influence of the blending method on the conductivity of PVC/CB composites has been examined previously. Chung (1982) investigated the electrical conductivity and permittivity of PVC/CB composites. They dry-blended PVC with different weight percentages of spherical as well as moderate- and high-structure CBs to obtain uniform powder blends. Each batch of PVC compound was then melt-blended at 200 °C. The blended sample was compression-molded into plate-shaped specimens using a procedure known as the segregation method (Popplewell *et al.* 1989; Yacubowicz *et al.* 1990; Pinto *et al.* 1999). Chung et al. found that high-structure CBs reach the percolation threshold at lower concentrations as compared to low-structure blacks.

Das *et al.* (2002) examined the electrical conductivity of CB-filled and short carbon fiber-filled composites that were produced using the mill mixing method. They concluded that factors such as the applied pressure and temperature in the mixing process can significantly influence the formation and breakage of the conductive network within the composite, which in turn, influence the electrical conductivity of the filled polymer.

Noguchi *et al.* (1986) studied the influence of the CB structure on the electrical conductivity of PVC/CB composites that were produced through the mill mixing method. The PVC resin was made of one part polyvinylacetate and seven parts PVC. Noguchi *et al.* (1986) found that the milling time changed the geometry of the carbon particles from amorphous to cylindrical. Further milling time altered the particles geometry from cylindrical to spherical. They concluded that maximum electrical conductivity was obtained when the cylindrical CBs were able to form a continuous conductive network in the composite.

Guoquan and Peng (2004) used two different methods to blend short carbon fibers with PVC to form a conductive network of fibers in the composite. The two methods included the use of mechanical stirring and mill mixing. Guoquan and Peng concluded that mechanical stirring was more effective than mill mixing in forming a conductive network in the composite at lower fiber concentrations. The higher concentration required in the latter method was attributed to the fiber breakage in mill mixing.

The above survey indicates that the dispersion technique can influence the structure and conductivity of the CB network in filled polymer composites. In this study, the performance of three different mixing methods in blending two different types of CB with plastisol was investigated. Plastisol (denoted here as PL) consists of PVC resin suspended in a compatible plasticizer. A plasticizer is a substance of low molecular weight that is incorporated in a host polymer to increase its workability, flexibility or dispensability (ASTM D883 2012). A plasticizer is considered compatible with a host polymer when the two can be easily mixed and fused into a homogenous compound with no substantial migration of the plasticizer from the compound when subjected to mechanical or chemical stress (ASTM D3291 2011; ASTM D2383 2014). After a suitable mixing method was identified, the influence of the thickness of the coating specimens on the measured conductivity performance of the PL/CB samples was examined. PL/CB coating specimens were fabricated using the selected blending method at a desired CB concentration. A series of electrical conductivity and tensile strength tests were carried out on the specimens to measure their tensoresistivity properties. Scanning electron microscopy (SEM) images were obtained to help interpret the electrical conductivity results. It was found that the composite formulation developed in this study

would consistently result in specimens with satisfactory tensoresistive and mechanical performance.

3.1.2. Study approach

Details of the materials, fabrication procedure and laboratory tests are described in the following sections.

3.1.2.1. Materials

In accordance with the current practice in the manufacturing of PVC-coated PET woven geogrids, PVC plastisol (denoted here as PL) with a density of ϱ_p = 1.37 g/cm^3 was used as the primary polymeric matrix to fabricate the conductive coating specimens in this study.

Two types of CB in powder form with measurably different oil absorption numbers (OANs) were used as conductive fillers. The properties of selected CBs are comparable to those used in conductive applications such as "self-diagnosis" fiber-reinforced polymers (FRPs), developed for damage detection in concrete structures (Okuhara *et al.* 2001). The OAN (also known as the dibutylphthalate oil absorption or DBPA number) is the amount of oil in milliliters absorbed by 100 grams of CB particles which is a measure used to classify CB as low-, moderate- or high-structure particles (Laube *et al.* 2001). The structure of CB depends on the aggregate size, shape and the number of particles per aggregate. A high-structure CB is characterized by primary aggregates that are composed of many prime particles and have an extensive degree of chaining and branching. In contrast, primary aggregates in an agglomerated shape with relatively few chains and branches result in low-structure blacks. Compared to low-structure blacks, more energy is required to separate more heavily

connected aggregates in high-structure blacks (Accorsi and Romero 1995; Huang 2002). Also, higher structure blacks percolate at lower concentrations (Chung 1982; Yacubowicz *et al.* 1990).

Contact angle is a parameter which quantifies the wettability of a material. Generally, a solid is considered to be easily wet by a particular liquid if a droplet of the liquid spontaneously spreads on its surface. In this case, less energy is needed to overcome the intermolecular interactions to disperse the solid material in the liquid. The Washburn capillary rise method (Washburn 1921) is commonly used to determine the contact angle of porous media. In this theory, the contact angle, θ, between the liquid and solid phases is calculated as:

$$\cos\theta = \frac{m^2}{t}\frac{\eta}{c\sigma\rho^2} \tag{3-1}$$

where m is the mass of liquid adsorbed on the solid surface, t is the time after contact, ρ, η and σ are the liquid density, viscosity and surface tension, respectively, and c is a material characteristic constant for the solid sample. The application of this theory in determining the contact angle in Equation (3-1) is based on the assumption that the cross-section and tortuosity of the micropores within a thin layer of uniformly-graded particles are fairly uniform.

In this study, the Washburn theory was used to determine the wettability of the carbon blacks by water. The contact angles measured in this study were found to be less than 90°, which is consistent with the range of values reported in the literature (e.g. USDOE (2005)). The set-up designed and used to measure the water absorbed by the CB fillers is shown in Figure 3.1. 100 g CB was poured in a filter funnel mounted on a support stand. A beaker of water

was placed on a precision scale, and the filter funnel was lowered and positioned in the middle of the beaker such that the filter would always remain above the water surface and the funnel had no contact with the beaker. A digital camera equipped with an intervalometer was then used overnight to record in every 15 minutes the changes in the water weight. The changes were assumed to be equal to the amount of water absorbed by CB. Equation (3-1) was then used to calculate contact angle. The types and properties of the CB fillers used in this study are listed in Table 3-1.

Figure 3.1. The setup used to measure the water absorbed by CB

Table 3-1. Properties of the CB particles used in the study (as measured, or provided by the supplier)

CB ID	ASTM designation	Mean particle size[1] (nm)	Oil absorption number (OAN)[2] (ml/100g)		NSA[3] (m^2/g)	Surface area[4] (m^2/g)	Porosity (NSA/STSA)	Volatility[5] (%)	Water contact angle[6] (°)
			Bead	Structure classification[7]					
1	N110	22	113	Moderate	155	109	1.42	0.9	82
2	S212	21	77	Low	124	112	1.11	1.0	80

[1] ASTM D3849 (2014)

[2] ASTM D2414 (2013)

[3] Nitrogen adsorption surface area measured using the BET theory (Brunauer *et al.* 1938) (ASTM D6556 (2014) – micropores are included)

[4] Measured using the statistical thickness surface area (STSA) method (ASTM D6556 (2014) – micropores are excluded in the measurements due to the inability of the high-viscosity wetting material to penetrate smaller micropores)

[5] Measured using the thermogravimetric analysis (TGA – ASTM D5832 (2014))

[6] Measured using the Washburn theory (Washburn 1921)

[7] Inferred from Laube *et al.* (2001)

Adding plasticizer to a polymer matrix typically lowers the melt viscosity and percolation concentration, and increases electrical conductivity of the plasticized polymer (Huang *et al.* 1999).

In this study, an auxiliary plasticizer (bis(2-ethylhexyl) phthalate; denoted here as PR) with a density of ϱ_p = 0.985 g/cm^3 was used to blend the CB powder in the form of a suspension before adding the mix to the plastisol. The PR/CB mixture is referred to as the pigment blend in this paper. The amount of PR was selected proportionally to the CB concentration following two series of viscosity tests carried out following the ASTM D5225 (2014) test protocol using a Brookfield viscometer.

The first series of viscosity tests was carried out on a coating material supplied by MarChem in order to determine the range of viscosity used in the industry and also to determine the proper spindle and rotational speed to use in further testing to meet the following two criteria: 1) it was important that the measured viscosity of the mixture would not depend significantly on the spindle number used, and 2) it was important to minimize any probability of damage to the composition of the blend (and even to the mixing equipment in the case of higher viscosity blends) at higher rotational speeds, especially in the case of mixtures with high CB concentration. Results shown in Figure 3.2 indicate that a combination of a rotational speed in the range between 5 and 10 rpm and a spindle number in the range between 3 and 5 satisfy these two criteria. Accordingly, spindle #5 with a rotational speed of 5 rpm was used for the subsequent viscosity tests.

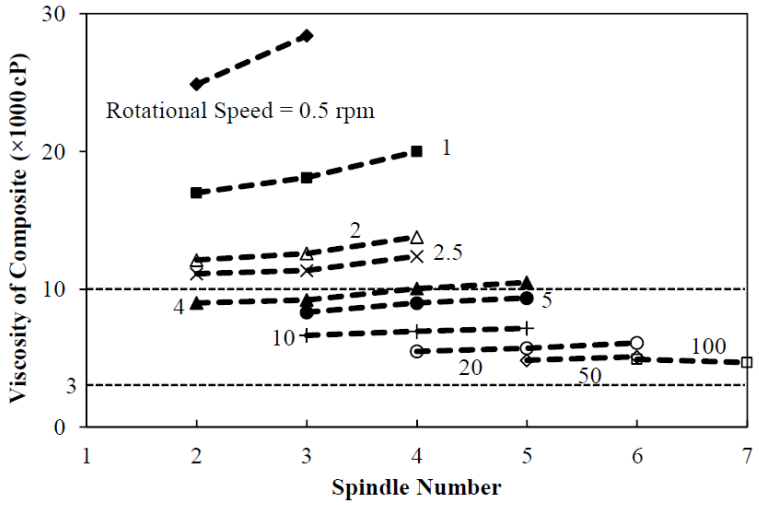

Figure 3.2. Combinations of rotational speed and spindle number examined to measure the viscosity of an industrial geogrid coating material. Notes: The concentrations of CB and primary plasticizer in the coating were unreported; T = 23 ± 1 °C; one sample was tested for each rotational speed and spindle number combination.

Using the results of the first series, the second series of the viscosity tests was carried out on mixtures with different mixing ratios of the composite ingredients (i.e. PL, PR and CB) in order to obtain a PR/CB ratio that would result in a processable and workable pigment blend with a viscosity in the range shown in Figure 3.3 (i.e. 3,000–10,000 cP). This range of viscosity values was targeted after consultation with industry (MarChem 2011). The CB concentration was kept constant at 3% on a PL/PR/CB basis in all tests while the PR/CB ratio was increased from 3 to 6. The CB concentration in different samples was determined such that the final formulations would contain target CB concentrations for the subsequent conductivity tests. Plastisol was subsequently added to the pigment blend until the total weight of the mixture reached 500 g according to the ASTM D5225 (2014) test standard. The tests were mainly carried out on the CB1-filled composites and the applicability of the results to the CB2-filled composites was examined using tests on composites loaded with two different PR/CB ratios. The room temperature in the laboratory was kept fairly constant

during the tests (T = 23 ± 1°C) to minimize its impact on the viscosity of the blends. Figure 3.3 shows that increasing the CB portion in the pigment blend can significantly increase the composite melt viscosity. King *et al.* (2006) and King *et al.* (2009b) also reported an increase in a composite melt viscosity with CB concentration. Based on the results shown in Figure 3.3, a PR/CB ratio of 5 was used throughout this study for both CB1 and CB2 fillers.

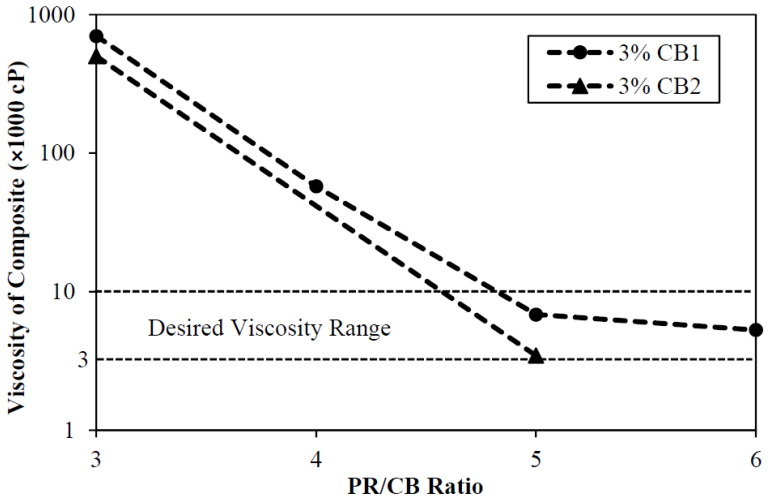

Figure 3.3. Viscosity of the PL/PR/CB composite with different PR/CB ratios. Notes: T= 23 ± 1 °C; spindle #5; rotational speed= 5 rpm; one sample was tested for each PR/CB ratio.

3.1.2.2. Sample preparation and mixing methods

Proper dispersion is crucial in order to produce conducting polymer composites that would exhibit a desired level of accuracy and consistency in their electrical and mechanical performance. Shearing forces affect the dispersion during the compounding process. When the shearing forces acting on the CB agglomerates during the mixing process overcome the weak van der Waals forces between the CB aggregates, the agglomerates are broken up into primary aggregates (Huang 2002). During the very first stages of mixing, the conductivity of CB composites increases rapidly mainly due to the establishment of conductive pathways

among the CB particles and agglomerates. After an optimum mixing time, conductivity decreases gradually by further mixing primarily due to the breakage in the CB agglomerates and formation of gaps between individual aggregates (Dannenberg 1952). Bigg (1984) showed that conductivity of high-structure CB-filled composites is even more sensitive to the processing time than highly-porous CB composites. Mixing effort also influences the mechanical properties of a CB-filled composite. By compounding two CBs of different structure with styrene-butadiene rubber, Cembrola (1982) concluded that long mixing duration would reduce the dynamic moduli of the blends.

The above studies indicate that dispersion procedures for conductive composites must be carefully controlled to avoid under- or over-dispersion of the CB in the polymer matrix. In this study, three different mixing methods, i.e. bath sonication, probe sonication, and mechanical stirring, were employed to disperse the CB powder in the auxiliary plasticizer to make a pigment blend. A series of tests was carried out to investigate the influence of factors such as the sonication power, duration and rotational speed on the electrical properties of the filled polymers and determine a procedure which would consistently result in specimens with maximum tensoresistive properties and adequate mechanical properties at the lowest possible CB concentration. Different dispersion techniques examined are described in the following sections.

3.1.2.2.1. Bath sonication

The bath sonication (BS) method utilizes the ultrasonic energy to agitate particles in a blend. Propagated through water, the ultrasonic vibration is transmitted across the walls of the blend container and uniformly affects the entire blend. It was hypothesized that this method

would be mostly effective for low-viscosity blends (i.e. blends filled with a lower-structure CB at lower concentrations) in terms of their homogeneity and repeatability. To start the mixing process, first 10 grams of CB powder was manually mixed with 50 grams of the auxiliary plasticizer to make a visually-uniform pigment blend. Then, this pigment blend was gently poured into a 100-ml Griffin-form beaker placed in a bath sonicator (Cole-Parmer, Model 08895-04). The sonicator power was set at 70 W for three different durations of 3, 4.5 and 6 hours in order to determine an optimum combination of sonication power and duration that would result in satisfactory pigment blend specimens. The pigment blend was then manually blended with the plastisol for 5 minutes to make a visually-homogenous mixture. It was found that a significant amount of time and energy was needed to obtain consistent and high-quality conductive samples using the BS method. As a result, more rapid blending methods were investigated and the qualities of the corresponding blends were compared as described in the following sections.

3.1.2.2.2. Probe sonication (PS)

A probe sonicator (also known as sonic dismembrator) fractures and disperses solids primarily through a bubble nucleation and collapse sequence. High-voltage pulses of energy generated by an ultrasonic electronic generator are transformed to mechanical vibrations which are transmitted to a probe. The rapid oscillation of the probe's tip in turn produces a conical field of high energy where the formation, growth and implosion of bubbles, collectively referred to as acoustic cavitation, takes place. The implosion of bubbles releases a significant amount of energy in the cavitation zone which results in the fragmentation and dispersion of particles in a blend. Compared with a bath sonicator, a probe sonicator has a

more-defined cavitation zone and produces localized energy. Size of the bubbles is inversely proportional to the frequency of the ultrasound. Large bubbles, which release higher energy forces when collapse, are produced at lower frequencies (~20 kHz). Nucleation and cavitation decrease as frequency increases until they cease at frequencies larger than 2.5 MHz (Hilding *et al.* 2003). One of the major problems with ultrasonic agitation, especially for temperature-sensitive samples, is the immense local heat that is produced in the sonication process. Hence, it is recommended for the probe to operate in the pulse mode to reduce the heat gain in the sample by repeatedly allowing it to resettle after each burst.

In this study, 60 grams of the manually-mixed pigment blend (as described in the previous section) was poured into a 100-ml Griffin-form beaker. Then, a 550 W-probe sonicator (Fisher Scientific, Model 500) was used to further mix the pigment blend. The pigment blend was then manually blended with the plastisol for 5 minutes to obtain a visually-homogenous composite. The sonicator was set at different power levels ranging from 55 W to 550 W for two different net durations of 30 and 60 minutes at the 50% pulse mode (i.e. total durations of 60 and 120 minutes) to produce the final pigment blend.

3.1.2.2.3. Mechanical stirring

In this method, a mechanical stirrer (Mixer Direct, Model AM425) was used to mix 60 grams of the pigment blend for 10 minutes. The mechanical stirrer had a propeller with three pitched blades inclined at 26.5° from horizontal and a 2-inch diameter swept area. Three different rotational speeds of 375, 750 and 1500 rpm were used in different test cases. The pigment blend was then manually blended with the plastisol for 5 minutes to make a visually-homogenous mixture.

3.1.2.3. Formulation of the coating blend

The concentrations of different ingredients in the coating blend were varied in order to determine their influences on the physical, mechanical and electrical properties of the coating and finalize its formulation. The coating composite samples were required to have smooth and uniform surfaces without visible signs of micro-bubbles in order to avoid discontinuity in the conductive network within the composite. Samples that did not meet this requirement were discarded. With respect to the physical attributes of the blends, their viscosity (Figures 3.2 and 3.3) and the flexural stiffness of the resulting samples were measured to examine their pliability for industrial production. With respect to their mechanical properties, tensile tests were carried out to measure the tensile strength and ductility of the samples made of the coating blend. In the case of PVC-coated polyester yarn geogrids, it is reasonable to expect that the elasticity, ductility and tensile strength of the coating blend should be compatible with those of the coated material to prevent premature cracking and discontinuity in the coating when the product is handled, installed or put in service. With respect to the electrical properties of the coating blend, conductivity tests were carried out to measure the tensoresistivity (i.e. tensile strain-conductivity response) of composite specimens at different CB concentrations. The electrical conductivity of the plasticizer ingredient (without CB) was also measured as a control (i.e. baseline) case and compared with those of the CB-filled samples. The information germane to the CB-filled samples that were prepared and tested in this study is summarized in Table 3-2.

Table 3-2. Information related to the CB-filled samples prepared and tested in this study

Sample no.	CB type	CB (wt.%)	Plasticizer (wt.%)	Plastisol (wt.%)	Mixing method	No. of samples
1	1	1	5	94	MS	3
2		1.5	7.5	91	MS	3
3		3	15	82	MS	9
4					BS	9
5					PS	12
6		5	25	70	MS	9
7					BS	9
8					PS	12
9	2	3	15	82	MS	9
10					BS	9
11					PS	12
12		4	20	76	MS	3
13		5	25	70	MS	9
14					BS	9
15					PS	12
16		7	35	58	MS	3

3.1.2.4. Molding of samples for conductivity tests

A compression-molder (Kato and Miyashita 1990; Yacubowicz *et al.* 1990; Pinto *et al.* 1999) was used to prepare the filled polymer samples for conductivity tests. Once the mixing of the coating was complete, the blended material was cured using a compression-molder using 1 MPa pressure at 180 °C for 10 minutes to fabricate disk-shaped specimens for conductivity tests (Figure 3.4). Afterwards, the specimens were allowed to cool down gradually to the ambient temperature (typically, 23 °C) while kept under the same sustained pressure. Preliminary trials revealed that rapid cooling using a water quenching method would lead to the formation of fine bubbles in the specimens. Bubbles would increase the sample-to-sample scatter in the conductivity results, which was attributed to the formation of discontinuities in the conductive network within the specimens. The specimens were prepared in two thicknesses of 0.8 mm and 3 mm. The 0.8 mm thickness was chosen as a representative value for the coating thickness in PVC-coated polyester yarn geogrids. The 3-

mm thickness was selected to investigate the effect of specimen thickness on the conductivity results.

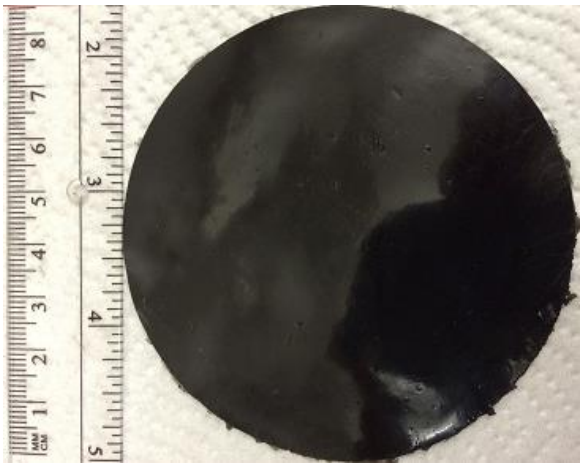

Figure 3.4. Coating sample used for electrical conductivity tests (mean thickness = 0.8 mm)

It should be noted that the entire annular body of the coating covering polyester yarns in the woven SEGG contributes to their conductivity. Therefore, the value 0.8 mm was considered to be a reasonable coating thickness in the planar coating samples used in this study and would be equivalent to what is collectively available around the polyester yarns in actual coated specimens for conductivity and sensing applications. However, the broader findings and conclusions of the study with respect to the influences of factors such as the fabrication method, confining pressure and strain rate on the tensoresistivity performance of SEGG samples are not limited to the specific thickness used in this study and could be extended to slightly different thicknesses that might be representative of different PVC/PET geogrid products.

Compression-molding was used to fabricate samples in this study due to the following main reasons: 1) its ease of use in the samples fabrication, 2) its extensive use in similar studies

(Kost *et al.* 1984; Flandin *et al.* 2000; Flandin *et al.* 2001; Yamaguchi *et al.* 2003; Al-Saleh and Sundararaj 2008; Hatami *et al.* 2009; Jha *et al.* 2010; Fathi *et al.* 2012) and 3) complex microstructure of injection-molded CB-filled composites (Wu *et al.* 2011) which would make the interpretation of results more difficult and would not yield any additional benefits with respect to the objectives and scope of the study.

Both injection- and compression-molding techniques can induce preferential alignment in the dispersed phase within the polymer matrix. This is especially true for CNTs (Parmar *et al.* 2013) and carbon fibers (Das *et al.* 2002), but it is also true for the fillers that can form complex and anisotropic aggregates with large shape factors (e.g. high-structure CBs – Wu *et al.* (2011)). The shape factor of CB aggregates is practically independent of their particle size (Yamaguchi *et al.* 2003). Compared with injection-molded specimens, a more random distribution and orientation of fillers has been reported in compression-molded specimens. Such specimens percolate at a lower filler concentration and exhibit a higher electrical conductivity (Abbasi *et al.* 2010). Same specimens when fabricated using injection molding even at low pressures exhibit a higher degree of particle alignment. Such an anisotropy results in a lower strain sensitivity in the flow direction (perpendicular to the pressure applied and the filler alignment) compared to that in the cross-flow direction (Parmar *et al.* 2013). Therefore, compression molding was considered to be more suitable for the purpose of this study. Finally, the composites tested in this study were intended for the coating of geogrid polyester yarns, which cannot be produced by injection molding. The fabrication stages are schematically shown in Figure 3.5.

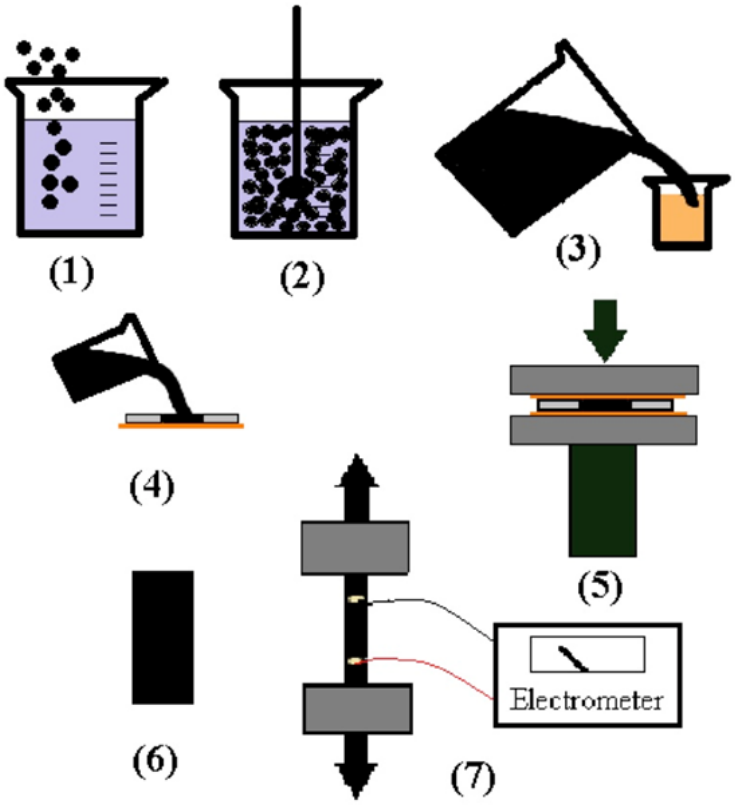

Figure 3.5. Sample fabrication stages: 1) filler is poured into the plasticizer and 2) the resulting blend is mixed and 3) added to PVC plastisol. 4) the composite is poured into a mold and 5) compression-molded to obtain 6) a sample which is tested in 7) a tensile testing machine or an electrometer

3.1.2.5. Conductivity measurements of molded samples

Three nominally-identical samples were fabricated for each formulation listed in Table 3-2 to improve the statistics of the conductivity test results and the results reported are an average of the values for the three samples. The surface of each sample was cleaned with ethanol prior to each conductivity measurement to ensure that it was clean and free of any CB residues. The sample thickness (which was necessary for the calculation of resistivity) was measured with a precision of 0.01 mm using a micrometer. The calculated specimen thickness was the mean value of the thickness measured at four locations (i.e. the central

point and three points on the sample circumference 120° apart). A direct current (DC) high-resistance meter (Agilent Model 4339B), working based on the two-point probe method (Schroder 2006), was used to measure the volume conductivity of the specimens. The device can apply contact loads between 10 and 100 N on the sample inside its resistance cell. Low values of contact load would result in inconsistent readings due to a poor contact with the sample. Excessively-high contact loads, on the other hand, would damage the specimen or at a minimum, change its thickness. The entire range of contact loads within the device was tried on different samples in order to find a value which would result in consistent measurements without imparting visible damage to the sample. Eventually, an optimum contact force of 50 N was selected for all electrical conductivity tests in this study. All measurements were carried out using an electrification time of 60 s as recommended in the device manual to ensure that a steady-state current had been established in the specimens. The maximum electric potential difference installed on the specimens was kept at 10 V to protect the specimens from overheating.

The two-point probe method was preferred over the four-point probe method since none of the acceptable types of contacts, delineated in the ASTM D4496 (2013) standard, between current electrodes and filled specimens in the four-point probe method was found practical for the composites tested in this study. According to this standard, either a large contact force or a conductive connection between the electrodes and the specimen is required in the four-point probe method. For the composites studied, it was practically impossible to apply the contact force required (which is a function of the specimens' width) to the specimens without damaging them or (at a minimum) changing their thickness significantly. Nevertheless, we experimented with the four-point method and used silver epoxy adhesive

to affix four short copper wires (electrodes) to a specimen. However, the epoxy was not able to establish a strong and reliable connection between the specimen and the electrodes, leading to significant scatter in the data. In addition, resistivity values of the composites were found to be typically greater than 10^4 Ω.m, which falls within the operating range of the two-point probe method. Therefore, the two-point probe method was deemed more suitable and reliable for this study.

3.1.2.6. Scanning electron microscopy

Scanning electron microscopic (SEM) images were taken using a Zeiss Neon 40 EsB microscope to examine the dispersion quality of the CB particles and aggregates in the coating samples. For selected combinations of composite formulation and mixing method, samples were first frozen in liquid nitrogen and then fractured to view their outer and cross-sectional surfaces under the microscope. The specimens were bonded to the SEM stubs using conductive silver paint. No coating was necessary since CB particles in non-coated specimens were visible because of a charge contrast mechanism. A series of incident electron beams with different voltages and incident angles was tried on the specimens in order to maximize the signal-to-noise ratio and the contrast in the charging patterns of the specimens. Eventually, a 20-kV electron beam at a 45° incident angle with respect to the specimen surface was selected to scan the specimen outer surfaces. In comparison, Chung *et al.* (1983) used a 60° incident angle for the same purpose. An incident angle normal to the specimen thickness was used to scan the cross-sectional surface of the specimens.

3.1.2.7. Flexural stiffness of the CB-filled coating material

Flexural stiffness is a mechanical property of geogrids which is evaluated to determine their suitability in construction projects, especially those involving weak and compressible foundations (Koerner 2012; ASTM D1388 2014). In this study, the cantilever test method of the ASTM D1388 (2014) test protocol was adopted to determine the flexural stiffness of the coating samples as a measure of their pliability. For each CB type, composite samples were made at three CB concentrations of 1.5, 3 and 5 wt.%. The samples were mixed using the MS method and were compression molded at 180 °C for 10 minutes. Four 200 × 25 × 0.8 mm strip specimens were prepared for testing from each sample. An apparatus was fabricated to meet the essential requirements of the ASTM D1388 (2014) test standard (Figure 3.6). A movable slide connected to a tensile test machine was used to push the specimens forward at a specified rate of 120 mm/min. Each specimen was slid four times (i.e. on both sides and from both ends of each specimen) on the low-friction horizontal surface of the setup until its leading end projecting from the edge of the horizontal surface came in contact with the surface of the ramp. The total length of the overhang was measured and the flexural stiffness of the specimen (termed as the flexural rigidity, G, in μJoule/m in the test standard) was calculated as:

$$G = 1.421 \times 10^{-5} \times W \times L^3 \tag{3-2}$$

where L is the bending length (one half of the overhang length) in mm and W is the mass per unit area of the composite in g/m^2.

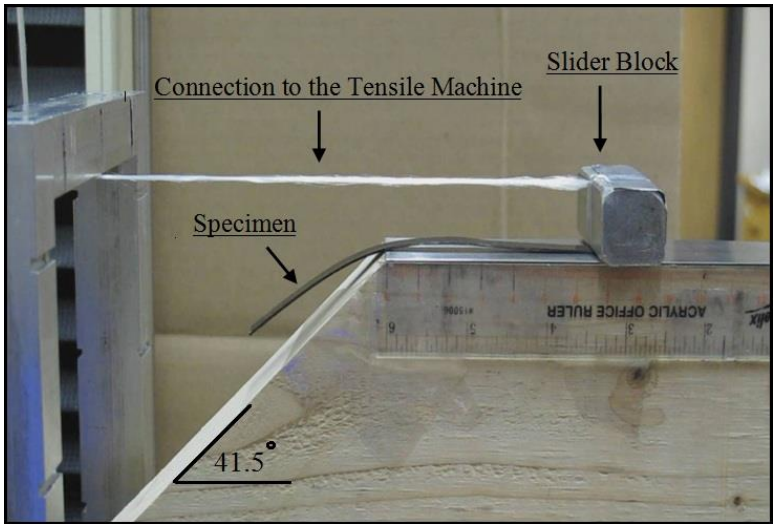

Figure 3.6. Laboratory setup for measuring flexural rigidity of polymer specimens in overall conformance with the ASTM D1388 (2014) test standard

3.1.2.8. Tensile properties and tensoresistivity response of the CB-filled coating material

The stress-strain response of the CB-filled coating was investigated in order to determine its in-plane tensile strength and ductility, following the ASTM D3039 (2014) test protocol. Additionally, the tensoresistivity response of the coating was determined by measuring the variation of its electrical conductivity with tensile strain. Strip specimens having a constant thickness of 0.8 mm were mounted in the grips of a mechanical testing machine. The gauge length of all specimens was kept constant and equal to 30 mm. The CB1-filled specimens were prepared at three different widths of 2.5, 5 and 10 mm and the CB2-filled specimens were prepared at two different widths of 2.5 and 5 mm to investigate the influence of the specimen length-to-width ratio on the measured tensoresistivity response of the coating material. Inspection of several commercially available geogrid samples indicated that the 2.5 mm and 5 mm widths are reasonable representative values for geogrid ribs used in practice.

Four specimens were prepared for each combination of CB type and rib width and were subsequently subjected to a monotonic tensile load at three different strain rates while changes in their electrical resistance were recorded in 0.5%-strain intervals. A reference strain rate of 0.15 %/min was selected as a lowest strain rate possible in the laboratory to represent the rates that could be expected in field applications (Hatami and Bathurst 2005). The tests were also carried out at faster strain rates of 2 %/min and 10 %/min in order to investigate the strain rate-dependency of the coating tensoresistivity and mechanical performance. The electrical resistance of the filled polymer specimens was measured using an analog Keithley electrometer and the two-point probe method in which two alligator clips 25 mm apart were attached to the specimens that were partly coated with silver paint (Figure 3.7). The global strain in the gauge length between the alligator clips (i.e. the bright marks next to the clips in Figure 3.7) was measured using a digital imagery approach (Wang *et al.* 2009b). These strains were compared with those measured from crosshead movements to ensure that the elongation rate would be fully transmitted to the specimen and would not be partially dissipated as a result of the slippage between the specimen and the clamps of the tensile test machine.

As previously stated in Section 1.3.3, the electrical conductivity of semi-conductive materials (including CB-filled polymers) can be also influenced by temperature. However, by and large in civil engineering applications of geogrids, they are installed in sufficient depth such that their temperature does not change significantly during service. Therefore, it is considered safe to assume that the strain sensitivity of SEGG products will not be adversely affected by temperature in typical applications.

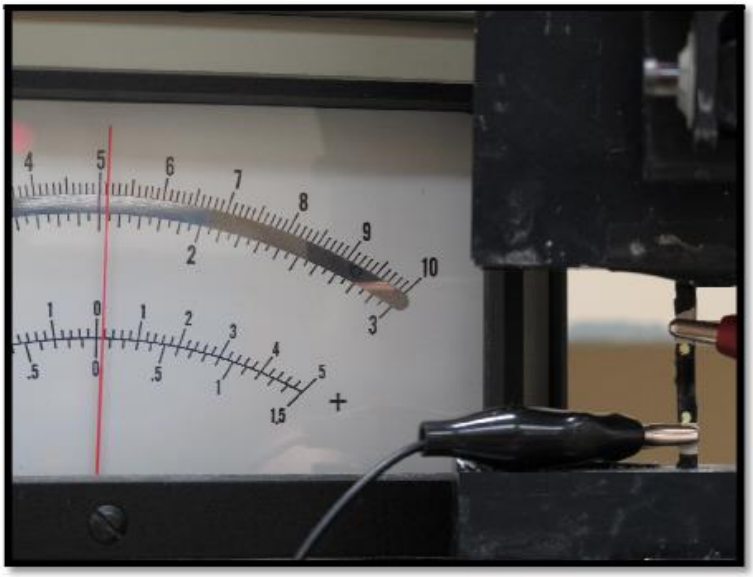

Figure 3.7. Setup to measure the tensoresistivity response of filled polymers

3.1.3. Results and discussion

3.1.3.1. Electrical conductivity

The influences of the plasticizer and CB concentrations, mixing method and sample thickness on the electrical conductivity of the PL/PR/CB composites are described in the following sections.

3.1.3.1.1. Influence of plasticizer concentration

The influences of the plastisol and plasticizer conductivity on the measured conductivity of the PL/PR/CB samples were evaluated by testing the conductivity of three samples for each of the following three cases: pure plastisol, plastisol-plasticizer combination (PL/PR) and plastisol-plasticizer-CB (PL/PR/CB) formulation. Figure 3.8 shows a comparison of electrical conductivity results for the aforementioned samples. The results show that

conductivity values of the samples made of the plasticizer and the plastisol are at least three orders of magnitude smaller than those of the samples containing the CB particles used in this study. Therefore, the influences of the plastisol and plasticizer conductivity on the measured conductivity of the composites could be considered as negligible.

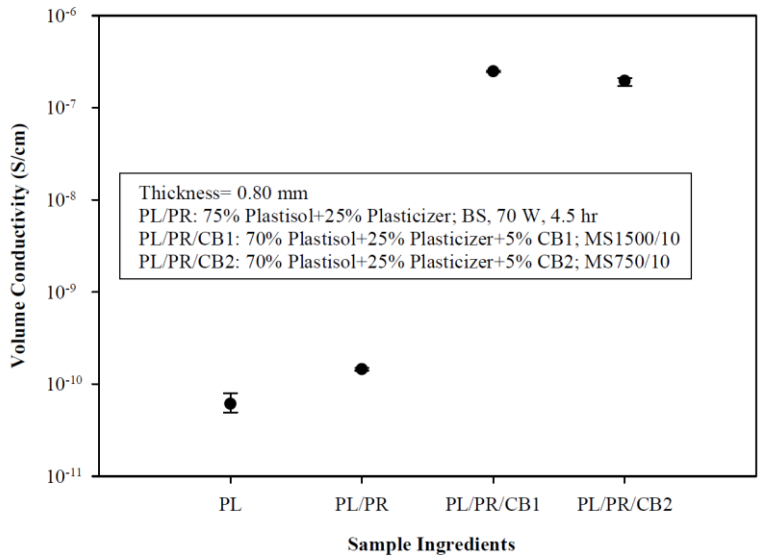

Figure 3.8. Comparison of electrical conductivity values of different ingredients in the composite. Notes: three samples were tested for each case; BS: bath sonication, MS: mechanical stirring.

3.1.3.1.2. Influence of mixing method

Figures 3.9 and 3.10 summarize the results of electrical conductivity measurements for composite samples produced using different blending methods and CB concentrations (See Table 3-2). The quality of CB dispersion using each mixing method shown is judged by the magnitude and repeatability of the conductivity results. The parameters shown on the horizontal axis include the sonication power, rotational speed and mixing duration. It can be seen that overall, the MS method within the range between 750 and 1500 rpm for 10 minutes of blending resulted in samples with greater conductivity and narrower scatter in the test results compared to those made using the BS and PS methods. Results in Figure 3.9 indicate

that for CB1-loaded specimens, mechanical stirring at a rotational speed of 1500 rpm for 10 minutes was optimal for high electrical conductivity and low scatter in data. A rotational speed of 750 rpm or 1500 rpm for 10 minutes provided the highest conductivity for CB2-filled specimens at 5% concentration but the results at the reduced rotational speed of 750 rpm were more consistent, which confirms that the lower structure CB (i.e. CB2, see Table 3-1) required a smaller shearing effort to establish a conductive network within the polymer matrix (Narkis *et al.* 1981). Conductivity results for the CB1-filled specimens that were made using the PS method were not very consistent. Also, low values of electrical conductivity were obtained for CB2-filled specimens that were mixed using the PS method. Figure 3.10a shows that the BS method is mostly effective in terms of homogeneity and repeatability for the blends filled with low concentrations of the moderate-structure CB2. This finding confirms the hypothesis stated earlier that this method would be mostly effective for low-viscosity blends.

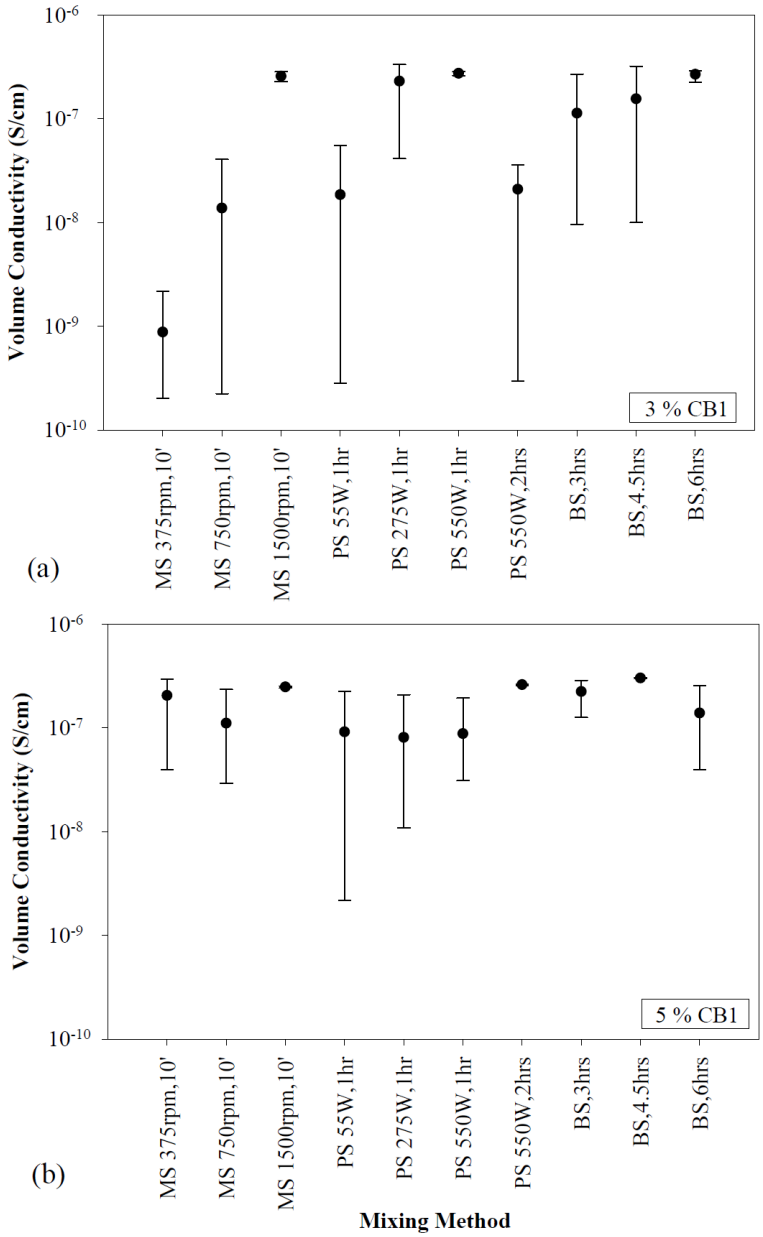

Figure 3.9. Volume conductivity results for electrically conductive composite specimens filled with a) 3% CB1, b) 5% CB1, and produced using different mixing techniques. Notes: three samples were tested for each mixing case shown; specimen thickness, t = 0.8 mm; time periods on the horizontal axis refer to the stirring or sonication durations (as applicable).

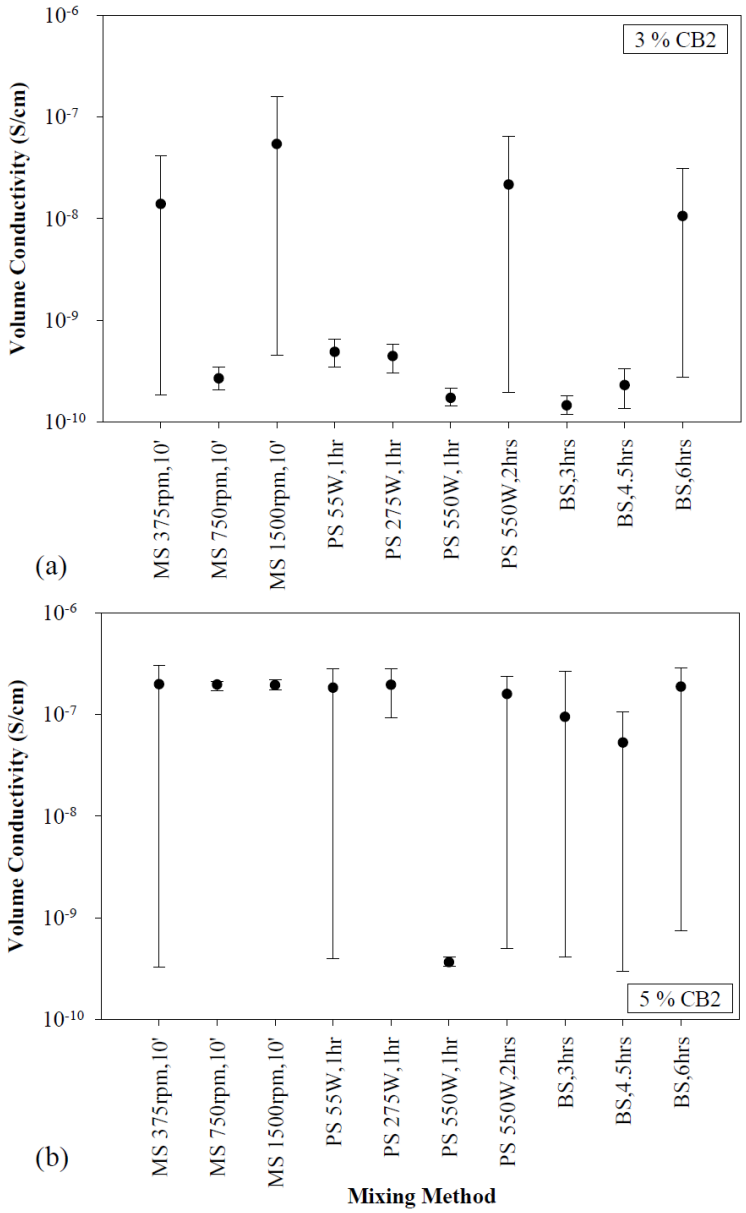

Figure 3.10. Volume conductivity results for electrically conductive composite specimens filled with a) 3% CB2, b) 5% CB2, and produced using different mixing techniques. Notes: three samples were tested for each mixing case shown; specimen thickness, t = 0.8 mm; time periods on the horizontal axis refer to the stirring or sonication durations (as applicable).

The conclusions made from Figures 3.9 and 3.10 can be explained using SEM images in Figures 3.11 and 3.9. The density of the brighter spots in the SEM images is a direct indication of the density of conductive fillers present in the insulating matrix while the visual

arrangement of fillers in a composite is an indication of the quality of their dispersion. The few spots observed in the pure specimen (Figures 3.11a and 3.9a) are attributed to the presence of impurities and contaminants in the plastisol matrix. This type of reflections can be readily distinguished from the white spots representing the CB particles (Figures 3.11b-d and 3.9b-d). Figures 3.11b and 3.9b show that the energy generated by the PS method was not adequate to completely break the intermolecular interactions between the agglomerated CB particles. This is another indication that the sonication-based methods (i.e. PS and BS) are mostly effective for blends filled with low CB concentrations. Figures 3.11c and 3.11d compare the influence of rotational speed in the MS method on the dispersion quality of CB1 particles. Figures 3.113.9c and 3.9d provide the same comparison for the CB2-filled composites. It can be observed that a higher rotational speed of 1500 rpm provided sufficient energy to develop a more uniform conductive network throughout the polymer matrix filled with CB1 particles. In comparison, a lower rotational speed was sufficient to form a conductive network in samples filled with the lower-structure CB (i.e. CB2). These observations are consistent with the results from electrical conductivity tests (e.g. see Figures 3.9 and 3.10). The SEM images also confirm the findings of Bourrat (1993) and Donnet (1994) indicating that CB is composed of primary particles fused into primary aggregates.

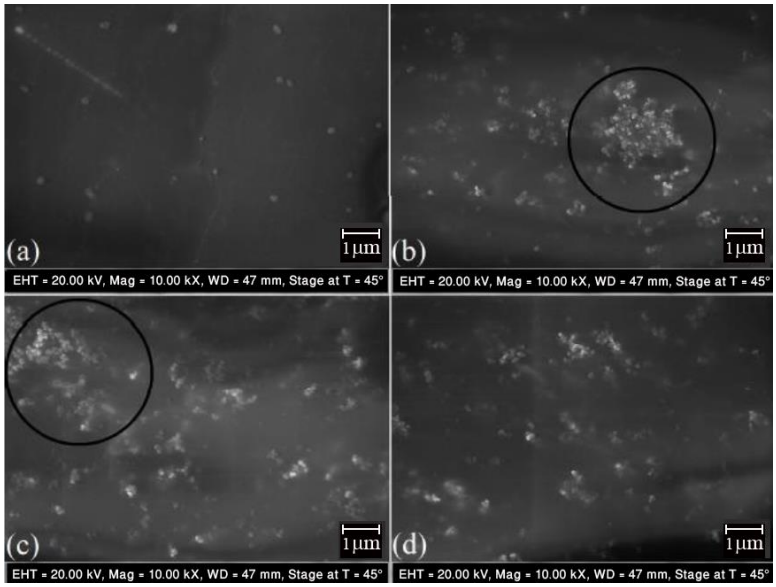

Figure 3.11. SEM images for a) pure plastisol, b) 3 wt.% CB1-filled composite mixed with the PS method (550 W, 2 hrs), c) 3 wt.% CB1-filled composite mixed with the MS method (750 rpm, 10 minutes), and d) 3 wt.% CB1-filled composite mixed with the MS method (1500 rpm, 10 minutes). Note: black circles show areas where CB particles were not adequately separated in the blending process.

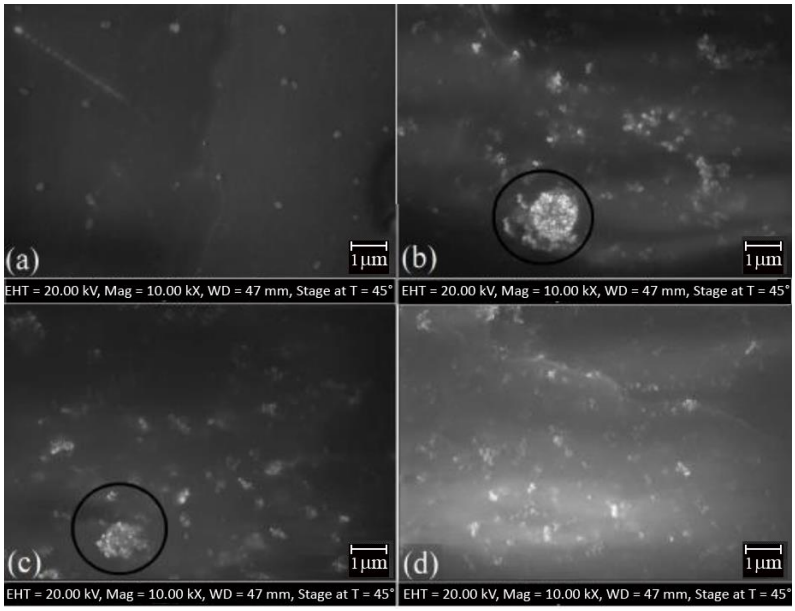

Figure 3.12. SEM images for a) pure plastisol, b) 5 wt.% CB2-filled composite mixed with the PS method (550 W, 1hr), c) 5 wt.% CB2-filled composite mixed with the MS method (375 rpm, 10 minutes), and d) 5 wt.% CB2-filled composite mixed with the MS method (750 rpm, 10 minutes). Note: black circles show areas where CB particles were not adequately separated in the blending process.

3.1.3.1.3. Influence of sample thickness

Sample thickness can influence the measured volume conductivity because a greater number of cavities and air bubbles of different size are likely to form in thicker samples which result in a higher probability of developing discontinuities in the conductive network. Figure 3.13 shows the influence of sample thickness on the measured electrical conductivity of CB1-filled composites made using the three mixing methods. It can be observed that measured volume conductivity values of the 3-mm samples are between two and three orders of magnitude smaller than those of otherwise identical 0.8-mm samples. These results confirm a lower measured conductivity anticipated in thicker specimens as per the earlier discussion in this section. The results in Figure 3.13 indicating that the measured conductivity normalized to a specimen dimension is a function of the specimen thickness highlight the challenge in determining the conductivity of filled polymers independent of their specimen size. With respect to the application pertaining to the current study, since the 0.8-mm thickness is more representative of the coating of actual geogrid products, this thickness was adopted for the subsequent tests in this study.

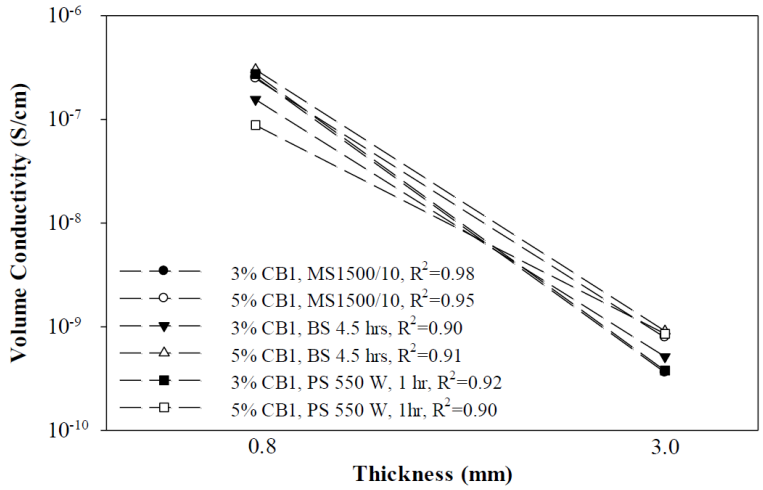

Figure 3.13. Influence of the sample thickness on its measured volume conductivity. Notes: results are the mean values of three tests for each case; the time periods shown in the legend are the stirring or sonication durations (as applicable).

3.1.3.1.4. Influence of CB concentration

Figure 3.14 shows the influence of CB concentration on the volume conductivity of plastisol/CB samples that were made using the MS method. As a starting point, the conductivity of pure plastisol samples was measured (i.e. CB% = 0) which gave a mean value of 3.4×10^{-11} S/cm. As shown in Figure 3.14, the measured conductivity results of the pure plastisol specimens are well within the range of values reported in the literature (i.e. 10^{-9}–10^{-13} S/cm – Patrick (2005)). In comparison, the conductivity of CB particles is in the range 10^{-1}–10^{+2} S/cm (Sánchez-González *et al.* 2005; King *et al.* 2009a; Wang and Ding 2010). In both cases shown in Figure 3.14, well-defined percolation thresholds and percolation regions are identified in the form of a jump in the measured electrical conductivity with an increase in the CB concentration for each CB type tested.

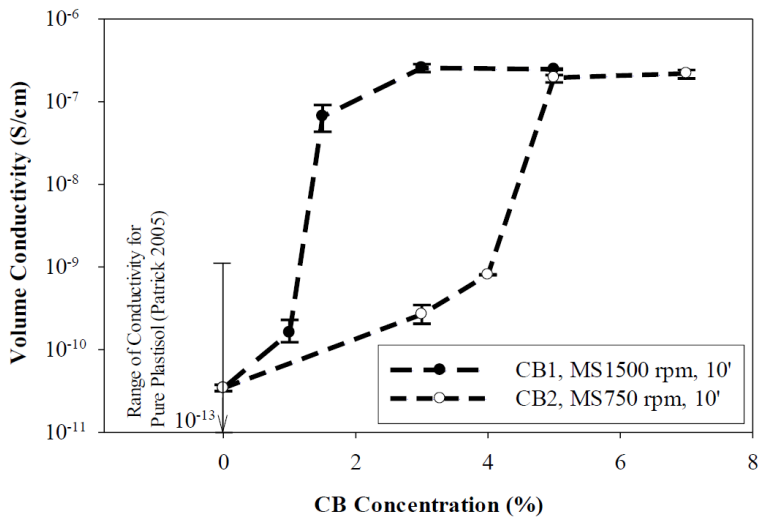

Figure 3.14. Volume conductivity of PVC/plastisol as a function of CB concentration. Note: thickness of specimens = 0.8 mm.

The percolation threshold is the lower-bound value for a critical range of conductive filler concentrations corresponding to the formation of global conducting networks (spanning clusters) within a polymer composite (Bunde and Dieterich 2000; Torquato 2001). The range of filler concentrations in which the conductivity is highly sensitive to the CB concentration is called the percolation region. An important property of the percolation region is that the connectivity of the filler network (and hence the conductivity of the filled polymer) is sensitive to the applied stress (Zhao *et al.* 2013).

Results in Figure 3.14 also show that the percolation threshold of CB1 is lower than that of CB2 (approximately, 1.0% for CB1 vs. 4% for CB2) which is consistent with the fact that CB1 is a higher-structure black than CB2 as per their OAN values given in Table 3-1. Therefore, samples with 1.5% CB1 and 5% CB2 concentrations were made to test their tensoresistivity response. Beyond the percolation threshold, at a given filler concentration, the composites reach comparable levels of conductivity. The electrical conductivity of the

composites typically reaches a plateau by adding more CB beyond the percolation region indicating that the conductive network has already been established within the filled polymer.

3.1.3.2. Flexural stiffness of the CB-filled coating material

Figure 3.15 shows the mean values of flexural rigidity and the corresponding ranges of sample-to-sample variations for the CB1- and CB2-filled coating specimens. Results shown in Figure 3.15 indicate that the flexural stiffness of the CB-filled composites decreases significantly with an increase in the CB concentration. For instance, the amount of reduction is more than 75% between 1% and 5% concentrations for both CB types. These results also indicate that the amount of reduction in the specimens' flexural stiffness as a function of the CB concentration was consistent and independent of the CB type blended in the composite. While stiffer geogrids are required in the construction projects that involve compressible foundations, higher flexibilities would generally be more desirable for the coating material in the applications relevant to this study because a more flexible coating will help form a more strain-compatible, extensible and ductile coating around the polyester yarns, and hence will be more durable in field applications.

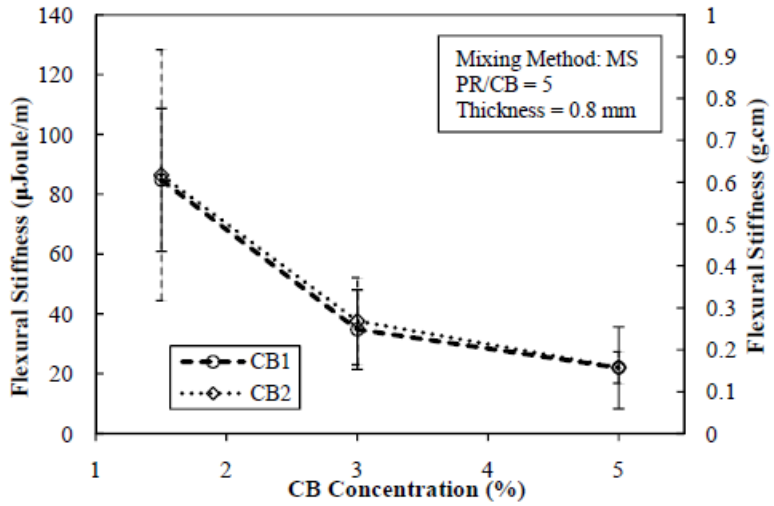

Figure 3.15. Flexural stiffness (rigidity) of the coating material

3.1.3.3. Tensoresistivity and tensile properties of the CB-filled coating material

A series of tensoresistivity tests was carried out on 0.8 mm-thick coating specimens that had been made using different combinations of MS rotational speed and duration, and CB concentrations. Figures 3.16 and 3.17 show the tensoresistivity responses of the CB1- and CB2-filled specimens, respectively, having different widths and tested at different strain rates. The influence of specimen width on the measured tensoresistivity of the coating material is summarized in Figure 3.18. The results show that the measured tensoresistivity of the coating material is essentially independent of the specimen width for the range of the widths examined. However, the scatter in the test results is larger for wider specimens. This could be attributed to the fact that wider specimens can develop a larger number of alternative conductive pathways between the measuring points, which could lead to a wider variability between the conductivity results.

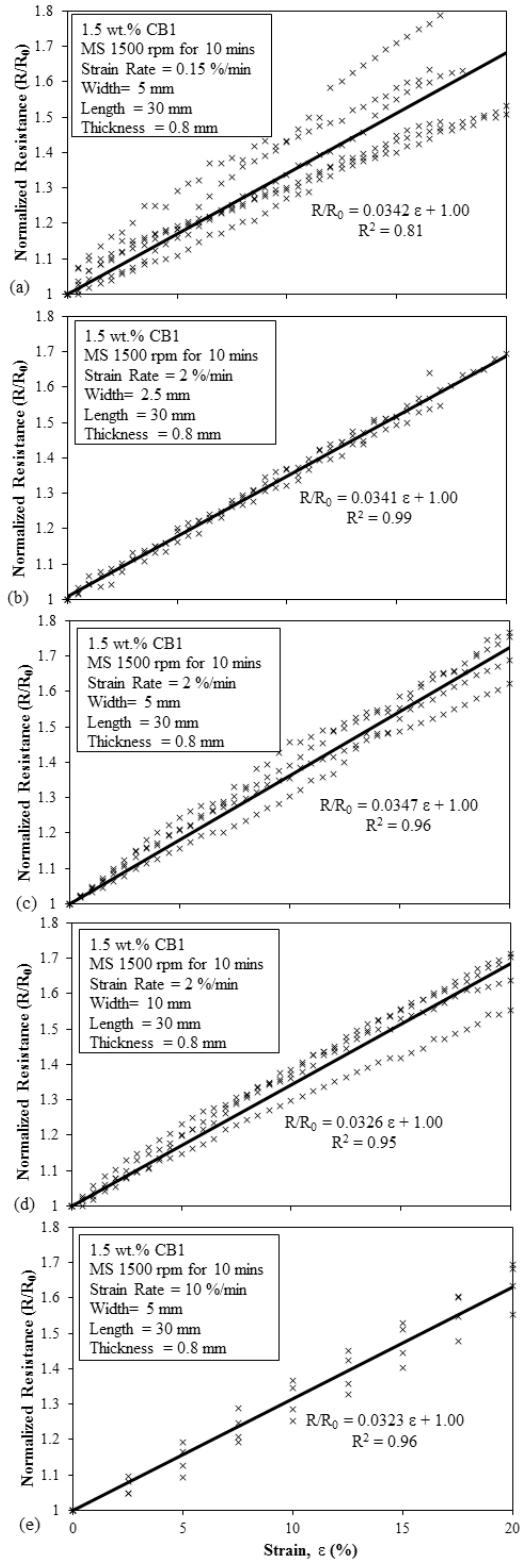

Figure 3.16. Strain-sensitive electrical conductivity response of 1.5 wt.% CB1-filled coating material

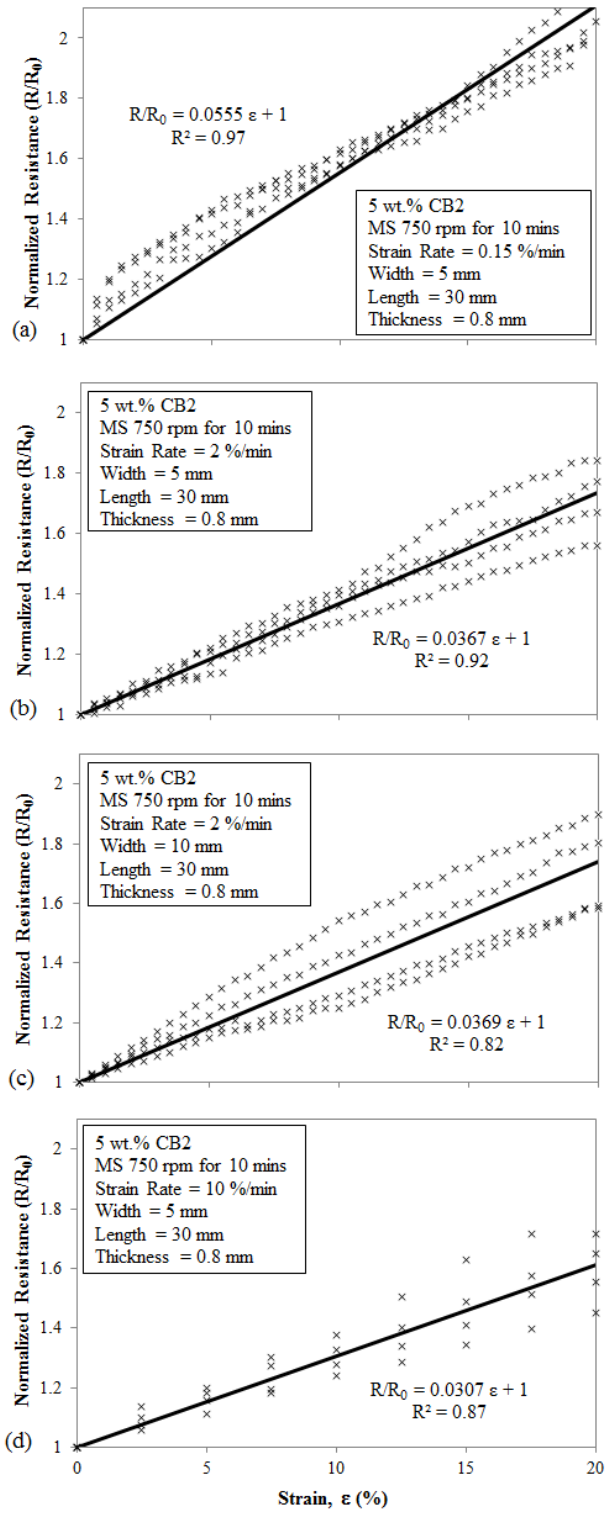

Figure 3.17. Strain-sensitivity electrical conductivity of 5 wt.% CB2-filled coating material

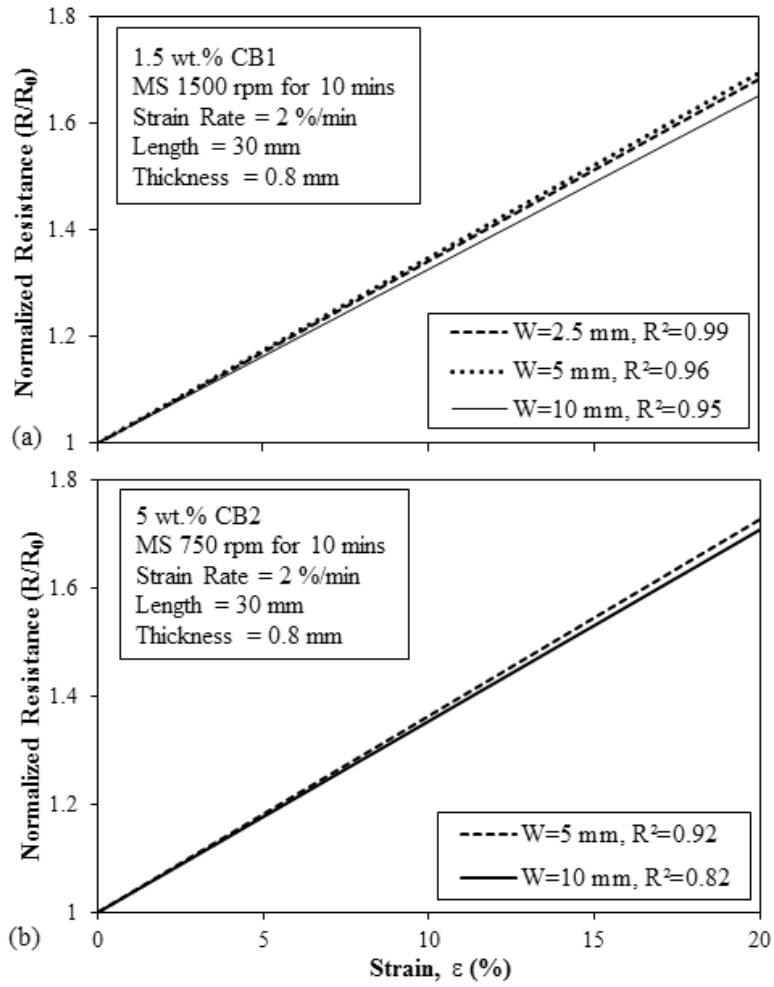

Figure 3.18. Influence of specimen width on the strain-sensitivity response of the CB-filled coating material

Figures 3.19 and 3.20 show the tensoresistivity response and the tensile properties of the coating material at different strain rates. The following observations are made: (1) The results show that the tensoresistivity response of the CB2-filled specimens is more sensitive to the strain rate than that of the CB1-filled specimens, and (2) the tensoresistivity of filled specimens is generally greater when they are subjected to slower-rate tensile loads. Tensoresistivity of a lower-structure black is expected to be more sensitive to the magnitude and the rate of strain. This is because the relatively smaller amount of chaining and branching

in a low-structure black is expected to make the connectivity of its conductive network more vulnerable to both the magnitude and rate of the applied load. The second observation suggests that the relaxation that is greater with a slower rate is more able to disrupt CB-CB interactions vs. a more affine deformation corresponding to a faster rate.

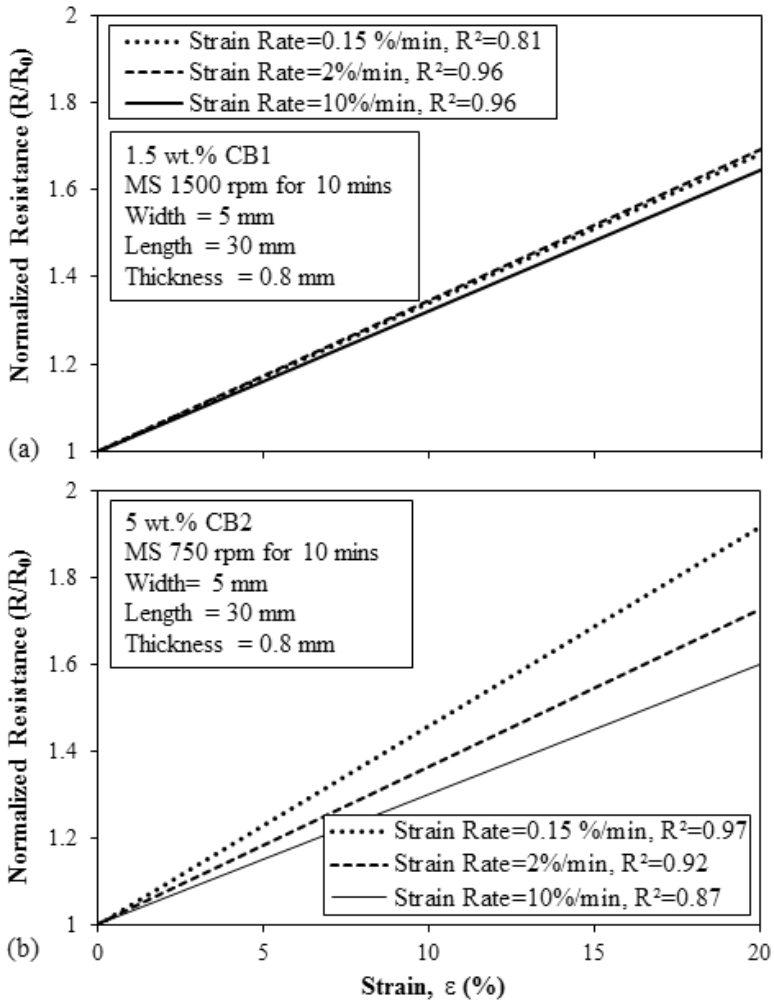

Figure 3.19. Influence of strain rate on the strain-sensitivity response of the CB-filled coating material

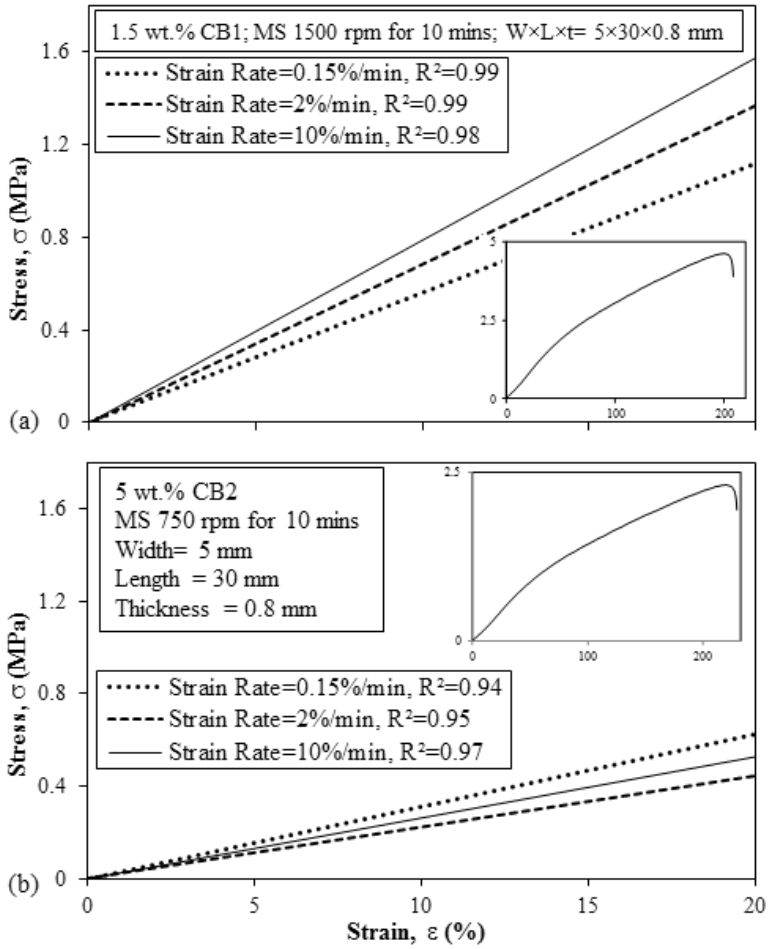

Figure 3.20. Influence of strain rate on the tensile properties of the CB-filled coating material. Note: the insets show the full-range stress-strain behavior of the material.

In summary, results shown in Figures 3.16 through 3.19 indicate that both CB1 and CB2 exhibit strain sensitivity for detecting tensile strains in health monitoring applications of geosynthetic structures. However, the specimens filled with CB1 (i.e. higher structure) show a more consistent and reliable behavior in that their response is less sensitive to the strain rate and specimen width. In addition, comparison of R^2 values in Figures 3.16 and 3.17 indicates that CB1-filled specimens resulted in a smaller scatter in their measured tensoresistivity performance.

3.1.4. Conclusions

The tensoresistivity performance of geogrid coating samples made of carbon black-filled polyvinyl chloride composites (plastisol/CB) was studied. PVC-coated, polyester-yarn geogrids are commonly used in reinforcement applications in geotechnical engineering. The objective of the study was to develop geogrid coating materials that would exhibit reliable and reproducible tensoresistive response that can be used to measure mechanical strains in field applications. The effectiveness of three different mixing methods to blend the plastisol/CB mixtures and the influence of the plastisol/CB coating thickness on the measured electrical conductivity of the specimens were investigated.

Results of the study showed that mechanical stirring yielded higher quality samples with respect to the quality of dispersion and the magnitude and consistency of the measured tensoresistivity as compared to the sonication-based methods. Blending CB with plastisol increased the viscosity of the composite. Therefore, a solvent (plasticizer) was used to control the rheological behavior of the composite. A series of viscosity tests on the CB/plasticizer mixtures revealed an optimum ratio for the two materials to increase the pliability of the composite as a geogrid coating. Tensoresistivity tests on coating specimens showed that both types of CB examined in this study exhibited significant strain sensitivity for detecting tensile strains in health monitoring applications of geosynthetic structures. However, the specimens filled with the higher-structure CB showed a more consistent and reliable behavior in that their response was less sensitive to the strain rate and specimen width. In addition, the same specimens showed a smaller scatter in their measured tensoresistivity response as compared to those filled with a lower-structure CB. Additionally, the coating specimens filled with either of the CB types showed significant tensile strength and ductility.

Finally, results of the study indicate that there is a sizeable scatter inherently present in the measured tensoresistivity of SEG specimens due to the random nature of dispersed conductive fillers with respect to their spatial distribution within the host polymer, connectivity, structure and other related factors. One main objective of the study was to reduce this scatter by identifying fabrication methods and conditions that would result in the most accurate and repeatable strain measurements possible for the filler and polymer materials used in the study. However, for practical applications, an advantage of the SEG instrumentation approach is that strains can be measured and monitored readily at several comparable locations in the structure (e.g. at locations that are at the same distance from the facing of a highway embankment or a retaining wall which is subjected to plane-strain loading conditions). The measured strain data from several nominally identical locations within the structure will be significantly more accurate and reliable than each individual data point, which helps reduce the impact of any scatter and uncertainty inherently present in each of the individual measuring locations significantly.

3.2. Strain-sensitive electrical conductivity of CB-filled PVC composites subjected to cyclic loading

3.2.1. Introduction

The development of SEGG for practical applications requires an understanding of the recoverability and reproducibility of their tensoresistivity response in field conditions. By recoverability, we refer to the capability of the coating material to maintain its tensoresistive properties when subjected to cyclic loading. Geogrids are commonly used to stabilize a wide

range of earthwork structures (e.g. pavements, embankments, retaining walls and bridge abutments) which are subjected to cyclic loading (e.g. traffic). Therefore, the CB conductive network in SEGG would invariably be subjected to cyclic loading which could result in irreversible deformations that could alter the tensoresistive properties of the SEGG materials.

The cyclic loading of CB-filled composites for sensor applications has been the subject of limited studies. Kost *et al.* (1984) studied the resistivity behavior of CB-filled silicone rubbers under cyclic loading. They concluded that mechanically-preconditioned composite samples would behave "nearly reversibly" when cyclically strained below 50% of a preconditioning strain. Moreover, a greater degree of recoverability would be expected for a greater preconditioning strain. Preconditioning strain, whether tensile or compressive, is an indication of the stress history of a particular sample and is defined as the initial strain that is applied to a sample before actual testing in order to increase its tolerance to subsequent strains, which are typically kept below the preconditioning strain.

Flandin *et al.* (2000) and Flandin *et al.* (2001) evaluated the performance of three types of fillers (i.e. carbon fiber, low structure CB and high structure CB) in ethylene-octane elastomer matrix and concluded that the composites containing high-structure CB exhibited remarkable electrical and mechanical properties with significant recoverability. Yamaguchi *et al.* (2003) studied the influence of pre-straining on the electrical and mechanical properties of natural rubber (NR) doped with a moderate-structure N330 CB (made by oxidation of oil in a furnace) in both tension and compression. The composite's behavior was observed to be significantly sensitive to the size of the CB aggregates and the quality of filler dispersion. The tensoresistivity of composites increased with CB concentration, and pre-straining of

samples improved the recoverability of their tensoresistivity. Jha *et al.* (2010) carried out the same experiments as Yamaguchi *et al.* (2003) except that they used a high-structure Printex XE2 CB (which is produced using controlled partial oxidation of heavy oil, known as the gasification process). Jha et al.'s results showed that a higher structure black could improve the recoverability of the composite's conductive response.

The literature survey above indicates that the resilience of the tensoresistive properties of PVC/CB composites subjected to cyclic loading needs further investigation. Hence, a primary objective of this part toward developing SEGG materials was to a use a series of cyclic tensile tests with varying régimes and strain rates in order to examine the recoverability of tensoresistive properties of PVC/CB coating composites under cyclic loading including the influence of mechanical preconditioning.

3.2.2. Experimental program

3.2.2.1. Materials

The same materials as those used for the monotonic tests (see Section 3.1.2.1) were used for the cyclic loading tests.

3.2.2.2. Fabrication technique

Comparison of the results shown in Figures 3.9 and 3.10 indicated that the MS method with a duration of 10 minutes and a rotational speed of 1500 rpm for CB1- and 750 rpm for CB2-filled specimens would result in greater and lower-scatter conductivity results as compared to those made using the bath sonication and probe sonication methods. Therefore, these

mixing methods were used to mix the specimens that were subsequently compression-molded using the same procedure as given in Section 3.1.2.4.

3.2.2.3. Conductivity measurement of filled samples

The same procedure as given in Section 3.1.2.5 was followed to measure the samples conductivity.

3.2.2.4. Cyclic loading tests

The tensile tests were carried out in general conformance with the ASTM D6637 (2013) test protocol. However, the loading applied was cyclic in nature as described in this paper and single-rib test specimens were used to isolate the conductivity response of the rib from any adverse influence of transverse members, which are otherwise typically included at both ends of the specimens to improve clamping conditions. Depending on the loading type, two or four 100 × 5 × 0.8 mm (length × width × thickness) geogrid rib specimens with a 30-mm gauge length were tested. The specimens width and gauge length were chosen as representative values for the rib width and aperture size in commonly-used PVC-coated polyester yarn geogrids, respectively.

3.2.2.5. Network damage index and gauge factor

When an unstretched (virgin) specimen doped at a critical concentration is subjected to a loading-unloading cycle with a maximum strain of ε_p (Figure 3.21), its electrical resistance typically shows hysteretic behavior. Gauge factor is the relative change in the specimen's electrical resistance per unit strain and defined as (Aneli *et al.* 1999):

$$GF = \frac{\Delta R / R}{\varepsilon} \tag{3-3}$$

where ΔR is change in resistance at the strain ε and R is unstrained resistance. The gauge factor during loading (GF_L) is usually greater than that during unloading (GF_U). As a result, the specimen has a greater electrical resistance than its original value when the strain is fully removed. This increase in electrical resistance is due to a net reduction in the number of conduction paths within the composite. The filled specimen typically shows continuous hysteretic response when subjected to additional loading-unloading cycles. The magnitude of change in electrical resistance of the filled specimen at the end of the ith cycle with respect to its initial value is defined here as the network damage index corresponding to the ith cycle (NDI_i). The NDI_i value represents the damage accumulated in the specimen during the loading-unloading cycling process from the beginning of a test until the end of the ith cycle. A few recent studies have shown that stretching (i.e. preconditioning) specimens to strains (ε_p) greater than a set peak value in subsequent cycles (ε_c) could help reduce the cumulative damage in the specimen when subjected to continued load reversals (e.g. Kost *et al.* (1984)). Therefore, it is hypothesized that the damage accumulated in the specimen over a given number of cycles is inversely proportional to the over-elongation ratio (OER) defined here as:

$$OER = \frac{\varepsilon_p}{\varepsilon_c} \tag{3-4}$$

In other words, preconditioning a specimen by stretching it to an initially larger strain of ε_p might improve the resilience of its tensoresistive properties in subsequent loading-unloading cycles with a maximum strain of ε_c.

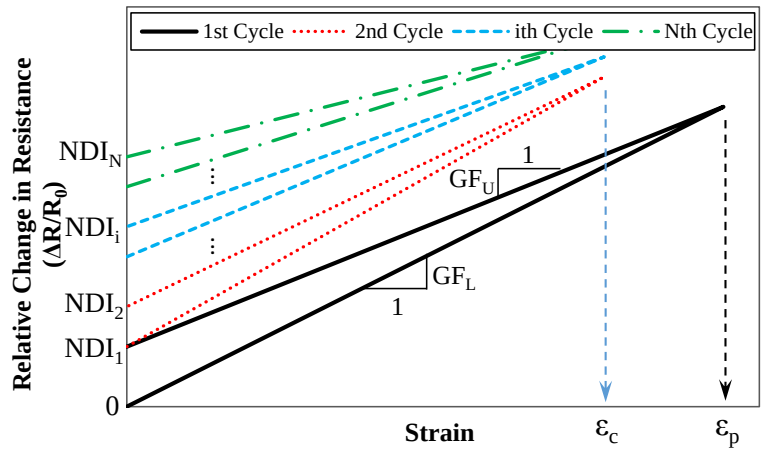

Figure 3.21. Hysteretic behavior of electrical conductivity

3.2.2.6. Loading types

Five different cyclic tensile tests with varying régimes and strain rates were carried out in order to examine the recoverability of tensoresistive properties of the coating composites under cyclic loading. Details of the tests are described in the following sections.

3.2.2.6.1. Type I: Incremental cyclic loading with rapid unloading

The tensoresistive properties of composite specimens subjected to incremental cyclic loading were studied to examine the accumulation of irreversible damage occurring in the composite. For each CB type, four specimens were stretched at three different cross-head strain rates ($\dot{\varepsilon}$) of 0.15, 2 and 10%/min to five levels of cumulative strain, ε (2, 5, 10, 15 and 20%) with frequent rapid unloading to zero strain in between subsequent loadings (Figure 3.22a). The peak strain was selected as ε_c = 20% which was close to the ultimate strain, ε_{ult}, of the PET yarns commercially used to manufacture geogrids (Shinoda and Bathurst 2004). Therefore,

the selected strain levels spanned from low to high fractions (i.e. 10, 25, 50, 75 and 100%) of ε_{ult} of the PET yarns.

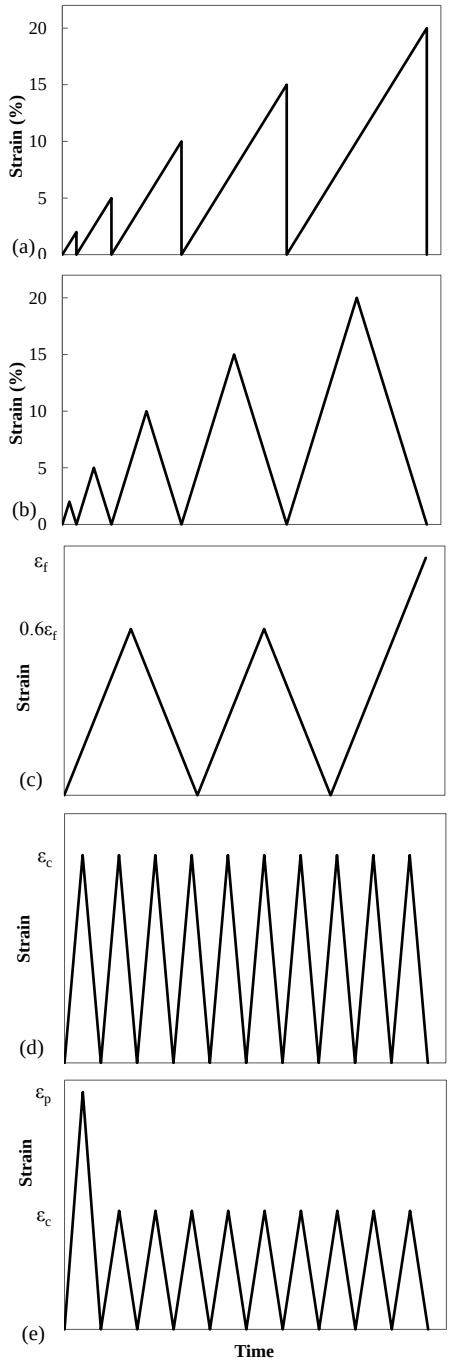

Figure 3.22. Loading-unloading régime for a) Type I, b) Type II, c) Type III, d) Type IV, and e) Type V

3.2.2.6.2. Type II: Incremental cyclic loading with gradual unloading

The second loading type was identical to Type I except that instead of rapid unloading the specimens were unloaded at the same strain rate as the loading phase in order to understand the influence of gradual unloading on the formation and destruction of conductive paths in the network of CB particles (Figure 3.22b).

3.2.2.6.3. Type III: Large-strain cyclic loading

Studying the hysteretic electrical conductivity response under large strains can help develop better understanding of the microstructural changes in the CB conductive network. In this loading régime (Figure 3.22c), two coating specimens (for each CB type) were subjected to two full loading-unloading cycles with ε_c = ~ 0.6 ε_f at 2% strain/min after which the specimens were stretched to failure. A smaller number of specimens was used in these tests (as compared to the previous series) due to the satisfactory reproducibility observed in Types I and II at the strain rate of 2 %/min.

3.2.2.6.4. Type IV: Cyclic loading

In this loading régime, specimens were subjected to a greater number of strain cycles (10) at lower strains. Two specimens for each CB type were stretched up to a target strain of ε_c = 5% (Figure 3.22d) at the strain rate of 2%/min for both loading and unloading paths.

3.2.2.6.5. Type V: Cyclic loading with prestraining

This loading régime was used to study the influence of prestraining on the tensoresistivity hysteresis of the composites. It was identical to loading Type IV except that in the first cycle,

a larger strain, ε_p, was applied on the specimens followed by nine cycles of a smaller peak strain at $\varepsilon_c = 0.3\varepsilon_p$, $0.5\varepsilon_p$ and $0.7\varepsilon_p$ in three different test series (Figure 3.22e). The same strain rate of 2%/min was used for both loading and unloading paths in these tests.

Details of the cyclic load tests carried out in this study are summarized in Table 3-3. For all loading types, CB-filled specimens were subjected to a tensile load at a specified strain rate while changes in their electrical resistance were recorded using an electrometer in 0.5%-strain intervals. A reference strain rate of 0.15%/min was selected as a lowest strain rate possible in the laboratory to represent the rates that could be expected in field applications (e.g. Hatami and Bathurst (2005)). The tests were also carried out at faster strain rates of 2%/min and 10%/min in order to investigate the strain rate-dependency of the coating tensoresistivity and mechanical performance.

Table 3-3. Information of the cyclic load tests

CB type	Test type	Strain rates (%/min)	No. of specimens
1, 2	I	0.15, 2, 10	4
	II	0.15, 2, 10	4
	III	2	2
	IV	2	2
	V	2	2

3.2.3. Results and discussion

3.2.3.1. Type I: Incremental cyclic loading with rapid unloading

Tensoresistivity results of representative CB1- and CB2-filled coating specimens are shown in Figures 3.23 and 3.24. The specimens were subjected to loading Type I at three different strain rates of 0.15, 2 and 10%/min. The NDI_i values for all specimens tested are shown in Figure 3.25. Both CB1- and CB2-filled specimens exhibit considerable hysteresis in their

tensoresistivity response. This hysteretic behavior can be attributed to a disruption in the tunneling mechanism of electron transfer between adjacent CB particles as a result of physical damage to the conductive network (Jha *et al.* 2010). The tunneling effect is the principal mechanism governing the change in the electrical conductivity of filled polymers, especially under small strains (less than about 25% – Kost *et al.* (1984)), where the growth of spaces between filler particles result in a net reduction in the number of conduction paths established through the composite (Aneli *et al.* 1999).

Figures 3.23 and 3.24 also indicate that the extent of hysteresis in the tensoresistivity response of filled composites depends on the CB type and strain history, including maximum strain attained during loading (Böger *et al.* 2008; Zhang *et al.* 2013a) and the strain rate employed (Ku-Herrera and Avilés 2012). The data show that the first loading cycle resulted in a smaller amount of breakdown in the conductive network in specimens filled with the higher-structure black (i.e. CB1). This is consistent with Jha et al.'s conclusions (Jha *et al.* 2010) that a larger filler surface area (and hence, the surface attraction to the polymer) would be more effective in reducing the relative movement between the filler and the polymer subjected to applied strain. The higher surface area available in higher-structure blacks allow the weak van der Waals forces to hold the filler network structure together and to reform during the unloading period.

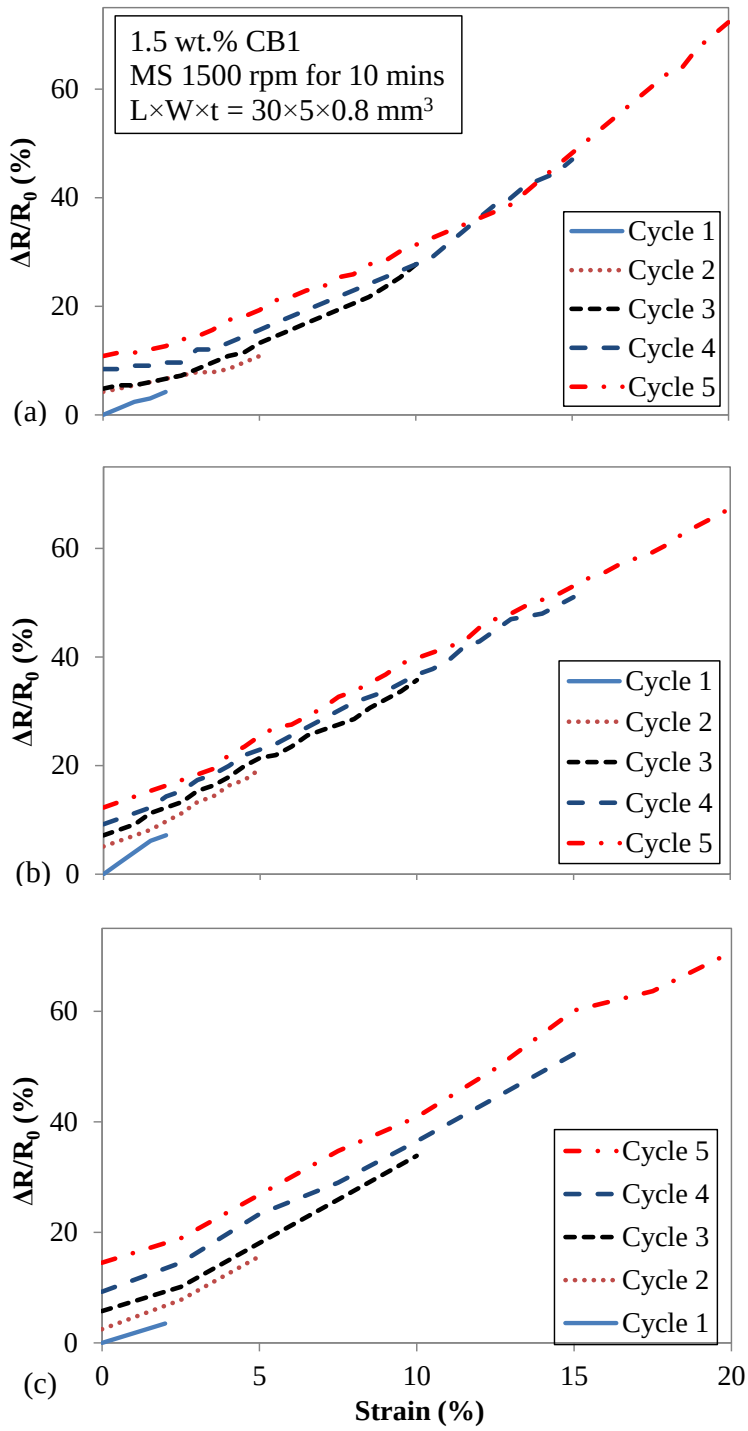

Figure 3.23. Tensoresistivity of CB1-filled coating composite subjected to loading Type I, a) $\dot{\varepsilon}$ =0.15 %/min, b) $\dot{\varepsilon}$ =2 %/min, and c) $\dot{\varepsilon}$ =10 %/min.

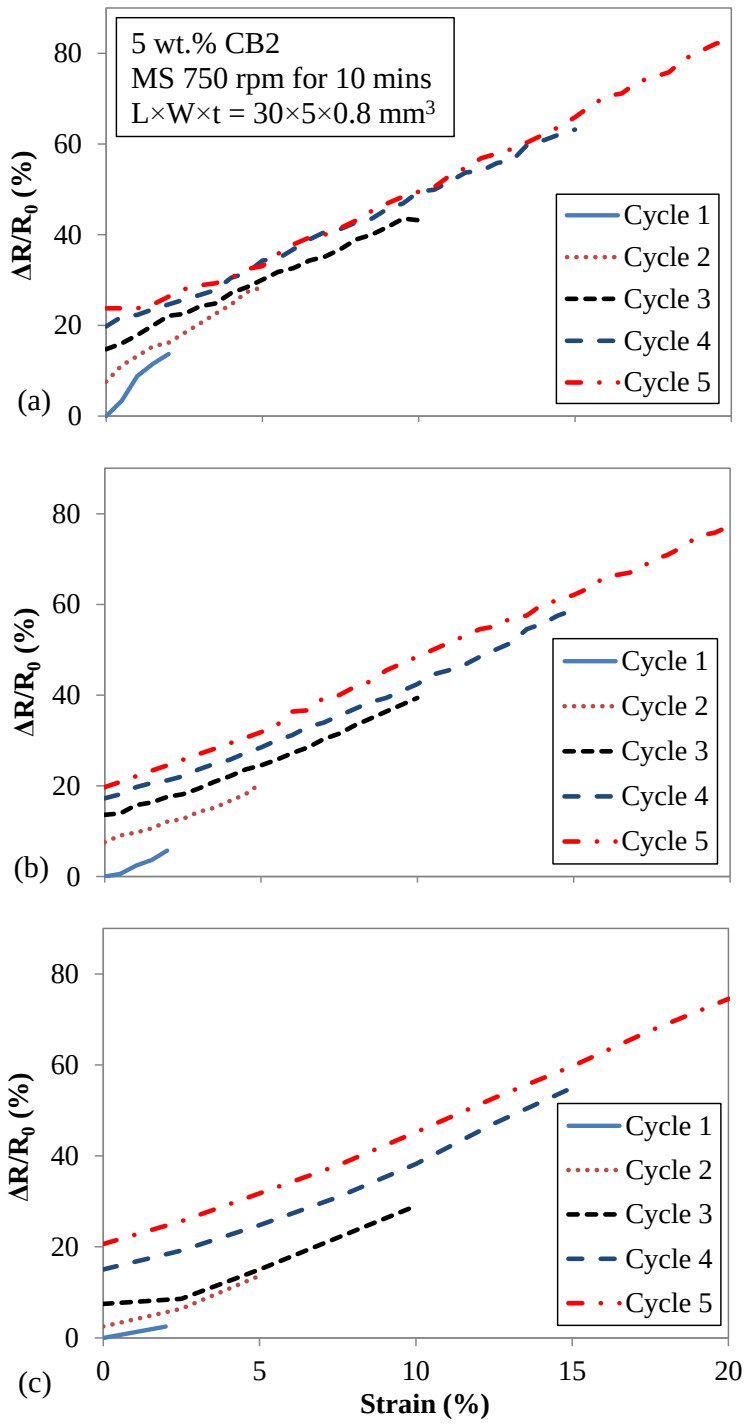

Figure 3.24. Tensoresistivity of CB2-filled coating composite subjected to loading Type I at a) $\dot{\varepsilon}$ =0.15 %/min, b) $\dot{\varepsilon}$ =2 %/min, and c) $\dot{\varepsilon}$ =10 %/min.

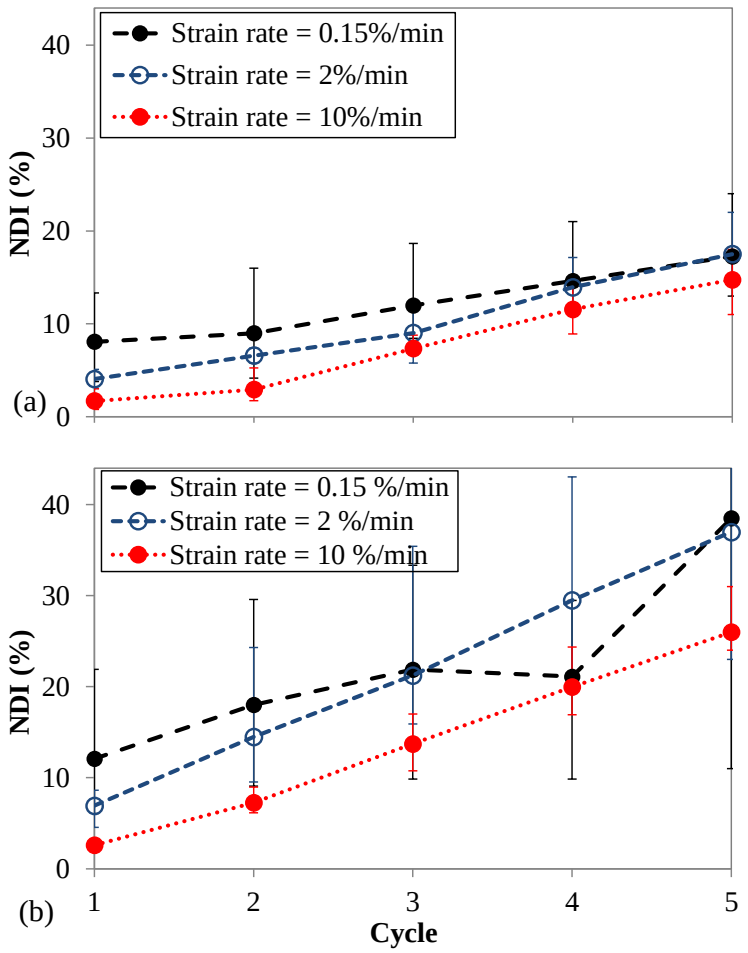

Figure 3.25. NDI vs. number of cycles for a) CB1- and b) CB2-filled coating composite subjected to loading Type I

It is also observed that the tensoresistivity of filled specimens is generally greater when they are subjected to slower-rate tensile loads. This observation suggests that loading at a slower rate is more able to disrupt CB-CB interactions versus a more affine deformation corresponding to a faster rate. Another observation is that the tensoresistivity response of the CB2-filled coating specimens is more sensitive to the strain rate than that of CB1-filled specimens. A lower-structure black is expected to be more sensitive because of the lower capability of overlapping regions which would not be as disrupted by strain as two blacks

only connected at a point. These observations are in agreement with the strain-rate dependency of the tensoresistivity of CB-filled PVC composites under monotonic loading described in Section 3.1.3.3.

A comparison of the results shown in Figure 3.25 indicates that a higher-structure CB (e.g. CB1) leads to a less-pronounced hysteretic response (i.e. milder slopes in the *NDI*-Cycle response) because a more-branched CB structure (i.e. a higher structure) is more capable of recovering lost connectivity between the conducting aggregates when the tensile load on the specimen is reduced or removed. A lower scatter is also observed in the NDI-Cycle response of CB1-filled coating specimens, which can be explained by the capability of branched fillers to establish relatively more uniformly distributed connections with the host polymer and other fillers, thus experiencing less damage under tensile loading.

3.2.3.2. Type II: Incremental cyclic loading with gradual unloading

The typical tensoresistive response of a coating specimen subjected to Type II loading is shown in Figure 3.26. A magnified segment of the low-strain response is shown in the inset which indicates a clear hysteretic tensoresistive response throughout the test where in the cycle *i* the gauge factor during loading is greater than that during unloading (i.e. $GF_{Ui} < GF_{Li}$). The slope of the specimen tensoresistivity response for any given loading cycle shows a tendency to revert to that of the first cycle at zero strain every time any subsequent elongation exceeds the previous peak strain. A normal tensoresistivity line (NTL) is introduced here as a 'back-bone' curve to help demonstrate the aforementioned tendency in the cyclic response of filled polymers observed in this study. The NTL is shown using a dashed line in Figure 3.26. The increase in the resistivity of the specimen at the end of each load cycle at zero

strain is attributed to rupturing of the conductive CB network with partial recovery of its connectivity when the tensile load is removed. A subsequent loading up to the peak strain previously experienced by the filled specimen first nullifies the recovered connections, which results in $GF_{Li+1} \approx GF_{Ui}$. However, beyond the previous peak strain a well-fabricated specimen should exhibit the same tensoresistivity slope as the NTL. The proximity of the loading portions of each load cycle beyond previous peak strain relative to the NTL could be considered as a measure of the quality of conductive particle dispersion in a filled sample.

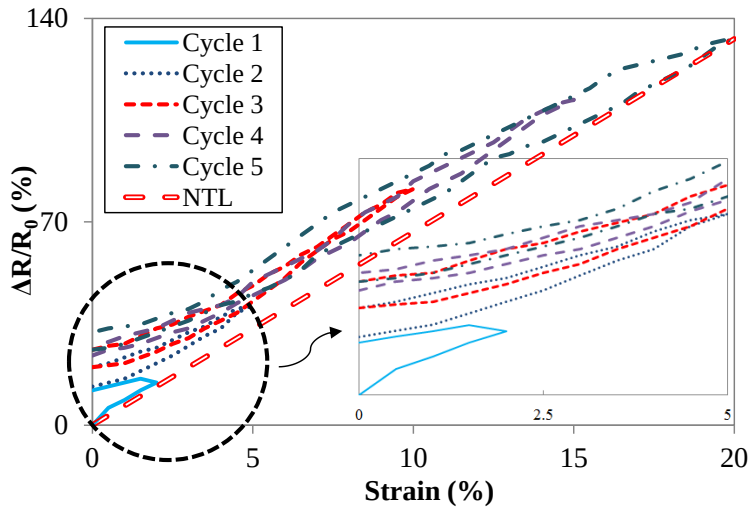

Figure 3.26. Tensoresistive response of a CB-1 filled coating composite subjected to load Type II. Note: $\dot{\varepsilon} = 2\%/\text{min}$. The encircled area is magnified in the inset.

Hysteresis loops in the tensoresistivity response of a sample with low-quality dispersion of conductive particles are expected to show a more random behavior with respect to their GF_{Li+1}/GF_{Ui}/NTL slopes. The breadth of the hysteresis loops could be considered as another measure of the quality of filler dispersion and filler-polymer compatibility. A narrower loop indicates a smaller increase in the resistivity of the filled specimen when it is

subjected to cyclic loading and therefore, indicates better dispersion quality and filler-polymer compatibility.

Similar to the observations made for specimens subjected to load Type I (Figure 3.25), NDI_i values shown in Figure 3.27 indicate that the conductive CB network in a filled sample experiences extensive damage at lower strain rates. However, the generally smaller NDI_i values in Figure 3.27b as compared to those shown in Figure 3.25b suggest that a slower unloading rate could moderate the extent of this damage. This observation can be attributed to partial reformation of the conductive network during gradual unloading. However, gradual unloading of the CB1-filled specimens does not lead to significant recovery of their conductive network within the range of strains examined. This could be explained by the fact that, at any a given level of strain, CB1-filled specimens possess a greater number of interagglomerate connections (as compared to otherwise identical CB2-filled specimens) and therefore, their measured conductivity is comparatively less influenced by any recovered connections during the unloading process.

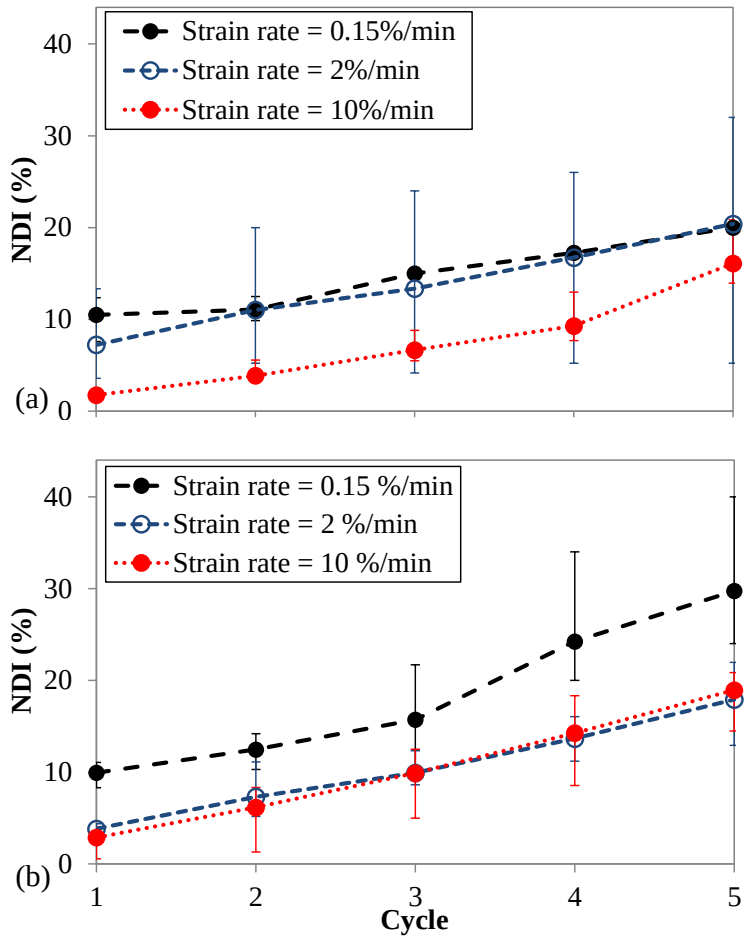

Figure 3.27. Tensoresistive response of a CB-1 filled coating composite subjected to load Type II. Note: $\dot{\varepsilon}$ =2%/min . The encircled area is magnified in the inset.

3.2.3.3. Type III: Large-strain cyclic loading

Typical tensoresistivity responses of filled coating specimens subjected to cyclic strains approaching failure strain are shown in Figure 3.28. Results shown in this figure indicate that the hysteretic behavior of filled specimens at large strains follows a bilinear path. The results also indicate that composites filled with low-structure blacks experience significant loss of conductivity after the first loading cycle (due to the comparatively few interconnections among the particles and aggregates) and do not show further change in conductivity in

subsequent cycles. In contrast, the higher-structure CB1-filled composite exhibits a more gradual decrease in conductivity as a result of a progressive depletion of available conduction paths. The gauge factors of the sensing composites during cyclic loading are summarized in Table 3-4. A sharp increase in the gauge factor occurs during reloading which is defined as ε_t in Figure 3.28. As shown in the table, the value of ε_t is specific to the CB type used and increases with CB structure. ε_t is 80% for CB1 and 50% for CB2 which are, respectively, 50% and 31% of the maximum strain attained in the first cycle (i.e. 160%). The composites filled with the lower-structure black (i.e. CB2) essentially show no tensoresistivity at the strains below ε_t. According to Figure 3.28, failure strains of CB1- and CB2-filled composites are approximately 230% and 270%, respectively, which indicate a highly ductile behavior. In comparison, the ultimate strain of CB-filled polypropylene and polyethylene composites are between 40% and 60% at comparable CB concentrations (Fathi *et al.* 2012).

The resistivity of composites filled with anisotropic particles (particles with large shape factors) at moderate strain levels (e.g. 25%–50%) is predominantly governed by the orientation of the particles (Kost *et al.* 1984). During unloading, the resistivity of these composites increases initially due to gradual randomization of the particles' orientation. However, after some degree of unloading has taken place, resistivity starts to decrease to roughly its original value due to the reformation of the conduction paths previously destroyed during loading. Since such a reduction in the electrical resistivity was not observed in the cyclic tests reported in this study (Type III), it is concluded that the CBs tested have a fairly low shape factor, and any realignments that might have occurred during the applied tensile tests did not have a measureable influence on the conductivity of the composites.

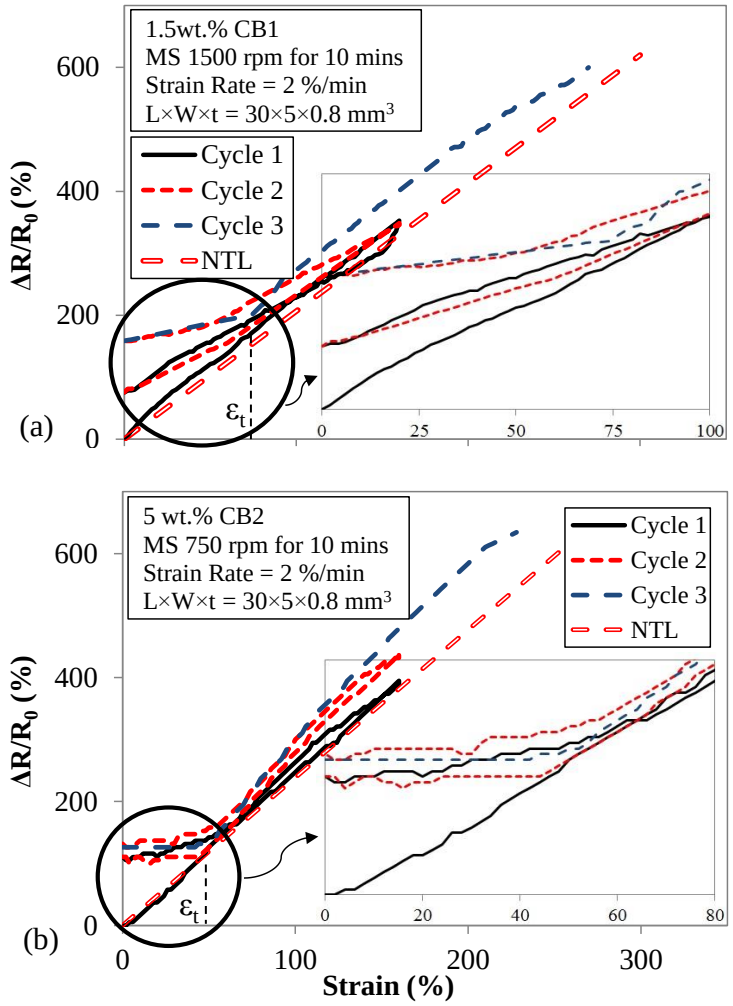

Figure 3.28. Tensoresistive of a) CB1- and b) CB2-filled coating at large strains. Note: The encircled area is magnified in the inset.

Table 3-4. Gauge factors[1] of the coating composite at large strains

CB ID	ε_t[(2)] (%)	GF_L					GF_U			
		1st cycle	2nd cycle		3rd cycle		1st cycle		2nd cycle	
			$\varepsilon < \varepsilon_t$	$\varepsilon \geq \varepsilon_t$	$\varepsilon < \varepsilon_t$	$\varepsilon \geq \varepsilon_t$	$\varepsilon < \varepsilon_t$	$\varepsilon \geq \varepsilon_t$	$\varepsilon < \varepsilon_t$	$\varepsilon \geq \varepsilon_t$
1	80	2.20	1.33	1.93	0.57	1.91	1.47	1.47	0.57	1.42
2	50	2.43	0.00	2.04	0.00	2.77	2.17	0.52	0.05	2.03

(1) Relative change in a specimen's electrical resistance per unit strain (Equation (3-3))

(2) The strain where a sharp increase in the gauge factor occurs during reloading (Figure 3.28)

3.2.3.4. Type IV: Cyclic loading

Figure 3.29 shows typical tensoresistivity results of CB1- and CB2-filled specimens subjected to load Type IV with a constant peak strain of 5% (OER = 1) and variation in their corresponding NDI_i and GF values. The test results show that the tensoresistivity responses of both specimens are in phase with the cyclic load regardless of the CB type used in the composite (Figure 3.29a and b). The peaks of the tensoresistivity response in the case of higher-structure black (i.e. CB1) slightly increase with the load cycle throughout the test (Figure 3.29c). However, a clear jump in the resistivity of the specimen after the third cycle is found due to scissions in the conductive network as a result of load reversals. The CB2-filled specimen shows a jump in its resistivity after the first load cycle. However, its cyclic tensoresistivity response approaches a steady-state performance at a constant peak amplitude (GF) for the remainder of the test after a transient period (i.e. after ~ 1500 s – Figure 3.29 d). The amplitude of the tensoresistivity cyclic response is larger as compared to the case of higher-structure black. The NDI_i and GF values in Figure 3.29 indicate that the conductive CB network in the samples filled with the lower-structure black suffer more extensive damage during cyclic loading and its conductivity response reaches a steady state at a relatively faster rate. These observations suggest that rupture in the conductive network starts from loosely connected agglomerates and spreads to stronger intra- and inter-agglomerate connections when the network is subjected to prolonged load reversals. The results shown in Figure 3.29 also indicate that the polymer/filler interface, when subjected to sufficient cycles of stress, undergoes irreversible microstructural damage leading to interfacial cracking and delamination (Carey *et al.* 2011). The rate of damage is lower in CB1-filled specimens

possibly due to the higher porosity and more open structure of CB1 which collectively promote a stronger interface with the host polymer. In contrast, plastic deformations along the interface occur to a greater extent and at a relatively faster rate in the specimens filled with a low-structure black.

3.2.3.5. Type V: Cyclic loading with prestraining

The typical influence of prestraining on the tensoresistive response of filled coating specimens is shown in Figures 3.30 and 3.31. Figure 3.32 shows the corresponding *NDI* values as a function of *OER*. Prestraining a conductive composite to strains greater than its steady-state cyclic operating strain stabilizes its conductivity performance and yields a consistent and recoverable tensoresistivity response with a practically constant gauge factor. Further, prestraining reduces the tensoresistivity response since the damage accumulated in the conductive network decreases with increasing *OER*. These observations agree with those of Kost *et al.* (1984) who studied the resistivity behavior of CB-filled silicone rubbers under cyclic loading and observed an improved recoverability in the samples mechanically preconditioned to an extent twice the operating strain. This positive influence is greater in the case of composites filled with lower-structure blacks. The relative profusion of intertwined CB chains in the composites filled with higher-structure blacks helps them possess more CB connections when undergoing mechanical preconditioning. Therefore, a greater number of subsequent cycles is required to break up more chains, especially those loosely connected.

The key findings of the cyclic load tests carried out in this study are highlighted in Table 3-5.

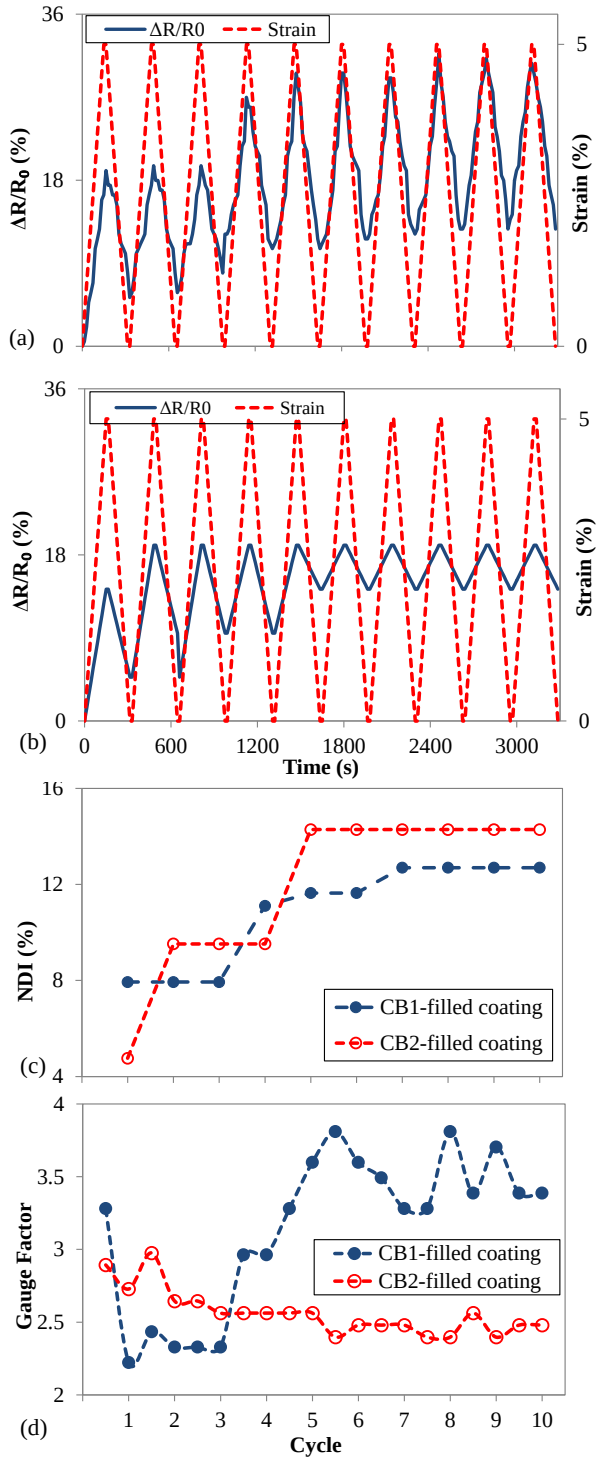

Figure 3.29. Tensoresistive responses of a) CB1- and b) CB2-filled coating specimens subjected to low-strain cyclic loading at OER = $\varepsilon_p/\varepsilon_c = 1$, variations of c) the NDI and d) *GF* with low-strain (5%) cyclic load for CB1- and CB2-filled coating specimens

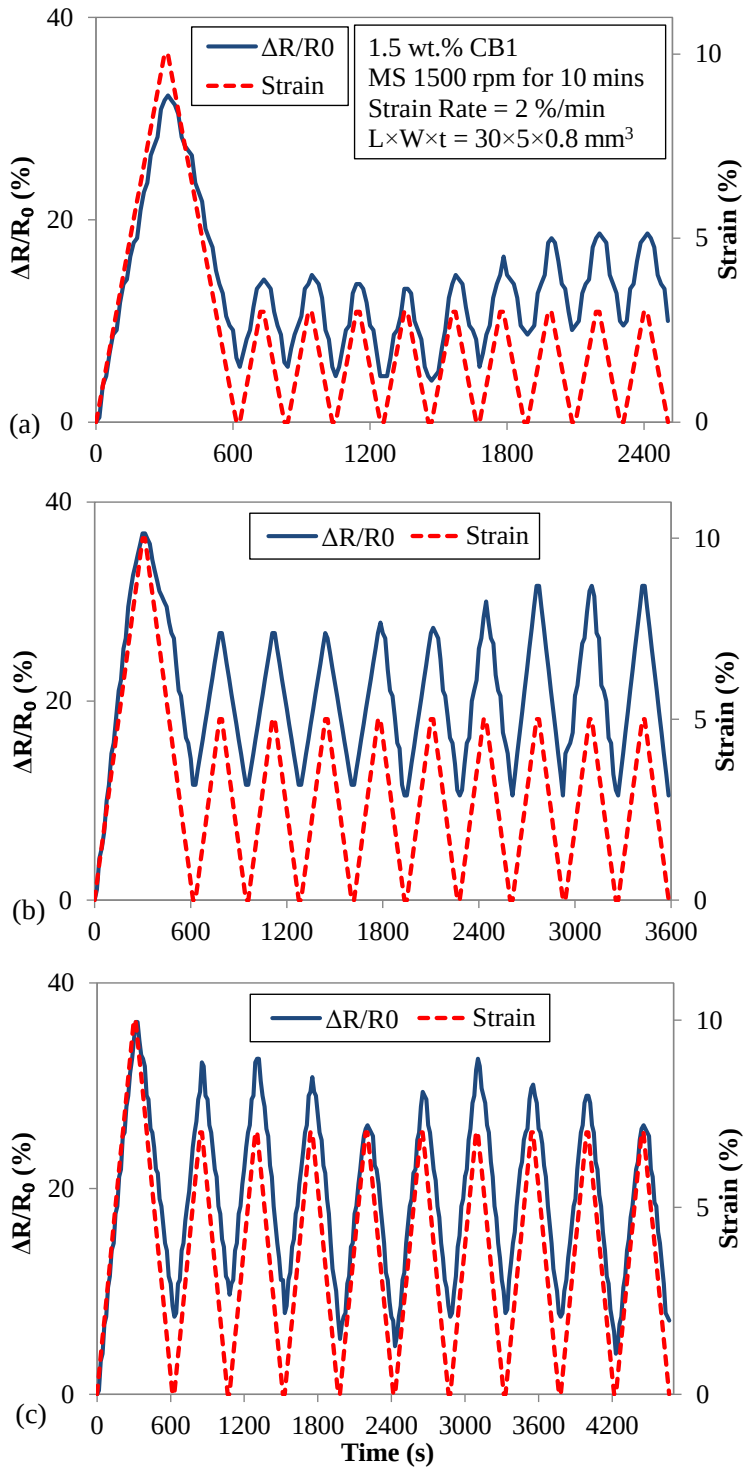

Figure 3.30. Influence of prestraining on the tensoresistivity of a CB1-filled coating specimen with a) OER = 3.3, b) OER = 2, and c) OER = 1.4

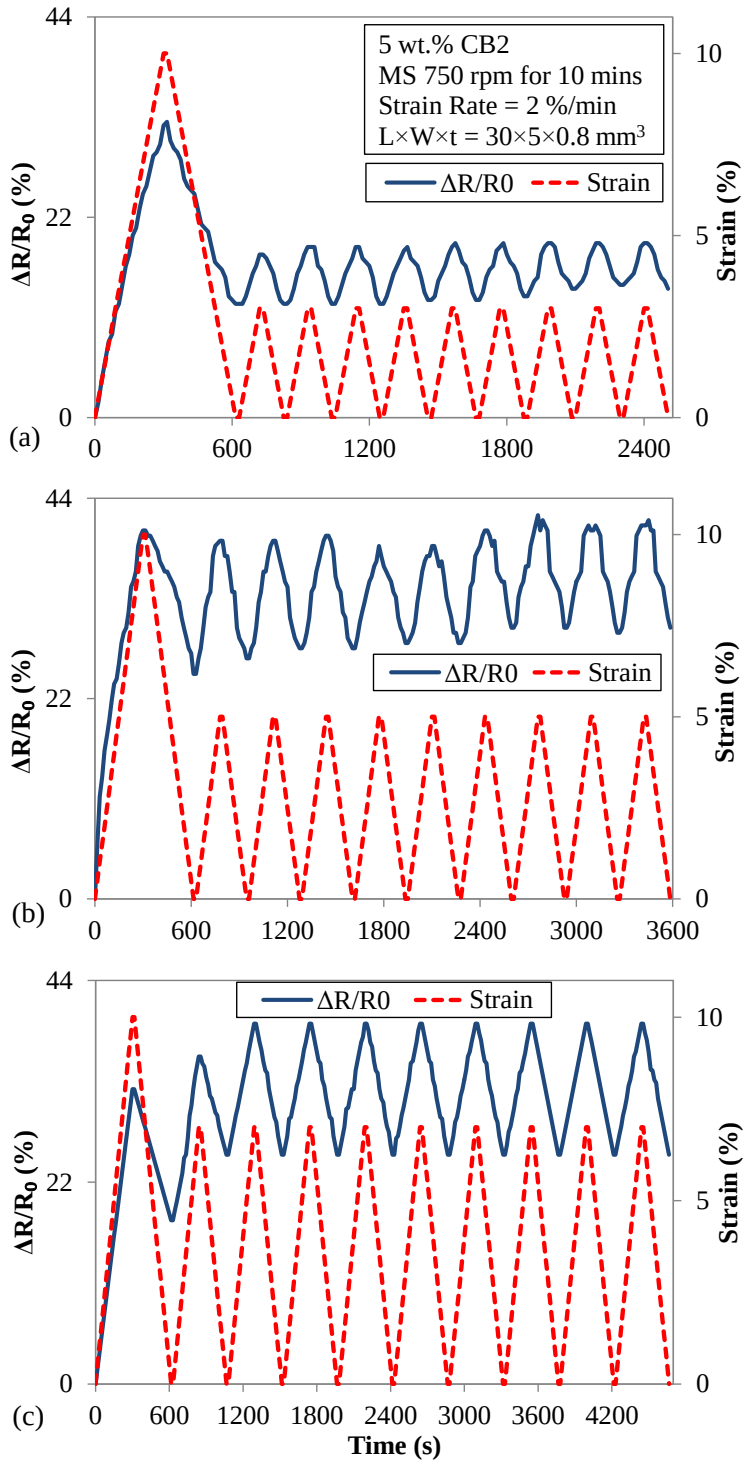

Figure 3.31. Influence of prestraining on the tensoresistivity of a CB2-filled coating specimen with a) OER = 3.3, b) OER = 2, and c) OER = 1.4

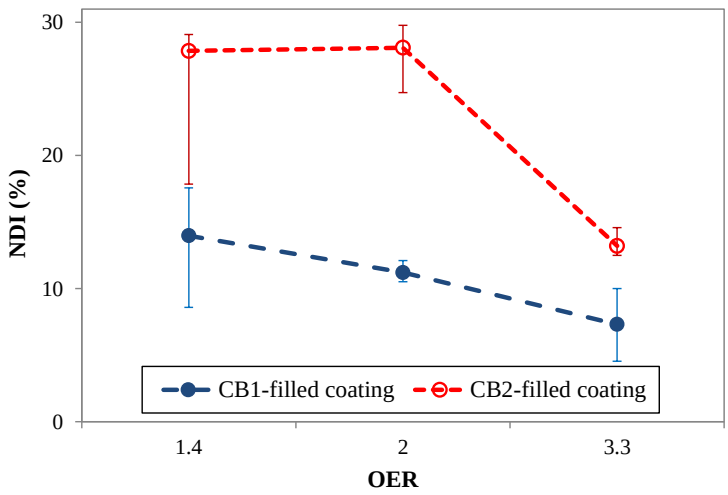

Figure 3.32. Influence prestraining on the damage experienced by the conductive network. Note: The error bars indicate the max/min NDIs observed during a full test.

Table 3-5. Key findings of the cyclic load tests

Test type and description	Main observations
I: Incremental cyclic loading with rapid unloading	Composites filled with higher-structure blacks exhibit a less-pronounced hysteresis in their strain sensitivity response. The hysteresis decreases at higher strain rates.
II: Incremental cyclic loading with gradual unloading	Slower rate of unloading moderates the damage experienced by the conductive network, possibly due to the reformation of some conduction paths during gradual unloading.
III: Large-strain cyclic loading	The depletion of available conduction paths is faster in low-structure blacks. CB-filled PVC composites exhibit significantly more ductility when compared to CB-filled PE and PP composites.
IV: Cyclic loading	Cyclic tensoresistivity response of CB-filled PVC composites approaches steady state preceded by a transient period. The lower-structure black resulted in a larger peak during the samples' steady state response.
V: Cyclic loading with prestraining	Prestraining of coating specimens improves the recoverability of their tensoresistivity response, especially for those filled with lower-structure blacks and subjected to larger prestraining.

3.2.4. Conclusions

Strain sensitivity of a geogrid-coating material made of polyvinyl chloride-carbon black (PVC/CB) composite subjected to tensile cyclic loading was examined with a medium and high-structure black. Five different cyclic loading régimes were used to investigate the influences of factors such as the strain magnitude, stress-relaxation, loading rate and prestraining on the tensoresistivity performance of the coating composite.

Each loading type described in this paper was used to understand different aspects of the filled polymers tensoresistivity performance when subjected to cyclic loading. Therefore, there was no compelling reason to use the same cyclic amplitude in all tests carried out in the study. For instance, Types I and II were designed to understand the accumulation of irreversible damage in the composite as a result of incremental cyclic loading (e.g. a retaining wall subjected to a strong earthquake, which can cause large strains). Type IV, in contrast, was designed to understand the tensoresistivity response of the composite to a constant-amplitude cyclic loading (representing the traffic load on a bridge abutment or machine foundations reinforced with geogrids), which typically experience service load-level strains less than 5–10%.

Specimens filled with the higher-structure CB experienced less damage upon cyclic deformation and showed a higher degree of recoverability, i.e. less hysteresis, in tensoresistivity. Prestraining of coating specimens had a positive influence on the recoverability of their tensoresistivity response. Increasing the ratio (maximum prestrain:cyclic strain amplitude) resulted in a more consistent recoverability tensoresistivity response with cycle number.

3.3. In-soil tensoresistivity of sensor-enabled geogrids

3.3.1. Introduction

The results shown in Sections 3.1.3 and 3.2.3 indicated that both types of CB (Table 3-1) exhibited adequate strain sensitivity for the performance monitoring of structures reinforced with geogrids. However, the electrical conductivity of the composites filled with the low-structure CB (i.e. CB2) was shown to be more sensitive to strain because of the lower capability of the filler network in the composite to hold its original extent of interconnectivity during loading. In addition, the cyclic loading results (Section 3.2.3) indicated that PVC composites filled with the low-structure black experienced a greater jump in their resistivity after the first load cycle, and their strain sensitivity response approached a steady state at a faster rate when compared to the moderate-structure black.

Sections 3.1.3 and 3.2.3 were solely focused on the in-isolation performance of the unitized SEGG and the coating of yarn-type SEGG. However, it is expected that the tensoresistivity performance of SEGG would be influenced by the confining pressure when they are installed in the soil in field projects. As a step toward developing the SEGG for practical applications, this section describes the in-soil tensoresistivity tests on PVC-coated PET yarn SEGG specimens. Details of the materials, test setup and the corresponding results are provided in the following sections.

3.3.2. Laboratory tests

3.3.2.1. Materials

The same polymer and plasticizer as those used for the tensoresistivity tests on the coating composite (see Section 3.1.2.1) were also used for the cyclic loading tests. Although CB1 showed a lower percolation threshold, the low-structure CB (i.e. CB2 used) was employed as the conductive filler in the in-soil tests due to its better performance under cyclic loading.

3.3.2.2. Molding of specimens for conductivity, strain sensitivity and mechanical tests

For the fabrication of SEGG specimens, first an aluminum mold with five identical grooves, 2.5 mm wide and 0.8 mm deep, was fabricated. A single multi-filament woven PET yarn (Figure 3.33a) was then laid in each groove and firmly secured at its two ends (Figure 3.33b). Afterwards, the coating composite was carefully brushed on the yarns to make sure that it fully covered the yarns (Figure 3.33c). Then, the mold was compressed under the same conditions as those which were used for the electrical conductivity tests to fabricate rib-shaped SEGG specimens for strain sensitivity tests (Figure 3.33*d*). All specimens were allowed to cool down gradually to ambient temperature (typically, 23 °C) while the pressure was sustained. Cured SEGG specimens are shown in Figure 3.33e and f.

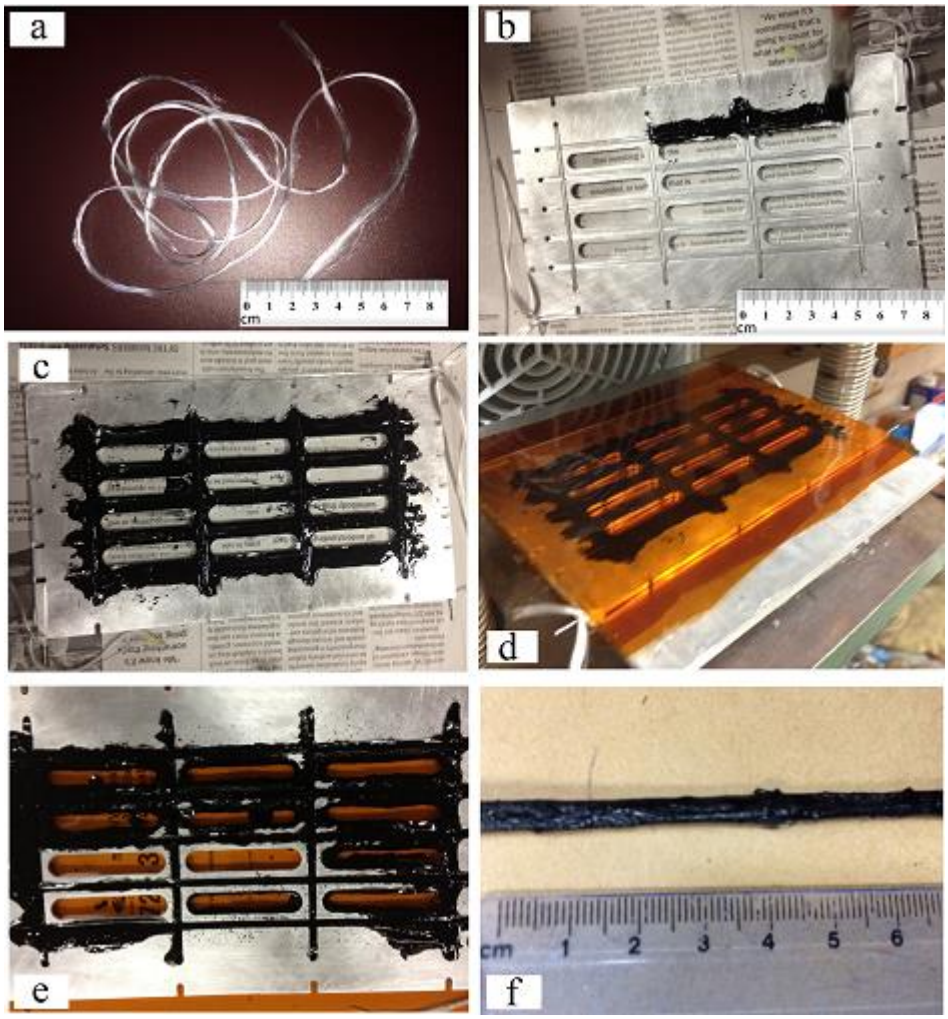

Figure 3.33. Fabrication of SEGG specimens: a) virgin PET yarns, b) brushing the coating composite on PET yarns, c) coated yarns, d) compression molding the coated yarns, e) SEGG specimens, f) a SEGG rib

3.3.2.3. Strain sensitivity tests under confining pressure

A standard direct shear test (DST) apparatus (ASTM D3080 2011) was modified to carry out strain sensitivity tests on SEGG specimens under confining pressure. These tests are referred to as "in-soil" tests in this study. An exploded view of the adjusted apparatus and its individual parts is illustrated in Figure 3.34.

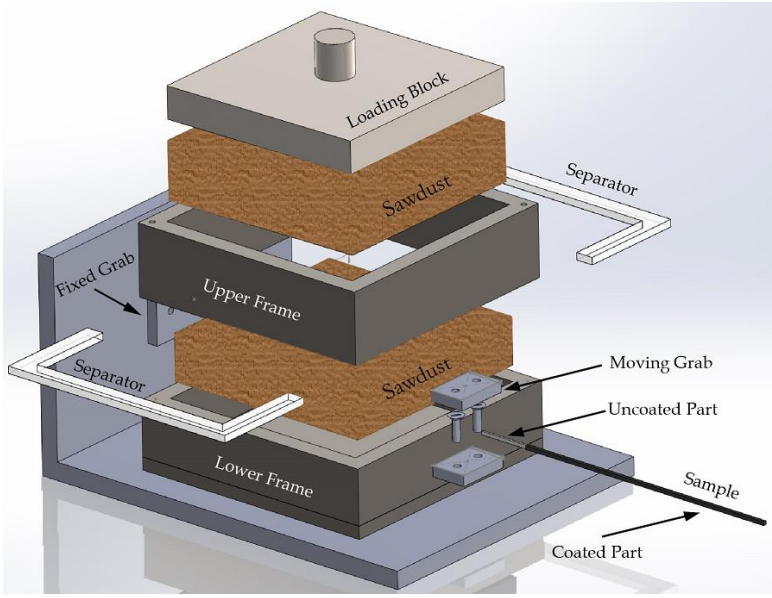

Figure 3.34. Exploded view of the DST apparatus modified for in-soil tests

Testing the strain sensitivity of SEGG specimens in the DST apparatus required overcoming some challenges. The first challenge was to prevent the slippage between the specimen and the end supports which would otherwise result in erroneous strain readings. To this end, the ends of the specimens were wrapped around two supporting clamps, one (i.e. the left clamp in Figure 3.35) firmly affixed to the DST frame and the other one (i.e. the right clamp in Figure 3.35) moving with the shear box. The two ends of the specimens were left uncoated in order to facilitate wrapping of the yarns around the clamps and secure firm connection at each end.

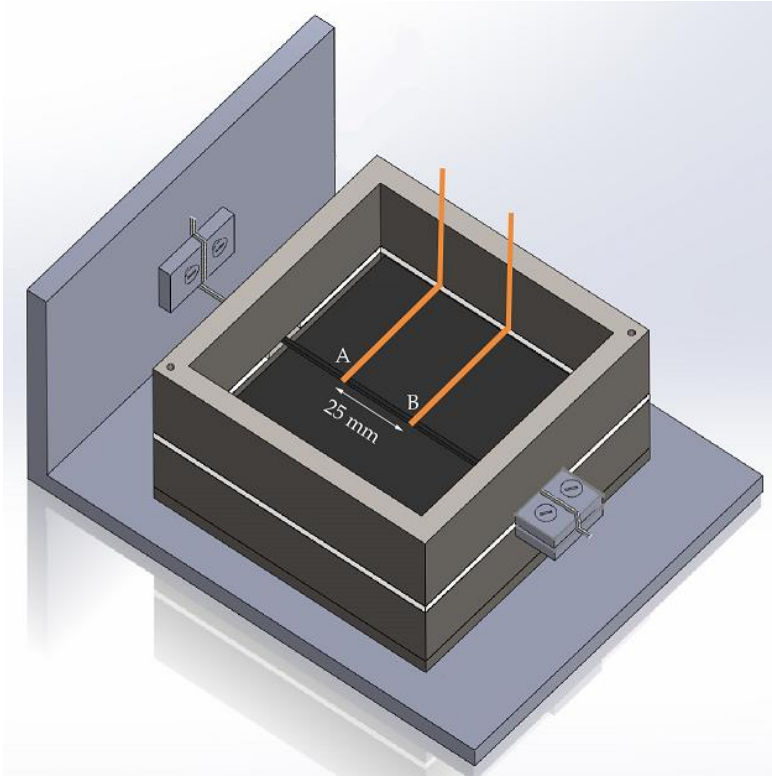

Figure 3.35. A SEGG specimen clamped in the DST test cell with electric terminals attached 25 mm apart

In order to examine the performance of the clamps, first, a specimen identical to those prepared for the in-soil tests was fabricated using the same materials and curing techniques and was tested in-isolation in a tensile testing machine. The strain within a 30-mm gauge length on the specimen was measured using a digital imagery technique. The time-history of strain from digital imagery was compared with that measured from the crosshead movements in the tensile testing machine (Figure 3.36) to ensure that the elongation rate would be fully transmitted to the specimen. The in-isolation load–strain curve of the specimen on the tensile testing machine was used as a reference to evaluate the response of an identical specimen in the modified DST apparatus. The setup in the DST machine (including the performance of the clamps used to secure the SEGG specimen outside the test cell) would be considered satisfactory if the difference between the observed responses of the in-air and in-soil

specimens was less than 5%. The results shown in Figure 3.37 indicate that the clamps that were used later in the in-soil tests would provide reliable (no-slip) grip up to approximately 8% strain. This range of strains was deemed acceptable for the objectives of this study because it was greater than the typical strain at failure in soils (i.e. 2–6% – Hatami and Bathurst (2005); Wanatowski and Chu (2006)).

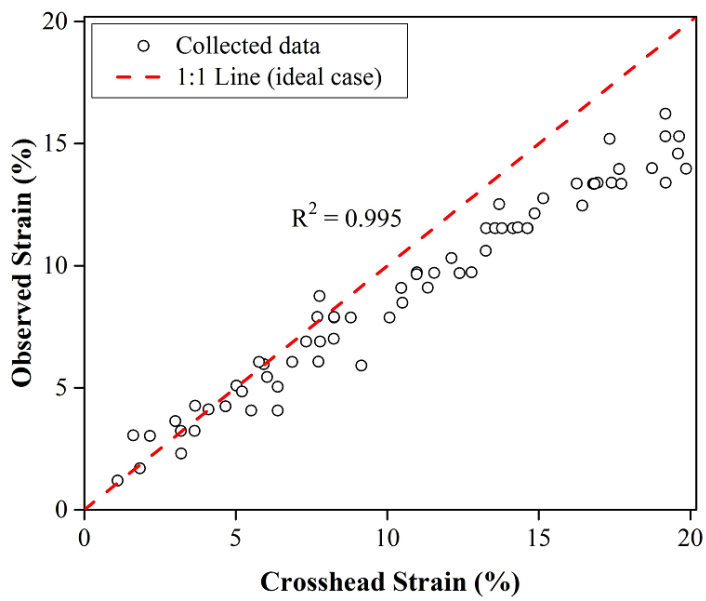

Figure 3.36. Comparison of the strains observed using the digital imagery approach with those measured from the crosshead movements in three independent experiments

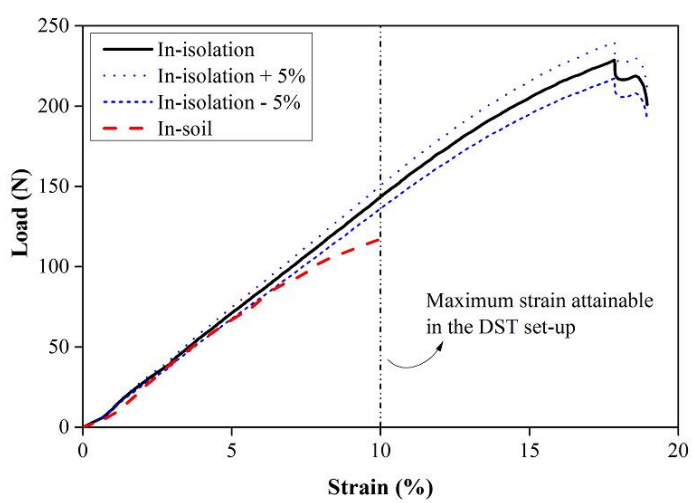

Figure 3.37. Evaluation of the clamps performance

Another challenge in testing the in-soil performance of SEG samples was to design a setup to measure the electrical conductivity of the specimens embedded in the DST apparatus. The electrodes located on the surface of the specimen (Figure 3.35) were required to be as small as possible to minimize their interaction with the surrounding soil (or soil-imitation material). To meet this requirement, electrically conductive silver paste (epoxy) was applied on two points 25 mm apart on a SEGG specimen. Before the paste set, two adequately long pieces of fine, stranded wire were wrapped around the specimen at these points and covered with additional silver epoxy. This smooth connection exhibited acceptable in-soil physical stability as well as consistency in electrical conductivity measurements.

Depending on their water content and cation-exchange capacity, soils could exhibit electrical conductivities as large as 10^{-2} S/m (Palacky 1988), which is considerably greater than the measured value of 10^{-5} S/m for the SEGG specimens. In order to eliminate the interference of actual soils with the measured conductivity of the SEGG specimens at this stage of the study, oven-dry red oak sawdust was used as a simulated soil material to apply confining pressure on the SEGG specimens (Figure 3.34). Electrical conductivity of wood is on the order 10^{-16} to 10^{-14} S/m and that of air is on the order of 10^{-14} S/m (Stamm 1964; Pawar *et al.* 2009), both of which are several orders of magnitude less conductive than SEGG specimens. Therefore, compressed oven-dry sawdust was considered to be a suitable insulating material for the confined tensile testing of SEGG specimens in this study.

The sawdust was first oven dried at 110 °C for 15 min and then passed through the #10 sieve (opening size: 2 mm). The sieved sawdust was subsequently compacted in the lower half of the DST box and a SEGG specimen was placed in the gap between the two halves of the text box. The upper half of the box was filled with more sawdust and a confining

pressure was applied on the entire test assembly. The in-soil tensile tests were repeated at three different confining pressures of 10, 30 and 50 kPa to represent upper levels of reinforced soil structures where larger deformations typically occur (Hatami and Bathurst 2005).

For each confining pressure, three specimens were tested at a strain rate of 2 %/min. It should be noted that the sawdust was merely used to facilitate the in-soil testing of SEGG specimens. The authors envision that the SEGG products in actual field applications will be protected with an additional insulating coating to protect them from the detrimental effects of installation damage and the surrounding environment (i.e. bioactive and other aggressive materials such as aqueous solutions of salts, acids and alkalis, as well as any electrical interference from wet soils).

3.3.3. Results and discussion

The in-isolation strain-sensitive conductivity of the SEGG specimens is shown in Figure 3.38. It is observed that specimens tested in-isolation generally exhibit greater strain sensitivities when subjected to slower-rate tensile loads. This observation is in agreement with the results in Section 3.1.3.3 for the strain sensitivity response of coating specimens and suggests that a greater stress relaxation at a slower loading rate is more effective in disrupting CB-CB interactions versus a more affine deformation corresponding to a faster rate. Consequently, the SEGG specimens exhibit greater strain sensitivity in their conductivity (resulting in greater gauge factors) under slower loadings. However, according to Figure 3.38, irrespective of the loading rate applied, the gauge factors of the SEGG specimens are significantly greater than that of typical commercial strain gauges (e.g. $GF = 2$).

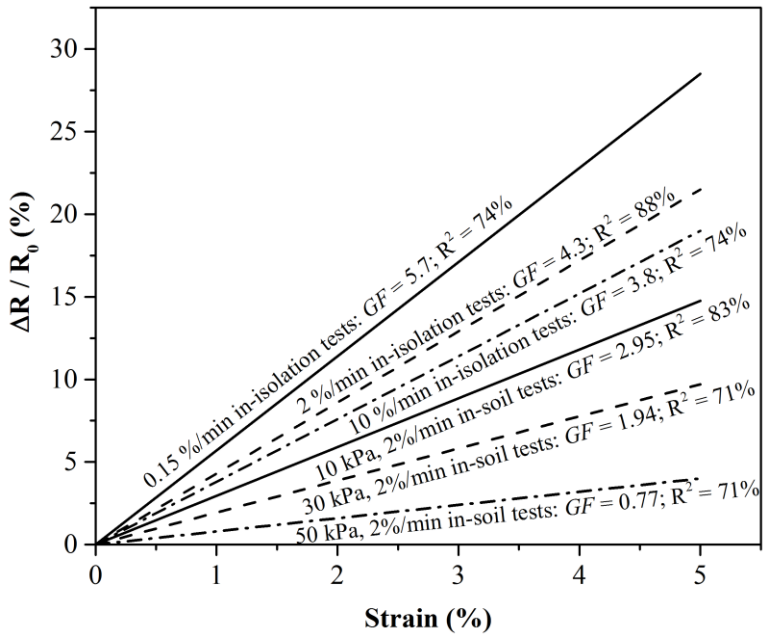

Figure 3.38. In-isolation (strain rates = 0.15, 2 and 10 %/min) and confined (confining pressures = 10, 30 and 50 kPa) normalized resistance of SEGG specimens as a function of strain. Note: The data shown correspond to three independent experiments.

The in-soil strain sensitivity performance of the SEGG specimens is also shown in Figure 3.38. It is observed that the confining pressure tends to reduce the sensitivity of the specimens to deformation. This observation can be explained by the fact that the confining pressure on a SEGG layer reduces the thickness of the coating composite of a SEGG layer which in turn brings the filler particles and aggregates closer to one another in the conductive network of the coating composite. As a result, the composite behaves as if it were filled at a concentration greater than the critical concentration and, therefore, shows less strain sensitivity (Kang *et al.* 2006). In addition, the nominal strain plotted in Figure 10 is calculated based on the displacement of the test cell as measured externally by the test apparatus. It is anticipated that the local strain within the gauge length between the two lead wires in the middle of the specimen inside the test cell would be somewhat smaller, which could also

contribute to the apparent reduction in the strain-sensitivity of specimen conductivity when tested under confining pressure.

The coefficients of determination (i.e. R^2 values) shown in Figure 3.38, while not ideal, are still considered as acceptable given the random nature of the dispersed conductive fillers with respect to their spatial distribution within the host polymer and the imperfect microscale contact between the specimens and the lead wires. In practical applications, the accuracy of measured strains can be improved significantly by increasing the number of probing locations on the SEGG ribs in the field.

The influence of strain rate on the tensile strength of the SEGG specimens is shown in Figure 3.39. As expected from the general viscoelastic behavior, the ultimate strength of the SEGG specimens increases while its ultimate strain decreases with strain rate. This strain-rate dependency of the mechanical behavior of polymeric materials is prevalent and could be correlated to the decrease in the molecular mobility of the polymer at higher strain rates which in turn results in a stiffer but more brittle behavior for the composites (Richeton *et al.* 2006; Sarva and Boyce 2007).

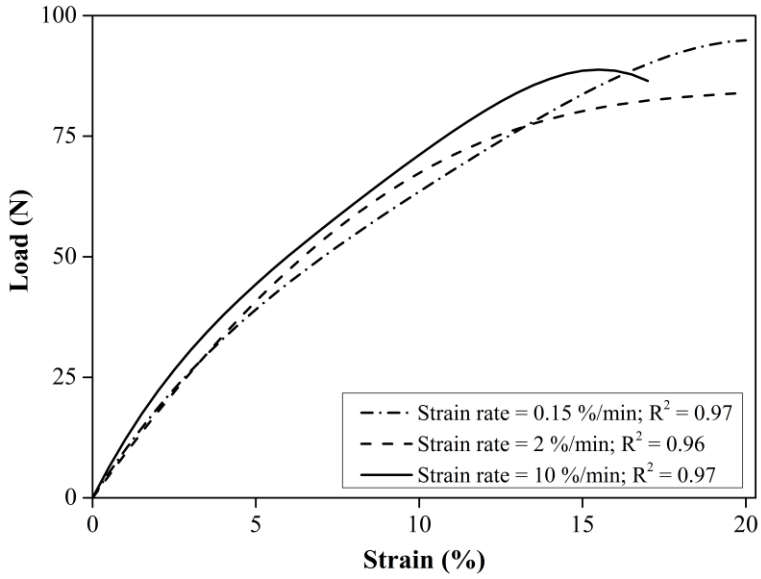

Figure 3.39. Tensile response of SEGG specimens at different strain rates. Note: The data shown correspond to three independent experiments.

3.3.4. Conclusions

A formulation was developed for a strain-sensitive conductive coating of SEGG specimens for health-monitoring applications of geotechnical structures involving geogrids. The coating was a CB-filled PVC composite with an optimum CB concentration that was determined from a series of conductivity tests. The strain sensitivity performance of the SEGG specimens was studied in isolation and when subjected to confining pressure. The specimens exhibited fairly reliable and reproducible strain sensitivity response. The gauge factors for the specimens tested in isolation were greater than those for otherwise identical specimens that were tested at the same loading rate but subjected to confining pressure in a modified DST apparatus. This reduction in the gauge factor was attributed to the effect of confining pressure in reducing the distances between the CB particles and aggregates in the conductive network of the coating composite. The influence of strain rate on the strain sensitivity of conductivity and tensile strength of the specimens was also studied. Specimens that were

subjected to slower-rate tensile loads exhibited greater strain sensitivities (represented by larger gauge factors) and lower tensile strength and failure strain.

Results of this study provided proof-of-concept for the use of SEGG technology to monitor the performance of earthen structures during and after construction. The scatter in the strain sensitivity response of the in-isolation specimens was found to be fairly acceptable. However, the specimens tested under confining pressure showed larger scatter in their measured electrical conductivity. The scatter in the measured results for the in-isolation specimens was partially attributed to the random nature of the dispersed conductive phase in the host polymer. However, the larger scatter observed for the confined specimens was primarily attributed to the quality of connections between the SEGG specimens and the electrodes that were embedded in the confining material. Possible techniques to reduce the scatter in the conductivity data (e.g. grinding and polishing the surface of the specimens, built-in electrodes, etc.) are currently under investigation.

Finally, upon further development and addressing practical issues such as durability and protective measures for field installation, the SEGG technology holds promise to offer a practical and cost-effective alternative to the existing technologies for performance-monitoring of a wide range of geotechnical structures.

CHAPTER 4. LABORATORY TESTS ON CARBON NANOTUBE-FILLED PVC COMPOSITES

The application of carbon blacks (CBs) in the development of sensor-enabled geogrids (SEGG) products was studied in CHAPTER 3. This chapter reports the laboratory studies that were carried out in order to develop and examine the performance of a tensoresistive coating composite for SEGG filled with carbon nanotubes (CNTs). This chapter is a collection of a book chapter (Yazdani *et al.* 2015a) and three journal papers of which one has recently been published (Smith *et al.* 2015) and the other two are currently under review (Yazdani *et al.* 2015c, b).

4.1. Introduction

It was previously discussed that dispersing fillers such as CBs, metal nanopowders and CNTs into a polymer matrix results in a nanocomposite with desirable properties (e.g. conductivity, flexibility, durability and affordability) for a wide range of industrial applications beyond what would otherwise be possible using its constituents alone. Compared to CBs and metal nanopowders, CNTs provide more desirable mechanical and electrical properties (Hilding *et al.* 2003) together with characteristics such as high flexibility (Cooper *et al.* 2001), low mass density (Gao *et al.* 1998) and large aspect ratio (length-to-diameter ratio). However, CNTs possess an inherent thermodynamic drive to create physical entanglement with neighboring

tubules, which form aggregated morphologies, called bundles. Each bundle contains hundreds of tightly-packed CNTs, which are bound to each other by van der Waals attraction energies of approximately 500 eV/μm per CNT-CNT contact (Thess *et al.* 1996; Girifalco *et al.* 2000). This entanglement tendency is especially strong due to the generally high aspect ratio and flexibility of CNTs (Lourie *et al.* 1998).

The extent of the improvement offered by dispersed fillers depends not only on the concentration of the filler but also on the quality of its dispersion. Improving the quality of CNT dispersion, which generally refers to the nearly-uniform distribution of individual fillers in a matrix in a composite, reduces the experimental percolation threshold that could otherwise compromise the weight, strength and manufacturability of the composite (Ajayan *et al.* 2000). The adverse effects observed in their strength, particularly, are due to the presence of CNT agglomerates within a composite that generally serve as zones of stress concentration (Hilding *et al.* 2003; Liu and Wagner 2005). Although perfect dispersion favors the strength of composites (see Section 4.2.2.3 for further details), it is not advantageous from the electrical conductivity standpoint. A higher percolation threshold filler can have significantly better dispersion than a lower percolation threshold filler as bundling can reduce the percolation threshold (Grady 2010). Therefore, the identification of the most efficient dispersion approach becomes a pivotal, albeit challenging step in the design of CNT-polymer composites.

The statement above implies that the mutual relationship between the dispersion quality of CNTs on the one hand and their influence on the properties of the host composite on the other can be exploited to indirectly assess the dispersion quality by means of changes in measurable properties. However, this sort of assessment will be qualitative to a large extent,

and a dispersion state described as "uniform" or "good" for CNT individuals in the bundle scale might be a misleading or inaccurate description for their dispersion state in micro- or macroscale systems, where CNTs are typically found in the form of bundles and agglomerates. Therefore, nanoscopic and microscopic visualization techniques will be required as an essential means toward a deeper and more direct insight into the nature of aggregate dispersion in filled composites. Since no visualization technique is capable of handling dispersion evaluation across a range of length scales, distinction should be made between nanoscopic dispersion, which refers to the disentanglement of CNT bundles/agglomerates, and micro- and macroscopic dispersion, which refers to the distribution of individual CNTs and more likely their bundles or agglomerates throughout the composites (Li *et al.* 2007b).

The proper dispersion of CNTs in a blend requires an optimum input of shear force/energy to overcome the van der Waals forces within and between bundles. By optimum, we refer to the shear force/energy that is primarily used to disentangle bundles, and any effort exceeding that will be (partly) spent on breaking up the CNT particles and aggregates, thus reducing their aspect ratio. It should be noted that a truly-random distribution and orientation of CNTs cannot be generally expected since the van der Waals interactions between aligned CNTs are stronger, promoting their mutual alignment and giving rise to a lower energy for the CNT network. Consequently, the orientation of CNTs is rather skewed in the direction of aligned CNTs (Grujicic *et al.* 2004).

Although CNTs have been actively investigated in recent years as electrically-conductive fillers in polymer composites (e.g. see Bauhofer and Kovacs (2009)), conductivity of CNT-filled PVC composites has been the subject of fairly limited studies. Broza *et al.* (2007) used

a combination of mechanical stirring and ultrasonication to disperse SWCNTs and MWCNTs into a solution comprising of 98.30 phr (parts per hundred rubber) of tetrahydrofuran (THF), 1.65 phr of PVC and 0.05 phr of a stabilizer. Compression-molding was used to fabricate the specimens. Results showed that both CNT types could be used to make PVC composites conductive. However, in comparable samples, the composites filled with SWCNTs exhibited conductivity at a significantly lower concentration compared with those filled with MWCNTs (0.1 wt.% vs. 5.0 wt.%). Although the composites showed significant conductivity, large quantities of solvent (i.e. tetrahydrofuran) were needed for their fabrication, which compromised their mechanical strength.

Mamunya *et al.* (2008) and Mamunya *et al.* (2010) reported that they successfully used the so-called segregation (or sintering) method to reduce the percolation threshold of MWCNT-filled PVC composites. Segregation is to form a solid material by applying heat and/or pressure without melting it and it is particularly effective in the composites where polymer particles are greatly larger than filler particles (Yacubowicz *et al.* 1990; Mierczynska *et al.* 2007). In a segregated system, fillers are locally concentrated on the boundaries between polymer grains and create an ordered structure in the polymer matrix as opposed to their random distribution in conventional filled composites. As a result, composites made using the segregation method exhibit significantly lower percolation thresholds. Although the segregation method offers advantageous improvements in the conductivity response of a filled composite, its application for industrial processes (especially in the geosynthetics industry) is hindered by its incompatibility with the techniques currently used in the industry for large-scale production of geosynthetics. In addition, mechanical properties are typically

worse than in the case where the composite is not sintered because the grain boundaries along the sintering lines typically act as mechanical defects.

The survey above indicates that there is currently limited information on the processing, electrical conductivity, mechanical properties and tensoresistivity of CNT-filled PVC composites. This section aims to address these knowledge gaps.

4.2. Experimental program

4.2.1. Materials

The same PVC plastisol and auxiliary plasticizer as those described in Section 3.1.2.1 were used as the polymer matrix. A type of MWCNT, which had been used in recent studies (e.g. Castillo *et al.* (2011); Guo *et al.* (2014)), was used as the filler with properties as given in Table 4-1. The density of the CNT was assumed to be the same as that for pure graphite (i.e. ρ_f = 2.045 g/cm^3 – Mamunya *et al.* (2008)).

4.2.1.1. Specimen fabrication

The MWCNTs were first dispersed into the plasticizer using a mixing method, as described later, to form a pigment. The resulting pigment was subsequently mixed with the plastisol to obtain the final composite. A series of viscosity tests, following ASTM D5225 (2014), was carried out on mixtures with different mixing ratios of the composite's ingredients (i.e. PL, PR and MWCNT) in order to obtain a PR/MWCNT ratio that would result in a processable pigment blend with a viscosity in the range of 3 – 10 Pa•s. This range of viscosity values was targeted as it is typically used for the coating of woven geogrids (MarChem 2011). A

Brookfield viscometer with a #5 spindle at a rotational speed of 5 rpm was used for the viscosity tests. Room temperature in the laboratory was kept fairly constant during the tests ($T = 23 \pm 1°C$) to minimize its impact on the viscosity of the composite. MWCNT concentration was kept constant at 0.5 wt.% in all tests while different PR/MWCNT ratios were tested. Ultimately, a PR/MWCNT ratio of 24 was found that resulted in a composite with the target viscosity.

Table 4-1. Properties of the MWCNT used in this study (as measured, or provided by the supplier)

Outer diameter (nm)	**Length (μm)**	**Aspect ratio**	**Carbon purity (%)**	**D/G ratio from Raman[1]**	**BET surface area (m^2/g)**	**Density, ρ_f (g/cm^3)**
7.8	0.74	95	> 98	1.52	250	2.045

[1] The ratio of the G-band (graphitic carbon) to the D-band (disordered carbon) in Raman spectroscopy used as a measure for the purity and defects of CNTs. It is inversely proportional to the quality of CNTs.

4.2.1.2. Mixing techniques

As previously stated, proper dispersion of filler particles in a host polymer is crucial in order to produce conducting polymer composites that exhibit a desired level of accuracy and consistency in their electrical and mechanical performance. In general, two different approaches have been used to disperse CNTs in polymer matrices: chemical methods (covalent treatment) and physical methods (non-covalent treatment). Chemical methods utilize surfactants (third component) or surface functionalization to improve the wetting or adhesion characteristics of CNTs, reducing their tendency to agglomerate (Barrau *et al.* 2003; Islam *et al.* 2003; Bryning *et al.* 2005). Physical dispersion methods, in contrast, use mechanical energy to separate agglomerates and bundles of CNT (Castillo *et al.* 2011). Both physical and chemical methods can alter the aspect ratio and statistical distribution of the nanotubes and hence, change the properties of the composites in which they are embedded (Hilding *et al.* 2003).

In this study, four physical mixing methods were examined in order to identify the most suitable technique and related factors that would result in consistent and high-quality pigments. The pigments were then manually blended with plastisol for 5 minutes to make a visually-homogenous composite. Further details of the mixing methods investigated are given in the following sections.

4.2.1.2.1. Bath sonication

As described in Section 3.1.2.2.1, bath sonication (BS) method utilizes the ultrasonic energy to disperse particles in a blend. In this study, first 2.4 g of MWCNT was manually mixed

with 57.6 g of the auxiliary plasticizer (PR/MWCNT = 24) in a beaker to make 60 g visually-uniform pigment blend. Then, the beaker was placed in an ultrasonication bath. Water in the ultrasonication bath was kept at least at the same level as the pigment in the beaker so as to promote a uniform energy distribution within the blend. The sonicator power was set at 70 W for three different durations of 60, 120 and 240 minutes in order to determine a practically-optimum combination of sonication power and duration that would result in pigment blends with an adequate quality of dispersion.

4.2.1.2.2. Probe sonication (PS)

The operational mechanism of probe sonicators in dispersing solid particles in a host matrix was thoroughly described in Section 3.1.2.2.2. In this study, 60 grams of the manually-mixed pigment blend was poured into a 100-ml beaker. Then, the pigment was sonicated at 55 W of power for three different net durations of 30, 60 and 90 minutes at the 50% pulse mode (i.e. total durations of 60, 120 and 180 minutes) to produce the final pigment blend.

4.2.1.2.3. Batch mixing

Batch mixing (BM), especially high shear batch mixing, is commonly used in the process industries for solid-liquid dispersion, dissolving and grinding as well as liquid-liquid homogenization, dispersion and emulsification. In this study, a batch mixer (Reliance Electric Company, Model RS-1A) comprising of a bowl-shaped, closed chamber with a maximum volume of 300 ml and two up-mounted, corkscrew-patterned, eccentric fins was used to disperse the MWCNT into the plasticizer. In a batch mixer, the disentanglement of CNT bundles and fragmentation of CNT individuals concurrently take place due to the flow with

high velocity gradients and turbulence formed in the small gap (here ~10 mm) between the surrounding, stationary chamber and the rotary fins. The controllable heat applied through the oil circulating through the body of the chamber decreases the viscosity of the blend. In this study, 60 grams of manually-mixed pigment blend was poured into the chamber. Then, the mixer was run at a rotational speed of 150 rpm and two different temperatures of 65 and 100 °C for two different durations of 10 and 20 minutes.

4.2.1.2.4. Mechanical stirring (MS)

A mechanical stirrer was used to mix 60 grams of the pigment blend at room temperature. The mechanical stirrer had a propeller with three pitched blades inclined at 26.5° from horizontal and a 2-inch diameter swept area. Three different rotational speeds of 750, 1,500 and 3,000 rpm were used for three minutes. The stirring duration of three minutes was selected because it had been observed that CNT particles agglomerate in the blends that were mixed for more than three minutes, regardless of the rotational speed used.

4.2.1.3. Formulation of the composites

Different concentrations of the coating blend ingredients (i.e. PL, PR and MWCNT) were examined in order to determine their influences on the physical, mechanical and electrical properties of the coating and finalize its formulation. Before each test, it was ensured that the specimens had smooth and uniform surfaces without visible signs of micro-bubbles in order to avoid discontinuity in their conductive network. With respect to the physical attributes of the blends, their viscosity (described in the 'Specimen fabrication' section) was measured to examine their processability and workability for industrial production. Tensile

tests were carried out in order to examine the influence of dispersion quality on the elasticity, ductility and tensile strength of the coating composite. Additionally, tensile tests were carried out to ensure that the mechanical properties of the coating composite would be adequate to prevent premature cracking and discontinuity in the coating when the final product (i.e. PVC-coated polyester yarn geogrids) is handled or installed in practice. With respect to the electrical properties of the coating composite, conductivity tests were carried out on specimens that were filled at different MWCNT concentrations in order to determine the percolation behavior of the composite and its dependency on the processing method used.

4.2.1.4. Molding of samples

Once the mixing of the coating was complete, the blended material was compression-molded using 1 MPa pressure at 180 °C for 15 minutes to fabricate approximately 0.8-mm-thick specimens for the conductivity and tensile tests. The pressure was sustained while the specimens were allowed to cool down gradually to the ambient temperature (typically, 23 °C) at a typical rate of 2.5 °C/min. The 0.8 mm thickness was chosen as a representative value for the coating thickness in PVC-coated polyester yarn geogrids. Additional curing durations were also used for selected specimens to examine their influence on the electrical conductivity of MWCNT-filled PVC composites.

4.2.2. Assessment of filler dispersion

As mentioned earlier, dispersion quality has been shown to have contradictory effects on the mechanical and electrical properties of CNT-filled composites. Therefore, such properties as indirect indicators together with more direct nanoscopic and microscopic visualization

techniques could offer a more complete insight into the quality of filler dispersion in polymer composites. The following sections provide further details on the conductivity measurements, mechanical tests and visualization techniques used in this study.

4.2.2.1. Conductivity measurements of the composites

Three nominally-identical specimens were tested for each formulation listed in Table 4-2 to improve the reliability of the conductivity test results. The same procedures as those given in Sections 3.1.2.5 and 3.1.2.8 were followed for conductivity measurements.

Table 4-2. Information related to the specimens prepared and tested in this study. Note: three specimens were used for all electrical conductivity tests listed in the table. Only a subset of cases were also subjected to mechanical testing as indicated.

Mix ID	Mixing method	Values for the related factors in the mixing methods				CNT concentration (wt.%)	Curing Time[3] (min)	No. of specimens for mechanical properties
		Power (W)	Rotational speed (rpm)	Temperature (°C)	Total duration (min)			
Manual	Manual	–	–	–	5	0[1]	15	3
PS/55/60	PS	55	–	–	60[2]	0.5	15	–
PS/55/120	PS	55	–	–	120[2]	0.5	15	4
PS/55/180	PS	55	–	–	180[2]	0.5	15	–
–	PS	55	–	–	120[2]	0.5	5, 10, 20, 25	–
–	PS	55	–	–	120[2]	0.1, 0.2, 0.3, 0.4, 0.7, 1.0, 1.5	15	–
BS/70/60	BS	70	–	–	60	0.5	15	–
BS/70/120	BS	70	–	–	120	0.5	15	–
BS/70/240	BS	70	–	–	240	0.5	15	–
BM/150/65/20	BM	–	150	65	20	0.5	15	4
BM/150/100/10	BM	–	150	100	10	0.5	15	–
BM/150/100/20	BM	–	150	100	20	0.5	15	4
MS/750/3	MS	–	750	–	3	0.5	15	–
MS/1500/3	MS	–	1,500	–	3	0.5	15	–
MS/3000/3	MS	–	3,000	–	3	0.5	15	–

[1] 75% PL + 25% PR

[2] Duration corresponding to the 50% pulse mode (i.e. net duration is half the value shown)

[3] Compression-molded under 1 MPa pressure at 180 °C.

4.2.2.2. Microscopic characterization

Different imaging techniques such as atomic force microscopy (AFM), scanning probe microscopy (SPM), scanning electron microscopy (SEM), transmission electron microscopy (TEM) and bright-field microscopy (BF) have been used to visualize inclusions from micrometer-sized agglomerates to nanoscale, suspended CNTs (Islam et al. 2003). However, these techniques have different advantages and drawbacks as described below.

The AFM, SPM and SEM techniques are primarily suitable for observations near the surface of a composite sample or a cross-section that contains the CNT network (Li and Bauhofer 2014). Many studies have involved the use of a particular SEM mode known as charge-contrast imaging in order to examine the morphology of the filler network in conductive nanocomposites (Campbell *et al.* 1983; Croitoru *et al.* 2005; Loos *et al.* 2005; Kovacs *et al.* 2007; Lillehei *et al.* 2009; Zhao *et al.* 2015). Compared to the conventional SEM, the charge-contrast imaging mode enables a deeper penetration of highly-energetic electrons into the sample, yielding more information about the structure of its 3D filler network. However, this subsurface information is localized (e.g. on the scale of a few nanotubes at a time) and limited to shallow depths (a few hundred nm), and therefore, cannot reliably represent the quality of CNT dispersion in the entire sample. Also, the compositional similarity between polymers (carbon as the constituent element) and CNTs (carbon as the only element) reduces the contrast between the CNT and the polymer matrix, particularly at relatively high CNT concentrations (Li *et al.* 2011; Li and Bauhofer 2014). Furthermore, insulating materials (e.g. PVC in the study described here) when subjected to sufficiently high-voltage electrons accumulate electrical charge. As a result, it would be difficult to produce a threshold contrast

at high voltages and therefore, the conductive filler cannot be readily distinguished from the imagery background noise and the insulating matrix.

Other techniques such as TEM and BF lack positional information (e.g. interferometry and percolation), or require destructive sectioning of the material (Loos *et al.* 2005). To circumvent these shortcomings, laser diffractometry has been used as an alternative (and effective) technique to characterize dispersion. However, this method does not provide information on positional distributions. Particle-sizing methods, such as laser diffractometry are based on the assumption that the filler particles are primarily spherical in shape (e.g. Ma *et al.* (2000)). Therefore, these methods have been shown to be inaccurate in determining the size of extremely non-spherical particles such as CNTs in suspension form before they are embedded in a polymer matrix (Ivakhnenko and Eremin 2006).

Optical microscopy has also been used to visualize individual CNTs (Huang *et al.* 2008; Zhang *et al.* 2013b; Novak *et al.* 2014). However, observation of CNTs in these studies has been limited to those deposited on a substrate. In this study, a successful visualization of CNTs that were deeply embedded in a composite using laser scanning confocal microscopy (LSCM) is reported (Section 4.2.2.2.3). The technique is unprecedented with respect to its capability to provide a substantial deal of subsurface information on a composite sample. However, the limit of the voxel resolution of LSCM images (1 μm^3) does not allow the precise measurement of small CNT bundles.

The above discussion indicates that none of the conventional imaging techniques available to date is capable of characterizing filler dispersion in all instances and for all desired length scales. Therefore, a combination of different imaging techniques, each operating on a

particular length scale, should be used for the multiscale visualization and dispersion assessment of fillers in composites. The following sections provide further details about the microscopy techniques used and developed in this study.

4.2.2.2.1. Scanning electron microscopy

SEM images were taken using a Zeiss Neon 40 EsB microscope to examine the dispersion quality of the CNTs in the coating specimens. For selected combinations of composite formulation and mixing method, cryo-fractured specimens were prepared to view their cross-sectional surfaces under the microscope. A conductive silver paint was used to bond the specimens to the SEM stubs. The SEM charge-contrast imaging mode (Kovacs *et al.* 2007; Lillehei *et al.* 2009) was used. No metal coating was necessary since the CNTs charged by a high-accelerating voltage were visible due to emitting enriched secondary electrons. A series of incident electron beams with different voltages and incident angles were tried on the specimens in order to maximize the signal-to-noise ratio and the contrast in the charging patterns of the specimens. Eventually, a 10-kV electron beam at an incident angle normal to the specimen thickness was used to scan the cross-sectional surface of the specimens.

In charge-contrast imaging mode, beam electrons emitted at high voltages penetrate deeper into the specimen, yielding more information about the structure of the three-dimensional filler network in the specimen. However, this subsurface information is localized (e.g. on the scale of a few nanotubes at a time) and limited to shallow depths and, therefore, cannot reliably indicate the quality of CNT dispersion in the entire sample. In addition, insulating materials (e.g. PVC in this study) when subjected to sufficiently high-voltage electrons undergo a charge buildup. Consequently, at too high of a voltage a threshold contrast is not

produced and the conductive filler cannot be distinguished from the noise of background fluctuations and the insulating matrix.

4.2.2.2.2. Transmission electron microscopy

TEM forms images from the interaction of a beam of electrons passing through an ultra-thin specimen, making it possible to visualize very high-resolution images to a scale of 0.2 nm. Compared to SEM, TEM tomography creates a 3D reconstruction of a specimen from a series of tilted 2-D images at 5–10-nm resolution. However, the 3D image is not manifest, as the limitations of TEM only make it possible for the specimen to be tilted ± 60/70°. In addition, the preparation of specimens is laborious and requires thin-sectioning in a technical and tedious procedure (Wilson and Bacic 2012).

A TEM was used in order to determine the volume occupied by CNTs in CNT bundles. Samples were cryosectioned at 150 K with a section thickness of 100–110 nm. The sections were then mounted on 600-mesh hexagonal grids and imaged in bright field on a JEOL 2000FX TEM at an accelerating voltage of 200 kV.

4.2.2.2.3. Laser scanning confocal microscopy

4.2.2.2.3.1. Imaging details

Test samples were imaged using a Leica SP8 laser scanning confocal microscope. The PVC was found to autofluoresce with UV excitation, so the samples were imaged using a 405 nm diode laser, and the emission intensity was measured between 446 nm and 554 nm.

High resolution 3D images of the CNT bundles were acquired using a 63 × 1.4 NA oil immersion objective. Oil immersion was chosen primarily because the refractive index of immersion oil, 1.52, is similar to that measured for PVC (Masadome *et al.* 2002), helping to reduce optical aberrations that would otherwise compromise the resolution.

4.2.2.2.3.2. Imaging samples under tensile load

The samples were imaged under tensile strain using a modified tensioning microscope stage (Micro-Vice Holder, ST Japan-USA, LLC). Test samples were loaded onto the vice at a starting length of 11.0 mm. The samples were then imaged via a series of optical sections from the sample surface to 200 μm below the sample surface, measuring the UV excited autofluorescence with a 10 × 0.3 NA objective. The samples were then put under increasing tensile strain in 2.0 mm increments, and imaged at the same position at each increment, until sample failure. The pinhole aperture was opened to 6.00 Airy units to allow us to use a lower laser intensity, which helped to mitigate photobleaching while imaging. When tears within the material were observed, they were imaged in three dimensions by acquiring a series of optical sections in the Z direction with the pinhole aperture closed to 1.00 Airy units for better axial resolution.

High resolution images of fractured CNT bundles were acquired on samples that had been pulled to failure. 3D images were acquired using a 63 × 1.4 NA oil immersion objective, imaging the UV excited autofluorescence.

4.2.2.2.3.3. Image processing and quantification

In order to better delineate the boundaries of the bundles (Figures 4.1a,d,g and Figure 4.2a) in the high resolution 3D images, the image series were deconvolved using an adaptive point-spread function over 10 iterations (AutoQuant X v3.0.3 64-bit) (Figures 4.1b,e,h and Figure 4.2b).

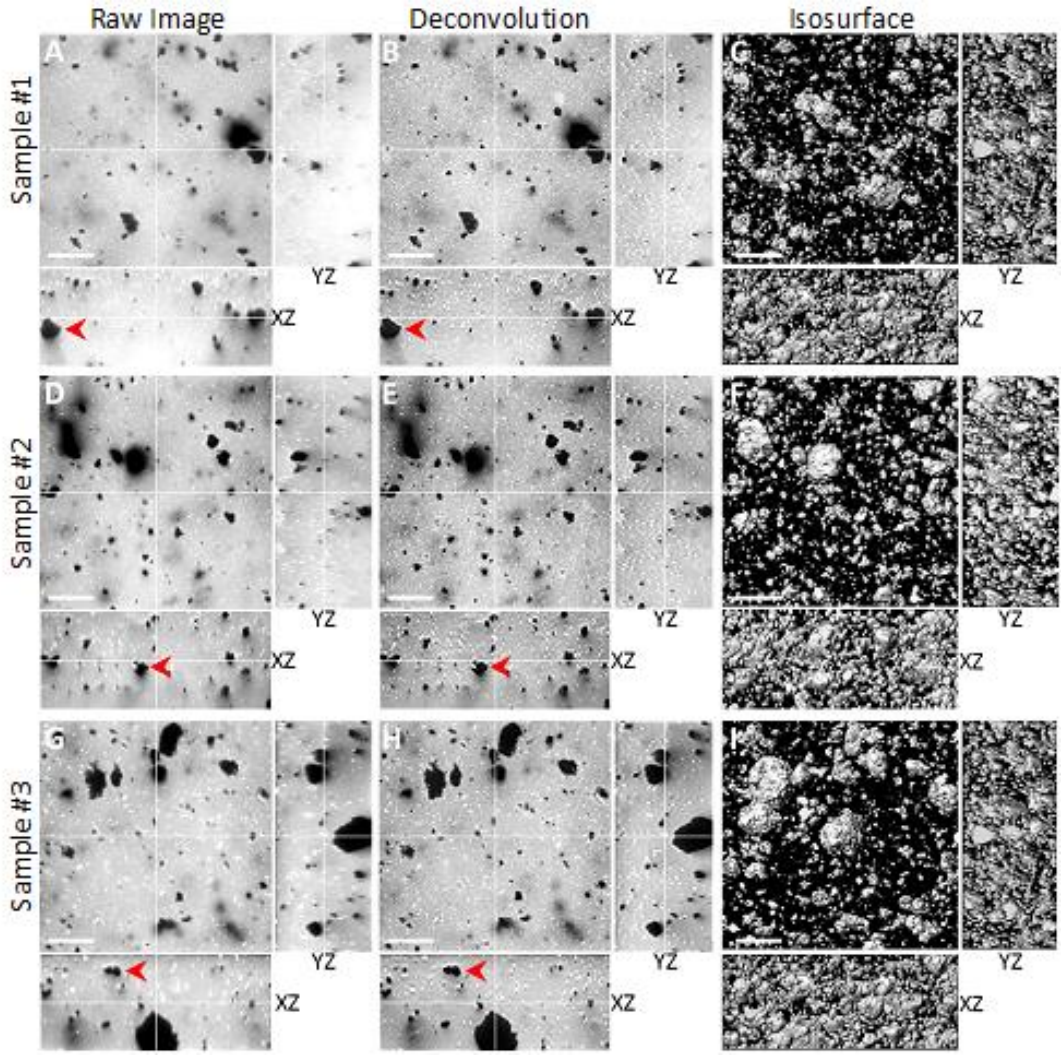

Figure 4.1. LSCM 3D Imaging of CNT bundles in composite samples prepared using PS/55/120. (a, d, g) Orthogonal sections from 3D images of PVC autofluorescence in three separate samples. The white lines show where the corresponding orthogonal sections are located in each image. These images were then deconvolved (b, e, h) and then rendered with an isosurface (c, f, i), revealing the shape and position of each CNT bundle within the 3D image. Arrowheads point to a CNT bundle within the sample. Scale bars = 50 μm.

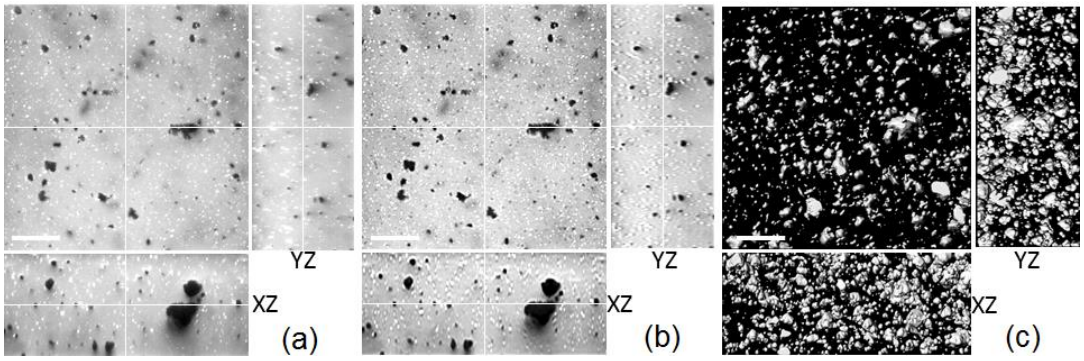

Figure 4.2. LSCM 3D imaging of CNT bundles in BS/70/120. (a) Orthogonal sections from a 3D image of PVC autofluorescence in a CNT composite sample. The white lines show where the corresponding orthogonal sections are located in each image. (b) Image (a) post-deconvolution. (c) Orthogonal views of the entire 3D image with an isosurface rendering around each bundle. Note: Scale bars = 50 μm.

The boundary of each bundle was then determined by inverting the deconvolved image intensities (yielding bright bundles on a dark background) and then generating an isosurface within each image, delineating the bundles from the surrounding PVC (Imaris ×64 v8.0.1) (Figures 4.1c,f,i and Figure 4.2c), allowing for a quantitative 3D analysis of dispersion. The same isosurface threshold was used for every image to ensure that the samples were comparable.

The volume and position of each bundle within an image was quantified by measuring the volume and centroid of each isosurface within an image (Imaris ×64 v8.0.1). The distribution of bulk carbon within each image was measured by binarizing an image series, such that a voxel containing carbon had an intensity of 1 while PVC had an intensity of 0 (ImageJ v1.49m). The percentage amount of the total volume of a 3D bin that was occupied by CNTs was calculated as:

$$\text{Total volume } (\%) = \frac{\#\text{ of voxels containing CNTs}}{\text{total }\#\text{ of voxels}} \tag{4-1}$$

Statistical analysis and plotting was performed using R (R ×64 v3.1.2).

4.2.2.3. Characterization of the mechanical properties of the composites

The interfacial bonding of CNTs with the host matrix together with their specific surface area, type, concentration, aspect ratio and degree of imperfection determine the mechanical properties of the composites in which they are embedded (Gojny *et al.* 2005; Eftekhari *et al.* 2013; Arash *et al.* 2014; Eftekhari *et al.* 2014). Because the stress transfer from the matrix molecules to a CNT could only be achieved via the outermost layer of the CNT, theoretically, almost the entire surface area of SWCNTs can effectively be exploited for mechanical reinforcement. In contrast, for an MWCNT with an outer diameter of 7.8 nm (as is in this study), an inner diameter of 4 nm and a layer distance of 0.34 nm (7 concentric tubules), it can be geometrically shown that only 9.5% of its total surface area (the external surface of the outermost layer) could contribute to the reinforcement of the host matrix (Gojny *et al.* 2005). A full exploitation of this effective surface area requires a high-quality MWCNT dispersion to maximize the interface between the ingredients of the MWCNT/matrix composite. Therefore, the mechanical properties of a composite could be used as an indicator for the quality of filler dispersion in the composite.

Tensile strength tests were carried out to determine the relationship between dispersion quality and the stress-strain behavior of the composites, and also to determine the influence of CNT concentration on their elasticity, ductility, tensile strength and Poisson's ratio. Studying the Poisson's ratio of the composite was particularly useful in the analysis of its strain sensitivity, which is discussed in the Section 4.2.3. PVC plastisol specimens as well as specimens made of the pristine (i.e. no CNT) host matrix comprising of 75% PL and 25% PR were also tested and compared with those filled with the MWCNT. Three different strain rates were examined. A reference strain rate of 0.15 %/min was used to represent the rates

that could be expected in practice and practically achieved in the laboratory (e.g. Hatami and Bathurst (2005)). The tests were also carried out at faster strain rates of 2 and 10 %/min in order to investigate the influence of loading rate on the mechanical properties of the coating composite. The results were used to ensure that the mechanical properties of the coating composite would be adequate to prevent premature cracking and discontinuity in the coating when the final products (i.e. PVC-coated polyester yarn geogrids) are handled or installed in the field. The information germane to the MWCNT-filled specimens that were prepared for conductivity and mechanical property tests is summarized in Table 4-2. For the mechanical property tests, for each formulation listed in Table 4-2, four nominally identical, dog-bone-shaped specimens were punched out from the compression-molded specimens using a die-expulsion press and tested in a tensile testing machine.

In addition to macroscopic tensile tests, the imaging technique described in Section 4.2.2.2.3 was used to investigate the subsurface effects of tensile loading on composite materials in situ and also to explore the mechanics of failure in real time. Previous studies have evaluated the failure mechanism of CNT composites based on the surface topology of previously-tensioned specimens via SEM (e.g. Shokrieh *et al.* (2013)). SEM, however, is limited to observations near the surface of a specimen. The technique developed and used in this study, in contrast, uses LSCM and offers a deeper and more direct insight into the dispersion characteristics of CNT bundles and the failure mechanics of CNT composites. In order to observe the failure mechanics of the MWCNT-filled PVC specimens subjected to tensile loading, 11-mm-long, dog-bone-shaped test specimens were loaded onto a tensioning microscope stage (Micro-Vice Holder, ST Japan-USA, LLC) and subjected to a tensile strain in 2-mm (18% strain) increments (Figure 4.3). The specimens were imaged from the surface

to a depth of 200 μm at the same position at each load increment until failure. When tears within the material were observed, they were imaged in three dimensions by acquiring a series of optical sections in the vertical direction.

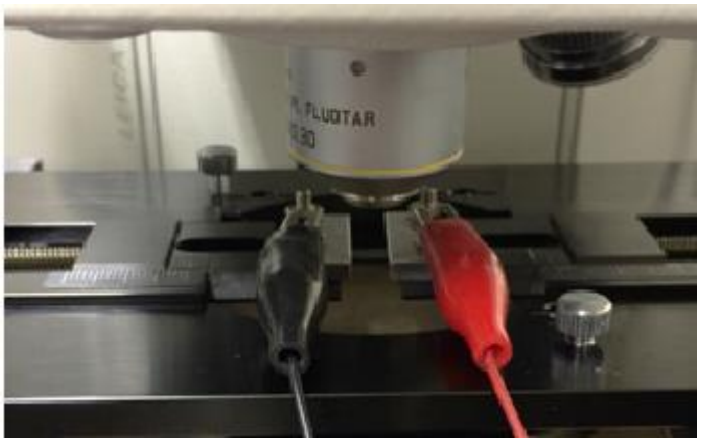

Figure 4.3. Experimental setup used to image the subsurface failure mechanics in CNT composite samples under tensile strain. The composite sample is mounted directly under the objective.

4.2.3. Tensile-conductivity tests

The change in the electrical resistance of a subset of the coating specimens tested for their mechanical properties (i.e. those doped at the critical MWCNT concentration) was recorded at 0.5%-strain intervals in order to determine the change in their electrical conductivity as a function of the applied tensile strain. The same three strain rates that had been used in the tensile tests were used to investigate the strain rate-dependency of the coating composites tensoresistivity response. The electrical resistance of the specimens was measured using an analog Keithley electrometer and the two-point probe method in which two alligator clips 25 mm apart were attached to the specimens (Figure 3.7). Silver paint was used to enhance the electrical contact at the alligator clips attachments. Although the two-point measurement scheme includes the resistance of lead wires and contacts, this added resistance is deemed to be negligible relative to the resistance of the specimens throughout the tests.

The strain-dependent response of the specimens' electrical conductivity was also measured during the LSCM tests in order to understand how microstructural changes would contribute to the changes in conductivity. To this end, the specimens were electrically isolated from the stage using several sheets of polyethylene, and the electrical leads were connected directly to the specimens (Figure 4.3).

4.3. Results and discussion

4.3.1. LSCM analysis

4.3.1.1. Validation of the methodology

CNTs are known to have high absorption in the UV range (Nakanishi *et al.* 2013), which is also the wavelength found here to efficiently excite autofluorescence in the host polymer, PVC. The absorption proved problematic when trying to image deep into the composite samples, and especially when resolving the side of the CNT bundles opposite the objective. To resolve this issue, the samples were imaged starting 100 μm below the surface of the sample with a 27 μs exposure time per voxel, and were then imaged back towards the surface of the sample closest to the objective. The direction of the imaging resulted in photobleaching of the PVC closest to the objective giving a uniform image intensity, where the decreasing amount of UV absorption by the CNTs was offset by increasing photobleaching of the PVC as the sample was imaged closer to the surface (Figures 4.1a, d and g and Figure 4.2a). The total volume imaged for each test sample was 246 μm × 246 μm × 104 μm with a voxel dimension of 480 nm × 480 nm × 480 nm.

We were also able to detect autofluorescence from within the CNT bundles (Figure 4.4a), revealing that the CNT bundles were optically translucent rather than completely opaque. In order to confirm that the CNTs were organized in a manner to allow for the visualization of PVC within the composite, TEM was used to observe CNT composition within CNT bundles (Figure 4.4b and c). It was found that the bundles were a loose tangle of CNTs impregnated with PVC, confirming the observation of PVC fluorescence within the bundles via LSCM. Because of the translucent nature of the bundles, sufficient light was transmitted through the bundles for the full 3D structure of each bundle to be imaged via LSCM, including the side of the CNT bundles opposite the direction of illumination (Figure 4.1). Figure 4.4b and its magnified counterpart, Figure 4.4c, show a TEM micrograph of a single bundle showing the density and arrangement of loosely-entangled CNTs impregnated with PVC.

The TEM results can also be used to determine the CNT density in individual bundles. As previously stated, a predetermined amount of mixed pigment was blended with PVC plastisol to produce the final CNT-filled composite samples. Since the distribution of CNT bundles within the constituent pigment is not expected to be completely uniform, the CNT concentration in the resulting composite samples in their liquid form (and in the corresponding cured specimens) does not necessarily match that of their parent pigment. Therefore, information on the CNT density in individual bundles together with the bundle volume from LSCM could be used to estimate the density of CNTs in a cured composite specimen.

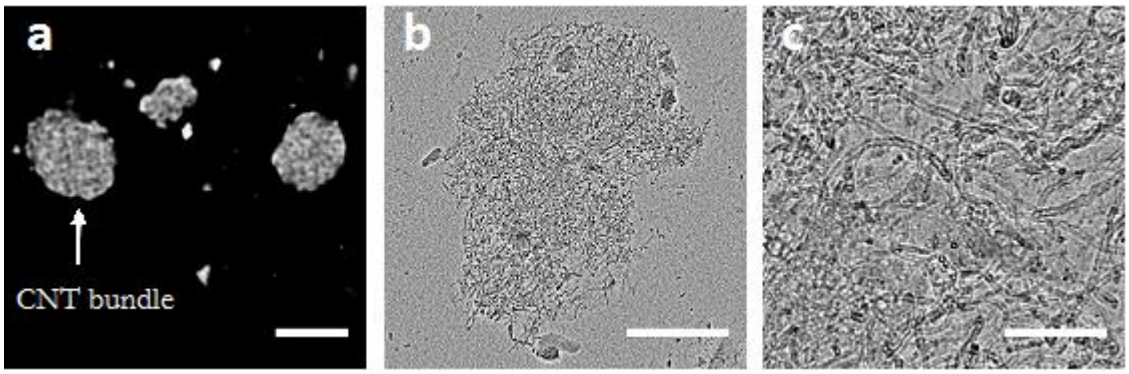

Figure 4.4. CNT bundles are optically translucent with PVC impregnation into CNT bundles (a) A single optical section of a CNT bundle (white). PVC (black) is clearly visible within the bundle itself. Scale bar = 20 μm. (b) A TEM micrograph of a CNT bundle showing that the bundles are a loosely entangled cluster of CNTs impregnated with PVC. Scale bar = 1 μm. (c) A magnified view from b. Scale bar = 200 nm.

Since the CNT bundles would have been stochastically sheared during sonication, a log-normal distribution was hypothesized for the volume distribution of the bundles (Kolmogoroff 1969), which has also been observed in previous studies of CNT dispersion by sonication (Frømyr *et al.* 2012). A histogram of bundle volumes within the images confirmed a log-normal distribution (Figures 4.5a-c and Figure 4.6a). As can be observed in the corresponding probability plots (Figures 4.5d-f and Figure 4.6b), the majority of the volumes fall along the reference normal distribution with 95% confidence, with the extreme tails outside the interval. The deviation of the lower tail from the expected distribution coincides with the limit of the voxel resolution of the LSCM images (1 μm^3), suggesting that while the aggregates smaller than 1 μm^3 are detectable, their volume cannot be precisely measured. On the other hand, the deviation of the upper tail from the expected distribution could be attributed to the sampling bias arisen from centering the largest aggregates in the microscope's field of view in order to avoid having them cropped out, which in turn may have resulted in an underestimation of their abundance. The null hypothesis that all specimens had a log-normal distribution was also tested using several methods including

those introduced by Kolmogorov and Smirnov (Kolmogorov 1933; Smirnov 1933), Anderson and Darling (1952), Shapiro and Wilk (1965), Jarque and Bera (1980) and Doornik and Hansen (2008). These normality tests, which are supplementary to the visual assessment of normality, compare the actual frequency distribution of a sample (the actual values) with a theoretical normal distribution (the expected values) that possesses the same mean and standard deviation. All these tests accepted the null hypothesis for the distribution of bundle volumes in the study described here. However, for brevity, only the Shapiro-Wilk test results are reported in Table 4-3.

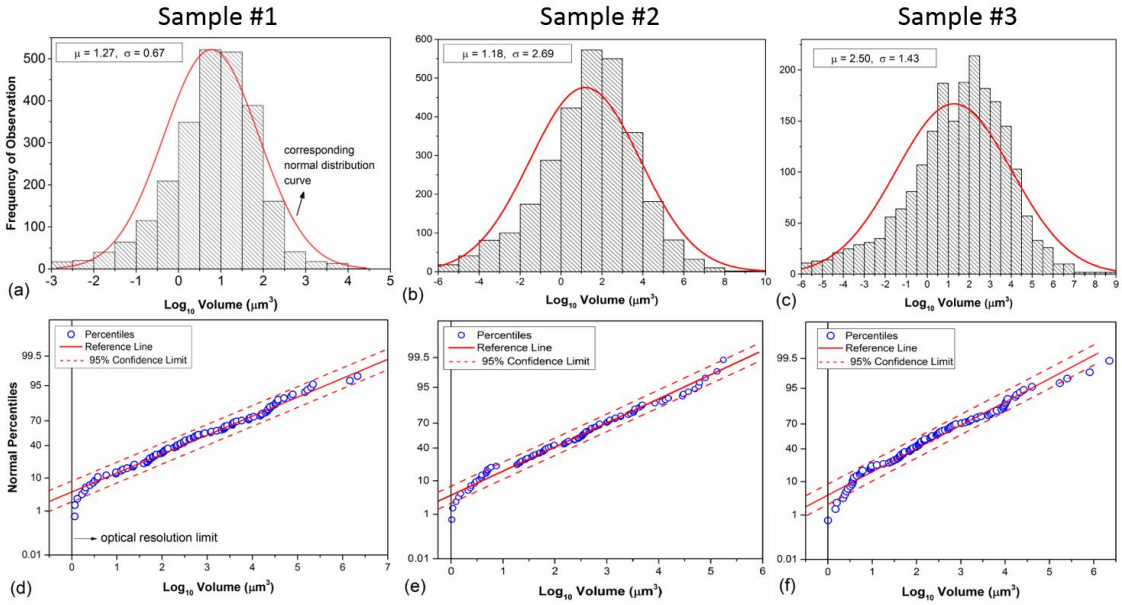

Figure 4.5. Distribution of CNT bundle volume within three different PVC composite samples composite samples prepared using PS/55/120. (a-c) Histograms of the distribution of CNT bundle volumes across three separate CNT composite samples. The red line shows the corresponding log-normal distribution of the same mean and standard deviation. (d-f) Probability plots comparing the bundle volume distributions to the corresponding log-normal distributions. Dashed lines = 95% confidence interval.

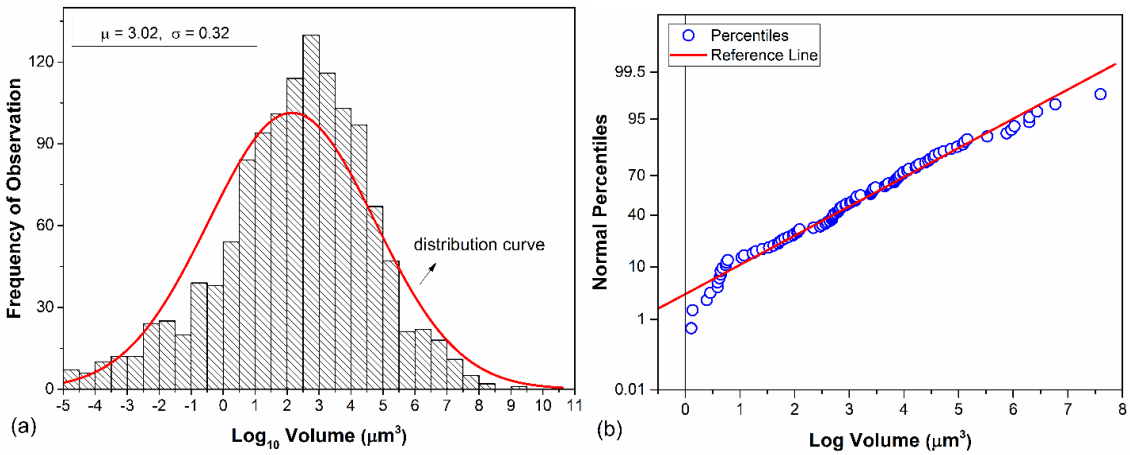

Figure 4.6. (a) Histogram of the distribution of the CNT bundle volumes in the BS/70/120 specimens, with the superimposed curve showing the corresponding log-normal distribution. (b) Corresponding probability plot showing the distribution of bundle volumes relative to a log-normal distribution

Table 4-3. Mean and standard deviations of MWCNT volume log-normal distributions in different filled specimens. Note: The values indicate the Shapiro-Wilk test results and the mean values of three independent experiments.

Mix ID	Mean volume (μm³)	Standard deviation (μm³)
PS/55/60	2.32	0.25
PS/55/120	2.43	0.21
PS/55/180	2.77	0.26
BS/70/60	3.04	0.08
BS/70/120	3.02	0.32
BS/70/240	2.84	–
BM/150/65/20	3.12	0.13
BM/150/100/10	3.19	0.12
BM/150/100/20	3.18	0.13
MS/750/3	2.70	0.17
MS/1500/3	3.24	–
MS/3000/3	1.89	0.20

4.3.1.2. Distribution of bundle volumes

Having validated the methodology for 3D quantitative imaging of the bundles within the sample, the spatial distribution of CNT bundles within the composite was then measured, determining whether there was a positional dependence in bundle volume distribution and/or total carbon distribution. To answer this question, each image was divided into five equal bins along the X, Y and Z axes (Figure 4.7a). The quality of dispersion was assessed

through two different metrics. First, the distribution of the individual bundle volumes along each image axis was quantified. Subsequently, the fraction of the total volume of each bin filled with CNT bundles was measured (Figure 4.7b). While the distribution of bundle volumes was not significantly different throughout the sample, the bulk CNT content was dominated by the largest aggregates within the image, resulting in local concentrations in carbon content.

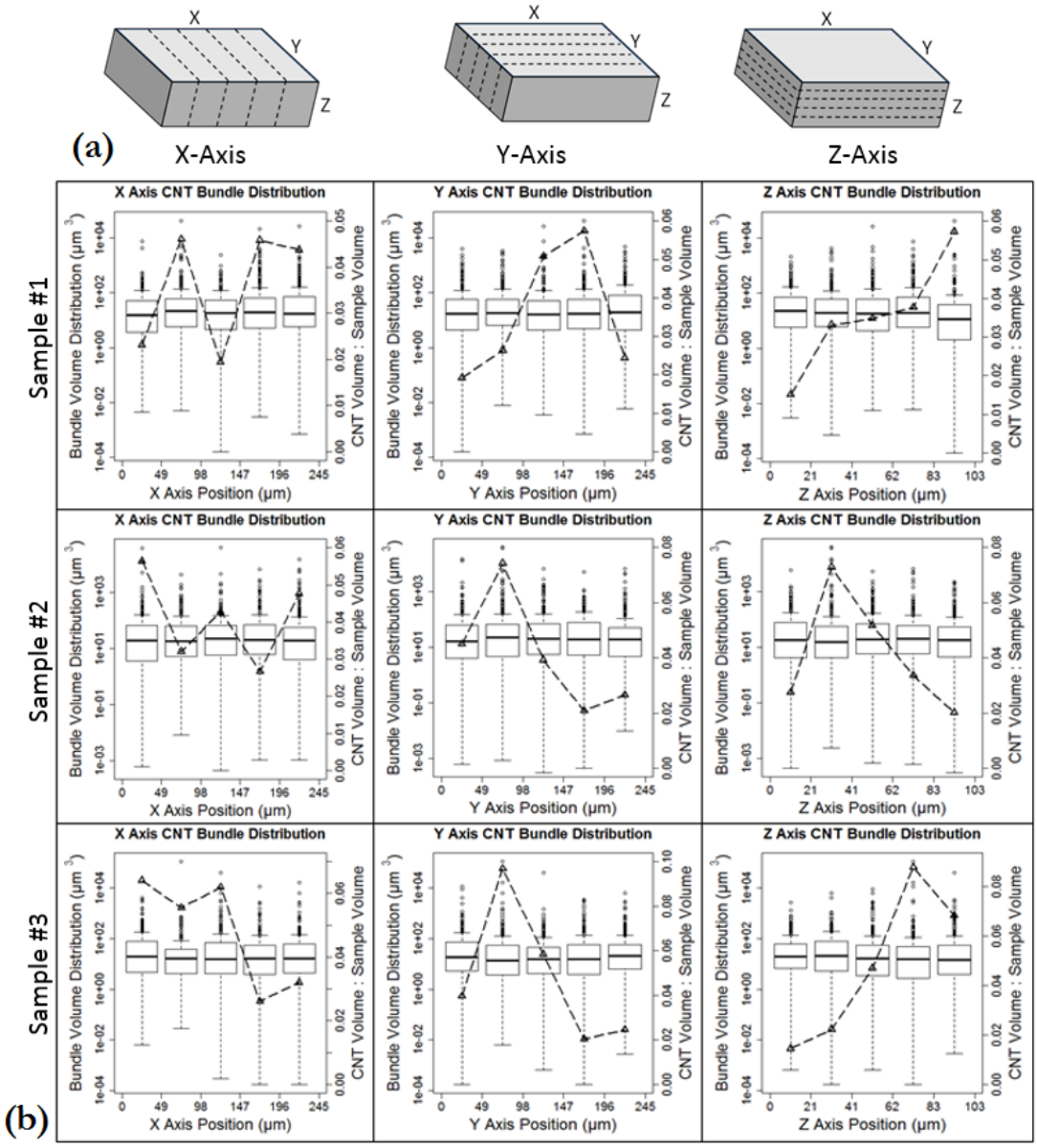

Figure 4.7. (a) A schema showing how the total 3D image was divided into 5 bins along each axis in a, with the side of the image that was closest to the objective facing up. Distribution of CNT bundles in PVC. (b) Plots showing the distribution of individual bundle volumes (box plots) as well as the bulk distribution of CNTs (dashed line) along the X, Y and Z axes of the image in Figure 4.1.

In addition to the quantitative analysis above, the 3D distribution of CNT bundles in a representative sample was characterized in order to visualize the position, size and appearance of bundles in a single image. To this end, the isosurface rendering of CNT

bundles from a 3D confocal image series shown in Figure 4.2c was overlaid by the corresponding color coded Z-position of each bundle (Figure 4.8).

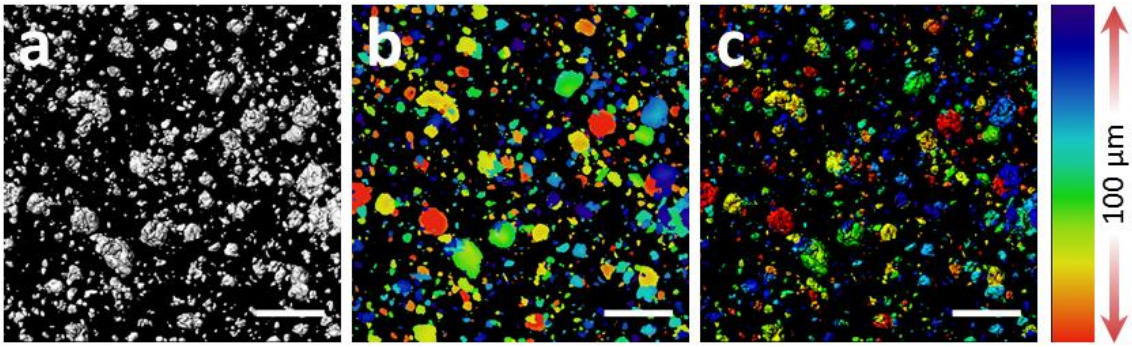

Figure 4.8. 3D distribution of CNT bundles in BS/70/120 specimens from LSCM images. (a) Isosurface rendering of CNT bundles from a 3D confocal image series. (b) The corresponding color coded Z-position of each bundle in image (a). (c) An overlay of images (a) and (b) showing the three-dimensional position of each bundle within the image stack. Scale bar in each image = 50 µm.

4.3.1.3. Comparison of mixing methods

Differences in the quality of CNT dispersion as obtained through the mixing methods described here were quantified in order to determine which method(s) would result in comparable dispersion of the MWCNT bundles in the specimens. As discussed previously, stochastic shearing of CNT bundles should theoretically yield a log-normal distribution of bundle volumes (Kolmogoroff 1969). Accordingly, the similarity in the degree of bundle shearing for a given methodology can be quantified as the Pearson product-moment correlation coefficient (PPMCC) (Pearson 1895). To measure the Pearson coefficient, the bundle volume measurements for each dispersion method were first binned logarithmically to get the normal percent frequency distribution of bundle volumes for each method. The percent frequency distributions were then compared against one another by calculating the corresponding PPMCC (ϱ) values, which were then plotted as a correlation heatmap (Figure 4.9).

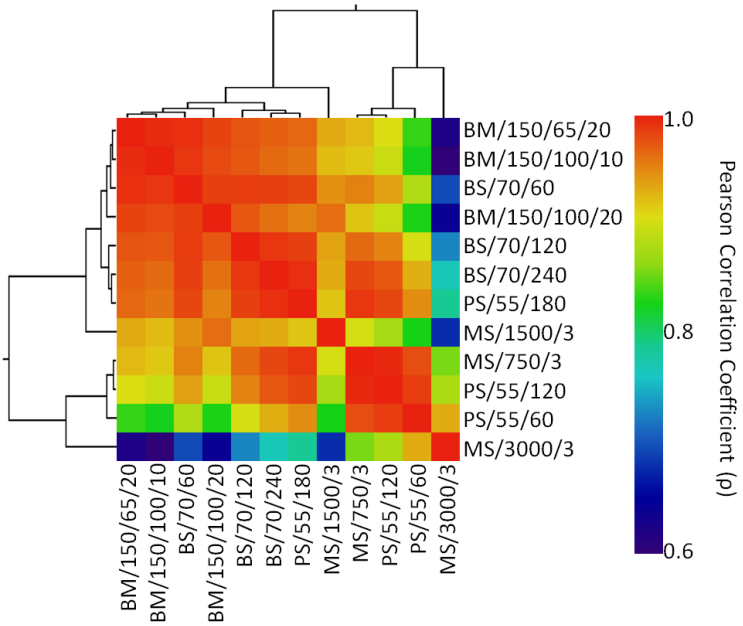

Figure 4.9. Hierarchical clustering of CNT dispersion methods in filled PVC composites based on the CNT aggregate volume distributions

The correlation matrix was used as a similarity matrix, or a distance matrix using the complement of the correlation coefficient (1 - ρ) to cluster methods with similar dispersion properties together. Specifically, the unweighted pair group method with arithmetic mean was used to generate a hierarchical dendrogram of the similarity between bundle volume distributions for different dispersion methods examined (Figure 4.9). In the example shown in Figure 4.9, there are two main groups of methods which are clustered primarily by the technique applied rather than their duration, suggesting that the method used to shear the CNT bundles has a greater influence on their size than the power or duration used in each method.

In addition to evaluating the dispersion quality of CNT particles in polymer composites as a function of the mixing method, the correlation between the dispersion quality and the composite sample conductivity (or resistivity) was examined. The Spearman correlation

coefficient was used to determine the correlation between an array of quantitative metrics of CNT aggregate volumes and sample resistivity. This was done to determine which characteristics of the CNT dispersion were most predictive of the conductivity of the composite samples. It was understood that the areas of the sample that were imaged in each technical replicate might not have been the best representatives of those which had the greatest contribution in the sample conductivity. Therefore, to remove any potential sampling effects, the CNT aggregate volume distributions within each technical replicate were iteratively shuffled and reassigned to the corresponding conductivity measurements followed by measuring the distribution of the resulting Spearman correlations (Figure 4.10). A technical replicate in the above discussion refers to the same sample which was analyzed multiple times.

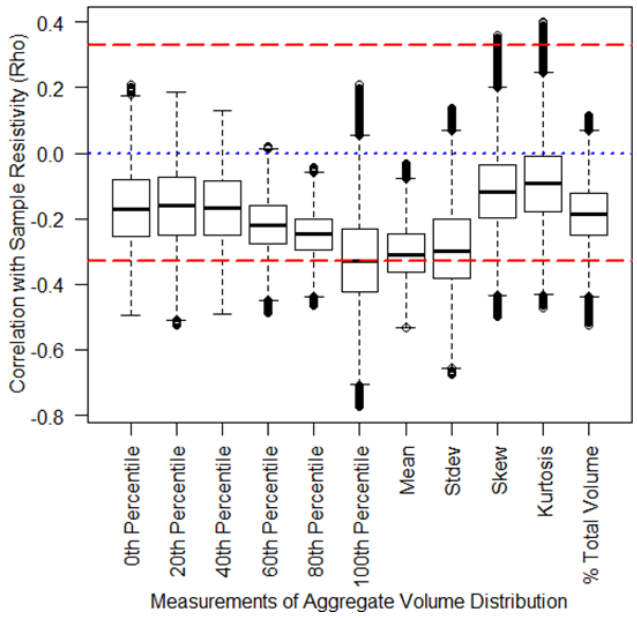

Figure 4.10. Correlation between quantitative metrics of CNT dispersion and resistivity. Note: the dashed lines represent correlations that are statistically significant ($p < 0.05$).

The volume of the larger aggregates within a sample had an increasingly-negative correlation with sample resistivity, suggesting that as the largest aggregates within a sample increased in volume, so did the sample conductivity. Interestingly, contrary to previously-published studies (e.g. Rui *et al.* (2014)), no significant correlation was observed between the conductivity of the polymer composite and the percent sample volume filled by the CNT aggregates.

4.3.2. Electrical conductivity

The influence of MWCNT concentration, mixing method and curing time on the electrical conductivity of the PL/PR/MWCNT composites is discussed in the following sections.

4.3.2.1. Dispersion and electrical conductivity

The measured electrical conductivities of the specimens listed in Table 4-2 are plotted in a descending order in Figure 4.11. The magnitude and repeatability of the conductivity results together with the analysis of the data corresponding to the 3D imaging of samples using LSCM were collectively used to quantitate the quality of CNT dispersion that was obtained using each mixing method. Also, SEM images shown in Figure 4.12 are used for the qualitative assessment of CNTs dispersion.

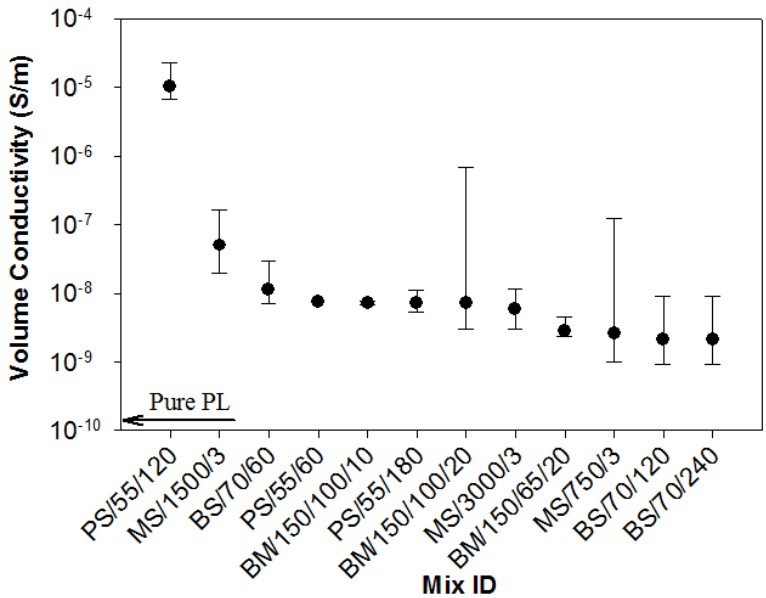

Figure 4.11. Volume conductivity of composite specimens filled with 0.5 wt.% MWCNT and produced using different mixing techniques. Note: three specimens were tested for each mixing case shown.

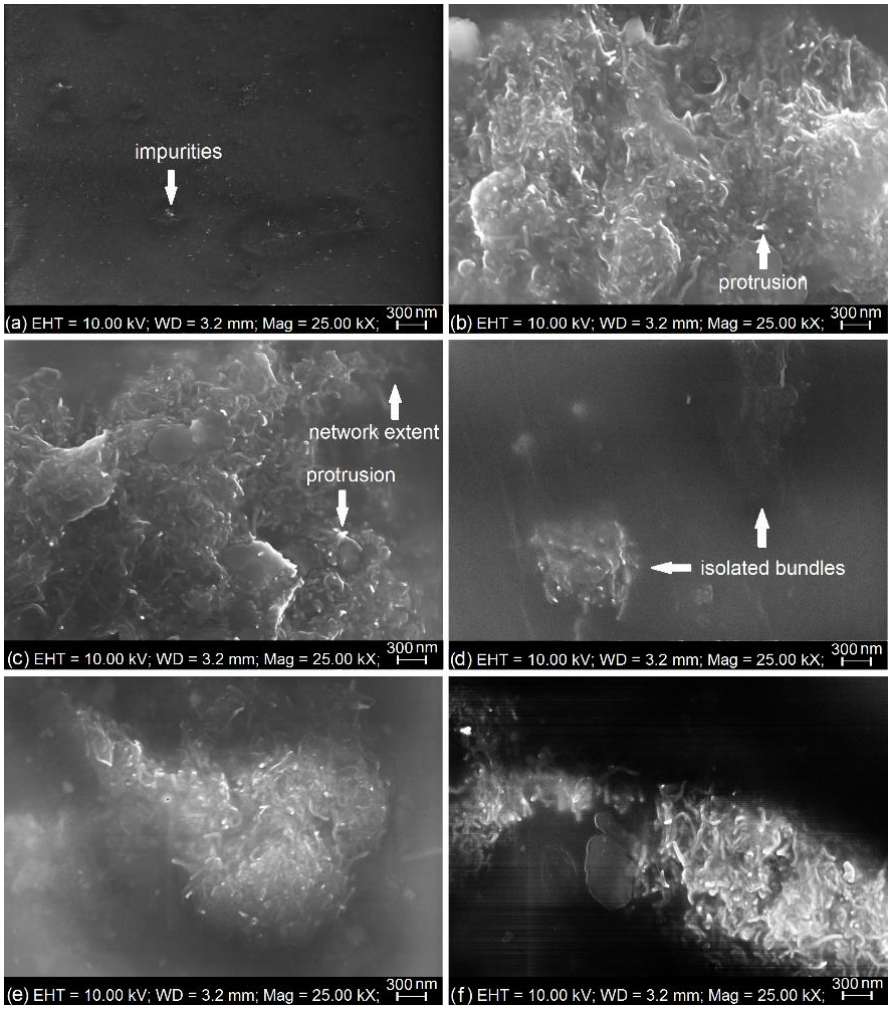

Figure 4.12. SEM images for (a) pure PL, (b) PS/55/60, (c) PS/55/120, (d) PS/55/180, (e) BS/70/120, and (f) BM/150/100/20

The density of the brighter spots in the SEM images is a direct indication of the density of CNTs in the composite while the visual arrangement of the brighter spots indicates the quality of CNT dispersion. The few spots observed in the pure specimen (Figure 4.12a) are attributed to the presence of impurities and contaminants in the plastisol matrix and lack the fibrous appearance of the CNTs. In addition, due to the needle-like structure of CNTs, fracturing frozen specimens splits the CNTs crossing the fracture line leaving protrusions

on the fractured surfaces. These protrusions generate large quantities of secondary electrons causing them to appear brighter in SEM images (e.g. Figure 4.12b).

It can be seen from Figure 4.11 that the PS method, with a total sonication duration of 120 minutes (PS/55/120), resulted in a significantly-higher conductivity in the specimens with fairly low variation in the test results compared with those made using other mixing methods. Comparison of the conductivity of the PS/55/120 specimens with PS/55/60 and PS/55/180 and their corresponding SEM images in Figure 4.12b-d indicates that 120 minutes is a (near-)optimal sonication duration that, when coupled with the sonication power, provides an adequate energy to construct a three-dimensional, interconnected network of CNTs (Figure 4.12c). Longer durations deliver excessive energy that breaks the CNT network into isolated CNT aggregates (Figure 4.12d). This is in agreement with the findings of Lu et al. (Lu et al. 1996) who observed a significant increase in the intensity of D band in the Raman spectroscopy of CNT-filled composites subjected to prolonged ultrasonication. This increase arises from disordered sp^3 carbon in CNTs, suggesting the generation of defects on their surface that convert CNTs into amorphous carbon nanofibers and deteriorate both the electrical and mechanical properties of the composites (Mukhopadhyay *et al.* 2002). The brightness variations visible in Figure 4.12c show the extent of an aggregate and can be related to the position of the CNTs in the specimen; high brightness indicates the shallow position of the CNTs, whereas CNTs located deeper in the specimen appear darker. Nonetheless, no information was accessible from the regions located deeper than approximately 50 nm even by increasing the acceleration voltage, as also observed by Loos *et al.* (2005) and Kovacs *et al.* (2007).

The results of the BS method shown in Figure 4.11 indicate that no combinations of the sonication power and duration were adequate to overcome the intermolecular interactions between the bundled CNTs (e.g. Figure 4.12e). Even though the energy transmitted to the pigment in the BS method was comparable to that in the PS method, the more defined cavitation zone and localized energy in the PS method (probably paired with the locally generated heat) was able to provide a situation that resulted in the disentanglement of the CNT bundles.

The results corresponding to the BM and MS methods in Figure 4.11 show that these methods are not effective in producing specimens that would exhibit high conductivity at low filler concentrations. The poor dispersion obtained using these methods can be seen in a representative SEM image shown in Figure 4.12f. This poor dispersion is possibly due to CNT fragmentation during mixing process that dominates the disentanglement of CNT bundles and results in split and partially-disentangled bundles. Comparison of the results of the two mixtures of BM/150/100/10 and BM/150/100/20 indicates that increasing the mixing duration from 10 minutes to 20 minutes did not influence the mean electrical conductivity. However, one of the specimens' conductivity was two orders of magnitude larger than the mean value possibly due to the local concentration of CNTs in the source pigment. In addition, comparison of the results for BM/150/65/20 and BM/150/100/20 shows a slight increase in the mean conductivity of the composite as a result of increasing temperature from 65 °C to 100 °C during the mixing process. Among all the mixing methods and combination of influential factors examined, the BM/150/100/10 combination was found to yield the highest degree of consistency (i.e. lowest scatter) in the conductivity results indicating that the higher mixing temperature improved the homogeneity of the pigment.

4.3.2.2. Influence of curing time

Curing (vulcanization) parameters (i.e. duration and temperature) have been proven to considerably influence the electrical conductivity of filled composites (e.g. Das *et al.* (2002); Martin *et al.* (2004)). The influence of curing time in compression-molding on the electrical conductivity of MWCNT-filled PVC composites is shown in Figure 4.13. It can be observed that a prolonged curing time increases the conductivity especially during the first 10 to 15 minutes of vulcanization. This may be due to the formation of firm bonds between CNTs and the matrix molecules (crosslinking) during the initial stages of the vulcanization period. Over time, this process is accompanied by the evaporation of low-molecular fractions and diffusion of otherwise isolated CNT aggregates (Böhm and Nguyen 1995; Zhang *et al.* 2007a). As a result of this crosslinking, the volume of the composite decreases, which in turn increases the CNT-CNT contact and consequently the electrical conductivity of the composite (Zhang *et al.* 2007a). The vulcanization at this stage is promoted by the presence of MWCNTs due to their high thermal conductivity (10^3 W/m/K Song and Youn (2005)), which is approximately 5,000 times greater than that of PVC. The high thermal conductivity of MWCNTs also helps to eliminate the difference in the degree of crosslinking between the surface and the bulk of thick polymeric products (Sui *et al.* 2007).

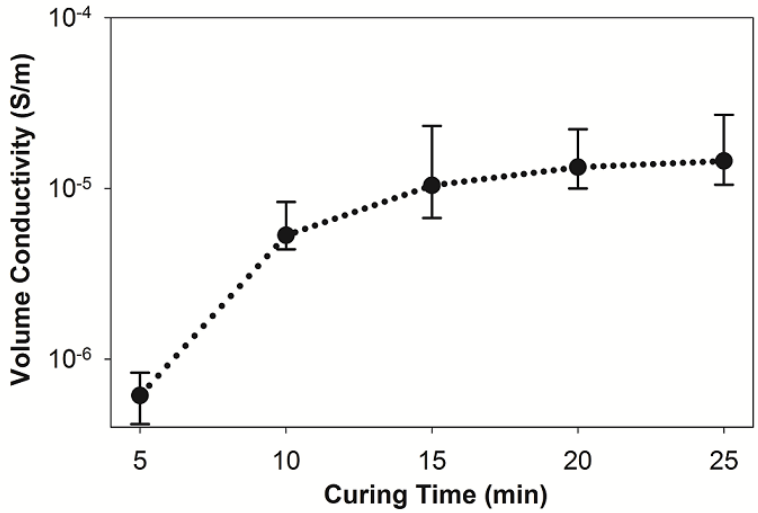

Figure 4.13. Influence of curing time in compression molding on the conductivity of PS/55/120

The time, t_D, required for a CNT aggregate with a hydrodynamic radius of R_H to diffuse an interaggregate distance of d through a liquid with a viscosity of η can be estimated using the Stokes-Einstein law as (Tsvetkov 1989):

$$d^2 / t_D = k_b T / (3\pi\eta R_H) \tag{4-2}$$

where k_b is the Boltzmann's constant (1.38×10^{-23} J/K) and T is the absolute temperature. For η = 3 Pa•s (described in the 'Specimen fabrication' section), R_H = 500 nm for MWCNTs (Pyshkina *et al.* 2012), d = 500 nm (assuming that an aggregate would have to diffuse a distance approximately equal to its radius of gyration to fuse to another aggregate (Böhm and Nguyen 1995)) and T = 453.16 K (180 °C), Equation (4-2) gives a diffusing time of about 10 minutes which is consonant with the data shown in Figure 4.13.

4.3.2.3. Influence of CNT concentration

The influence of the MWCNT concentration on the volume conductivity of the PVC composite is shown in Figure 4.14. A conductivity of 3.4×10^{-9} S/m was measured for pure

plastisol specimens (i.e. CNT% = 0). In the figure, a percolation threshold of 0.2 wt.% can be identified in the form of an upsurge in the measured electrical conductivity with an increase in the MWCNT concentration. According to Figure 4.14, as the level of doping exceeds the percolation threshold, the composite enters into a region, known as the percolation region, across which a conductive network of CNTs is developed and a transition in the nature of charge transport from tunneling to partial metallic diffusive transport is observed (i.e. 0.2 wt.% < φ < 0.4 wt.%). Due to the evolution of the existing or the formation of new conductive paths, the conductivity of the composite beyond the percolation region slightly increases with adding more CNTs until it levels off to 10^{-4} S/m. This level of conductivity opens the door for the composite for electrostatic discharge (< 10^{-4} S/m (Ferreira et al. 2012)) and electrostatic coating (> 10^{-5} S/m (Baughman et al. 2002)) applications. For comparison, the percolation threshold and conductivity of some amorphous polymers filled with MWCNT is shown in Table 4-4.

Electrical conductivity, σ, of a filled composite above the percolation threshold, φ_c, follows the scaling law (also known as the power law) as (Kirkpatrick 1973):

$$\sigma = \sigma_0(\varphi - \varphi_c)^t \tag{4-3}$$

where σ_0 is the conductivity of the composite when it levels off to a value close to the conductivity of the composite at high filler concentrations, φ is the probability of finding the dispersed phase within the polymer matrix which is usually set experimentally equal to the volume fraction of the dispersed phase, and t is a critical exponent, which is a universal parameter theoretically close to 2.0 for a three-dimensional composite filled with a randomly dispersed phase (Gingold and Lobb 1990).

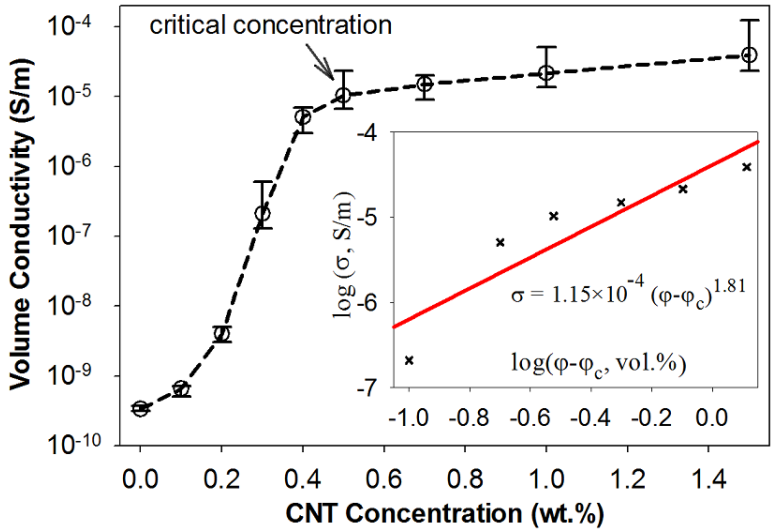

Figure 4.14. Volume conductivity of PVC/plastisol as a function of CNT concentration for PS/55/120. The inset is the scaling law of $\log \sigma \propto \log (\varphi - \varphi_c)$ (Equation (4-3)) to determine σ_0 and *t*.

Table 4-4. Summary of the percolation threshold of some common amorphous polymers filled with MWCNT

Matrix	Aspect ratio	Dispersion	φ_c (wt. %)	t	Maximum conductivity (S/m)	Source
PVC plastisol	~95	Probe sonicated	0.50	1.81	10^{-4} @ 1.4 wt.%	This study
Low viscous polyamide 12	~200	Melt mixed in a conical twin-screw extruder	0.50	–	10^{-2} @ 5 wt.%	(Socher *et al.* 2011)
High viscous polyamide 12	~200	Melt mixed in a conical twin-screw extruder	2.00	–	10^{-1} @ 5 wt.%	(Socher *et al.* 2011)
Polyimide	~300	Stirred under ultrasonication	7.00	1.14	10^{-4} @ 12 wt.%	(Zhu *et al.* 2006)
Polymethylmethacrylate	~160	Melt mixed	0.80	1.8	10^{-1} @ 8 wt.%	(Logakis *et al.* 2011)
Polystyrene	~160	Ultrasonicated	0.045	2.11	10^{-1} @ 1 wt.%	(Shrivastava and Khatua 2011)
Polysulfone	~290	Bath sonicated	0.10	–	10E-1 @ 1 wt.%	(Bautista-Quijano *et al.* 2010)

The CNT concentration in the composites studied here varied within the range between 0.1 wt.% and 1.5 wt.%, which can be converted to volume fraction, φ, (as required in Equation (4-3)) using (Mamunya *et al.* 2008):

$$\varphi = w_f \rho_m / (w_f \rho_m + w_m \rho_f) \tag{4-4}$$

where w_f is the weight concentration of the filler (MWCNT) and w_m is the weight concentration of the matrix (calculated as the summation of the weight concentrations of plastisol, w_{PL}, and plasticizer, w_{PR}), ρ_f is the density of the filler and ρ_m is the density of the matrix calculated as the weighted mean of the densities of plastisol, ρ_{PL}, and plasticizer, ρ_{PR}, as:

$$\rho_m = (\rho_{PL} w_{PL} + \rho_{PR} w_{PR}) / (w_{PL} + w_{PR}) \tag{4-5}$$

The solid line in the inset of Figure 4.14 made on the basis of fitting the conductivity data to the form of Equation (4-3) gives a critical exponent of t = 1.81, which is slightly below the value of 2 predicted by the percolation theory. Such deviations from the percolation theory prediction have also been reported for CB-filled composites (t = 1.85 to 2 – Carmona and Mouney (1992)), for carbon fiber-filled composites (t = 3 to 8.4 – Carmona and Mouney (1992); Feller *et al.* (2002)) and for MWCNT-filled composites ($t \approx 1.2$ in polycarbonate/MWCNT Guo *et al.* (2014)). Significantly greater critical exponents have been reported in the literature mainly for semicrystalline systems filled with MWCNT (e.g. 2.9 in poly(ethylene terephthalate)/MWCNT (Logakis *et al.* 2010a) and 4.5 in isotactic polypropylene/MWCNT (Logakis *et al.* 2010b)). In semicrystalline systems, a crystalline layer is developed around CNTs (*trans*-crystallinity) impeding the direct contact between them and giving rise to a wide inter-particle distance distribution which leads to exceptionally large t

values (Balberg 2002). In contrast, the amorphous nature of the polymer studied in the present work (i.e. PVC) is in line with the convergence of *t* to its theoretical value.

These deviations from a theoretically-predicted *t* value are also due to the difference between the assumptions inherent to the percolation theory and the conditions governing actual experiments. For instance, one of the basic assumptions of the percolation theory is that the occupation of a lattice site by filler particles is essentially a random process such that the probability of a site being occupied is independent of whether or not any of its nearest neighbors is already occupied (Kawakatsu 2004). In contrast, carbon-based fillers possess an inherent drive to agglomerate or create physical entanglement with their neighboring fillers which differs greatly from the assumption described above. This explanation also holds for the observations of Mamunya *et al.* (2008) who reported a value of 3.5 for the critical exponent of the scaling law describing the electrical conductivity of MWCNT-filled PVC composites that were prepared using the segregation method. However, this latter deviation could also be partially ascribed to the non-statistical, ordered distribution of the conductive fillers in the segregated composites as compared to their random distribution in a polymer matrix as assumed by the percolation theory.

4.3.3. Mechanical properties

4.3.3.1. Fracture mechanism

LSCM also offered a unique opportunity to observe the subsurface effects of tension on a composite material *in situ*. Previous studies have assessed CNT nanocomposite material failure mechanisms based on the surface topology of strained samples via SEM (Jogi *et al.*

2012; Shokrieh *et al.* 2013) and LSCM (Powell *et al.* 1993). The capacity of LSCM to image subsurface features also allows for monitoring the internal deformation of a composite sample while under a dynamic load (Plucknett *et al.* 2001). Since our imaging method also allowed us to observe the CNT bundles up to 100 μm below the sample surface, we combined these techniques in our study by using LSCM to investigate both the surface topography as well as the subsurface CNT bundle deformation while the composite samples were under an increasing tensile load.

Specifically, dogbone test samples were loaded onto a tensioning microscope stage and tightened until there was no slack in the sample (0% strain). The samples were then tensioned and imaged down to 200 μm below the surface of the material in 18% strain increments. The real-time observation of the tensile fractures within the samples indicated that the growth of fracture in the specimen is governed by the comparative resistances of the polymer matrix and the inclusions (i.e. CNT bundles/individuals) to cracking. Fractures were initiated from inside the largest bundles between 18–36% strain, which is close to the range of strain at failure reported for CNTs and graphene at room temperature (i.e. 8–20% Eftekhari *et al.* (2013)). The initiation of the fractures from bundles is possibly due to the weak van der Waals interactions between MWCNT individuals (Yu *et al.* 2000), and the small shear strength between the MWCNT concentric layers (the average shear strength for high-quality graphite is approximately 0.48 MPa – Soule and Nezbeda (1968)). Inside a bundle, the stress at the tip of a crack may exceed the van der Waals forces that hold the MWCNTs together, leading to progressive cracking across the bundles. As the tensile load increased, smaller bundles within the specimen progressively ruptured perpendicular to the direction of tension while the larger bundles continued to fail through further fractal-like fracturing. As the

sample approached failure, a large tear would predominate at the site of one of the largest aggregates, and propagate even under sustained constant strain (Figure 4.15).

A three-dimensional image of a large tear that formed preceding the failure of the material was acquired in order to better understand their formation mechanism (Figure 4.15). Large, fractured bundles can be observed at the base of these tears. The polymer near the tear was raised relative to the rest of the specimen, possibly causing stress relief as the material began to fail, preventing further polymer tearing around nearby aggregates. Six test samples in total were then imaged at a different relative position each, and found that the sequential bundle rupturing occurred across the entire sample, independent of positon. The host polymer was also observed to have a low concentration of non-autofluorescent particles (Figure 4.15a); however, these particles did not fracture under tensile strain.

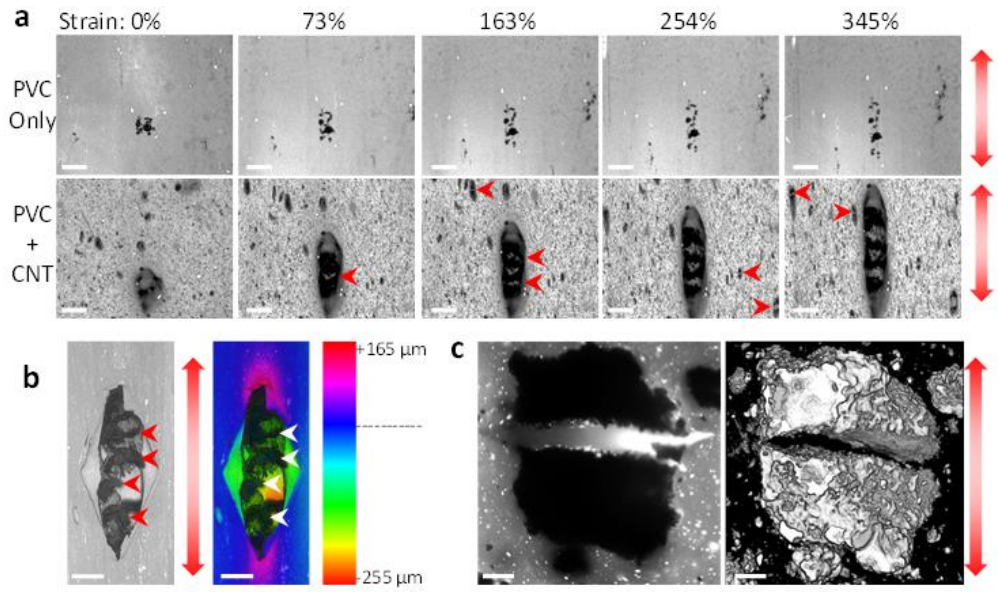

Figure 4.15. Failure mechanics of the composite material under tensile strain. (a) Maximum intensity projections of test samples with and without CNTs under increasing strain. Arrowheads show where new fractures have formed within the CNT bundles. Scale bar = 200 µm. Arrows show direction of tensile loading. (b) A 3D grayscale image and colorimetric surface profile of a large tear forming in a composite sample under tensile load, with a fractured CNT bundle clearly visible at the base of the tear (arrowhead). (c) A single optical section and 3D rendering of a fractured CNT bundle after tensile loading. Scale bar = 20 µm. Scale bar = 200 µm.

4.3.3.2. Dispersion and mechanical properties

Selected specimens were tested to examine the influence of dispersion quality on mechanical properties of the composite (Figure 4.16). The specimens were chosen using the data shown in Figure 4.11. Specimens exhibiting the highest electrical conductivity (i.e. PS/55/120) were compared against BM/150/65/20 as a representative of low-conductivity specimens. The specimen showing an abnormally-high conductivity among those prepared using the BM method (i.e. BM/150/100/20) was also tested to represent mediocre dispersion. In addition, specimens made of the pristine (i.e. no CNT) host matrix comprising of 75% PL and 25% PR were tested to obtain a baseline value for mechanical properties.

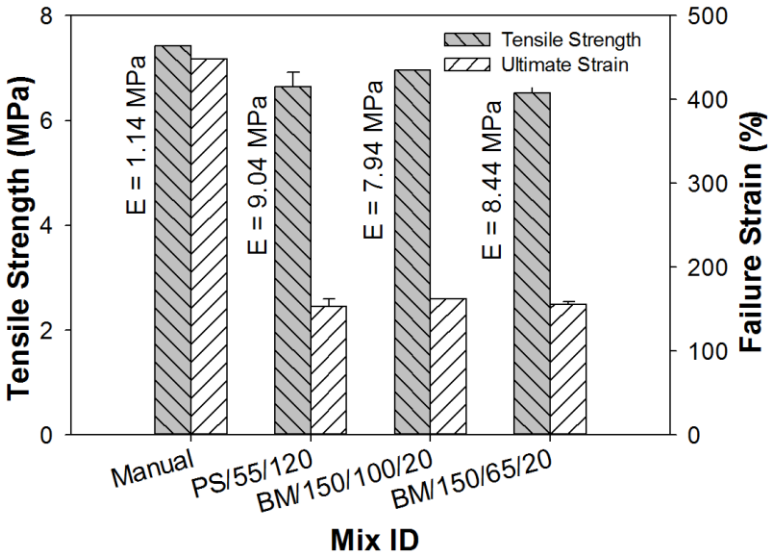

Figure 4.16. Influence of dispersion technique on the mechanical properties of the PVC composite. Note: manual refers to the pristine matrix.

According to Figure 4.16, the mean values of tensile strength, elastic modulus and failure strain for the pristine (i.e. no nanotube) specimens are 7.4 MPa, 1.14 MPa and 450%, respectively, which change in entirely different ways upon dispersing 0.5 wt.% MWCNT into the matrix. The tensile strength of the filled specimens with respect to dispersion quality

follows a reverse trend as compared to their electrical conductivity. The filler when well-dispersed into the matrix slightly enhances its tensile strength while postponing the percolation threshold. In contrast, a less-uniform dispersion of CNTs reduces the tensile strength of the pristine matrix at least for the concentration examined. The reduction in tensile strength in the latter case can be attributed to the formation of stress concentration zones at the polymer-CNT interface around CNT bundles promoting the failure of the composite (Song and Youn 2005; Blond *et al.* 2006).

The influence of MWCNT on the failure strain is found to be more significant. It can be seen in Figure 4.16 that the failure strain of the pristine matrix is significantly reduced when mixed with MWCNT regardless of the dispersion quality. However, a larger reduction is observed for less-uniformly-dispersed specimens. These observations can be explained by the fact that the bundles present in poorly-dispersed (less-uniformly-dispersed) specimens facilitate the formation of stress concentration zones and the initiation of nanocracks at the polymer-CNT interface promoting failure in the composite (Song and Youn 2005; Fathi *et al.* 2012). The crack initiation is primarily due to the weak interfacial bonding between the outermost layer of the MWCNTs and the polymer matrix which impedes a full stress transfer between the two solid phases at the nano-/microscale (Schadler *et al.* 1998; Allaoui *et al.* 2002; Kearns and Shambaugh 2002). Chemical functionalization of CNTs and covalent attachment of polymer chains can improve the dispersion quality and the CNT/polymer adhesion (Shanmugharaj *et al.* 2007; Koval'chuk *et al.* 2008). Apart from debonding at the CNT/polymer interface, the weak van der Waals forces between the individual graphene shells constituting MWCNTs allow them to slide over one another leading to so-called telescopic fracture, where MWCNTs are pulled out from the matrix due to the tensile stresses

at the tip of the cracks (Yu *et al.* 2000; Liu *et al.* 2004; Song and Youn 2005). A detailed description of the possible fracture mechanisms of CNTs in a polymer matrix can be found in a study by Gojny *et al.* (2005).

The elastic modulus values of the specimens are shown above their corresponding bars in Figure 4.16. It can be seen that incorporating 0.5 wt.% MWCNT into the matrix significantly increases its stiffness irrespective of the difference in the dispersion quality of the specimens. However, the specimens exhibiting higher conductivity (i.e. PS/55/120) are stiffer (possess larger elastic modulus values). This observation can be explained by the fact that the bundles in these specimens act as large particles as if a higher filler concentration were present. These bundles trap the polymer molecules in the interspace between themselves and cause the composite to behave as if it was mostly made from CNTs and had a lower polymer concentration (Song and Youn 2005).

The modified Halpin-Tsai model (Halpin Affdl and Kardos 1976) model was adopted to estimate the elastic modulus of MWCNT/PVC composites. Since the model assumes a perfect dispersion for the filler, the difference between the theoretically-predicted and experimentally-obtained elastic modulus values could be used as a measure for the dispersion quality in the composite. The model is commonly used to predict the elastic modulus of polymer composites reinforced with uniformly-dispersed fillers as a function of the constituent elements properties. It was originally proposed for aligned, short-fiber composites and adapted by Thostenson and Chou (2003) for nanotube reinforced composites. The modified model predicts the value of the composite modulus, E_c, as (Gojny *et al.* 2004):

$$\frac{E_c}{E_m} = \frac{3}{8}\left(\frac{1+\zeta\eta_L\varphi}{1-\eta_L\varphi}\right) + \frac{5}{8}\left(\frac{1+2\eta_T\varphi}{1-\eta_T\varphi}\right) \tag{4-6}$$

where E_m is the elastic modulus of the pristine matrix (1.14 MPa), $\zeta = 2l/d$, with l and d being the length (740 nm) and the mean outer diameter (7.8 nm) of the filler (MWCNT), φ is the filler volume fraction (0.32% – Equation (4-5)), and

$$\eta_L = \frac{E_f / E_m - \vartheta}{E_f / E_m + \zeta} \tag{4-7}$$

$$\eta_T = \frac{E_f / E_m - \vartheta}{E_f / E_m + 2\vartheta} \tag{4-8}$$

where E_f is the elastic modulus of MWCNTs (1 TPa Gojny *et al.* (2004)) and $\vartheta = d/4s$, with s being the shell separation (0.34 nm). Substituting these values into Equation (4-6) yields E_c = 5.4 MPa, which is well within the range of experimentally-obtained values shown in Figure 4.16. The results shown in Figures 4.11 and 4.16 indicate that comparative differences between the theoretical prediction of the elastic modulus and the measured values for composites made using different blending methods together with measured electrical conductivity values of the corresponding specimens can be used to correlate the quality of filler dispersion in a composite with its mechanical properties.

4.3.3.3. Influence of CNT concentration

A typical stress-strain diagram of the composite filled with 0.5 wt.% MWCNT is shown in Figure 4.17 which indicates an initial linear portion (demarcated by a proportional limit) followed by a strain hardening behavior. The yield point is assumed to approximately coincide with the proportional limit. The strain corresponding to the proportional limit (i.e. yield strain) was consistently observed in the tensile tests to be 36.5±1%, which is close to

the range of strains corresponding to the initiation of fractures inside the largest CNT bundles as observed under the microscope (i.e. 18–36%). In contrast, the 'no-CNT' specimens made from 75% PL and 25% PR yielded at a strain of 18±1%. This observation (i.e. advantageous effect of CNT in extending the proportional limit of polymers) is in agreement with the findings of previous studies (e.g. Tang *et al.* (2003)).

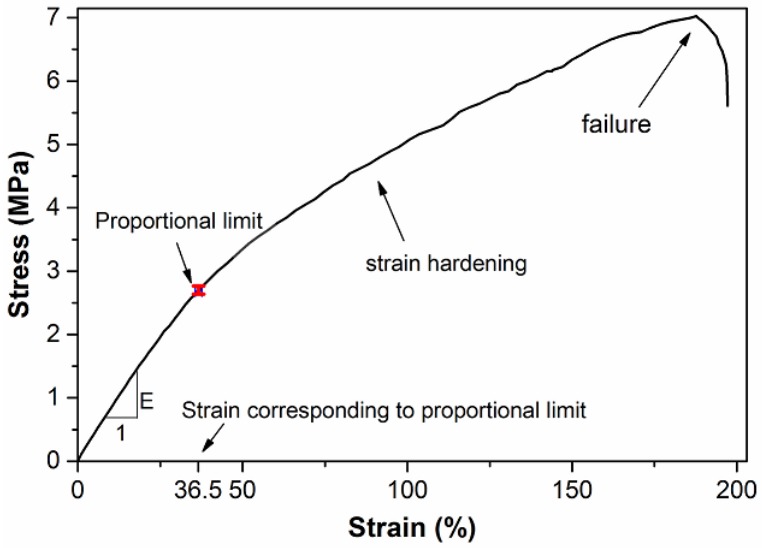

Figure 4.17. Typical stress-strain behavior of the composite filled with 0.5 wt.% MWCNT

The observed strain-hardening behavior observed in Figure 4.17 can be ascribed to the strain-induced alignment of polymer chains (Sarva and Boyce 2007). The stress-strain response of the composite shows that stretching the specimens to greater extents increased the stress nonlinearly until failure occurred. Localized necking was consistently observed as the macroscopic mode of failure of the specimens.

The influence of the plasticizer and the MWCNT concentration on the mechanical properties of the composite is shown in Figure 4.18. It is evident from Figure 4.18a that replacing 25% of the PVC plastisol (PL) with the plasticizer (PR) significantly decreases the

mean value of the tensile strength from 16.4 to 6.2 MPa (i.e. 62% reduction) while predictably allowing the composite to endure approximately 50% larger elongations before break. According to Figure 4.18a, the plasticizer only slightly decreased the elastic (Young's) modulus of the PVC plastisol but significantly reduced its Poisson's ratio. These observations are due to the reducing effect of the plasticizer on the physical intramolecular forces between the polymer chains, which in turn promotes the chain mobility and thereby reduces the tensile strength and increases the ductility and compressibility of the polymer (Stark *et al.* 2005).

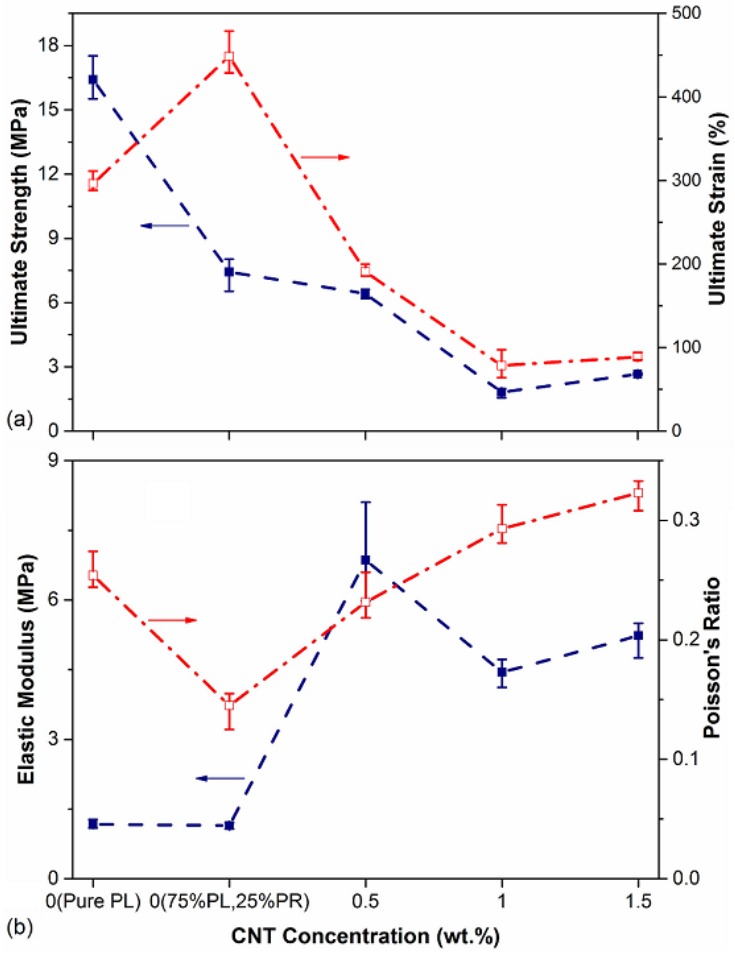

Figure 4.18. Influence of plasticizer and the CNT concentration on a) the tensile strength and ultimate strain and b) the elastic modulus and Poisson's ratio of the PVC composite (four samples were tested at each concentration shown)

With respect to the influence of the MWCNT on the mechanical properties of the PVC composite, Figure 4.18a shows that a composite with 0.5 wt.% MWCNT has a lower ultimate strength and failure strain as compared to an otherwise identical pristine (i.e. no-CNT) composite. Figure 4.18b, in contrast, indicates a five-fold increase in the tensile modulus and 59% increase in Poisson's ratio of the composite at 0.5 wt.% MWCNT as compared to those of the pristine samples. This contradictory dual function of MWCNTs in enhancing the tensile modulus of the composite while deteriorating its tensile strength has been reported in previous studies (Ogasawara *et al.* 2004; Bhattacharyya *et al.* 2005; Blond *et al.* 2006; Lahiff *et al.* 2006). The increase in the tensile modulus and yield strain of the composite could be due to the bridging function of MWCNTs between polymer chains which forms weak physical crosslinked networks that in turn reduce the failure strain of the composite (Xia *et al.* 2003).

According to Figure 4.18a, increasing the MWCNT concentration to 1 wt.% decreases the ultimate strength of the composite by 75% and its ultimate strain by 60% as compared to the values for the PL-PR matrix. It also results in 35% reduction in the elastic modulus and a 26% increase in the Poisson's ratio as compared to the 0.5%-MWCNT specimens (Figure 4.18b). The reduction in the mechanical properties of the composite at higher filler concentrations can be attributed to the CNT aggregation at higher loading levels which in turn results in the formation of stress concentration zones at the polymer-CNT interface leading to the premature failure of the composite (Song and Youn 2005; Blond *et al.* 2006). Increasing the MWCNT concentration to 1.5 wt.% only slightly changed the tensile modulus and ultimate strength and strain of the composite while its Poisson's ratio continued to increase. These observations can be explained by the fact that at this level of CNT

concentration (essentially one order of magnitude greater than the percolation threshold) the CNT aggregates trap the polymer molecules in the interspace between themselves and cause the composite to behave as if it was mostly made from CNTs and had a lower polymer concentration (Song and Youn 2005). For comparison, the mechanical properties of selected amorphous and semicrystalline polymers filled with MWCNTs are summarized in Table 4-5.

Table 4-5. Changes in mechanical properties of selected common polymers filled with MWCNT

Matrix	Aspect ratio	Dispersion	Concentration (wt. %)	Increase in composite tensile strength (%)	Increase in composite elastic modulus (%)	Source
PVC	NR[1]	Solution mixing	0.20	84	40	(Shi *et al.* 2007)
Epoxy	33–1,000	Solution mixing	0.50	62	54	(Špitalský *et al.* 2009)
Polyimide 12	NR	Melt extrusion fiber spinning	10.00	110	110	(Sandler *et al.* 2004)
Polystyrene	446–1 167	Sonication	1.00	25 25	36 42	(Qian *et al.* 2000)

[1] Not reported

It is noteworthy that the effectiveness of the CNT reinforcement in CNT-filled polymer composites could be enhanced by improving the stress transfer at the polymer-CNT interface. The extent of the stress transfer is governed by the interfacial adhesion between the CNT aggregates/particles and the polymer (Gojny *et al.* 2005), which is a function of the local polymer morphology at the polymer-CNT interface, and is maximized when the interfacial polymer forms a crystalline shell around CNTs (Cadek *et al.* 2002; Coleman *et al.* 2004). When the interfacial polymer remains amorphous, the weak van der Waals interactions at the polymer-CNT interface impede the complete stress transfer, hindering the full exploitation of the reinforcing function of CNTs (Bhattacharyya *et al.* 2005; Lahiff *et al.* 2006). Ensuring an effective stress transfer in MWCNTs with greater surface areas is even more challenging due to the difficulties associated with impregnating and dispersing mesoporous MWCNTs (Breton *et al.* 2004).

Figure 4.19 shows ultimate strength and failure (ultimate) strain values of MWCNT-filled composites as a function of strain rate at room temperature. Results show higher ultimate strength and lower failure strains for the specimens when tested at higher strain rates, which indicates a viscoelastic behavior. Strain-rate dependency is a common trait in the mechanical response of polymeric materials and could be explained by a reduction in the molecular mobility of the polymer at higher strain rates resulting in a more brittle behavior for the composite (Richeton *et al.* 2006; Sarva and Boyce 2007).

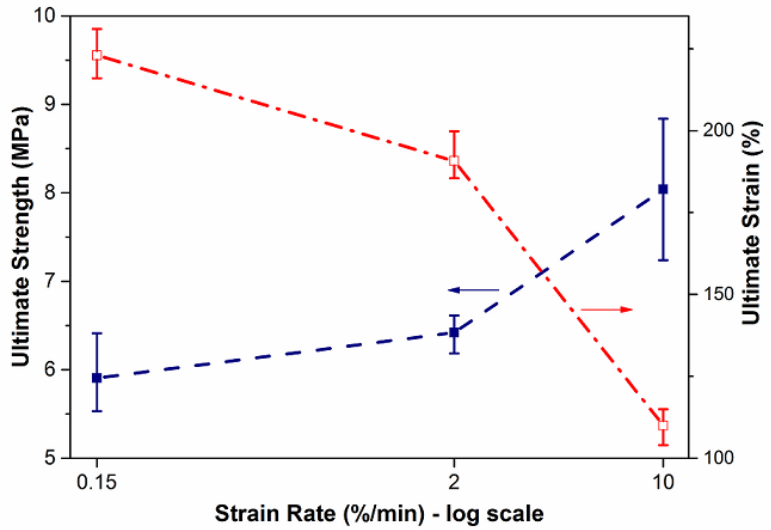

Figure 4.19. Influence of loading rate on the ultimate strength and strain of the composite (MWCNT = 0.5 wt.%)

4.3.4. Tensoresistivity response of the coating composite

From Figure 4.14, the critical concentration of the fillers was estimated to be 0.5 wt.% where a drastic strain-induced change in the electrical conductivity of the composite would be expected under tensile loading. Therefore, the specimens prepared for the strain sensitivity tests were doped at this concentration. It is worth noting that the tensoresistivity response of the CNT-filled composite is primarily due to increased gaps among the CNT aggregates with some minor contribution (e.g. on the order of 5%) from the tensoresistivity of the CNTs themselves (Oliva-Avilés *et al.* 2013).

Figure 4.20 shows the strain sensitivity of the coating specimens' electrical resistance (tensoresistivity) at different strain rates in normalized form ($\Delta R/R_0$) as a function of the applied tensile strain. The real-time changes in the resistivity of a test specimen under tensile strain in LSCM is also shown in Figure 4.21. The test results are approximated with linear regressions lines on the basis of Equation (3-3) resulting in gauge factors equal to 3.63, 3.17

and 2.51 for the strain rates 0.15, 2 and 10 %/min, respectively. The increase in resistivity could be in part attributed to the observed changes in the spatial distribution of CNT bundles and the progressive rupture of the CNT bundles as strain increased, resulting in a sequential loss of conductive pathways.

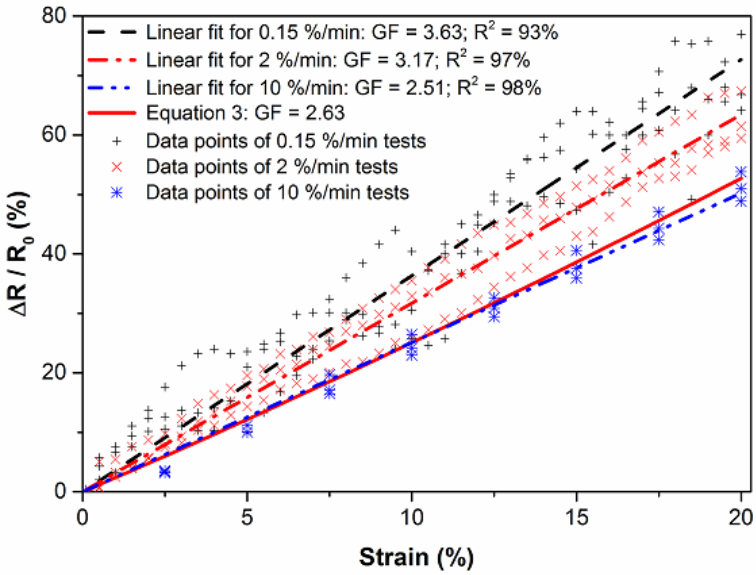

Figure 4.20. Strain-sensitivity response of the coating composite at the strain rates: a) 0.15%/min, b) 2%/min, and c) 10 %/min. Note: Data shown are for three specimens per strain rate.

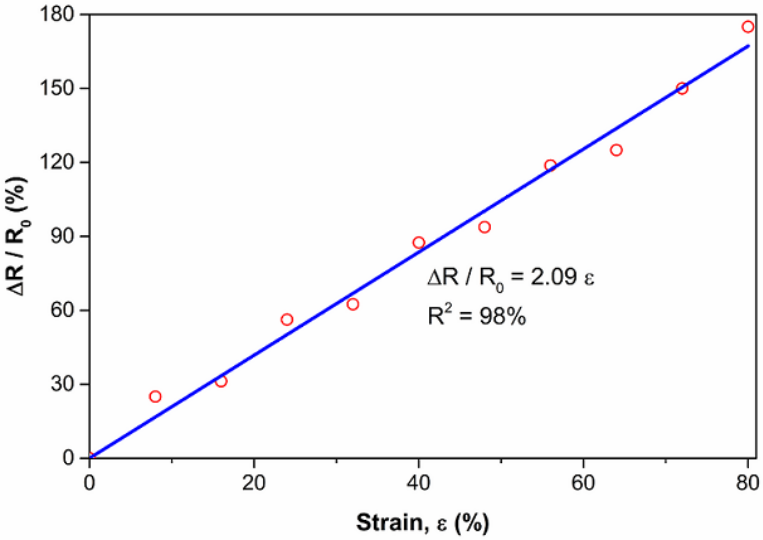

Figure 4.21. Strain sensitivity of a sample conductivity during imaging

Although the gauge factors are comparable to those obtained for CB-filled PVC composites (see Section 3.1.3.3), the composite studied here exhibited a considerably lower scatter in its strain sensitivity response, which is attributed to the fibrous geometry of CNTs as opposed to the agglomerated and generally bulkier structure of CBs. The *GF* values obtained are within the range of those for metal strain gauges (0.74–5.1 – Park *et al.* (2008)). For comparison, the *GF* values of some polymer composites filled with CB or MWCNT are summarized in Table 4-6. The significant *GF* values obtained for the MWCNT-filled PVC composites that were fabricated and tested in this study together with consistently high R^2 values for a wide range of strains (i.e. 20% in tensile testing and 80% in LSCM experiments) provide promising evidence for their strong potential in strain sensing and damage detection applications.

Table 4-6. Gauge factors reported for selected filled polymer composites

Matrix	Filler	Aspect ratio	Dispersion	Conc. (wt.%)	GF	Source
PVC plastisol	CB	NA[1]	Mechanical stirrer	1.50	3.2–4.6	Section 3.1.3.3
Epoxy vinyl ester	MWCNT	63–307	Mechanical stirrer and sonicator	0.30	2.6	(Ku-Herrera and Avilés 2012)
Polycarbonate	MWCNT	NR[2]	Injection molder	5.00	3.65–6.2	(Parmar *et al.* 2013)
Bisphenol-F epoxy	MWCNT	100	Planetary mixer	1.00	23	(Hu *et al.* 2010)
Polyethylene oxide	MWCNT	50–500	Magnetic stirrer and sonicator	0.90–2.50	3.7	(Park *et al.* 2008)
Poly(methyl methacrylate)	MWCNT	50–8,300	Mechanical stirrer and sonicator	1.00	15	(Pham *et al.* 2008)

[1] Not applicable; [2] Not reported

Greater tensoresistivity of the coating composite at slower loading rates as observed in Figure 4.20 suggests that stress relaxation (which is greater at slower rates) is more able to disrupt CNT-CNT interactions vs. a more affine deformation corresponding to a faster rate. This is also evident from the lower gauge factor of 2.09 obtained in the real-time microscopic tests, where deformation was applied incrementally and at a fast rate.

It is worth mentioning that the piezoresistive/tensoresistive response (gauge factor) of a material is made of an intrinsic component, $\Delta\varrho/\varepsilon\varrho$, caused by an increase in the tunneling resistances, and a geometric component, $1 + 2\nu$, where ν is the Poisson's ratio of the material (Costa *et al.* 2014). For the composite filled with 0.5 wt.% MWCNT, since the mean value of ν is 0.23 (Figure 4.18), the contribution of the geometrical effect to its *GF* value is 1.46. Therefore, the predominant component of the composite tensoresistivity response shifts from the intrinsic component for the specimens tested at slower rates to the geometric component for those tested at faster rates.

The tensoresistivity of MWCNT composites can be predicted using the method proposed by Park *et al.* (2008). The method predicts the electrical conductivity of a specimen, σ_s, subjected to a uniaxial strain of ε_x as:

$$\sigma_s = \sigma_0 \left(\frac{\varphi}{e+1} - (e+1)\varphi_c \right)^t \tag{4-9}$$

where σ_0, φ and φ_c are the same as those defined in Equation (4-3) and e is the volumetric strain of the specimen defined as:

$$e = (1+\varepsilon_x)(1-\nu_{xy}\varepsilon_x)(1-\nu_{xz}\varepsilon_x) - 1 \tag{4-10}$$

where ν_{xy} and ν_{xz} are the Poisson's ratios determined from the ratio of the strains in the transverse directions (y and z directions), respectively, to the strain in the axial direction (x direction) due to axial loading in x direction. Assuming the composite is isotropic, ν_{xy} and ν_{xz} are the same and equal to 0.23 (Figure 4.18). Substituting the required values into Equations 3 and 4 yields a *GF* value of 2.63 (the solid line in Figure 4.20), which is well within the *GF* values obtained in experiments.

4.4. Conclusions

The influences of dispersion quality and processing conditions on the electrical and mechanical properties of multi-walled carbon nanotube-filled polyvinyl chloride (MWCNT/PVC) composites were studied. Four different mixing methods (i.e. probe sonication, bath sonication, mechanical stirring and batch mixing) were used to make the composites, and their comparative efficacy to form adequately well-dispersed MWCNT/PVC composites was examined. Subsurface dispersion in the samples was quantified using laser scanning confocal microscopy along with scanning electron microscopy, indicating that MWCNT bundle volumes resulting from all dispersion methods had a log-normal distribution. Differences in the quality of dispersion between different mixing methods were evaluated using the Kolmogorov-Smirnov D-statistic in order to determine which mixing method(s) result in comparable dispersion of the MWCNT bundles in the samples. Electrical conductivity and mechanical properties of the composite samples that were made using different dispersion methods were also measured.

Results indicated that composite samples using an optimum combination of power and duration in the probe sonication method yielded the lowest percolation threshold with the

highest overall electrical conductivity and statistical consistency among all of the methods examined. The percolation curve for this composite was established and a scaling law (power law) was fit to the curve, yielding a critical exponent of 1.81. The curing (vulcanization) time required in compression molding was estimated using the Stokes-Einstein equation and experimentally validated through investigating the curing time vs. the electrical conductivity of the composite. The optimum curing time for compression molding of the resulting composite was found within the range between 10 and 15 minutes, beyond which the electrical conductivity of the composite did not improve.

Mechanical properties and tensoresistivity of a PVC/MWCNT composite subjected to tensile loading were also studied at different strain rates. Mechanical response of the composite was found to be linear at low strains leading to a strain hardening behavior at larger strains. It was found that on average, composite samples with 0.5 wt.% MWCNT concentration resulted in a 57% reduction in the ultimate (failure) strain and a five-fold increase in their tensile modulus when compared to otherwise identical pristine PL-PR samples. The failure mechanism of the composite was microscopically observed using LSCM to be initiated from inside the largest CNT bundles, followed by smaller bundles and debonding at CNT/polymer interfaces. The gauge factors for the tensoresistivity response of the composite samples were found to have a fairly low scatter and comparable to those of commercially available strain gauges over a large range of strains which is practically significant (i.e. $\varepsilon \leq 20\%$).

CHAPTER 5. MONTE CARLO SIMULATION OF THE PERCOLATION BEHAVIOR OF FILLED COMPOSITES

5.1. Introduction

Monte Carlo (MC) simulations have extensity been used to predict the percolation behavior and electrical conductivity of filled nanocomposites. However, as previously stated in Section 2.2.2.1, no study has taken into account the uncertainties in the degree of curviness of carbon nanotubes (CNTs) and the size of carbon black (CB) particles. This chapter is allocated to investigating the influence of these parameters on the percolation threshold of filled nanocomposites using MC simulations.

The curviness of CNTs arises during mixing. Conventional fabrication methods of CNT-filled polymer composites usually involve dispersing as-produced CNTs into a polymer matrix using a mixing method. Comparing the estimates of interCNT binding forces and the shear forces produced during mixing suggests that the complete separation of CNTs is only achieved at sufficiently-high shear energy densities (Huang and Terentjev 2012). This energy input has been experimentally shown to introduce tensile and shear stresses to CNT bundles and individuals, subjecting them to an undesirable successive CNT scission (Kerr *et al.* 2011). This mixing-induced tube scission is particularly prone to occur in sonicated samples (Huang *et al.* 2009). The filler is subject to further breakage if the sample is cured using compression-molding. In another scenario, the stress applied on a particular CNT might not be sufficient

to break it but could alter its shape into a curved CNT with its dominant point (local maximum curvature point) located near the middle (Ma and Gao 2008). This discussion indicates that the aspect ratio and shape of as-produced CNTs will undergo significant change during different stages of fabrication. The influence of these changes on the percolation behavior of CNTs is discissed in this chapter.

5.2. Mathematical models

5.2.1. CB model

Consider a random distribution of CBs represented by disk-shaped objects generated in a frame of dimensions $L_x \times L_y$. The coordinates of center of the ith CB in the 2D space, (x_i, y_i), is described as:

$$\begin{aligned} x_i &= rand \times L_x \\ y_i &= rand \times L_y \end{aligned} \tag{5-1}$$

where *rand* denotes a floating point, uniformly-distributed random number in the interval [0, 1]. In case a randomly-inserted CB falls partially outside the frame, periodic boundary conditions (Section 1.4.2.3) were applied where its mirror image was inserted onto the opposite side of the frame, simulating an infinite system with randomly-dispersed CBs.

5.2.2. CNT model

Consider a random distribution of CNTs generated in a representative frame of dimensions $L_x \times L_y$. As shown in Figure 5.1, each curved CNT in the model was approximately represented by two line segments intersecting at the dominant point, *O*. The coordinates of

the dominant point of the ith CNT in the 2D space, (x_i,y_i), was described using Equation (5-1). The segments of a particular CNT are not always identical as the dominant point might not necessarily be located in the middle. Therefore, how the dominant point divides a CNT into two segments was also considered random. For a CNT of length l, the lengths of the segments are given by:

$$\begin{aligned} l_1 &= rand \times l \\ l_2 &= (1 - rand) \times l \end{aligned} \tag{5-2}$$

Since the CNT particles are stochastically sheared during sonication, a log-normal distribution was assumed for the CNT's aspect ratio (Kolmogoroff 1969), and their lengths were then determined as per a given deterministic diameter. The orientation of the CNTs in the 2D space with respect to the x-axis, θ, and the angle between its segments, φ, were also considered random: θ_i is uniformly-distributed in the interval [0, 2π], whereas φ_i has a normal distribution. The coefficients of variation (i.e. the ratio of the standard deviation to the mean) for all normally-distributed variables were assumed to be 5%. The dimensions of the representative frame were set at unity. The variables required to define the location, size and shape of a "broken" CNT and their corresponding values used here are summarized in Table 5-1.

It should be noted that the end points of the ith CNT might be situated outside the representative frame. In this case, periodic boundary conditions (Section 1.4.2.3) were applied to simulate an infinite system with randomly-dispersed CNTs.

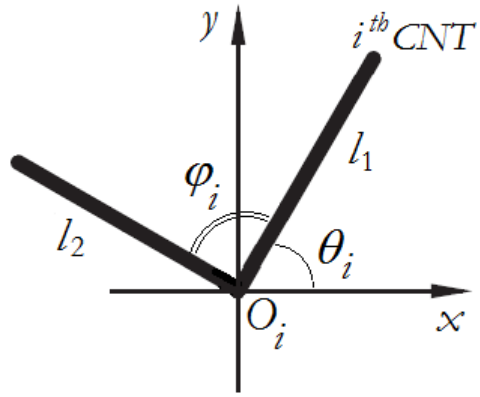

Figure 5.1. Configuration of the ith CNT

Table 5-1. Probability density function and corresponding parameters and values for the CNT model variables

Variable	PDF	Interval	Mean[1]
x_i	uniform	[0, 1]	–
y_i	uniform	[0, 1]	–
aspect ratio	log-normal	–	20:20:200
θ	uniform	[0, 2π]	–
φ	normal	–	90:30::180

[1]Standard deviation is 5% of the corresponding mean value (i.e. COV = 0.05)

5.2.3. Connection criteria

The hard-core soft-shell continuum percolation model (see Section 2.2.2.1) was adopted to define the condition under which two neighboring particles can be considered to be in electrical contact. Proposed by Wang and Ogale (1993), the model is comprised of a semi-penetrable soft shell of thickness δ and an impermeable hard core of diameter (d - 2δ) (Figure 2.5). The impenetrable hard core represents the actual physical inclusion thickened by the repulsive part of the van der Waals interatomic interactions that governs the proximity of neighbors by hampering local atomic rearrangements. The permeable soft shell, in contrast, represents the effective range for electron transfer in fillers and its thickness, δ, is approximately equal to one half of the tunneling distance, for which a range of values from

14 Å to 25 Å has been reported in the literature (Li *et al.* 2007a; Bao *et al.* 2012; Oskouyi *et al.* 2014). It should be noted that the shell thickness is a function of not only the filler type, but also the host matrix (Belashi 2011). As described later, the interfacial polarization effect, which is greatly influenced by the molecular and ionic processes in the insulating matrix, has a sizeable impact on the tunneling distance.

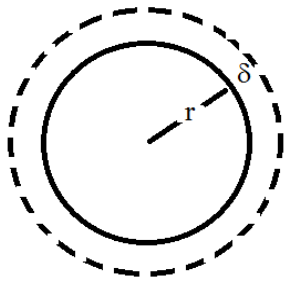

Figure 5.2. Schematic representation of the hard-core soft-shell continuum model

The discussion above indicates that whether two neighboring particles can be considered in electric contact depends on their minimum distance versus the maximum length for effective electron hopping. The approaches proposed by Ma and Gao (2008) and Belashi (2011) were adopted here to calculate the minimum distance of neighboring particles. The following sections provide further details about the approaches.

5.2.3.1. CB-filled composites

CBs were assumed to be spherical and, therefore, represented by circular objects in a 2D frame. The minimum distance between the centers of two i^{th} and j^{th} circles, d_{ij}, can easily be calculated as:

$$d_{ij} = \sqrt{(x_i - x_j)^2 + (y_i - y_j)^2} \tag{5-3}$$

The shell thickness of each object was considered to be a fraction of its diameter. The two circles were considered to be in electric contact if $(D_i/2 + D_j/2) \leq d_{ij} \leq (D_i/2 + \delta_i + D_j/2 + \delta_j)$, where D is diameter. $(D_i/2 + D_j/2) > d_{ij}$ is impossible as the cores were not allowed to overlap (Belashi 2011).

5.2.3.2. CNT-filled composites

Consider the CNT shown in Figure 5.1. For such an arm-shaped fiber, the coordinates (x, y) of any point on the right and left arms can be given in a vector-parametric form, respectively, by:

$$\begin{Bmatrix} x \\ y \end{Bmatrix} = \begin{Bmatrix} x_i \\ y_i \end{Bmatrix} + s_i \begin{Bmatrix} \cos\theta_i \\ \sin\theta_i \end{Bmatrix} \tag{5-4}$$

$$\begin{Bmatrix} x \\ y \end{Bmatrix} = \begin{Bmatrix} x_i \\ y_i \end{Bmatrix} + t_i \begin{Bmatrix} \cos(\theta_i + \varphi_i) \\ \sin(\theta_i + \varphi_i) \end{Bmatrix} \tag{5-5}$$

where $s(\in [0,l_1])$ and $t(\in [0,l_2])$ are the distances to the points of interest on the right and left arms. The unit vectors corresponding to each of the arms can be represented by:

$$\begin{Bmatrix} \mathbf{e}_r^i \\ \mathbf{e}_l^i \end{Bmatrix} = \begin{Bmatrix} \cos\theta\,\vec{\mathbf{i}} + \sin\theta\,\vec{\mathbf{j}} \\ \cos(\theta+\varphi)\,\vec{\mathbf{i}} + \sin(\theta+\varphi)\,\vec{\mathbf{j}} \end{Bmatrix} \tag{5-6}$$

where **i** and **j** are the unit vectors in the x and y directions.

Let P_i and P_j represent the dominant points of the ith and j^{th} CNTs, and $\mathbf{u}_i$ and $\mathbf{u}_j$ be the unit vectors corresponding to two points located on the ith and j^{th} CNTs. Also, let $\mathbf{n} = \mathbf{u}_i \times \mathbf{u}_j$ be a vector perpendicular to both lines. The norm of the projection of vector P_iP_j over **n** will give the minimum distance D as (Gilles 2006):

$$D = \frac{\left| \overrightarrow{P_i P_j} \cdot \vec{n} \right|}{\|\vec{n}\|} \tag{5-7}$$

Ogale and Wang (1993) introduced two additional contact mechanisms known as end-to-end and end-to-body connections (Figure 5.3). However, the Ma and Gao (2008) showed that the relative contribution of the three mechanisms to the formation of conductive paths depends on the aspect ratio of CNTs, and for aspect ratios greater than approximately 24, the combined contribution of the end-to-end and end-to-body mechanisms can be considered negligible. Since the aspect ratios studied here are in the range 20 to 200 (see Table 5-1), only the body-to-body contact mechanism was considered in percolation assessment.

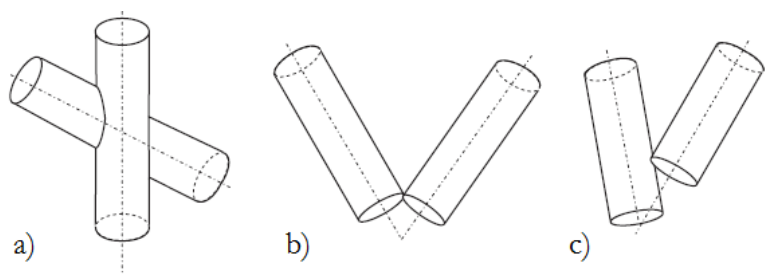

Figure 5.3. Fiber contact mechanisms: a) body-to-body, b) end-to-end and c) end-to-body (after Ma and Gao (2008))

5.3. Simulation procedure

Periodic boundary conditions were applied in all directions in order to mimic infinite-size systems. A simulation procedure as described below was followed.

The information of each CNT is stored in a 3D matrix during the simulations. The rows of the matrix represent clusters (bundles) while the columns contain the ID of the CNTs belonging to a particular cluster. For each particle, the third dimension of the matrix stores

the positional and geometrical information of each CNT. For a given diameter, particles are inserted one at a time randomly into a unit square (Figure 5.4). To this end, the first CNT is added onto the square frame. Since no cluster has so far been formed, this CNT is assigned to the first cell of the matrix. The next CNT is randomly inserted onto the frame and its and its images' (e.g. Particles #8 and #16 in Figure 5.4) distances with respect to all the previously-inserted particles were calculated. If these calculations indicate that the new CNT or any of its images overlap with the first particle, it is rejected and replaced with another CNT. This process continues until an available spot is found for the new particle.

The same procedure was followed to situate the next particles. After each insertion, the distances between the cores of the just-inserted particle and its images and that of the existing particles is calculated and checked against the tunneling distance. If the neighboring particles are found adequately close (i.e. distance ≤ tunneling distance), they are considered to be in electric contact and therefore assigned to the same cluster (see Figure 5.5 to Figure 5.7). Finally, the minimum *x*-coordinate (*y*-coordinate) available in the updated cluster in checked against its maximum counterpart. If they are found far enough to span two opposite sides (left and right or up and down) of the frame, the cluster is considered to have percolated, the simulation is terminated and the particle percentage at percolation is computed.

The insertion of Particles #16 and #20 are of particular interest in Figure 5.4. Particle #16 is in electric contact with Particle #9 and therefore belong to a cluster on the left side of the frame. However, because this particle falls partly outside the frame, a mirror image of the section that is sticking out is inserted onto the opposite side of the box, touching Particle #13. Therefore, Particle #16 acts as a link between two previously-isolated clusters (Figure

5.6). Finally, the insertion of Particle #20 results in the formation of a larger cluster that spans two opposite sides of the frame, allowing percolation to happen.

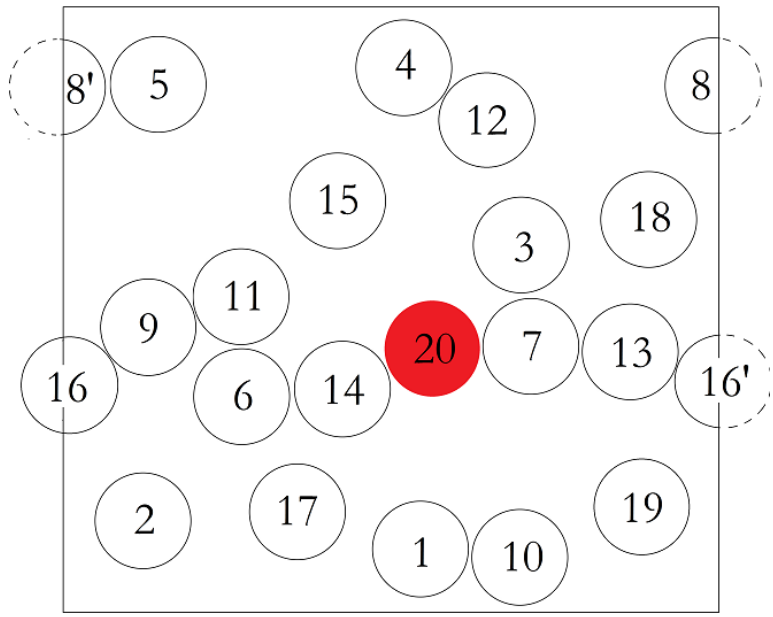

Figure 5.4. Graphical representation of percolation simulated by the MC algorithm

$$\begin{bmatrix} 1 & 10 & & \\ 2 & & & \\ 3 & 7 & 13 & \\ 4 & 12 & & \\ 5 & 8 & & \\ 6 & 9 & 11 & 14 \\ 15 & & & \end{bmatrix}$$

Figure 5.5. Clusters' information matrix before the insertion of Particle #16 in Figure 5.4

$$\begin{bmatrix} 1 & 10 & & & & & & \\ 2 & & & & & & & \\ 3 & 6 & 7 & 9 & 11 & 13 & 14 & 16 \\ 4 & 12 & & & & & & \\ 5 & 8 & & & & & & \\ 15 & & & & & & & \end{bmatrix}$$

Figure 5.6. Clusters' information matrix just after the insertion of Particle #16 in Figure 5.4

$$\begin{bmatrix} 1 & 10 & & & & & & & \\ 2 & & & & & & & & \\ 3 & 6 & 7 & 9 & 11 & 13 & 14 & 16 & 20 \\ 4 & 12 & & & & & & & \\ 5 & 8 & & & & & & & \\ 15 & & & & & & & & \\ 17 & & & & & & & & \\ 18 & & & & & & & & \\ 19 & & & & & & & & \end{bmatrix}$$

Figure 5.7. Clusters' information matrix at percolation (after the insertion of Particle #20 in Figure 5.4)

There is a possibility that the simulation algorithm is trapped in a loop when situating a particle in the simulation frame. This is particularly likely when the frame contains isolated clusters each comprising of uniformly-dispersed, densely-packed particles. To avoid this, a maximum number of 10,000 iterations was imposed. If this number is exhausted (i.e. the number of attempts to find an available spot for a new particle exceeds the limit), the simulation will be terminated and its results will be ignored, the frame will be erased and a substitute simulation will be launched.

The statistical measures of the percolation threshold for a model were obtained as a function of simulation runs in order to determine the minimum number of iterations required to reach

equilibrium, where the difference between two consecutive states is less than a limit referred to as convergence rate. The convergence rate was set to 4% in this study.

The results for a model containing CNTs with a diameter of $0.01L_x$, r/δ of 100 and mean values of 100 and 120° for aspect ratio and φ are shown in Figure 5.8. As evident from the results, the statistical metrics of the percolation threshold of the model remain almost unchanged for simulation runs greater than 450. Consequently, 500 simulations were carried out for each set of diameter, r/δ, aspect ratio, θ and φ.

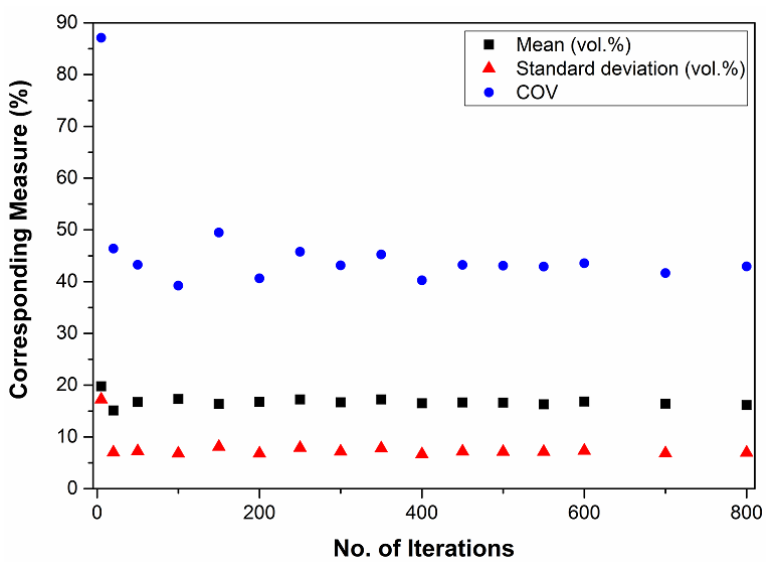

Figure 5.8. Mean, standard deviation and COV of the percolation threshold of a model as a function of simulation runs. Note: the model contains CNTs with a diameter of $0.01Lx$, r/δ of 100 and mean values of 100 and 120° for aspect ratio and φ.

5.4. Results and discussion

A sample graphical representation of the percolation of CB-filled frames is shown in Figure 5.9. The actual inclusions (hard cores) are represented by thick inner circles, while the outer thin red circles represent the perimeters for the soft shells. It can be seen that the mirror images of the circles falling partially outside the frame have been inserted onto the opposite

side of the frame in order to maintain periodic boundary conditions (e.g. Particle #22). The last particle inserted onto the frame, shown by a thick red circle (Particle #49), has conjoined two large clusters represented by black and purple circles, forming a larger cluster spanning the frame and making percolation to occur.

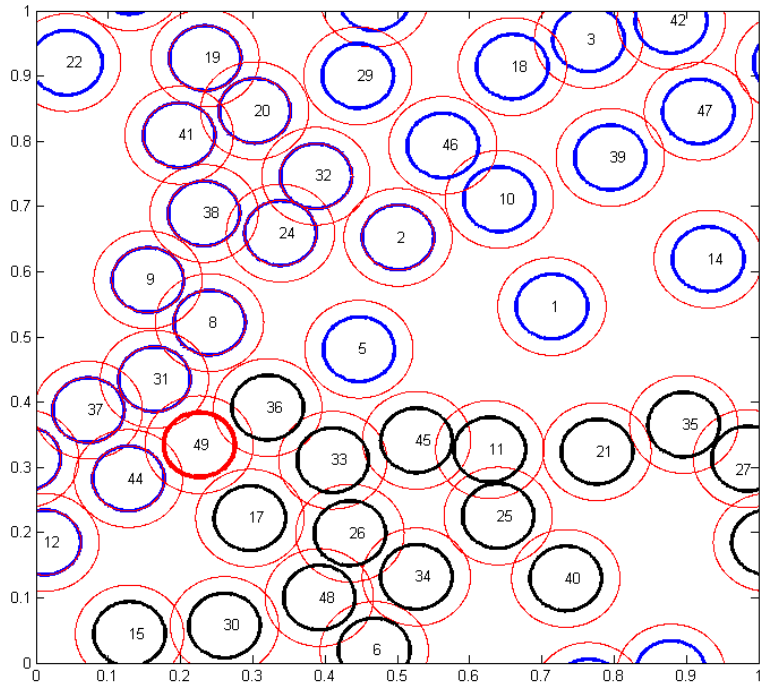

Figure 5.9. Sample graphical representation of the percolation of CB-filled frames. Note: CBs' diameter = 0.05Lx and $r/\delta = 2$.

The influence of shell thickness on the predicted percolation behavior of CB-filled composites for different L/r ratios is shown in Figure 5.10. The reason why the influence of particle size on the percolation threshold should be considered is because the mean interparticle distance decreases proportionally with decreasing particle diameter (Jing *et al.* 2000). Expectedly, the results indicate a significant increase in the predicted percolation threshold over the course of reducing the shell thickness from a value comparable to the radius of the filler to only a fraction of that (i.e. $\delta = 0.2r$).

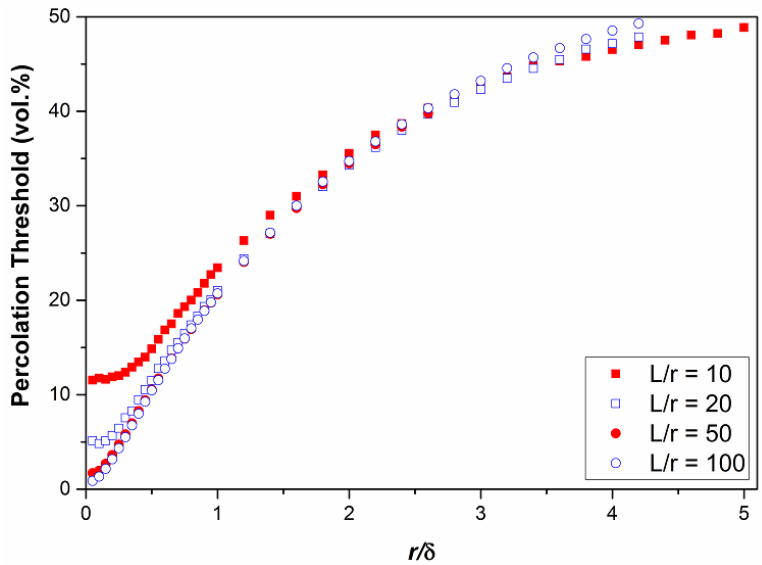

Figure 5.10. Percolation threshold prediction for CB-filled composites with different CB radii and shell thicknesses. Note: a mean COV of 25% was observed for 500 simulations that were carried out for each combination of L/r and r/δ.

Although the percolation thresholds in this study are reported in volume percentage units, in the laboratory, it is more customary to measure the quantities of the ingredients of a composite and its percolation threshold by weight. The volume percentages obtained in this study, ϕ, can readily be converted to their weight equivalents, χ, using the rule of mixture for two-phase composites (Chung *et al.* 1982):

$$\chi = \frac{\gamma_{\text{filler}}}{\gamma_{\text{comp}}}\phi \tag{5-8}$$

and

$$\gamma_{\text{comp}} = \phi\gamma_{\text{filler}} + (1-\phi)\gamma_{\text{polymer}} \tag{5-9}$$

where γ_{filler}, γ_{polymer} and γ_{comp} are the densities of the filler, polymer matrix and composite, respectively. The density of PVC is between 1.38 g/cc (Chung *et al.* 1982; Meier and Struik

1998) to 1.523 g/cc (Hirvi and Pakkanen 2006) and that for carbon black is 1.80 ± 0.05 g/cc, depending on the perfection of its crystallites (Chung *et al.* 1982).

Prediction of the electrical conductivity of the simulated composites is not the objective of this study. One could use the approaches used in this study together with a proper electron transport theory (e.g. see Bao *et al.* (2012)) to predict conductivity.

It is worth noting that numerous studies have consistently shown a drastic reduction in the resistivity of a composite upon incorporating more conductive fillers to it (see Section 1.3.3 for further details). There is a large degree of consensus among these studies as to how different mechanisms contribute to the conductivity of a composite as filler concentration increases. Chung *et al.* (1982) explains the conductivity mechanism as follows.

When the filler concentration is below the percolation threshold, the conductivity between filler particles is primarily due to the interfacial polarization effect. In this mode of conduction, the electron transport remains strongly coupled with the molecular and ionic processes in the insulating matrix (e.g. PVC). When the loading approaches the percolation threshold, the conducting phase (i.e. the filler) becomes connected and the hopping and tunneling mechanisms become more significant, thus enhancing conductivity in an exponential manner. If the loading exceeds the percolation threshold, the distribution of the gaps between the particles is governed by the interparticle interaction (cohesion by the continuous matrix phase and particle-particle repulsions) and is not expected to undergo a further considerable reduction. In this state, the tunneling gaps reach a critical value, and the additional conductive particles will merely supplement the already-established conductive paths or form new ones. The development of the conductive network will in turn result in a

slight increase in the conductivity of the composite. Eventually, the conductivity of the composite plateaus to a value fairly close to that for the filler, and the composite behaves as if it is a single-phase material (Chung *et al.* 1982).

A sample graphical representation of the percolation of CNT-filled frames is shown in Figure 5.11. The sticks represent the actual inclusions. It can be seen that the mirror images of the sticks falling partially outside the frame have been inserted onto the opposite side of the frame in order to maintain periodic boundary conditions. The last CNT inserted onto the frame, shown by thick, black lines, has bridged two large clusters, forming a larger series of CNTs spanning the frame and making percolation to occur.

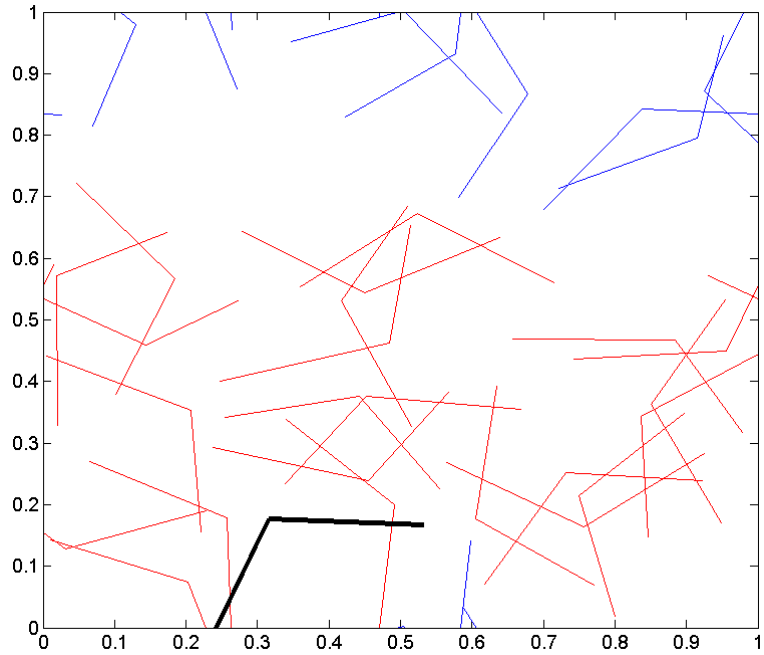

Figure 5.11. Sample graphical representation of the percolation of CNT-filled frames. Note: CNTs' diameter = $0.01L_x$, $r/\delta = 5$, and mean values of 40 and 120° for aspect ratio and φ.

The influences of aspect ratio and φ on the predicted percolation behavior of CNT-filled composites for different r/δ ratios are shown in Figure 5.12. The results indicate a significant reduction in the predicted percolation threshold by increasing aspect ratio. This reduction occurs approximately in the same rate regardless of the break angle, φ, of the CNTs. However, as the break angle more widens and approaches to that for intact CNTs (i.e. φ = 180°), the formation of an interconnected network is accelerated, reducing the percolation threshold. The results also indicate that, compared to aspect ratio, the influence of shell thickness on the percolation threshold is less pronounced. However, this observation, which is at odds with that made for CB, is influenced by the relatively large COVs (in the range 26% to 52%) computed for CNT models. If these large COVs, which are opted to be left out from Figure 5.12, are considered, one would see the reducing effect of shell thickness on the percolation threshold.

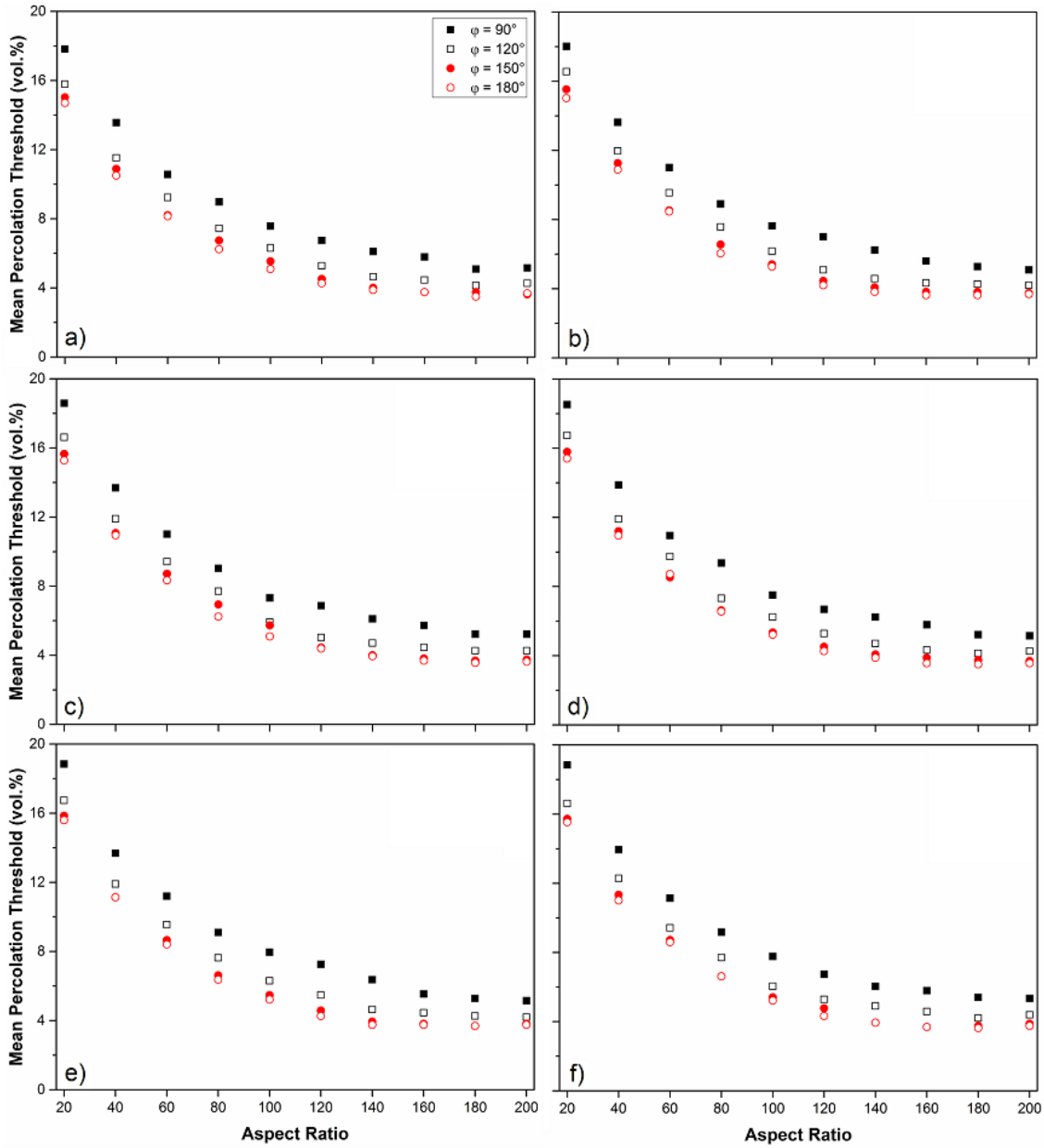

Figure 5.12. Percolation threshold prediction for CNTs with r/δ = a) 5, b) 7, c) 9, d) 11, e) 13 and f) 15. Note: a range of 26% to 52% and a mean value of 41% were observed for the COV of 500 simulations that were carried out for each combination of aspect ratio and r/δ.

5.5. Conclusions

The influences of aspect ratio, distortion, effective electron transfer range and size on the predicted percolation behavior of CB- and CNT-filled composites was investigated. The

results consistently and expectedly showed that increasing the effective electron transfer range will facilitate the formation of a conductive network in a model, lowering its percolation threshold. It was also seen that mixing-induced distortion of CNTs tends to increase their percolation threshold, so does increasing the particle size.

CHAPTER 6. MOLECULAR DYNAMICS SIMULATION OF NANOCARBONS AND FILLED POLYMER COMPOSITES

This chapter reports the molecular dynamics (MD) simulations that were carried out as complementary to the laboratory studies in order to promote our understanding on the mechanical behavior of common nanocarbons and the polymers conventionally used in the geosynthetics industry. Specifically, the focus is on graphene and carbon nanotubes as increasingly-popular fillers and polyvinyl chloride (PVC) and polyethylene (PE) as principal polymers in the production of geogrids.

Section 6.1 presents the development of a failure criterion for graphene in two-dimensional loading. The findings corresponding to this section can help to improve the design, reliability and functionality of the nanoscale devices made from graphene and provide a fairly simple computational tool to study the mechanical response of graphene to tensile loading. The majority of this section has recently been published in the journal *Modelling and Simulation in Materials Science and Engineering* (Yazdani and Hatami 2015).

A comprehensive study on the tensile and compressive mechanical properties of CNTs is reported in Section 6.2, and Sections 6.3 and 6.4 present MD simulations on PE and PVC polymers and composites.

6.1. Failure criterion for graphene in biaxial loading

6.1.1. Introduction

Graphene is a monatomic thick sheet of sp^2-hybridized carbon (Figure 1.1). Its extended hexagonal lattice is the motif of carbon allotropes (i.e. fullerenes (0-D – Figure 1.1), nanotubes (1-D – Figure 1.3) and graphite (3-D – Figure 1.2)). Since its discovery (Novoselov *et al.* 2004) (or more accurately, isolation), graphene has allured academic and industrial interest owing to its exceptional electronic (Fernández-Rossier *et al.* 2007), optical (Mak *et al.* 2008), thermal (Zhang *et al.* 2014) and mechanical properties. As a lightweight material but the strongest and stiffest ever known in the universe (Geim 2009), graphene holds promise as a reinforcing agent for composite materials (Koratkar 2013). In addition, the unique attribute of graphene in generating enormous strain-induced pseudo-magnetic fields opens the door for its application in nanoelectromechanical systems (Levy *et al.* 2010).

The exceptional mechanical properties of graphene have been consistently corroborated via first-principles (i.e. *ab initio*) calculations, semiempirical methods, laboratory experiments and numerical simulations. By means of first-principles calculations, Konstantinova *et al.* (2006) reported a Young's modulus of 1.24 ± 0.01 TPa for graphene. Using the density functional perturbation theory, Liu *et al.* (2007) calculated the graphene's Young's modulus and Poisson's ratio as 1.05 TPa and 0.186, respectively. They also reported strengths of 121 and 110 GPa in the zigzag (ZZ) and armchair (AC) directions for graphene. In addition, by nanoindenting the center of a free-standing graphene membrane in an atomic force microscope, Lee *et al.* (2008) measured the strength and Young's modulus of graphene to be

130 ± 10 GPa and 1 TPa, respectively (the corresponding values for the structural steel are 0.36 GPa and 0.21 TPa, respectively).

Due to its exceedingly small dimensions, it is challenging to pinpoint the properties of graphene via laboratory experiments. First-principles calculations are also computationally intensive. Alternatively, experimentally validated MD simulations have provided researchers with a virtual laboratory to probe the what-if scenarios that would otherwise be difficult (if not impossible) to investigate in the laboratory. MD simulations have shown that graphene exhibits an orthotropic behavior with different ultimate strength values along the zigzag and armchair directions (Zhao *et al.* 2009). MD simulations have also demonstrated that the mechanical response of graphene nanoribbons (GNRs) is nonlinear elastic and their size and chirality have significant influences on their mechanical properties (Zhao *et al.* 2009). It has been reported that 8 nm constitutes a critical width for GNRs beyond which the size effect largely disappears and their elastic properties converge to the values for bulk/infinite graphene (Zhao *et al.* 2009; Lu *et al.* 2011). In addition, MD simulations have shown that while the Young's modulus of graphene remains fairly insensitive to the temperature up to 1200 K, the values of its failure strength and strain undergo a steady fall as temperature is increased from the absolute zero (Zhao and Aluru 2010; Dewapriya *et al.* 2013).

In spite of a fairly considerable number of MD studies on the mechanical properties of graphene, to the best of the authors' knowledge, the behavior of graphene in biaxial loading has been the subject of only a few analytical studies. Marianetti and Yevick (2010) used the density functional theory to investigate the failure mechanism of graphene under a generic state of tension (including biaxial tension) at absolute zero temperature. They concluded that the uniaxial failure of graphene is caused by elastic instability while graphene maintains its

symmetrical structure. However, a soft-mode phonon instability, where the phonon frequency for some wavevectors vanishes, promotes failure in graphene when subjected to equi-biaxial tension. These findings are merely applicable to low temperatures where all atomic motions in a crystal can be decomposed into phonon-independent modes (Liu *et al.* 2007). Volokh (2012) and Tuleubekov *et al.* (2013) used a combination of continuum and molecular mechanics to study the behavior of graphene in biaxial loading. In both of the latter studies, graphene was decomposed into two simple Bravais lattices in order to tailor it to the continuum mechanics framework. None of the studies mentioned above reported a closed-form failure criterion for graphene. Furthermore, due to the limitations of the methods employed (i.e. continuum and molecular mechanics), the influence of temperature on the biaxial strength of graphene was not considered.

A series of MD simulations were carried out on defect-free infinite graphene models in order to develop a simple failure criterion for graphene in biaxial loading. Whether failure criteria should be expressed in terms of stress or strain has been a longstanding issue dating back to the emergence of the theory of materials failure. Although discussions on the subject remain inconclusive, it is supposed that characterizing failure criteria in terms of stress is more compatible with the physics of failure (e.g. dislocation dynamics in the ductile range) Christensen (2013). In this paper, and in the supporting studies upon which it is based, stress is taken as the fundamental form to express the failure of graphene. In this regard, the simulation cases investigated in this paper were different from one another with respect to the applied transverse stress magnitudes. The influences of temperature and strain rate were also studied.

6.1.2. Molecular dynamics simulations

All the simulations in this study were carried out using the MD package LAMMPS (Plimpton 1995). Details of the simulations are described in the following sections.

6.1.2.1. Simulation models

Simulations were carried out on a 82.95 Å × 82.28 Å (zigzag × armchair) monolayer graphene sheet consisting of 2,720 carbon (C) atoms with an equilibrium bond length of 1.42 Å and a bond angle of 120°. The sheet was considered adequately large (width > 80 Å – Lu *et al.* (2011)) to avoid the finite-size effects and to represent infinite graphene. Periodic boundary conditions were applied at all four edges in order to simulate the infinite dimensions of the sheet, further minimize the size effects, eliminate the effects of free edges on the mechanical properties of graphene and finally, guarantee constant strain in the desired loading direction.

6.1.2.2. Interatomic potential

The adaptive intermolecular reactive empirical bond-order (AIREBO – Brenner (1990)) potential and the corresponding parameters were used to define the interactions between carbon atoms in graphene. The AIREBO potential has been shown to accurately capture the bond interaction, bond rupture and bond reformation between carbon and hydrogen atoms in the MD studies on carbonaceous and hydrocarbon systems (Zhao *et al.* 2009; Pei *et al.* 2010). In the original version of the potential, a three-step function was proposed to specify the interaction between nearest-neighbor carbon atoms. In this function, two bonded carbon atoms fully interact with one another as long as their bond length is below 1.7 Å. When the

C-C bond length exceeds 1.7 Å, a cutoff function is actuated in order to attenuate the interaction between the adjacent carbon atoms until the bond length reaches 2.0 Å, where the interaction is terminated and the bond ruptures. The three-step cutoff function, however, generates spurious bond forces near the cutoff distance, especially at low temperatures, due to a discontinuity in its second derivative (Lu *et al.* 2011). Consequently, graphene exhibits a non-physical strain hardening behavior at a C-C bond length of 2.0 Å (Shenderova *et al.* 2000; Mattoni *et al.* 2007). In this study, as proposed by several researchers (e.g. Shenderova *et al.* (2000)), the intermediate step of the function (1.7 Å < bond length < 2.0 Å) was omitted by setting both its lower and upper limits to 2.0 Å. This *ad hoc* approach solved the aforementioned cutoff problem while it preserved the ability to describe bond breaking and the nearest-neighbor character of interactions.

It should be noted that the cutoff function in the AIREBO potential is restricted to bond breaking and rehybridization and cannot be used to quantify bond reformation in carbonaceous materials. However, ruptured bonds are generally unlikely to reform in fractured graphene unless the stress that causes a bond to stretch is significantly reduced or completely removed. In this case, other potentials (e.g. spontaneous thermal fluctuations) could bring a pair of atoms that are connected by a bond closer to each other than their breaking distance and thereby reform their bond (Costescu *et al.* 2014). In addition, the studies on defective graphene have consistently shown that its ultimate strength is proportionally lower as a function of the defect coverage up to approximately 7–10% and levels off to the strength of a highly defective graphene for more extensive defects (Xu *et al.* 2013). Therefore, it is expected that randomly distributed bond reformations (if any) will not considerably change the ultimate strength of graphene. However, bond reformation might

significantly increase the magnitude of strain at failure and, consequently, improve the ductility of graphene, giving another justification for expressing the failure criterion in terms of stress in this study.

6.1.2.3. Calculation of stresses and strains

A great number of approaches have thus far been proposed to define the stress tensor in atomistic mechanics, and many relationships have been developed to bridge the atomistic stresses to the macroscopic quantities in continua. In this study, the virial stress (also known as local atomic level stress or total stress) was used to calculate the atomistic stresses due to its simple form and ease of calculations. By definition, each virial stress component per unit volume within the graphene sheet is the aggregate of the corresponding stresses over all carbon atoms (each denoted by α) in the sheet and is calculated as (Tsai 1979; Subramaniyan and Sun 2008):

$$\sigma_{ij} = \frac{1}{\Omega}\sum_{\alpha}\left(\frac{1}{2}\sum_{\beta=1}^{N} r_i^{\alpha\beta} f_j^{\alpha\beta} - m^{\alpha}\upsilon_i^{\alpha}\upsilon_j^{\alpha}\right) \tag{6-1}$$

where i and j (which can take x, y and z) denote direction of the normal to the stress plane and the corresponding traction applied, respectively; β is an atom index running from 1 to N; N is the number of neighboring atoms for atom α; $r_i^{\alpha\beta}$ is the distance between atoms α and β along the i-th direction; $f_j^{\alpha\beta}$ is the force along the j-th direction on atom α due to atom β; m^{α} is the mass of atom α; υ_i^{α} and υ_j^{α} are the components of the thermal excitation velocity of atom α; Ω is the total volume of graphene, assuming a thickness of 3.35 Å.

It should be noted that the first term on the right-hand side of Equation (6-1), known as the potential term, takes into account the interatomic forces acting on an arbitrary plane, while

the second, known as the kinetic term, considers the momentum flux intercepted by it (Tsai 1979). Whether or not including the kinetic term in the virial expression yields atomistic stresses analogous to those measured by the Cauchy expression on a continuum scale has been a contentious topic in the literature. Premising on the fact that the stress in the Cauchy definition is stated solely in terms of the internal mechanical forces between different points in a body, Zhou (2003) asserted that the contribution of the kinetic term to the stress tensor is at odds with the Cauchy definition and provided some examples to demonstrate that the two expressions are not equivalent. Some researchers adopted this notion and tried to derive new atomistic stress definitions equivalent to the Cauchy stress (e.g. see Andia *et al.* (2006)). However, for a material such as graphene, the application of the continuum mechanics principles to measure its stresses typically leads to a residual stress at zero strain, particularly at elevated temperatures, which can be eliminated by using the virial stress (i.e. excluding the contribution of kinetic energy) (Dewapriya et al. 2013). Interested readers are referred to Mattoni *et al.* (2007) for further details.

It is worth mentioning that there is a variation across the literature for the virial stress expression. The author's interpretation of Equation (6-1) agrees with the physics of the virial stress explained by van Dommelen (2003). The following provides a synopsis of the van Dommelen's work.

Consider an RVE of a continuum of dimensions $\Delta x \times \Delta y \times \Delta z$ (Figure 6.1). For a random cross section AA' in the xz plane dividing two sets of atoms I and J along y, the macroscopic stress along y is equal to the aggregate of the forces on atom i and its peers in the set I exerted by atom j and its fellow atoms in J, sum(f_{ij}), divided by the cross-sectional area $\Delta x \Delta z$ (Equation 1.2 in van Dommelen (2003)). Assuming negligible variation for the macroscopic

stress over the stress plane and the y-direction (not applicable near boundaries and to heterogeneous media), for a given pair of atoms i and j, as shown in (Figure 6.2), the relative fraction of planes having i below and j above them is $(y_j - y_i)/\Delta y$. Thus the sum of the forces through AA' yields exactly the potential term in the virial stress theorem. However, there is not a consensus across the literature about this interpretation. Some authors (e.g. Wang *et al.* (2015)) consider the interactions among all particles irrespective of their relative position, thus missing the factor ½ for the potential term. van Dommelen (2003) correctly states that the factor must be considered since only pairs with $y_j > y_i$ should be counted, while the virial theorem counts them all (because of Newton's third law, $f_{ij} = -f_{ji}$).

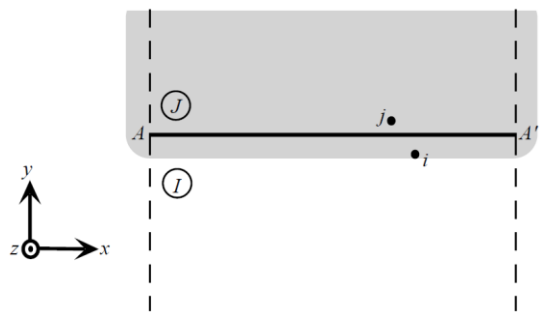

Figure 6.1. Straightforward evaluation of the macroscopic stress (after van Dommelen (2003))

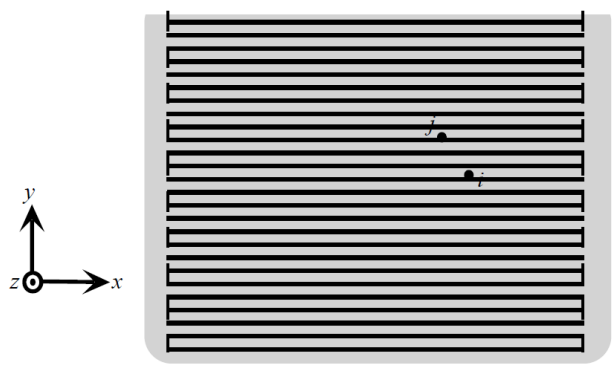

Figure 6.2. Averaging in the y-direction (after van Dommelen (2003))

The statement above is valid only for an arbitrary solid where the sets *I* and *J* are Lagrangian (i.e. the atoms comprising them do not change over time). This is not always the case since due to thermal activation, at least some atoms close to the plane *AA*' will be pushed to and fro across the plane, causing a momentum flux. In this scenario, a thermally-activated atom from set *I* crosses the plane *AA*' into the region *J*, bounces off the atoms there and returns back to the region *I* (cross-over problem – Figure 6.3). The forces associated with these collisions are clearly physical forces and should be considered in the stress calculations. The most-convenient way to deal with this is to adjust the momentum of the set *I*. Since the atoms that are temporarily on the other side of the plane (i.e. in *J*), the potential term of the virial stress has to be augmented, implying a negative value for the net momentum change. This is consistent with the negative sign in the expression given in Equation (6-1). Note that the atoms are not normally billiard balls, and an atom crossing the plane will probably be attracted by its fellow atoms in *I* due to van der Waals interactions. Fortunately, due to Newton's third law, the part of the momentum change of this atom caused by its peers in *I* exactly cancels falsely counting its reaction forces on its peers when it is in *J*. The same explanation holds in reverse for the atoms in *J* wandering into *I*.

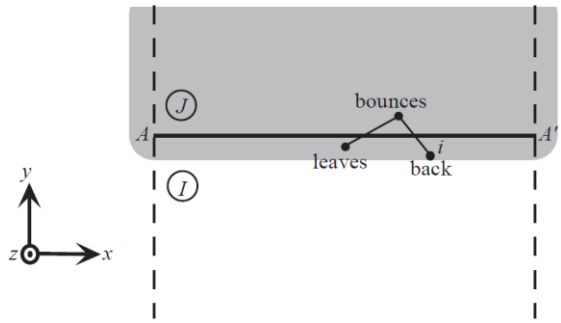

Figure 6.3. The cross-over problem in the virial stress calculation (after van Dommelen (2003))

Moreover, compared to Equation (6-1), the factors ½ and 1 have been interchanged in the expression given in Wang *et al.* (2015). Wang *et al.* (2015) correctly cited the work of Chandra *et al.* (2004) for this expression. However, looking into the Chandra et al.'s work, they have started from an inconsistent adoption of two preceding expressions proposed by Lutsko (1988) and Cormier *et al.* (2001), leading to a seemingly-erroneous viral stress equation.

In spite of the discrepancies mentioned above, the mechanical properties reported for graphene are fairly consistent across the literature. It is possibly due to the fact that graphene remains solid even at elevated temperatures, diminishing the contribution of the kinetic term in the overall stress.

For practical applications, the engineering (nominal) strain, defined as the elongation relative to the original length, was used to calculate the elastic properties of graphene and to plot its stress–strain response. The ultimate stress (σ_u) and strain (ε_u) values used in the analysis correspond to the point at the peak of the stress–strain plot.

6.1.2.4. Simulation sequence

In the simulations that were carried out in this study, the initial structure of each infinite graphene model was subjected to an equilibration sequence as described below to relax any high-energy configurations. A time step of 0.5 fs (0.5×10^{-15} s) was used in all simulations, in accordance with related previous studies (e.g. Dewapriya and Rajapakse (2014)). Five temperatures of 1, 300, 500, 1,000 and 1,500 K were examined. For each temperature, the simulation initially ran for 40 ps (80,000 time steps) using NPT (isothermal–isobaric) ensemble at a temperature 200 K greater than the desired temperature and zero pressure

components along the in-plane directions followed by relaxation for 30 ps at that temperature. The Nosé-Hoover thermostat and barostat were employed to control temperature and pressure, respectively. The subsequent relaxation cooled the structure down to the desired temperature over a period of 40 ps maintaining the pressure components at zero. Eventually, the structure was further relaxed for 30 ps at the desired temperature. The potential energy history of the sheet was observed to ensure negligible energy drift at the end of each stage. In addition, the microstructure of the sheet was frequently visualized in order to ensure that it was appropriate for deformation simulations.

Three loading régimes which were different in their sequence of loading along the zigzag and armchair directions were used to investigate the behavior of graphene in biaxial tension. In Régime I, the boundaries of the sheet were first decoupled from the NPT equations of motion (Hossain *et al.* 2010). Subsequently, the sheet was elongated at a constant strain rate using NVT (canonical) ensemble along the zigzag direction until a certain level of stress along that direction was mobilized. Next, the strain along the zigzag direction was held constant and the sheet was stretched along its armchair direction until failure. The second régime (Régime II) was used in order to test the hypothesis that reversing the sequence of the transverse loadings from zigzag–armchair to armchair–zigzag would not significantly change the combination of stresses resulting in failure. In this régime, the sheet was first stretched along the armchair direction and then elongated to failure along the zigzag direction. Régime III included equi-biaxial loading, where the sheet was simultaneously stretched along both directions until failure.

A strain rate of 0.001/ps was used for all the loading régimes used in this study. Strain rates of this order are very common in MD simulations (e.g. see Dewapriya *et al.* (2014)). The

experimental strain rates, in contrast, are on the order of 1/ms (Lee *et al.* 2008; Zandiatashbar *et al.* 2014). MD simulations at low strain rates are computationally prohibitive for the studies described in this paper, where a great number of simulations would be required to obtain meaningful results. The database generated in the present study is the result of 330 simulations with different combinations of temperature, loading régime and stress magnitudes within the first loading stage for Régimes I and II. Considering the fact that each simulation in this study took on average eight minutes on a supercomputer to complete, selecting a lower strain rate would have exponentially increased the required computational demand and time, making the study very lengthy, if not impossible. Nevertheless, Régime III (i.e. equi-biaxial loading) was repeated for two additional strain rates of 10^{-5}/ps and 0.1/ps in order to investigate the strain rate-dependent failure properties of graphene in biaxial loading, and it was assumed that the results would hold for the other loading régimes.

6.1.3. Results and discussions

The influence of temperature on the ultimate strength of graphene is shown in Figure 6.4. The results indicate that the mechanical performance of graphene is temperature-dependent and anisotropic (orthotropic) in that its ultimate strength varies in the AC and ZZ directions and deteriorates with temperature. In an independent separate simulation, it was observed that the graphene sheet completely restored its original configuration after a loading–unloading cycle, which indicated that it was completely elastic even when unloaded from stresses approaching failure. This observation together with the typical nonlinear stress–strain response (inset of Figure 6.4), which has been attributed to the anharmonic terms of

the C–C interatomic potential (Bu *et al.* 2009), suggest that the mechanical response of graphene prior to failure is nonlinear elastic (hyperelastic).

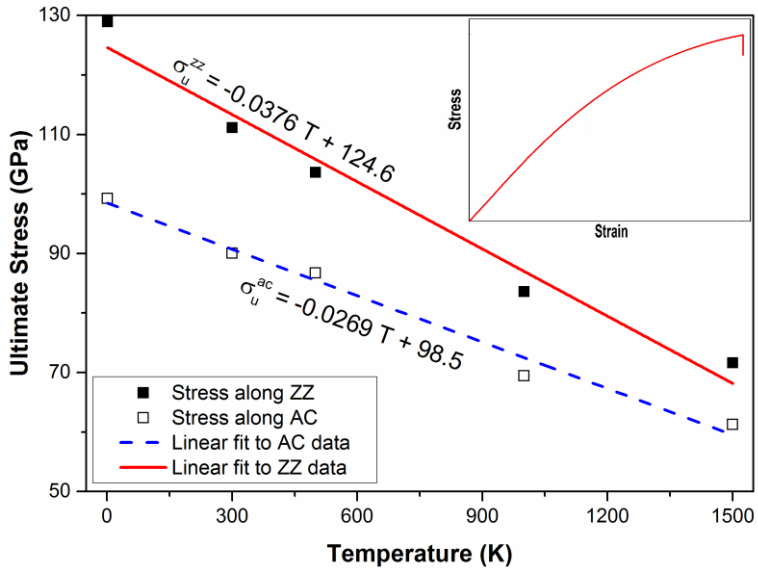

Figure 6.4. Variations of predicted ultimate strength of graphene in zigzag (ZZ) and armchair (AC) directions with temperature subjected to uniaxial loading (strain rate = 0.001/ps). The inset shows a schematic nonlinear behavior expected for graphene based on MD simulations. The data points at each temperature represent the mean values over three independent numerical experiments.

Typical biaxial stress–strain responses of graphene as calculated in this study are shown in Figure 6.5. According to Figure 6.5a, in the staged loading régimes (i.e. Régimes I and II), when the sheet is stretched from its initial unloaded configuration along a primary direction (either zigzag or armchair), stress is developed in both the primary (σ^I_p) and transverse (σ^I_s) directions, albeit at different rates in order to maintain the equilibrium of the sheet.

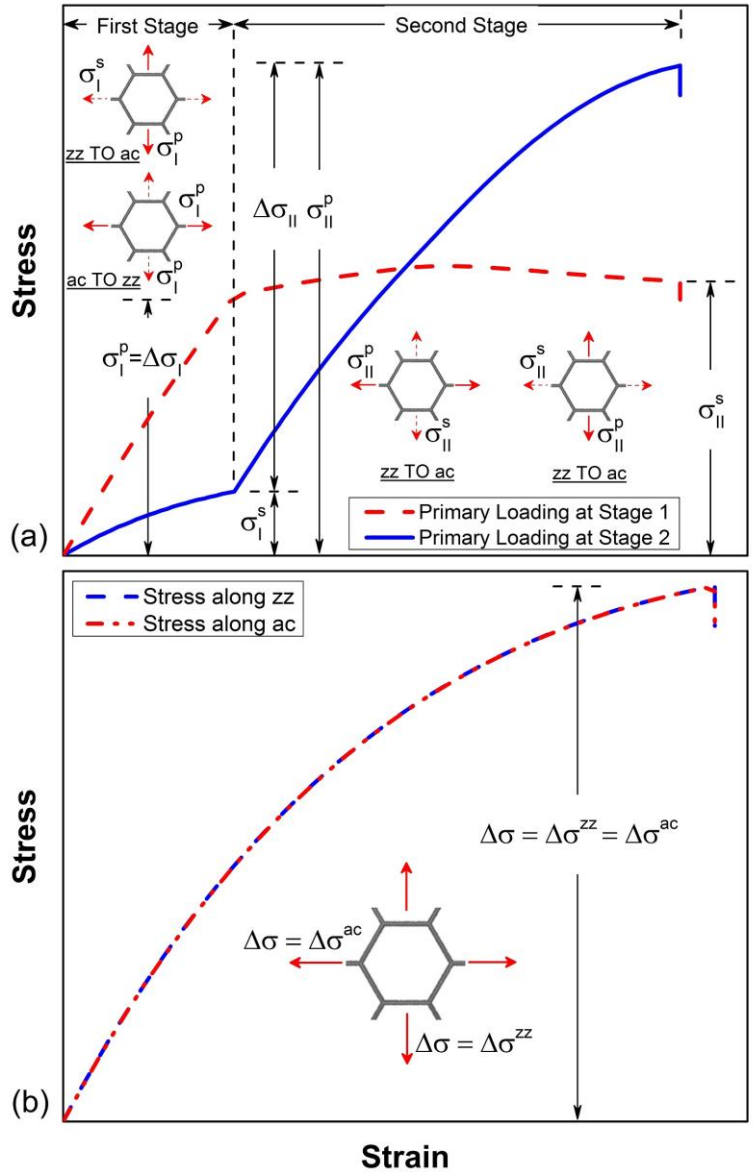

Figure 6.5. Typical stress–strain behavior of bulk graphene in a) staged (Régimes I and II) and b) equi- (Régime III) biaxial loading

During the second stage of loading (i.e. loading to failure), where the primary and secondary directions are interchanged, the stress along the secondary direction (previously the primary direction) initially increases as a result of continued elongation along the primary direction. Further elongation along the primary direction lowers the stress along the normal direction, possibly due to the reduction in the stiffness of the sheet as it approaches failure. Eventually,

a combination of stresses along the two mutually orthogonal directions (σ^{II}_p and σ^{II}_s) leads to failure in the sheet. In Régime III (i.e. equi-biaxial loading), the stresses along the zigzag and armchair directions increase synchronously until they collectively result in failure in the graphene sheet (Figure 6.5b).

In presenting the simulation results for failure envelopes of graphene in biaxial loading, the failure stress values calculated in each direction (i.e. ZZ and AC) were normalized with respect to the corresponding uniaxial ultimate strength values (σ^{zz}_u and σ^{ac}_u). Hence, the following stress ratios were defined along the zigzag and armchair directions to normalize the calculated failure stresses in each direction:

$$\gamma^{zz} = \frac{\Delta\sigma^{zz}}{\sigma_u^{zz}} \tag{6-2}$$

$$\gamma^{ac} = \frac{\Delta\sigma^{ac}}{\sigma_u^{ac}} \tag{6-3}$$

where $\Delta\sigma^{zz}$ and $\Delta\sigma^{ac}$ are defined below for each loading régime (Figure 6.5):

Régime I (zigzag–armchair):

$$\Delta\sigma^{zz} = \Delta\sigma_I; \quad \Delta\sigma^{ac} = \Delta\sigma_{II} \tag{6-4}$$

Régime II (armchair–zigzag):

$$\Delta\sigma^{zz} = \Delta\sigma_{II}; \quad \Delta\sigma^{ac} = \Delta\sigma_I \tag{6-5}$$

Régime III (equi-biaxial):

$$\Delta\sigma^{zz} = \Delta\sigma^{ac} = \Delta\sigma \tag{6-6}$$

The MD simulation data corresponding to the failure of graphene at different temperatures and loading régimes in $\Delta\sigma^{ac}$- $\Delta\sigma^{zz}$ space are shown in Figure 6.6. The notation $\Delta\sigma$ indicates incremental virial stress in graphene. Results indicate that the biaxial strength of graphene decreases at higher temperatures. Since both $\Delta\sigma^{ac}$ and $\Delta\sigma^{zz}$ approach the corresponding uniaxial ultimate strength values in the absence of the cross-direction loading as given in Figure 6.4 (i.e. values at the *x*- and *y*-axes in Figure 6.6), the biaxial strength of graphene decreases at higher temperatures at the same rate as its uniaxial strength in either direction. For instance, the area bound by the data points corresponding to a room temperature of 300 K in Figure 6.6 is reduced by nearly 50% at an elevated temperature of 1000 K. Consistently stronger performance of graphene at lower temperatures is possibly due to the fact that low temperatures obstruct the nucleation of discrete local failures within the graphene structure, thus enabling it to withstand larger loads before failure (Liu *et al.* 2007; Dewapriya and Rajapakse 2014). In addition, a greater C–C bond length at higher temperatures due to the thermal fluctuations arising from kinetic energy leads C–C bonds to store higher potential energy. Therefore, the initial configuration of the graphene sheet stores less strain energy at lower temperatures. According to the total strain energy theory (Beltrami–Haigh's theory), a body subjected to a combined stress state fails when the total strain energy exceeds the total strain energy corresponding to simple tension. Therefore, the graphene sheet at lower temperatures can accommodate larger stresses and strains before failure.

It can also be observed that for any given simulated temperature, the failure stress combinations corresponding to Loading Régimes I and II (sequential biaxial loading) are comparable. However, those for the Loading Régime III (simultaneous biaxial loading) indicate a comparatively stronger response, especially at lower temperatures. This

observation can be explained by the counteracting effects of the transverse forces on the changes in the bond angles of the sheet. The decrease in the bond angles due to the ZZ stress is partially neutralized by the tendency of the AC stress to widen the bond angles, thus minimizing the contribution of bond angles in the total strain energy of the sheet. As a result, the capacity of the sheet to store strain energy and, therefore, its strength increases.

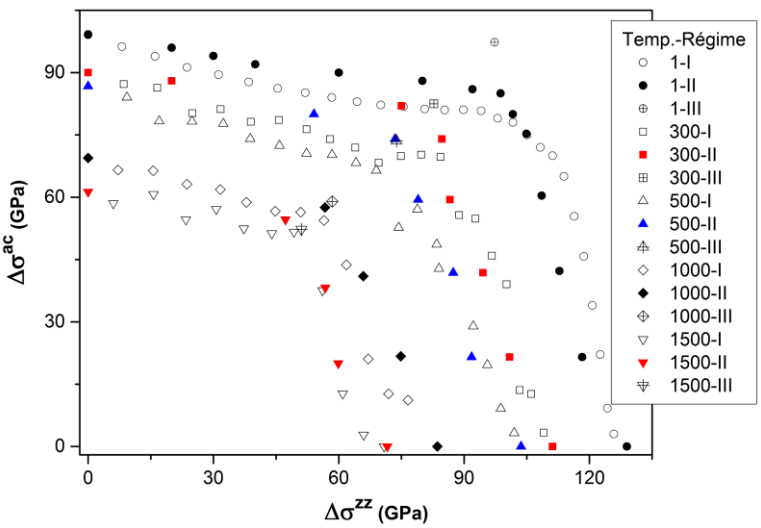

Figure 6.6. Combinations of biaxial stresses resulting in failure in graphene at different temperatures and loading régimes (strain rate = 0.001/ps)

Theoretical analyses and numerical simulations have identified two distinct modes of failure for defect-free graphene under a tensile load: brittle cleavage rupture and ductile failure by plastic flow instability. Brittle cleavage rupture, which prevails at low temperatures and high strain rates, is associated with sudden bond breaking and tearing along the fracture plane, leading to the formation of large open-ring structures. In contrast, external conditions such as slow strain rates and high temperatures (greater than 1000 K – Zhang *et al.* (2012), and below carbon's sublimation point: 3900 K – Whittaker (1978)) favor dislocation-induced plastic flow, which is characterized by localized bond rotations at a crack tip (Terdalkar *et al.*

2010). At room temperature, defect-free graphene is intrinsically brittle, manifested by a catastrophic fracture observed in the nanoindentation of freestanding graphene membranes (Lee *et al.* 2008). It is noteworthy that defective graphene (e.g. graphene with randomly distributed vacancies or Stone–Wales defects) exhibits ductility as a result of a complicated interplay among crack trap, crack-tip blunting and the structural rearrangement around the defects (Xu *et al.* 2013).

The failure modes of graphene under the three loading régimes at 0 K are shown in Figure 6.7. For the Loading Régime I (i.e. staged loading ZZ followed by AC), fracture nucleation occurs exclusively at some flaws along the armchair edges where the tensile stress exceeds the C-C bond strength (Figure 6.7a). An infinitesimal additional strain (i.e. 18.17% vs. 18.18%) results in the very fast formation and growth of cracks on the plane of maximum principal stress (i.e. ZZ direction), leading to brittle cleavage fracture. In contrast, in the Loading Régime II (i.e. staged loading AC followed by ZZ), cracks are initiated at a stochastic flaw at the interior lattice and grow at relative angles of 60° or 120°, indicating that failure is aligned with the crystallographic directions of graphene (Figure 6.7b). Similar to Régime I, fracture nucleation in Régime III occurs at some flaws along the armchair edges (Figure 6.7c). Cracks initially grow along the crystallographic directions of graphene, but are subsequently deviated due to the simultaneously and equally increasing stresses along the AC direction, resulting in the branching (splitting) and microscopic tortuosity of cracks. Similar failure modes were observed for graphene at room temperature in the numerical simulations carried out in this study. It is also noteworthy that the formation of suspended atomic chains immediately before failure (Figure 6.7b and c) is consistent with laboratory observations (Jin *et al.* 2009) and first-principles calculations (Topsakal and Ciraci 2010).

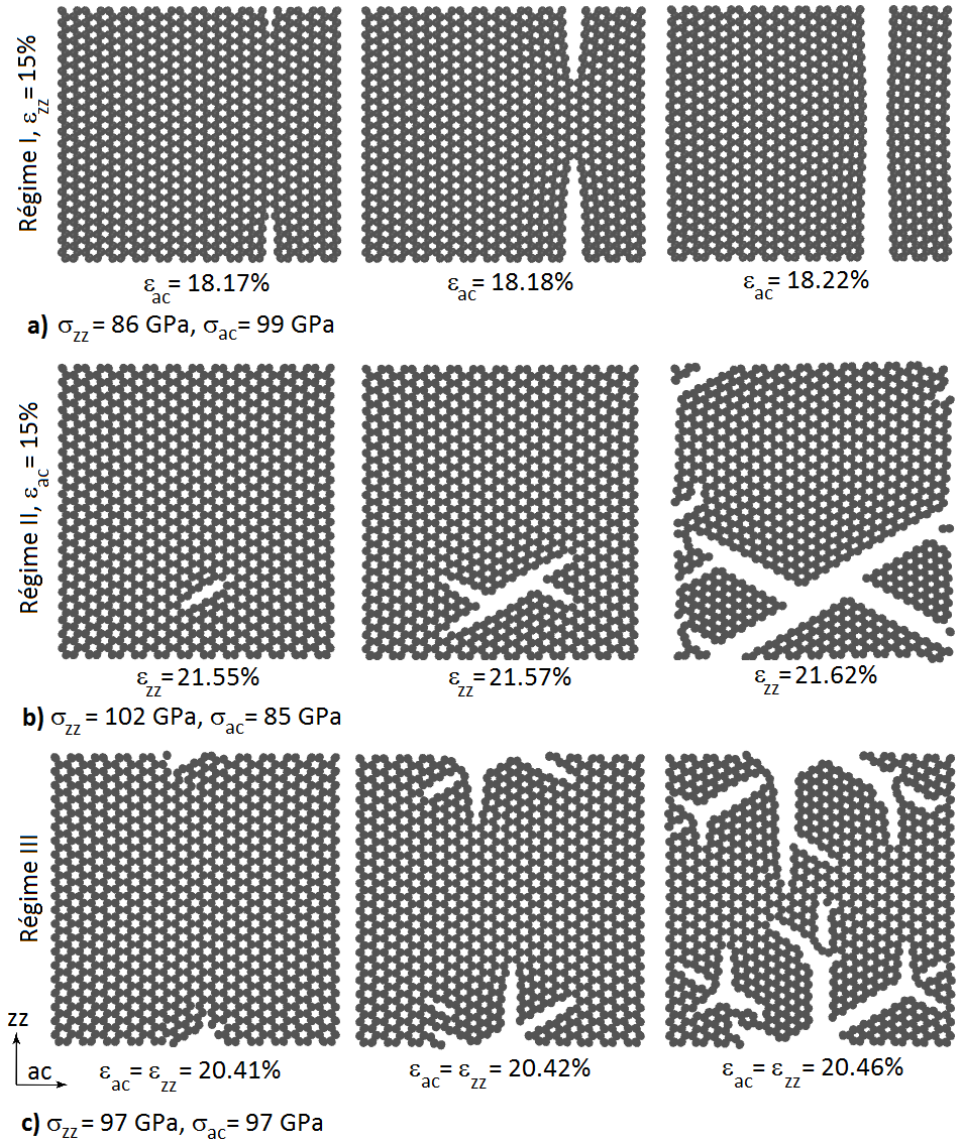

Figure 6.7. Failure modes of graphene at 0 K under Loading Régimes a) I, b) II and c) III

The influence of strain rate on the failure properties of graphene subjected to equi-biaxial loading is summarized in Table 6-1. Results clearly show that both the stress and strain at failure increase with strain rate. However the influence of strain rate is significant only at higher temperatures (> ~500 K) and is relatively insignificant compared with that due to

temperature variations. These observations are consistent with those reported by (Zhao and Aluru 2010; Dewapriya *et al.* 2013).

Table 6-1. Strain-rate dependent failure properties of graphene under equi-biaxial loading (Régime III)

Temp. (K)	Strain Rate (0.001/ps)								
	0.01			1			100		
	ε_u (%)	$\Delta\sigma^{ac}$ (GPa)	$\Delta\sigma^{zz}$ (GPa)	ε_u (%)	$\Delta\sigma^{ac}$ (GPa)	$\Delta\sigma^{zz}$ (GPa)	ε_u (%)	$\Delta\sigma^{ac}$ (GPa)	$\Delta\sigma^{zz}$ (GPa)
1	20.2	97.5	97.5	20.0	97.3	97.3	22.0	95.2	97.4
300	12.5	79.7	79.8	13.5	82.5	82.8	15.5	86.4	86.6
500	10.1	70.2	70.6	11.0	73.6	73.8	13.5	80.8	81.1
1,000	7.6	57.3	56.8	8.0	58.9	58.4	11.0	70.0	67.0
1,500	6.6	51.3	49.8	7.0	52.3	51.1	10.5	64.5	64.4

The data corresponding to the failure of graphene at different temperatures and loading régimes (Figure 6.6) are mapped to the normalized γ^{zz}–γ^{ac} domain and shown in Figure 6.8. Inspection of the results shown indicates that the entire ensemble of data points can be approximated with a bilinear curve reasonably well. The bilinear curve has two distinct segments on both sides of the 1:1 line in Figure 6.8. A best-fit curve was obtained using a least squares method in the form of:

$$\gamma_{max} + 0.2\gamma_{min} = 1 \tag{6-7}$$

which defines a simple bilinear failure envelope for graphene where $\gamma_{max} = \max[\gamma^{zz},\gamma^{ac}]$ and $\gamma_{min} = \min[\gamma^{zz},\gamma^{ac}]$. Equation (6-7) is a Bayesian change-point model that can capture the abrupt variation in the sequence of the data shown in Figure 6.8 at a change-point of $\gamma^{zz} = \gamma^{ac} = 0.83$ (Barry and Hartigan 1993). The non-smooth behavior evinced by Equation (6-7) is similar to that of the maximum shear stress criterion for yield (Tresca) and could be due to an interplay between ductile flow and brittle fracture modes of failure (Christensen 2013).

Since the strain rate was kept the same for all of the simulations that were used to develop Equation (6-7), it is assumed that the failure envelop holds its shape for other strain rates. However, the uniaxial ultimate strength values corresponding to a particular strain rate (see Figure 6.4) must be used to calculate actual applied stresses leading to failure in graphene.

The data and the best-fit bilinear curve shown in the γ^{zz}–γ^{ac} plot of Figure 6.8 represent the critical combinations of γ^{zz} and γ^{ac} which would lead to failure in the graphene sheet. Therefore, the best fit bilinear curve shown in Figure 6.8 is, by definition, a failure envelope for the graphene sheet in biaxial loading.

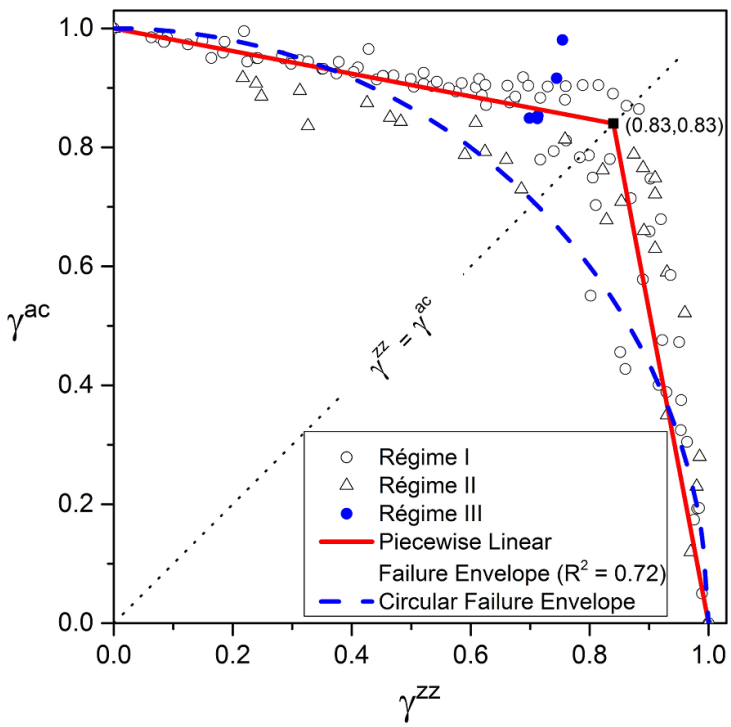

Figure 6.8. Biaxial failure envelopes for graphene subjected to different loading régimes

A second 'unit-circle' failure envelope was also obtained for the data shown in Figure 6.8 analogous to the plasticity models for the prediction of failure in biaxially-loaded metal plates (Kee Paik 2008). The 'unit-circle' failure envelope defined as:

$$(\gamma^{zz})^2 + (\gamma^{ac})^2 = 1 \tag{6-8}$$

provides an appealing, mathematically convenient approximation for the bilinear failure envelope that can be used for the back-of-the-envelope calculation of the graphene ultimate strength in biaxial loading. However, as can be observed in Figure 6.8, the 'unit-circle' failure envelope is less accurate than the bilinear envelope in capturing the predicted ultimate strength data shown in the figure.

6.1.4. Conclusions

MD simulations were carried out in order to develop failure criteria for defect-free, infinite graphene tested in biaxial loading at different temperatures. In the MD simulations, a model of graphene sheet was biaxially loaded to failure using different sequences of loading in its zigzag and armchair principal directions. The predicted biaxial failure stresses in the two principal directions were plotted normalized to their respective uniaxial ultimate strength values. Bilinear and circular failure envelopes were introduced using a least squares method for practical applications. Results showed that the biaxial failure envelopes for graphene in terms of actual applied stresses are consistently smaller (indicating reduced strength) at elevated temperatures. However, failure envelopes in terms of normalized stresses were found to be essentially temperature independent.

The failure criterion proposed in this study is merely valid for defect-free graphene. However, the structural defects arising during growth or processing of graphene severely deteriorate its mechanical properties. In addition, the potential used in this study (i.e. AIREBO) fails to consider bond-reformation. Similar studies on defective graphene using

conservative potentials (e.g. SED-REBO and SED-REBO-S – Perriot *et al.* (2013)) are encouraged in order to develop comprehensive and more accurate failure criteria.

6.2. Atomistic insight into the mechanical properties of single-walled carbon nanotubes

6.2.1. Introduction

Understanding the mechanical properties of CNTs under compression and tension is essential in developing CNT-filled composites with enhanced properties. The laboratory measurements carried out on CNTs have indicated different values for their elastic and strength properties. A Young's modulus close to 1 TPa was reported for CNTs using small-strain TEM (Treacy *et al.* 1996) or post-elastic AFM (Bellucci *et al.* 2007) measurements (see Section 4.2.2.2 for TEM and AFM descriptions). Larger values of 2.8–3.6 TPa have also been observed for SWCNTs (Lourie *et al.* 1998). In addition, wide ranges of 0.32–1.47 TPa for SWCNTs and 0.27–0.95 TPa for MWCNTs have been obtained using SEM measurements (Yu *et al.* 1999; Yu *et al.* 2000). A broad experimental range of 0.01–0.15 TPa has also been reported for the strength of CNTs (Yu *et al.* 2000; Demczyk *et al.* 2002).

The discrepancy observed for the mechanical properties of CNTs in laboratory measurements could be attributed to different factors, including the chirality, aspect ratio and imperfections of CNTs as well as the temperature of the tests and measurement errors. Because it is challenging to pinpoint the properties of CNTs via laboratory experiments, experimentally-validated MD simulations can be used as a virtual laboratory to probe the what-if scenarios that would otherwise be difficult to investigate in the laboratory.

In spite of a fairly considerable number of MD studies on CNTs (e.g. Wang *et al.* (2014)), the literature lacks a comprehensive study discussing the influence of the factors mentioned above on the mechanical properties of CNTs in the framework of a suitable force field. This section addresses this problem.

6.2.2. Molecular dynamics simulations

All the simulations in this study were carried out using the MD package LAMMPS (Plimpton 1995). Details of the simulations are described in the following sections.

6.2.2.1. Simulation models

6.2.2.1.1. Buckling analysis

On account of their tubular geometry, CNTs are prone to undergo localized or global buckling under a compressive axial load, mechanical torque or a bending moment. Buckling in CNTs is accompanied by a drastic reduction in their mechanical stiffness and an abrupt change in their transport properties. Therefore, understanding their buckling mechanism is essential in order to improve the design of the systems made with CNTs that might experience instability or failure upon buckling (e.g. electromechanical transducers, artificial muscles and AFM probes – Wang *et al.* (2014)).

The onset of buckling in an axially-compressed member is controlled by an important geometric parameter known as slenderness ratio. The slenderness ratio is the effective buckling length of the member divided by its radius of gyration. The effective buckling length

depends on the boundary conditions of the member or how it has been supported in its ends.

A series of simulations was carried out on axially-compressed SWCNTs with different chiral angles, sizes and slenderness ratios at varying temperatures in order to investigate their buckling behavior (Table 6-2). Note that all the chiral indices selected for the analysis yield the same radius of gyration, eliminating its influence on the analysis. A thickness of t = 3.4 Å, equal to the interlayer distance in graphite (Figure 1.2), was used to calculate the cross-sectional area, A, moment of inertia, I, and the radius of gyration, R_g, of an SWCNT with a diameter of D using the following equations:

$$A_{SWCNT} = \frac{\pi}{4}\left((D_{SWCNT}+t)^2 - (D_{SWCNT}-t)^2\right) \tag{6-9}$$

$$I_{SWCNT} = \frac{\pi}{64}\left((D_{SWCNT}+t)^4 - (D_{SWCNT}-t)^4\right) \tag{6-10}$$

$$R_{g\,SWCNT} = \sqrt{I_{SWCNT} / A_{SWCNT}} \tag{6-11}$$

Table 6-2. Information of the MD models made for compressive numerical experiments

Slenderness ratio	Temperature (K)	(n,m)	Chiral angle (°)	Diameter (Å)	A (Å²)	I (Å⁴)	R_g (Å)
5, 10, 15, 20	100, 300, 500	(0,17)	0	13.31	142.16	3 353	6.65
		(2,16)	5.82	13.38	142.90	3 403	6.69
		(4,15)	11.52	13.58	145.08	3 555	6.79
		(5,14)	14.70	13.35	142.65	3 386	6.67
		(7,13)	20.17	13.76	146.99	3 692	6.88
		(8,12)	23.41	13.65	145.80	3 606	6.83
		(9,11)	26.70	13.58	145.08	3 555	6.79
		(10,10)	30.00	13.56	144.84	3 538	6.78

6.2.2.1.2. Tensile tests

An aspect ratio of 10 was assumed for the SWCNTs subjected to tension. The chiral indices selected for the tensile numerical experiments cover different scenarios. For instance, the

influence of size (diameter) can be examined within each category of chirality (i.e. AC, chiral and ZZ). Also, the influence of chirality can be investigated by comparing the results of the SWCNTs (0,17), (9,11) and (10,10), which differ in chiral angle but have approximately identical sizes.

Table 6-3. Information of the MD models made for tensile numerical experiments (aspect ratio = 10)

Temperature (K)	(n,m)	Chiral angle (°)	Diameter (Å)	A (Å^2)	Length (Å)
100, 300, 500	(0,5)	0	3.91	41.81	39.14
	(0,10)	0	7.82	83.62	78.29
	(0,15)	0	11.74	125.43	117.43
	(0,17)	0	13.31	142.16	133.09
	(0,20)	0	15.66	167.25	156.58
	(0,26)	0	20.36	217.42	203.55
	(2,16)	5.82	13.38	142.90	133.78
	(4,15)	11.52	13.58	145.08	135.83
	(5,14)	14.70	13.35	142.65	133.55
	(7,13)	20.17	13.76	146.99	137.62
	(8,12)	23.41	13.65	145.80	136.50
	(9,11)	26.69	13.58	145.08	135.83
	(13,17)	25.60	20.40	217.90	204.00
	(5,5)	30.00	6.78	72.42	67.80
	(10,10)	30.00	13.56	144.84	135.60
	(15,15)	30.00	20.34	217.26	203.40
	(20,20)	30.00	27.12	289.68	217.20

6.2.2.2. Simulation details

Shrink-wrapped boundary conditions were applied along three dimensions in order to simulate the finite size of the CNTs. Similar to graphene (Section 6.1.2.2), the AIREBO potential and the corresponding parameters were used to define the interactions between carbon atoms in the CNTs. The virial stress was used to calculate the atomistic stresses. The engineering strain was used to calculate the elastic properties of graphene and to plot its stress–strain response. The ultimate stress (σ_u) and strain (ε_u) values used in the analyses correspond to the point at the peak of the stress–strain plot.

A time step of 1 fs (10^{-15} s) was used for the simulations. The lower end of the CNT models was held fixed and the other end was laterally fixed (clamped-clamped boundary conditions) while incrementally displaced (stretched up or pushed down depending on the type of loading) at a strain rate of 0.001/ps (Figure 6.9). Three temperatures of 100, 300 and 500 K were examined. For each temperature, the simulation ran for 20 ps (20,000 time steps) using the NVT ensemble at the desired temperature in order to relax any high energy configurations. The potential energy history of the models was observed to ensure negligible energy drift at the end of each stage. In addition, the microstructure of the models was frequently visualized in order to ensure that it was appropriate for deformation simulations.

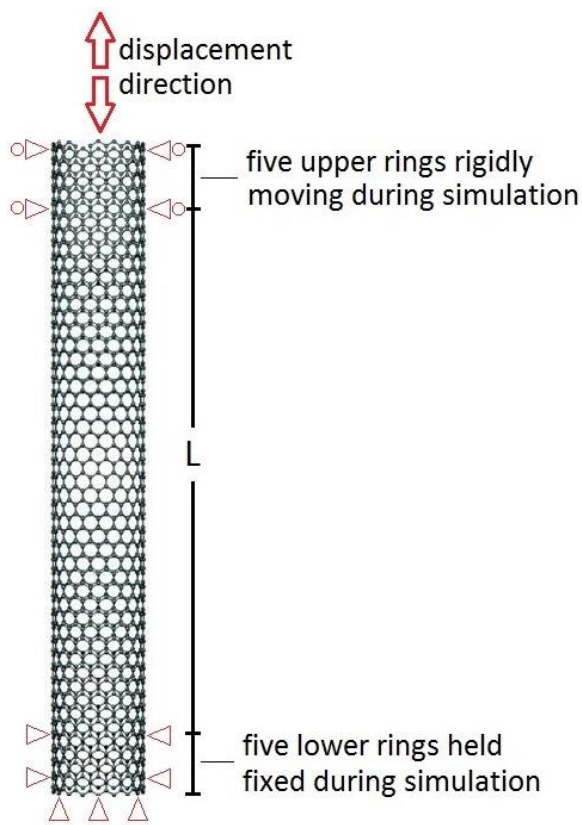

Figure 6.9. SWCNT model

6.2.2.3. Calculation of elastic moduli

Previous studies (e.g. WenXing *et al.* (2004)) have confirmed a nonlinear elastic (hyperelastic) behavior for CNTs in tension. A considerable number of models have thus far been proposed to describe the deformation-dependent response of hyperelastic materials. In this study, the symmetric second Piola–Kirchhoff stress (Lee *et al.* 2008), σ, expressed as follows was used to determine the elastic moduli of graphene:

$$\sigma = E\varepsilon + D\varepsilon^2 \tag{6-12}$$

where ε is the uniaxial Lagrangian strain, E is the Young's modulus and D is the third-order elastic modulus, which results from the third-order Taylor series approximation of the potential energy as a function of strain. Here, the values of E and D are determined using the nonlinear least squares fit (Gauss–Newton) method, which minimizes the sum of the mean square distances from the postulated curve (i.e. Equation (6-12)) to the data points.

6.2.3. Results and discussions

6.2.3.1. Buckling analysis

The compressive stress-strain behavior and corresponding buckling modes of SWCNT (0,17) with different slenderness ratios at varying temperatures are shown in Figure 6.10. The stress-strain diagrams indicate that all the modeled CNTs remain essentially linear up to the buckling stress even at high temperatures. Slenderness ratio and temperature, however, do alter the postbuckling behavior of the SWCNTs. The following observations can be made:

- The shortest SWCNTs (i.e. slenderness ratio = 5), exhibit a stable postbuckling behavior irrespective of the temperature applied (Figure 6.10a). The significant drop in the stress upon exceeding the peak strength is associated with an inward local buckling at the middle of the CNTs which continues through the formation of an hourglass-shaped pattern at larger strains. This deformation is accompanied by a residual strength that is a fraction (50–65%) of the peak strength.

- SWCNTs with a slenderness ratio of 10 show temperature-dependency in their postbuckling behavior (Figure 6.10b). At low temperatures, a stable postbuckling behavior similar to that of the short SWCNTs is observed. However, the SWCNTs at higher temperatures experience secondary buckling. The development of secondary buckling in high-temperature models could be attributed to the availability of the energy required for its activation. This energy is always greater than that required for initial buckling and is partially furnished at higher temperatures by the thermal fluctuations arising from kinetic energy (Eftekhari *et al.* 2013). An inward local buckling followed by larger lateral deformations and a stable postbuckling behavior were also observed for these CNTs.

- The influence of temperature on the stress-strain behavior of CNTs is pronounced in slender CNTs (slenderness ratio ≥ 15) subjected to low strains (Figure 6.10c,d). At larger strains, however, this distinction vanishes where all CNTs exhibit similar postbuckling stress-strain responses. The large slenderness ratios of these CNTs allow the occurrence of tertiary buckling. The CNTs with a slenderness ratio of 15 buckle through the gradual

formation of a uniform, circular bulge in their middle. More slender tubes undergo large lateral deformations at large axial strains, promoting their crumpling.

- The stable postbuckling behavior observed in all the models shows the potential of CNTs for use in mechanical energy storage and absorption devices.

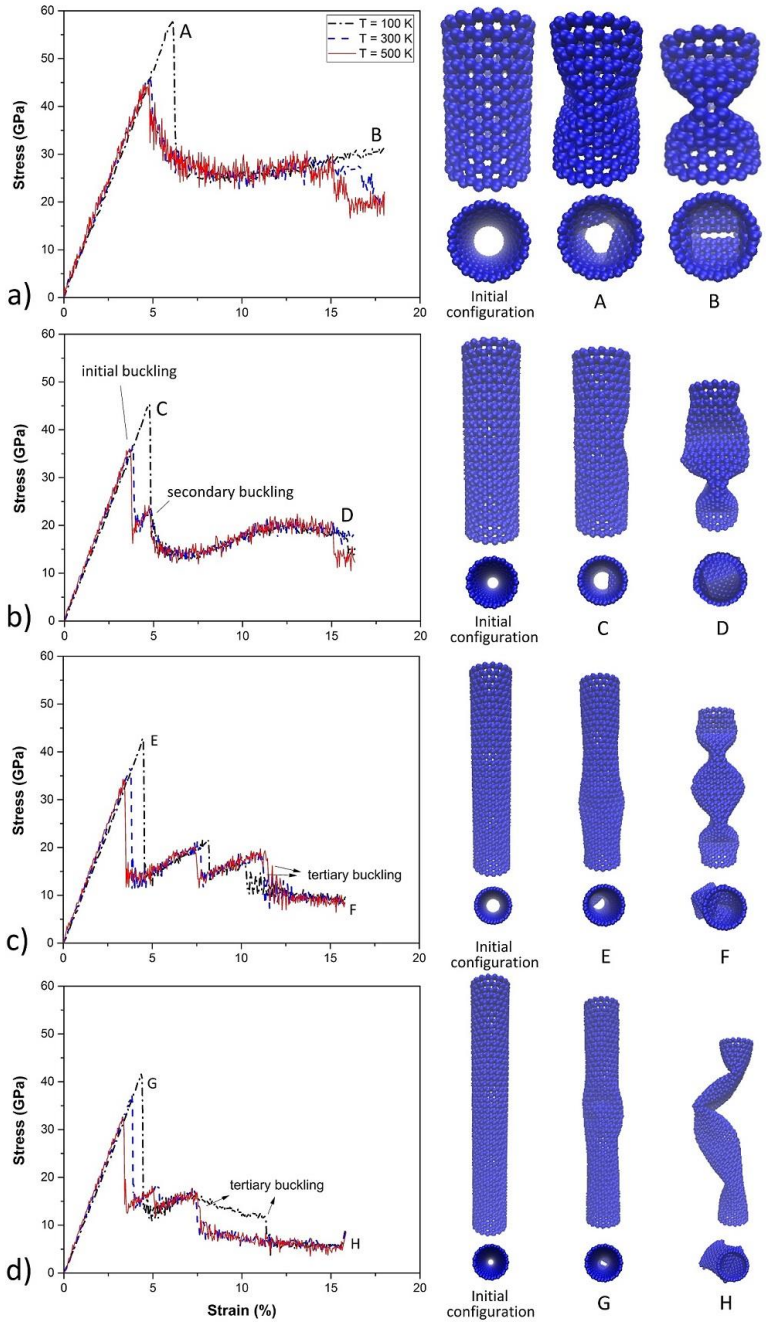

Figure 6.10. Compressive stress-strain behavior and buckling modes of SWCNT (0,17) with an slenderness ratio of a) 5, b) 10, c) 15 and d) 20

Comparison of Figure 6.10a to Figure 6.10d shows that the onset of buckling is inversely proportional to the slenderness of the tubes; shorter tubes buckle at relatively lower strains.

This observation can be better seen in Figures 6.11 and 6.12 where the influence of temperature and chirality on the buckling capacity and buckling strain of CNTs is shown. The results indicate that, expectedly, both buckling strength and its corresponding strain steadily decrease with increasing slenderness ratio and temperature, due to the increased thermal motion of the tube walls (Ni *et al.* 2002). The influence of chirality is interesting. Chiral CNTs buckle at essentially lower stresses and strains. This observation could be due to the more notable coupling of the transverse and longitudinal deformations of chiral CNTs which is more notable compared to that in AC and ZZ CNTs.

How the elastic modulus of CNTs in compression is affected by chirality and temperature is shown in Figure 6.13. Comparison of the results indicates that the elastic modulus at a given temperature is not considerably influenced by slenderness ratio and chirality. However, the CNTs simulated at higher temperatures surprisingly show higher stiffnesses. Considering the essentially-linear compressive behavior of the simulated CNTs, the last observation means that the buckling strain is more influenced by temperature than the buckling strength, possibly due to the increased thermal motion of the tube walls promoting the bending moments induced by the combined effect of axial stresses and lateral deformations.

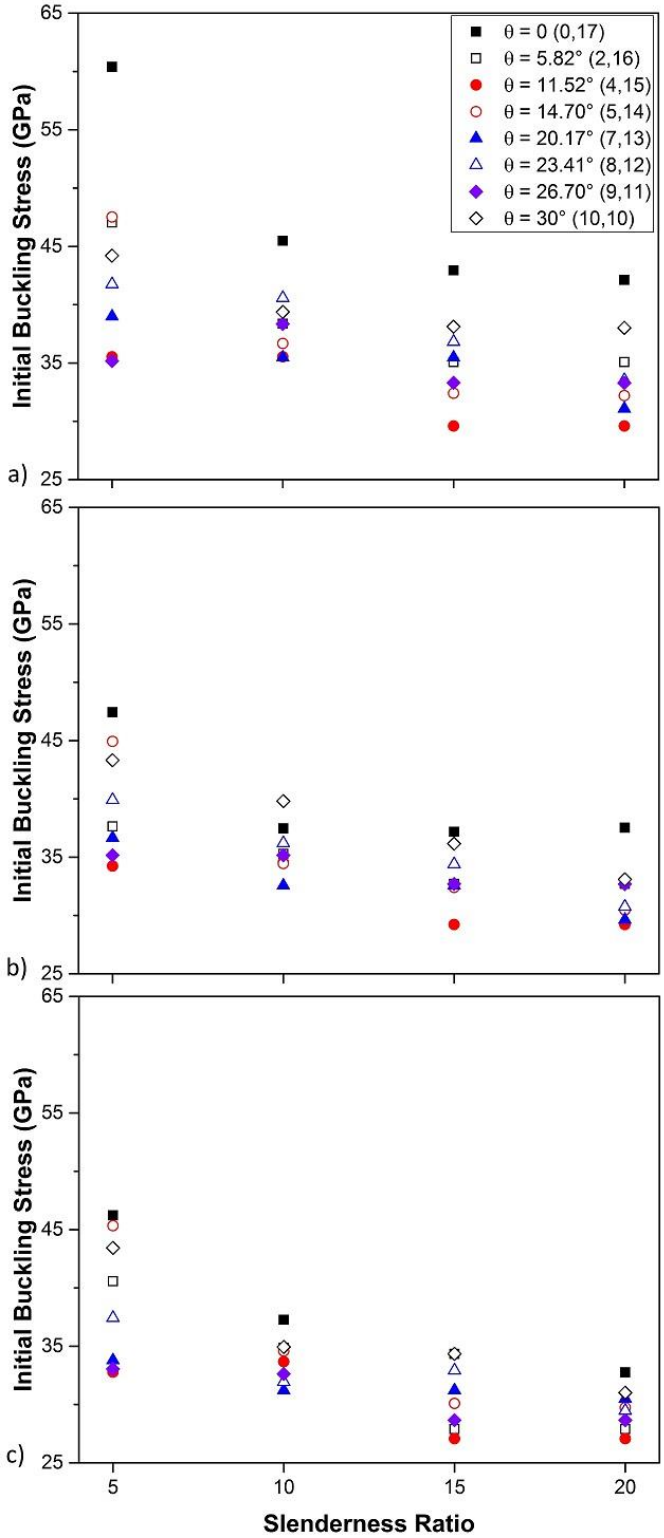

Figure 6.11. Influence of slenderness ratio and chirality on the buckling strength of SWCNTs at T = a) 100 K, b) 300 K and c) 500 K

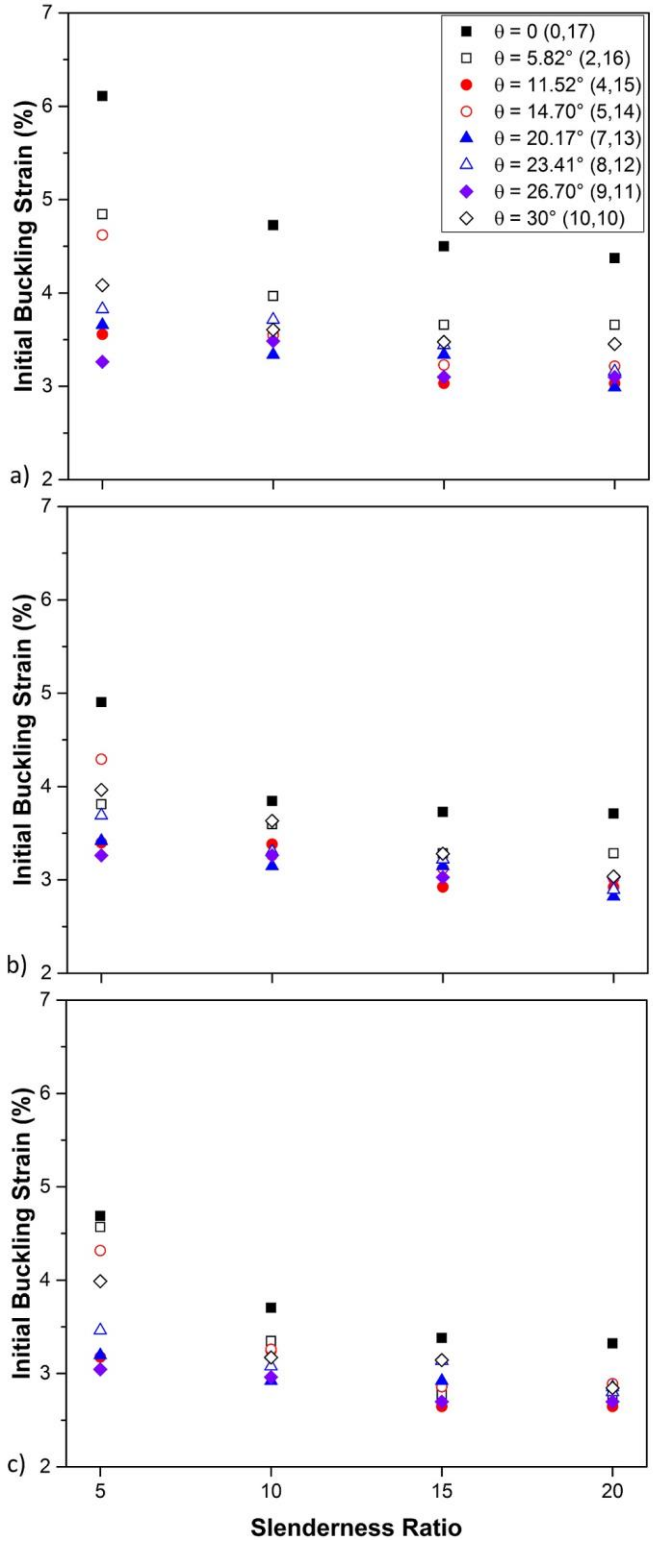

Figure 6.12. Influence of slenderness ratio and chirality on the initial buckling strain of SWCNTs at T = a) 100 K, b) 300 K and c) 500 K

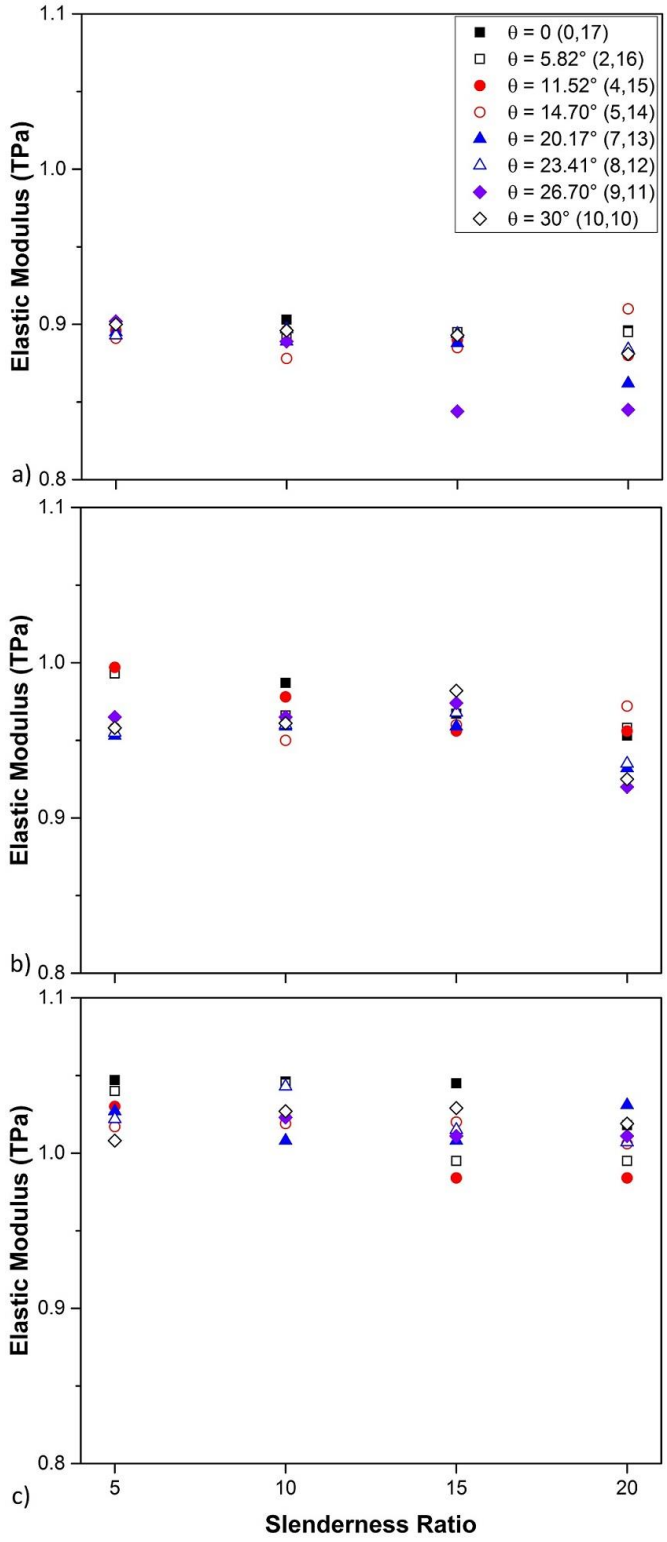

Figure 6.13. Influence of slenderness ratio and chirality on the elastic modulus of SWCNTs at T = a) 100 K, b) 300 K and c) 500 K

6.2.3.2. Tensile behavior

The tensile stress-strain behavior and failure modes of selected SWCNTs with an approximately equal diameter of 13.5 Å (i.e. (0,17), (9,11) and (10,10)) at different temperatures are shown and compared in Figure 6.14. Results show that all CNTs simulated exhibit nonlinear elastic behavior. It is also seen from the failure modes that the fracture of zigzag CNTs always occurs perpendicular to the loading direction, while diagonal fractures can be observed for armchair and chiral CNTs. This observation can be explained by considering the equilibrium of an individual C atom on the tubes wall (Figure 6.15).

At equilibrium, the relationship between the three forces acting on an atom can be written as:

$$T_1 = (T_2 + T_3)\cos(\theta / 2) \tag{6-13}$$

The symmetry about the T_1 direction requires $T_2 = T_3$, reducing Equation (6-13) to:

$$T_1 = 2T_2 \cos(\theta / 2) \tag{6-14}$$

In an unstrained CNT, $\theta = 120°$, and therefore $T_1 = T_2$. However, stretching a zigzag CNT along its axis decreases θ, making $T_1 > T_2$. Consequently, fracture is initiated at the bonds aligned with the loading direction and propagates normal to that. Straining armchair and chiral CNTs, in contrast, increases θ, making $T_1 < T_2$. As a result, fracture occurs at the inclined bonds (±30° for armchair CNTs) and develops at an angle (±60° for armchair CNTs) to the tube axis.

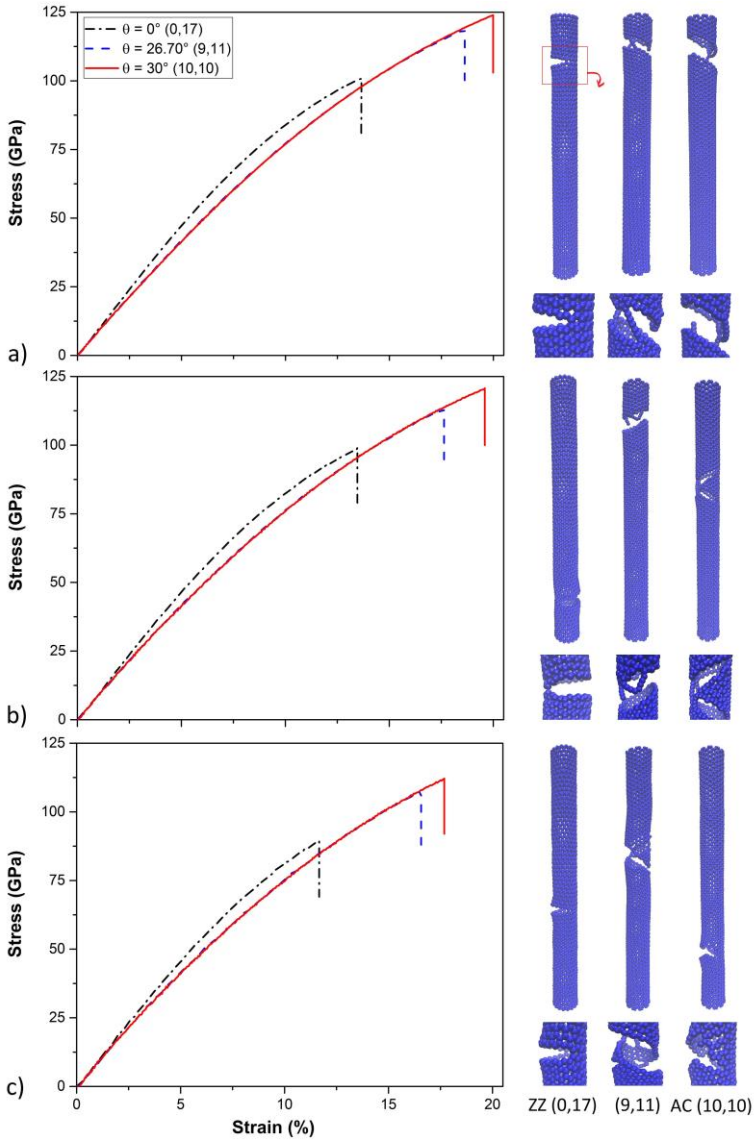

Figure 6.14. Tensile stress-strain behavior and failure modes of selected SWCNTs with similar diameters (~13.5 Å) at T = a) 100 K, b) 300 K and c) 500 K. Note: aspect ratio = 10.

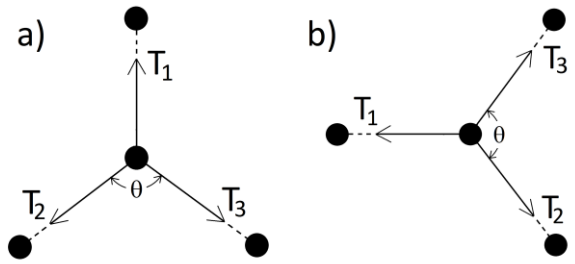

Figure 6.15. Equilibrium of carbon atoms in a) zigzag and b) armchair CNTs subjected to tension

Influence of chirality and temperature on the tensile properties of SWCNTs is shown in Figure 6.16. Results indicate that the tensile strength (Figure 6.16a) and strain at failure (Figure 6.16b) steadily increase as the chiral angle increases from 0 for zigzag CNTs to 30° for armchair ones. It is also seen that the CNTs stretched at higher temperatures fail at lower stress and strain. However, according to Figure 6.16c, the elastic modulus decreases as the chiral angle and temperature increase. The influence of temperature, however, is less notable in high-chiral CNTs. This observation is in contrary to the findings of Xiao and Hou (2006) who studied the mechanical properties of CNTs using molecular mechanics and found the CNTs' Young's modulus insensitive to chirality.

Influence of diameter on the tensile properties of zigzag and armchair SWCNTs is shown in Figures 6.17 and 6.18. Results show that larger CNTs possess lower tensile strengths and fail at lower strains. However, the elastic modulus remains insensitive to changes in diameter. It should be noted that the value of D was found typically negative for all CNTs in tension, which is consistent with the overt departure of graphene from linear proportionality where the stiffness of graphene decreases with tensile strain.

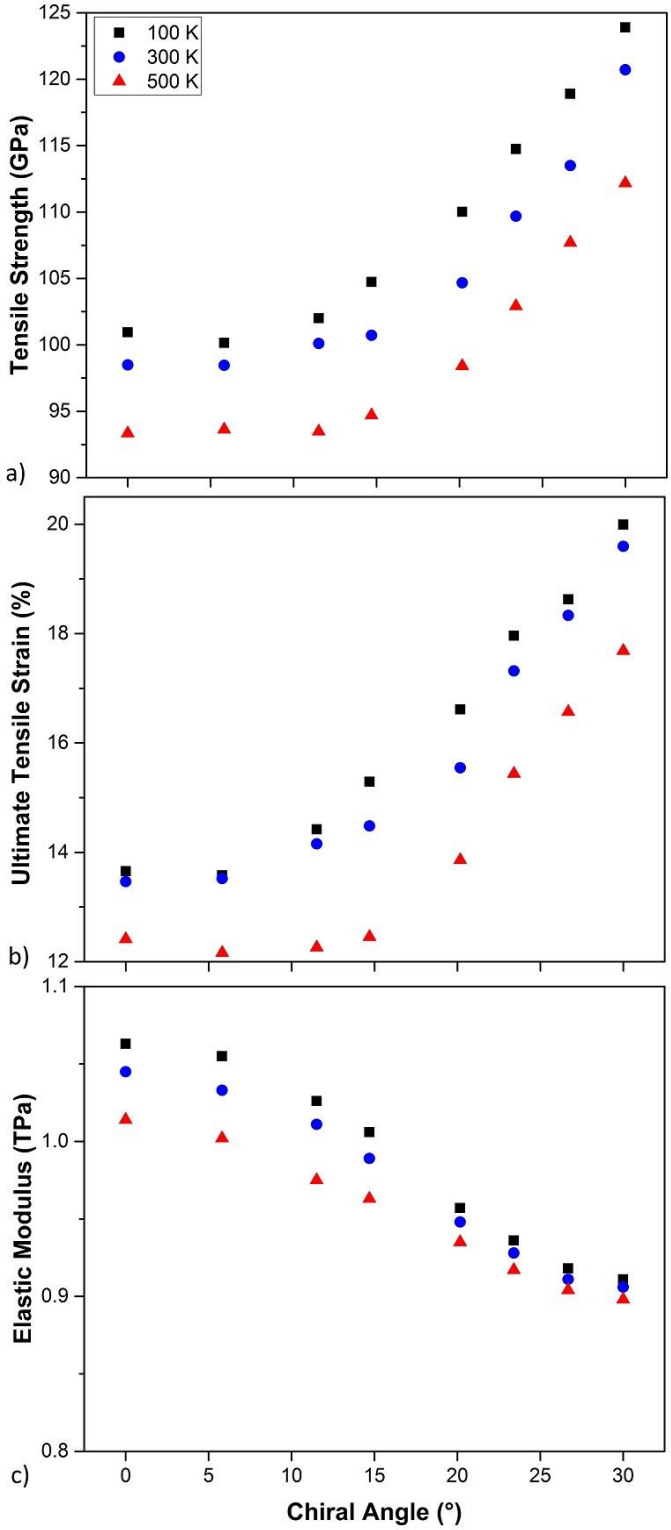

Figure 6.16. Influence of chirality and temperature on the a) tensile strength, b) ultimate strain and c) elastic modulus of SWCNTs

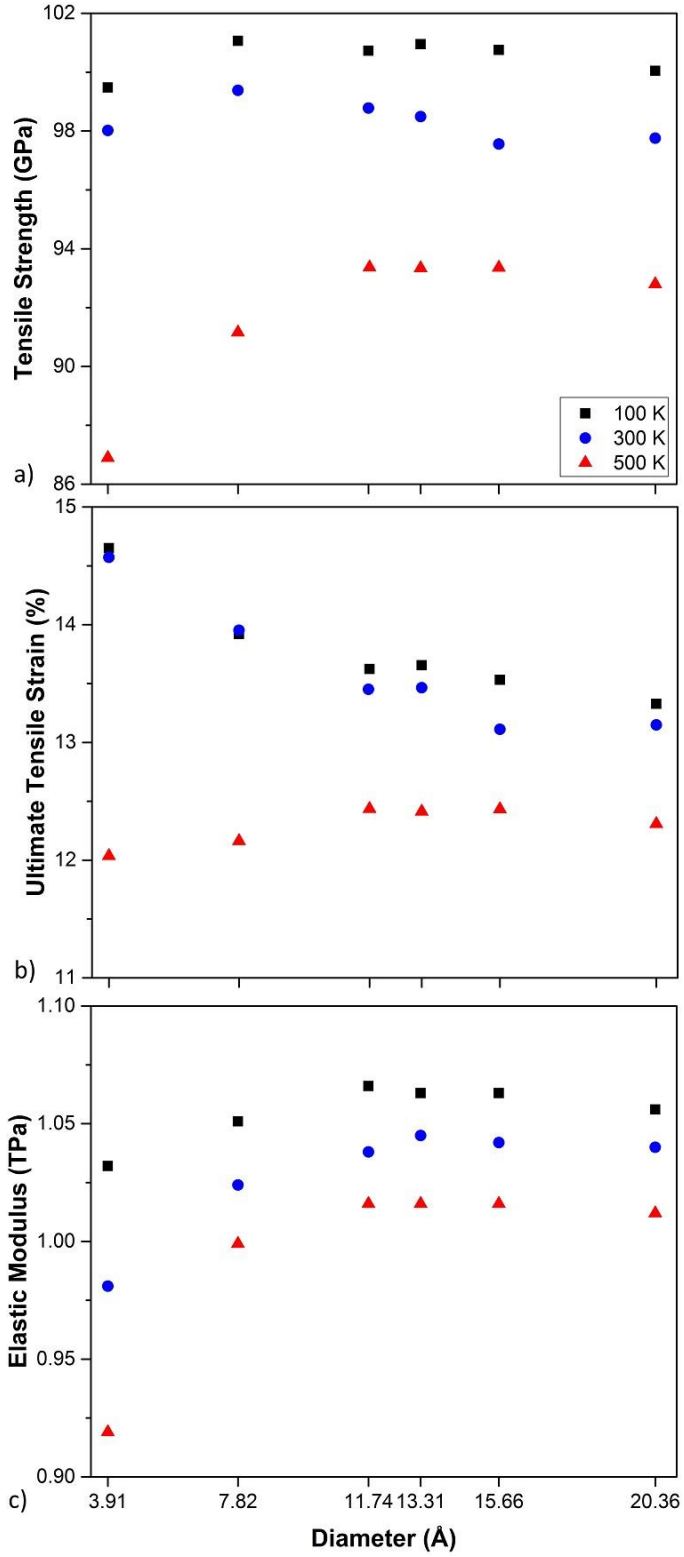

Figure 6.17. Influence of diameter on the a) tensile strength, b) ultimate strain and c) elastic modulus of zigzag SWCNTs

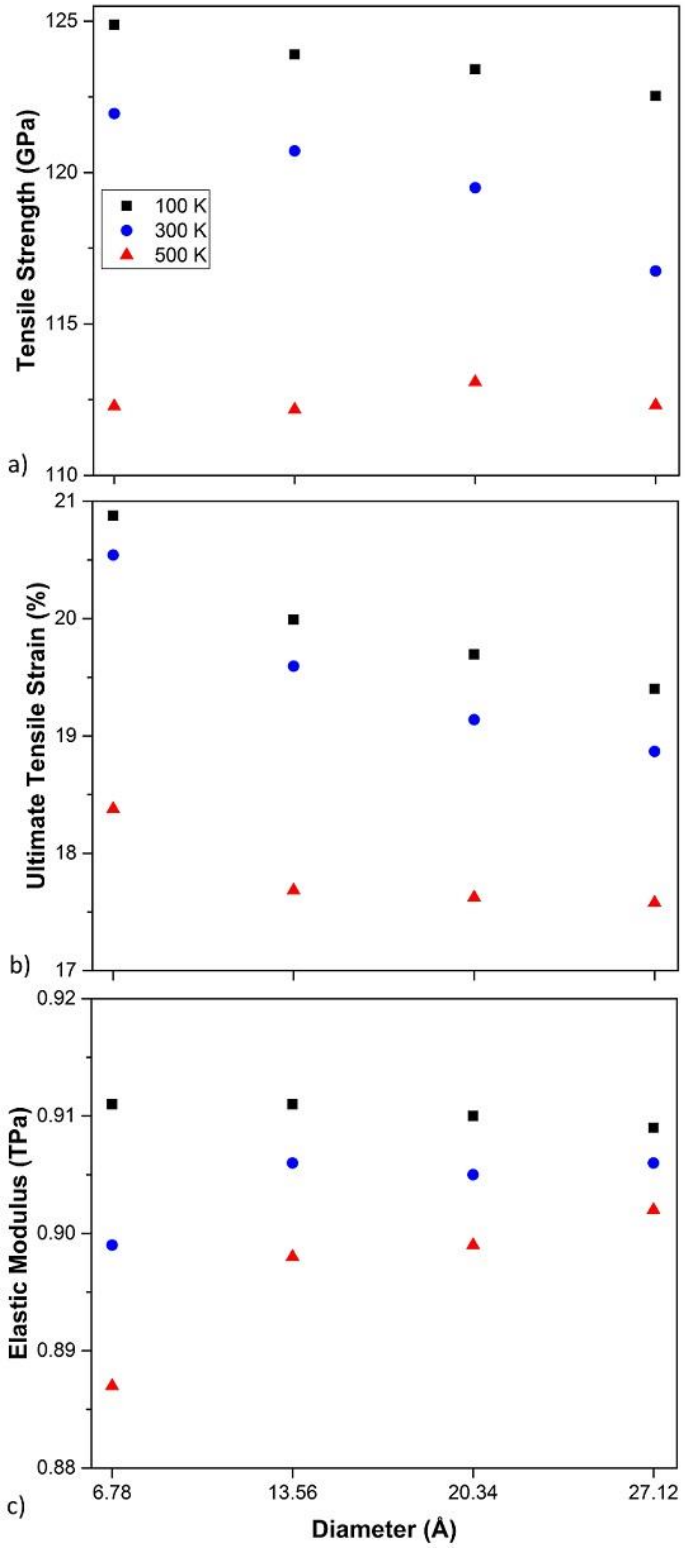

Figure 6.18. Influence of diameter on the a) tensile strength, b) ultimate strain and c) elastic modulus of armchair SWCNTs

6.2.4. Conclusions

MD simulations were carried out in order to investigate the influence of chirality, size, aspect ratio and slenderness ratio on the tensile and compressive mechanical behavior of SWCNTs. The results of the compressive numerical experiments showed that the shortest SWCNTs exhibit a stable postbuckling behavior irrespective of the temperature applied. Also, the SWCNTs with a slenderness ratio of 10 showed temperature-dependency in their postbuckling behavior. This dependency was found to be more pronounced in slender CNTs (slenderness ratio ≥ 15) subjected to low strains. At larger strains, however, this distinction vanished where all CNTs exhibit similar postbuckling stress-strain responses.

The onset of buckling was found to be inversely proportional to the slenderness of the tubes where shorter tubes buckled at relatively lower strains. In addition, it was seen that the elastic modulus at a given temperature is not considerably influenced by slenderness ratio and chirality.

The results of the tensile experiments revealed a nonlinear elastic behavior for all CNTs. The failure modes that the fracture of zigzag CNTs were consistently found to occur perpendicularly to the loading direction, while diagonal fractures were observed for armchair and chiral CNTs. The results also indicate that the tensile strength and strain at failure steadily increased as the chiral angle increased from 0 for zigzag CNTs to 30° for armchair CNTs. In addition, larger CNTs were found to possess lower tensile strengths and fail at lower strains.

6.3. MD simulation of pristine and SWCNT-filled polyethylene composites

6.3.1. Introduction

Polyethylene (PE) with the chemical formula of $(H_2C{=}CH_2)_nH_2$ is by far the most popular plastic that has enabled the innovative design and manufacture of countless commodities. In the geosynthetics industry, PE is the primary ingredient of geotextiles, geomembranes, geogrids, geopipes, geonets and geocomposites (Koerner 2012). Therefore, atomistic- and molecular-scale simulations on PE and other polymers used in geosynthetics industry will enable to better understand the underlying structural mechanisms controlling their mechanical properties in both pristine and composite forms and consequently improve the final products. These simulations are particularly advantageous to the development of SEG materials where the mechanical performance could be considerably influenced by the properties of the polymer and the carbonaceous filler (e.g. CNT) as well as the filler concentration.

There have been significant numerical efforts to understand and improve the mechanical properties of PE. Brown and Clarke (1991) carried out MD simulations on amorphous PE in order to characterize its elasticity, yield and plastic flow at different temperatures and reported a strong dependency of these characteristics to the temperature and an agreement between the MD results and laboratory measurements. These results were later reproduced by Depa and Maranas (2005, 2007) and Hossain *et al.* (2010) who used abstraction techniques to study larger PE systems. The following provides further details about how abstraction to models equivalent to the atomistic structure of polymers has enabled researchers to study large polymer systems that would have otherwise been impossible to investigate using the

current computational resources. One of the models is then used to study the mechanical properties of PE and CNT-filled PE composites.

6.3.2. Approximate models for polymer chains

In MD, it is tempting to construct a fully-atomistic computational model (also known as an explicit-atom (EA) model) of a sufficiently-large system of polymer chains where the chemical structure of monomers is elaborated. A sufficiently-large system refers to a simulation box with several hundred Å in dimensions where potential inaccuracies in simulation results cannot primarily be ascribed to the finite size or periodic boundary conditions of the box. The most computationally-intensive part of the MD simulation of an N-body system is the evaluation of pairwise interactions and the calculation of forces. The evaluation of pairwise interactions accumulates $N(N - 1)/2$ unique interactions. Therefore, $O(N^2)$ operations have to be solved if all pairwise interactions are sampled during a simulation. Usually, however, a cutoff is applied at a certain interatomic separation, beyond which the interactions are assumed to be negligible. This allows more efficiency in computing the forces, since all atom pairs need no longer be considered. In addition to the computational cost of fully-atomistic computational models, there is a broad spectrum of time scales associated with polymers ranging from 10^{-12} s for the vibration of an individual atom, to 10^{-6}–10^{-3} s for the conformational relaxation of polymer chains, to days (10^{13}–10^{15} s) for much slower phenomena such as phase separation and crystallization. Consequently, a fully-atomistic model of a sufficiently-large system with co-existing phenomena occurring at widely-different space and time scales is infeasible to solve, and abstraction to equivalent

coarse-grained models (e.g. the united atom model) on lattices with sufficient conformational flexibility is required (Baschnagel *et al.* 2000).

6.3.2.1. United atom approximation

United atom (UA) approximation is a coarse-grained approach where a particle obtained from the coalescence of a group of atoms is used to represent the group on a size scale larger than the atomic scale (Figure 6.19 – Bandyopadhyay *et al.* (2011)). Compared to the EA models, UA models provide a more computationally-efficient way for simulating molecular systems by means of reducing internal degrees of freedom and avoiding unnecessarily complicated details on the monomer level. Such an abstraction could extend the duration of an MD simulation to microseconds or even seconds, thus providing an insight into the long-term molecular-scale behavior of a system that would otherwise be infeasible to obtain in a fully-atomistic model (Toxvaerd 1990). UA models are particularly effective where the properties of a molecular system are primarily due to its intermolecular interactions (e.g. between monomers in a polymer) rather than its intramolecular bonds (e.g. the bonds between the atoms inside a monomer – Steinhauser and Hiermaier (2009)).

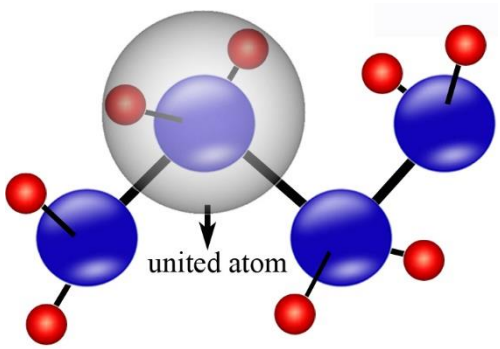

Figure 6.19. The united atom model

Coarse-grained and UA models are best suited for simulating the materials that are formed by repeating patterns of monomers and small molecules (e.g. macromolecular materials such as polymers). For the simulation of polymers, each monomer is conceived as a UA represented by a spherical bead. A sequence of these UAs forms a bead-string backbone that could be accordingly decorated with nonpolar, cationic, or anionic side chains to better represent a polymer (Ahadi and Konermann 2012). In general, the same concept as a UA can be used for a larger unit called segment, which is the minimum element of the statistical description of a polymer chain and is comprised of a set of monomers (a few to hundreds of monomers). For PE, the fast vibrations of the intramolecular bonds between C and H atoms in monomers are averaged out, and the polymer chain is modeled as a sequence of spherical UAs (CH_2 atomic units —methylene groups) connected by rigid rods or springs. Consequently, a 3-fold reduction in the number of particles is achieved that in turn decreases the computational cost 9-fold (Pant *et al.* 1993).

6.3.2.2. Lattice model of a polymer chain

A lattice model of a polymer chain is defined as a set of particles, denoted as segments, positioned sequentially on a spatial lattice structure to form a string-like polymer chain (Figure 6.20). The lattice can be of many possible forms such as 2D square lattice or 3D cubic lattice. The formation of the polymer chain is initiated from a point in the adopted lattice and evolved through a succession of random steps through nearest neighbors. The random selection of the nearest neighbors available to a point can be in accordance with a particular probability distribution. This distribution is usually considered as uniform, where each immediate neighbor is equally likely to be selected. It should be noted that although

assuming a lattice structure for a real polymer system is unrealistic, such simplification significantly reduces the complexity involved in real polymer systems and enables to investigate their essential and universal features in large scale (Kawakatsu 2004).

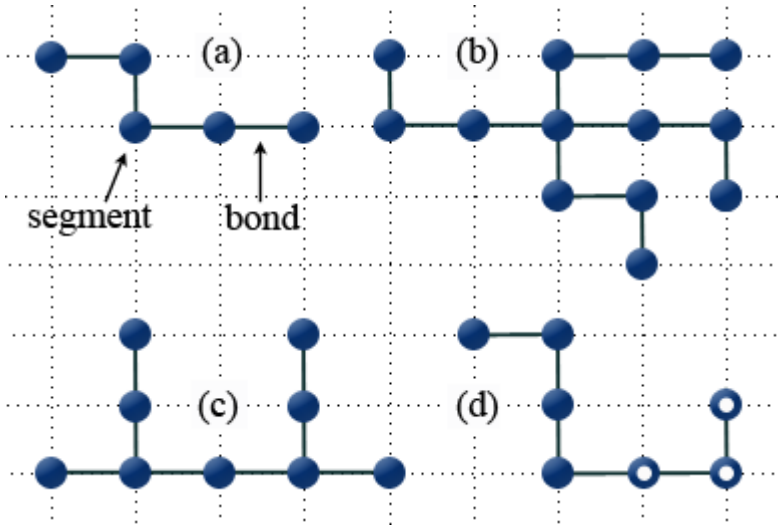

Figure 6.20. 2D lattice model for polymer chains with a) linear polymer, b) star polymer, c) comb polymer and d) copolymer chain topologies (after Kawakatsu (2004))

6.3.2.3. Configuration and conformation of a polymer chain

The macroscopic properties of a polymer chain are primarily controlled by its degree of polymerization. The degree of polymerization refers to the number of repeat units in the chain and gives a measure of molecular weight, which has a significant impact on the mechanical and rheological properties of a polymer; the mechanical properties (e.g. tensile strength and stiffness) and the flow viscosity of all polymers soar as the chain length increases.

The physical structure (topology) of a polymer chain is the other primary factor that substantially influences its macroscopic properties. The polymer topology is characterized by two distinct degrees of freedom: configuration and conformation. Configuration refers to

the arrangement of segments along the chain and cannot be altered unless chemical bonds are broken and reformed. The examples shown in Figure 6.20a-c illustrate different configurations on a 2D square lattice, and Figure 6.20d shows a copolymer which is a synthesis of different types of segments. In contrast to configuration, conformation refers to the possible 3D folding shapes that a polymer chain with a certain configuration can adopt through the rotation of molecules about single bonds. The distinction between configuration and conformation is further outlined in Figure 6.21. The two polymer chains shown in the figure have the same configuration; they are both comprised of a linear, 7-segment backbone with its middle segment connected to a 3-segment branch. However, their 3D structure is obviously different indicating different conformations.

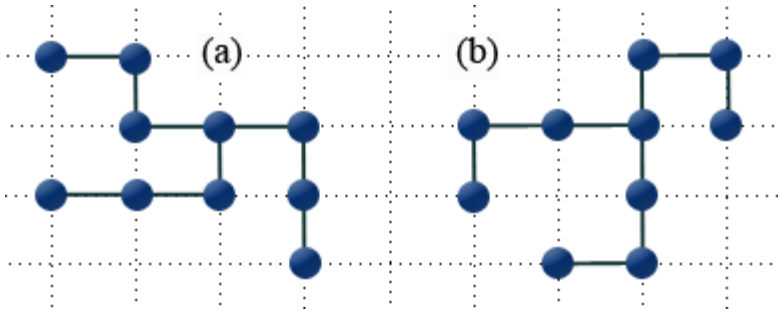

Figure 6.21. Polymer chains with identical configuration but different conformations (after Kawakatsu (2004))

6.3.2.4. Polymer confirmation and random walk model

From the mathematical point of view, the spatial configuration of a polymer chain can be ideally represented by visualizing the chain as a sequence of bonded monomer units (or segments) situated on a lattice. In this representation, a chain is formed by positioning a monomer/segment on a point in a prescribed lattice and moving randomly from this point to one of its nearest neighbors according to a probability density function and occupying it

with a new monomer/segment. Each two successive monomers are attached via a chemical bond of fixed length. The random selection of the nearest neighbors provides a considerable freedom of rotation about the individual bonds, thereby giving rise to a large number of configurations for this idealized polymer model. This mathematical formalization of stochastic succession of steps to define a complex structure is called random walk (also known as the drunkard's walk). Random walk is a nearly-ubiquitous concept in science and engineering with incredibly broad applications such as gas diffusion and heat conduction.

Self-avoiding random walk (SARW) is a type of random walks that does not permit visiting the same point on a lattice more than once (Figure 6.22). SARW is particularly suited for the modeling of real polymer molecules, where multiple occupancy of a monomer (self-intersecting) is physically unfeasible (Freed 1985). This property of polymers arises from the pair interaction between monomers and is known as the excluded volume property. This pair interaction is comprised of two contributions: short-range repulsion and long-range attraction. When two atoms (or molecules) approach each other quite closely, their electron orbitals start to overlap, creating a strong repulsion. This repulsive part of the interatomic interactions creates a spatial region referred to as hard core, which governs the proximity of neighbors by hampering local atomic rearrangements (Figure 6.23). At larger interatomic distances, an attractive interaction takes place between the electric dipoles of the two atoms where one of the dipoles, which is generated by an instantaneous deformation of the electron cloud of one atom, induces a dipole in the other atom. This attractive interaction that originates from the instantaneous dipoles is referred to as the van der Waals interaction.

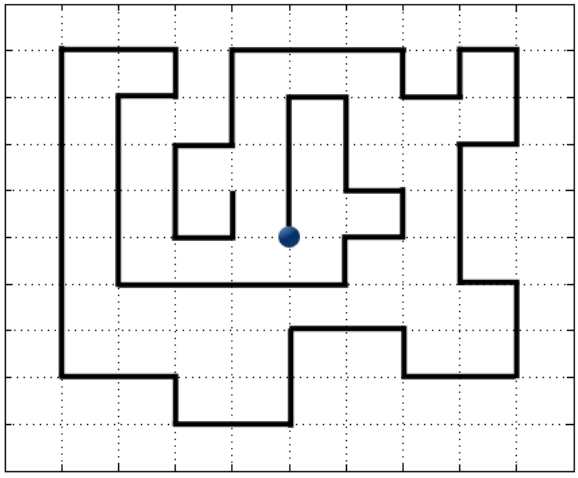

Figure 6.22. Self-avoiding random walk on a 2D square lattice

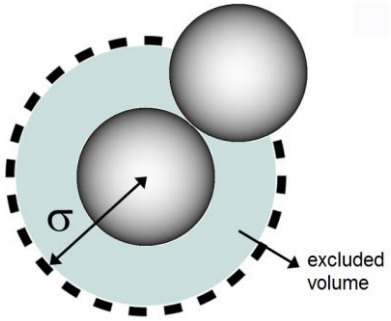

Figure 6.23. Physical meaning of excluded volume where hard cores severely hamper local atomic rearrangements (after Kawakatsu (2004))

6.3.3. MD simulation of PE and CNT-filled PE composites using UA approximation

6.3.3.1. Simulation models

Fully-atomistic representation of PE would involve a great number of atoms and their interactions into the simulations and require reducing the integration time step to a value smaller than the vibration period of hydrogen. Such a detailed representation would be computationally prohibitive. However, interactions in an H–C–H group are adequately strong to lump the atoms in a single bead and treat the group as a rigid cluster. In addition,

the objective of the simulations was to study the changes in the degrees of freedom in the backbone of each chain where the intermolecular interactions are more important. Therefore, a UA model was considered appropriate for the simulations.

Different combinations of chain length, number of chains, CNT type and CNT concentration as listed in Tables 6-4 and 6-5 were simulated in order to study their impacts on the mechanical properties of both low-density polyethylene (LDPE) and high-density polyethylene (HDPE) and their composites filled with CNT. The SARW algorithm proposed by Hossain *et al.* (2010) was adopted to create the initial configuration of the PE models. Each chain was formed by first positioning one UA (CH_2 unit) on a site in a face-centered cubic (FCC) lattice mapped onto a cubic simulation box and evolved through moving randomly from this site to one of its nearest neighbors according to a uniform probability density function until a certain number of sites, equal to the chain size, were visited (Figure 6.24a). Each two successive units were linked via a chemical bond of fixed length with the properties described in Section 6.3.3.2. The simulation cells were orthogonal with initial lateral dimensions chosen according to a density of 0.907 g/cc for LDPE and 0.986 g/cc for HDPE. For the composite models, a CNT with a length approximately equal to the lateral dimension of the cell was inserted in the middle of the cell along the z-axis (Figure 6.24c).

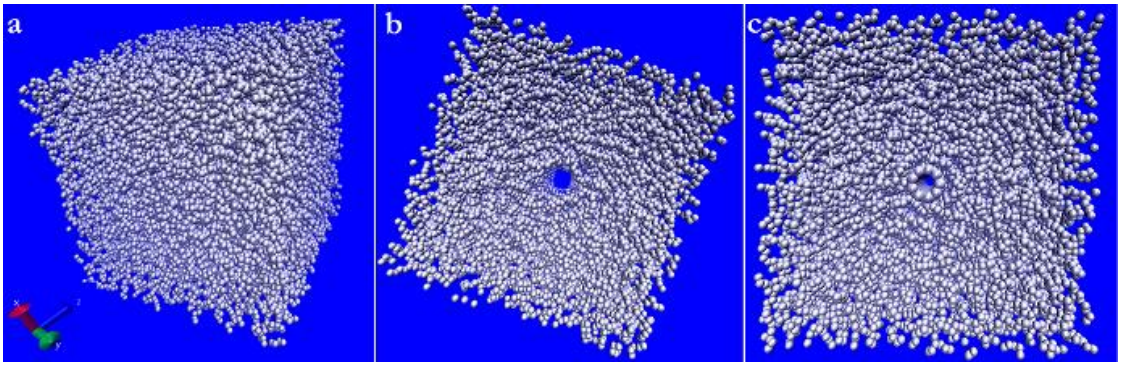

Figure 6.24. A CNT-filled PE model construction. a) polymer chains are generated according to a given set of density, chain length and number of chains, b) an indent is made at the center of the box along the z-axis, and c) a CNT is inserted in the hole.

Table 6-4. Information germane to the PE models studied. Temperatures studied: 100 and 300 K.

Model ID	Polymer	Chain length (monomers)	Number of chains	Number of monomers
LDPE-20-1000	LDPE	1,000	20	20,000
LDPE-40-1000			40	40,000
LDPE-80-1000			80	80,000
LDPE-120-1000			120	120,000
HDPE-20-1000	HDPE		20	20,000
HDPE-40-1000			40	40,000
HDPE-80-1000			80	80,000
HDPE-120-1000			120	120,000

Table 6-5. Information germane to the CNT-filled PE models studied. Temperatures studied: 100 and 300 K.

Model ID	Polymer	Chain length	No. of chains	No. of monomers	CNT (n,m)	No. of C atoms in CNT	CNT conc. (wt.%)
CNT09LDPE20k	LDPE	1,000	20	20,000	(0,9)	614	2.63
CNT09LDPE40k			40	40,000		793	1.69
CNT09LDPE80k			80	80,000		1008	1.08
CNT09LDPE120k			120	120,000		1188	0.85
CNT55LDPE20k			20	20,000	(5,5)	600	2.57
CNT55LDPE40k			40	40,000		780	1.67
CNT55LDPE80k			80	80,000		980	1.05
CNT55LDPE120k			120	120,000		1160	0.83
CNT216LDPE120k					(2,16)	2216	1.58
CNT415LDPE120k					(4,15)	2282	1.63
CNT713LDPE120k					(7,13)	2312	1.65
CNT812LDPE120k					(8,12)	2296	1.64
CNT911LDPE120k					(9,11)	2286	1.63
CNT09HDPE20k	HDPE	1,000	20	20,000	(0,9)	612	2.62
CNT09HDPE40k			40	40,000		783	1.68
CNT09HDPE80k			80	80,000		1008	1.08
CNT09HDPE120k			120	120,000		1116	0.79
CNT55HDPE20k			20	20,000	(5,5)	590	2.52
CNT55HDPE40k			40	40,000		750	1.60
CNT55HDPE80k			80	80,000		980	1.05
CNT55HDPE120k			120	120,000		1120	0.80
CNT216HDPE120k					(2,16)	2188	1.56
CNT415HDPE120k					(4,15)	2221	1.58
CNT713HDPE120k					(7,13)	2250	1.60
CNT812HDPE120k					(8,12)	2232	1.59
CNT911HDPE120k					(9,11)	2221	1.58

6.3.3.2. Interatomic potential

The Dreiding force field (Mayo *et al.* 1990) was used to describe the interactions between/among the UAs. The force field is comprised of four functional components: a harmonic bond energy, a harmonic bending energy, a three-term cosinusoidal torsional energy and a 6–12 LJ potential to consider van der Waals interactions (see Table 6-6). The interactions between carbon atoms in CNT were defined using the AIREBO potential (Brenner 1990). The non-bonded interactions between the UAs and the CNT carbon atoms

were described using the geometric mean combining rule (also known as the Good-Hope rule) as (Good and Hope 1970):

$$\sigma_{ij} = \sqrt{\sigma_{ii}\sigma_{jj}} \tag{6-15}$$

$$\varepsilon_{ij} = \sqrt{\varepsilon_{ii}\varepsilon_{jj}} \tag{6-16}$$

Table 6-6. Dreiding force field parameters and corresponding values used for the MD simulations of PE (Mayo et al. 1990)

Energy term	Functional form	Parameters
Stretching	$E_{\text{bond}}(r) = k_r(r - r_0)^2/2$	k_r = 1 464 kJ/mol; r_0 = 1.53 Å
Bending	$E_{\text{angle}}(\theta) = k_\theta(\theta - \theta_0)^2/2$	$k_{\theta 0}$ = 251 kJ/mol/rad^2; θ_0 = 109.5°
Torsion	$E_{\text{dihedral}}(\phi) = \sum_{i=0}^{3} C_i(\cos\phi)^i$	C_0 = 7.26; C_1 = -18.79; C_2 = 3.25; C_3 = 29.25 (kJ/mol)
van der Waals	$E_{\text{vdw}}(r) = 4\varepsilon\left[(\sigma/r)^{12} - (\sigma/r)^6\right], r \le r_c$	σ = 4.01 Å; ε = 0.489 kJ/mol r_c = 10.5 Å; E_{vdw} = 0 for $r > r_c$

6.3.3.3. Simulation sequence

The initial structure of each PE model was subjected to an equilibration sequence as described below to relax any high energy configurations that would otherwise generate huge forces blowing the model components out of the simulation box. A time step of 1 fs (1×10^{-15} s) was used in all simulations. Each model was initially subjected to Langevin dynamics at 500 K and the constant NVE for 10 ps (20,000 time steps). The maximum distance an atom can move in one time step was limited to 0.05 Å. Subsequently, NPT (isothermal–isobaric) ensemble at 500 K and zero pressure was applied for 10 ps (20,000 time steps). The Nosé–Hoover thermostat and barostat were employed to control temperature and pressure. The entire collection of atoms was ensured not to drift or rotate during the simulation due to random perturbations.

The subsequent relaxation cooled the structure down to the desired temperature over a period of 12.5 ps (25,000 time steps) maintaining the pressure components at zero (cooling rate between successive temperatures was 1 K/ps). Volume change of the system LDPE-20-1000 in pristine form due to cooling down from 500 K to 100 K is shown in Figure 6.25. A glass transition temperature of 267 K, which is the temperature corresponding to the point of maximum curvature in the temperature-volumetric strain curve, is quoted for PE, which is consonant with the values observed in the laboratory experiments (e.g. 240 K – Davis and Eby (1973)). The glass transition temperature corresponds to a distinct transition from a hard, glassy state to a soft, rubbery state where polymer chains obtain full segmental mobility (van Melick *et al.* 2003). Two different temperatures of 100 K and 300 K as representative temperatures for each state were studied.

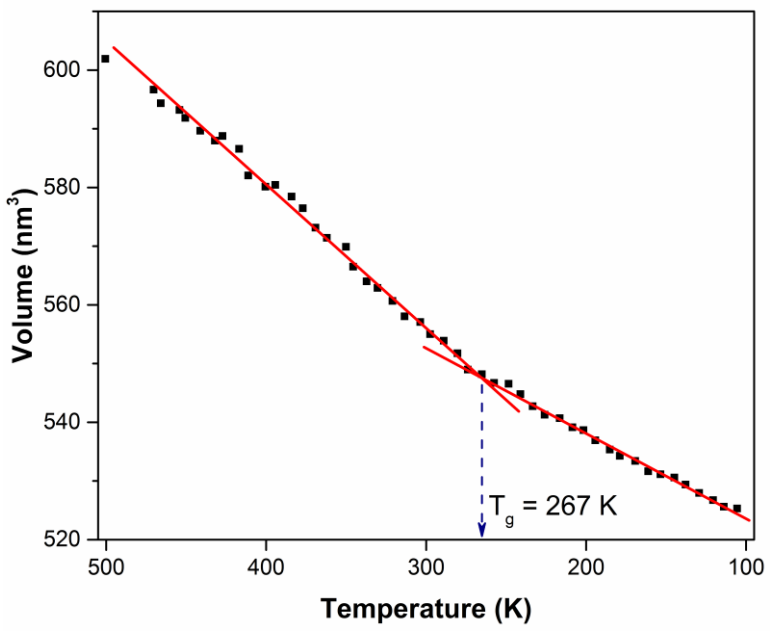

Figure 6.25. Volume change of the model LDPE-20-1000 in pristine form as a function of temperature

Following the cooling stage, the models were further relaxed for 10 ps (20,000 time steps) at the desired temperature using NPT ensemble. The energy history of the models was observed to ensure negligible energy drift at the end of each stage. In addition, their microstructures were frequently visualized in order to assure their appropriateness for the deformation stage. The corresponding statistics were collected at a frequency of 0.05 ps.

For CNT-filled PE composite models, a cylindrical hole was first indented into the center of the corresponding equilibrated simulation box along the z axis (FIG) through exerting a radial repulsive force (Figure 6.24b):

$$F(r) = -K(R - r)^2 \tag{6-17}$$

on the atoms with $r < R$, where K is the force constant (here 100 kJ/mol/Å^3); r is the distance from each atom to the center of the indenter; and R is the radius of the indenter. In this study R was selected to be 2 Å greater than the radius of the to-be-inserted CNT. This value is within the distance where van der Waals interactions between UAs and C atoms take place (from Equation (6-15) and Table 6-6, knowing σ_{cc} = 1.7–2 Å, according to the AIREBO potential). Having indented the cylindrical hole, a CNT with the chirality and information given in Table 6-5 was inserted in the hole to create a CNT-filled PE composite model (Figure 6.24c). The energy of the model was then minimized by iteratively adjusting the UA coordinates.

Eventually for all the models, the simulation box was subjected to uniaxial tensile deformation at a strain rate of 0.01/ps. This was achieved by decoupling the boundary along the z axis from the NPT equations of motion and holding the pressure along the other directions at zero. The stress components were computed from the symmetric pressure

tensor, which combines the stress components from kinetic energy tensor and the virial tensor. The contributions of bond, angle, dihedral and improper energies (collectively referred to as molecular energy) and the pairwise energy to the energy of the box were also tracked as a function of strain.

6.3.4. Results and discussion

6.3.4.1. Stress-strain behavior of PE

The stress-strain behaviors of the LDPE and HDPE models at 100 K and 300 K and their corresponding volumetric strain vs. uniaxial strain responses are shown in Figure 6.26 to Figure 6.29. Comparison of the results indicates that the models simulated at a certain temperature exhibited similar behavior regardless of their density, especially during the elastic stage. This observation is consonant with the findings of Hadley (1975) who reported that the impact of polymer structure and texture on the inelastic response is far greater than that on the elastic response, especially for glassy polymers.

The models simulated at 100 K showed typically three stages of deformation, i.e., elastic behavior up to the yield stress, post-yield strain softening and strain hardening (Figures 6.26 and 6.27).

The models stretched at 100 K showed an initial linear portion followed by yielding at a strain of approximately 20% and stresses ranging from 130 to 160 MPa for both LDPE and HDPE models, giving an elastic modulus in the range 650–800 MPa. For an idealized polymer consisting of a random array of long, entangled molecular chains intersecting one another and stretched at a temperature below its glass transition temperature, this stage

involves the exceedance of its isotropic intermolecular resistance to rotation, marking the onset of large-strain inelastic flow (Haward and Thackray 1968; Wu and van der Giessen 1993).

With respect to volume changes, it is well known that elastic strains produce significant changes in volume. However, Whitney and Andrews (1967) showed that polymers might undergo further volumetric strains during plastic flow. This notion together with the anisotropy of polymers at the yield stress and the pressure-dependency of the yield stress explain the deviation of the orientation of the plastic zone from 45° with respect to the principal planes of stress (Bowden and Jukes 1972).

It can be seen from Figures 6.26 to 6.29 further deformation causes the models to stress-soften, indicating by the so-called 'yield-drop' of the material up to 55% strain. Strain-softening includes the increasing alignment of chains in the loading direction and results in the strain localization in a specimen, hence dominating its macroscopic deformation behavior and failure mode. The impact of strain-softening, however, is greatly dependent on the thermal and mechanical histories of the polymer. For instance, a slowly-cooled specimen prepared by compression-molding exhibits more softening than a quenched specimen and consequently shows more-localized deformation behavior in tension and extensive plastic deformation (necking) before fracture (Cross *et al.* 1979). In contrast, mechanical preconditioning or predeformation of a specimen has been shown to suppress its strain-softening behavior (Govaert *et al.* 1999).

Consonant with the findings of Hadley (1975), the main difference between the models were found in their strain-hardening behavior which is characterized by a corresponding modulus

defined as the slope of the stress-strain curve in the strain-hardening stage. Strain-hardening stems from a decrease in the configurational entropy of a system known as orientational hardening. This stage involves the anisotropic internal resistance of a polymer to plastic flow. This resistance, which controls the evolution of the localized plastic zones developed during strain-softening, arises from the hindrance imposed by aligned neighboring chains on a chain's rotation either individually or in a cluster (Boyce *et al.* 1989; Han *et al.* 2000). As can be seen in Figures 6.27 and 6.29, all the HDPE models studied exhibit fairly similar behaviors in their strain-hardening response. The strain-hardening response of the LDPE models, however, is influenced by chain length where the LDPE models with longer chains show higher strain-hardening modulus. The impact of density on the strain at failure of PE was found insignificant.

Comparison of the results shown in Figures 6.26 to 6.29 also indicate that although both LDPE and HDPE models exhibit high ductility, the LDPE models fail at a relatively larger strain, possibly due to their less strong induced-dipole attractions that would in turn reduce the intermolecular forces. These findings are in qualitative agreement with previous simulations and experimental results (Capaldi *et al.* 2002, 2004).

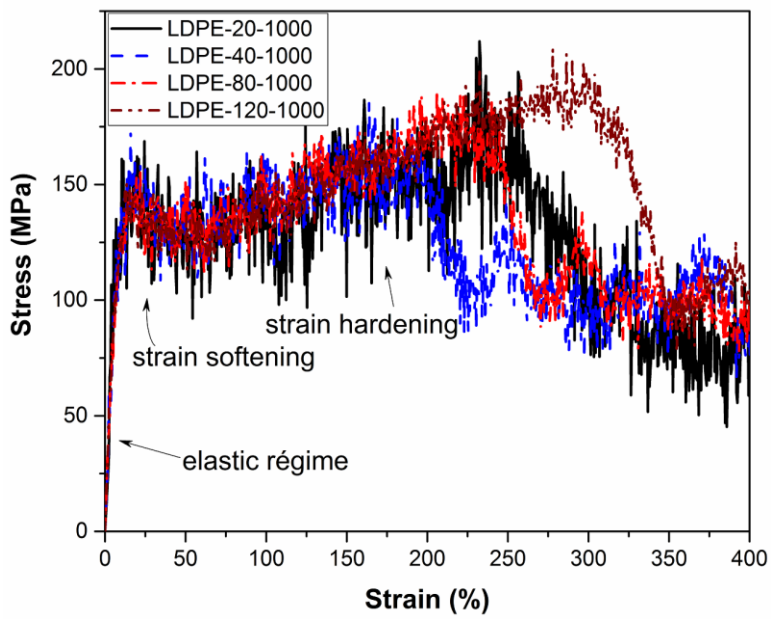

Figure 6.26. Stress-strain response of the LDPE models at 100 K. Strain rate = 0.01/ps.

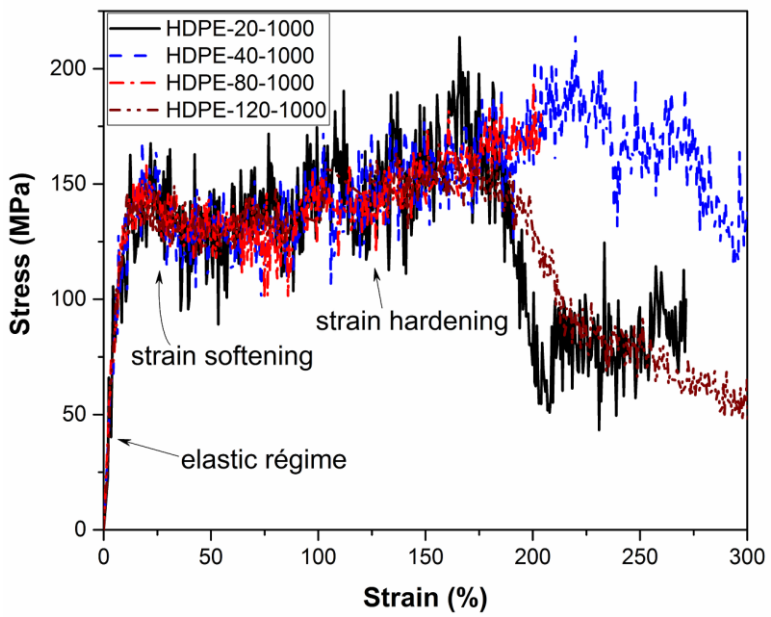

Figure 6.27. Stress-strain response of the HDPE models at 100 K. Strain rate = 0.01/ps.

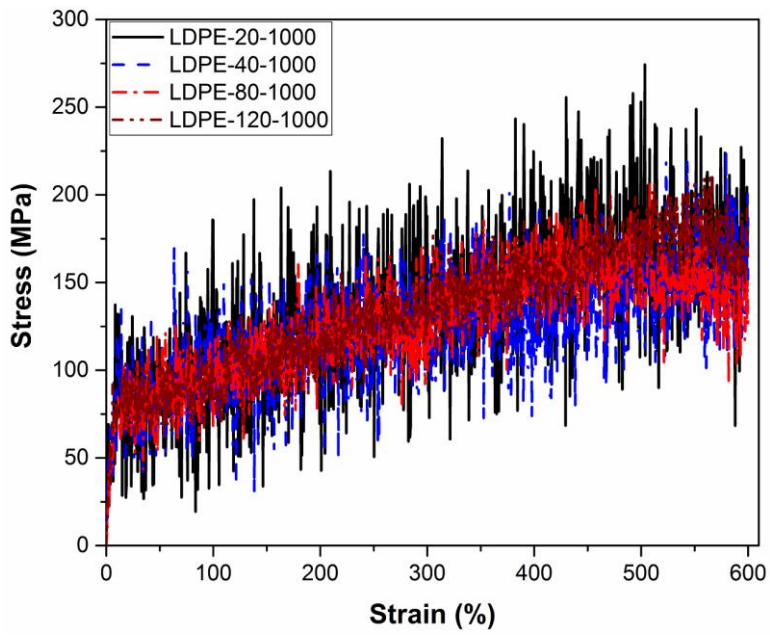

Figure 6.28. Stress-strain response of the LDPE models at 300 K. Strain rate = 0.01/ps.

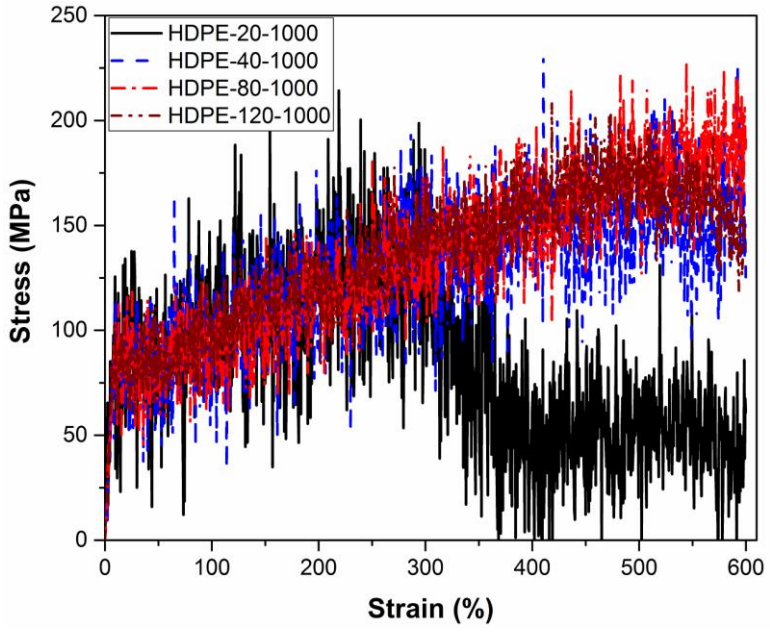

Figure 6.29. Stress-strain response of the HDPE models at 300 K. Strain rate = 0.01/ps.

6.3.4.2. Stress-strain behavior of CNT-filled PE composites

The stress-strain response of the model CNT09LDPE20k as a typical behavior for the models described in Table 6-5 is shown in Figure 6.30. It can be seen that the model follows a nonlinear behavior until an initial failure at a strain close to the failure strain of CNT (see Section 6.2.3.2). Once the CNT fails, the strength suddenly drops to a value close to the strength of pristine polymer (see Figure 6.28).

The influence of CNT concentration on the strength of PE composites is shown in Figure 6.31. Results indicate that the strength of both LDPE and HDPE composites increases linearly with CNT concentration. This trend is in qualitative agreement with that observed in the laboratory experiments. However, the values reported for the strength of CNT-filled PE composites in the literature are in the range 10–25 MPa (Zhang *et al.* 2006; Xiao *et al.* 2007). The anticipated strong discrepancy between the MD simulation results and experimental observations is common across the literature and could be attributed to the following factors:

- The very short length scales used in MD simulations compared to experiments: in MD simulations, a perfect simulation box is first constructed and then duplicated using periodic boundary conditions in order to mimic infinite-size systems. However, this *ad hoc* does not necessarily result in a model fully representative of a laboratory specimen, as the dispersion of CNTs in real specimens is not perfect, CNTs are short compared to the specimen dimensions and not all CNTs are oriented along the loading direction. In addition, periodic boundary conditions stiffen the simulation box through restraining the

lateral movement of the simulation box, enabling the composite to withstand larger stresses at a certain strain.

- The very short time scales used in MD simulations (e.g. nanoseconds) compared to experiments (e.g. hours or days) does not allow the constituents to interact with one another as extensively as they do in laboratory specimens.

- It is usually impossible to fully consider all fabrication stages (e.g. mixing and curing) in an MD simulation, whereas, as consistently shown in previous chapters, the preparation method used for laboratory specimens significantly influences their properties.

- The defects developed in CNTs during manufacturing have a profound impact on their properties. However, the CNTs modeled in this study were assumed to be defect-free.

- A perfect interface that was assumed between CNTs and the host matrix in the simulations is impaired in laboratory specimens due to the deformed shape of CNTs and their defects as well as the impurities existing in the samples.

- The inaccuracy of the force fields that were used in the simulations.

The influence of CNT chirality on the strength of PE composites is shown in Figure 6.32. Results indicate that all chiral CNTs have approximately the same reinforcing effect on the polymer. The general trend, however, is descending, where the composites filled with more chiral CNTs exhibit less strength.

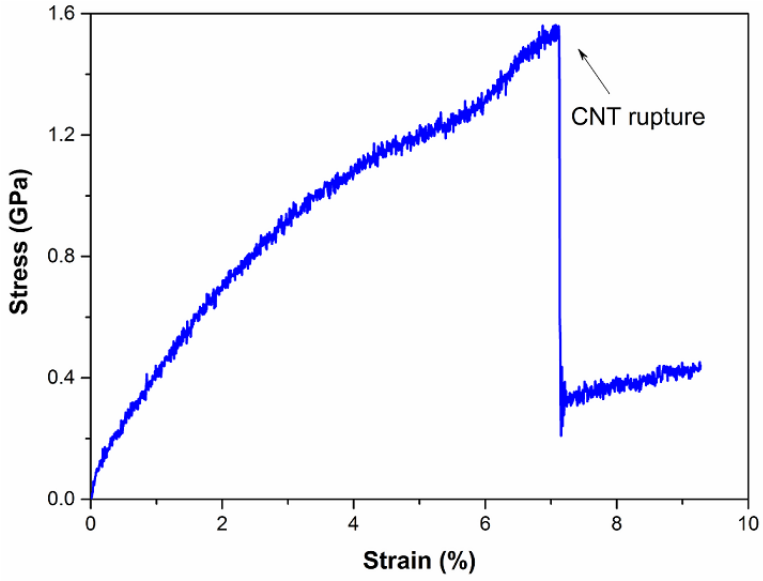

Figure 6.30. Stress-strain response of the model CNT09LDPE20k at 300 K. Strain rate = 0.01/ps.

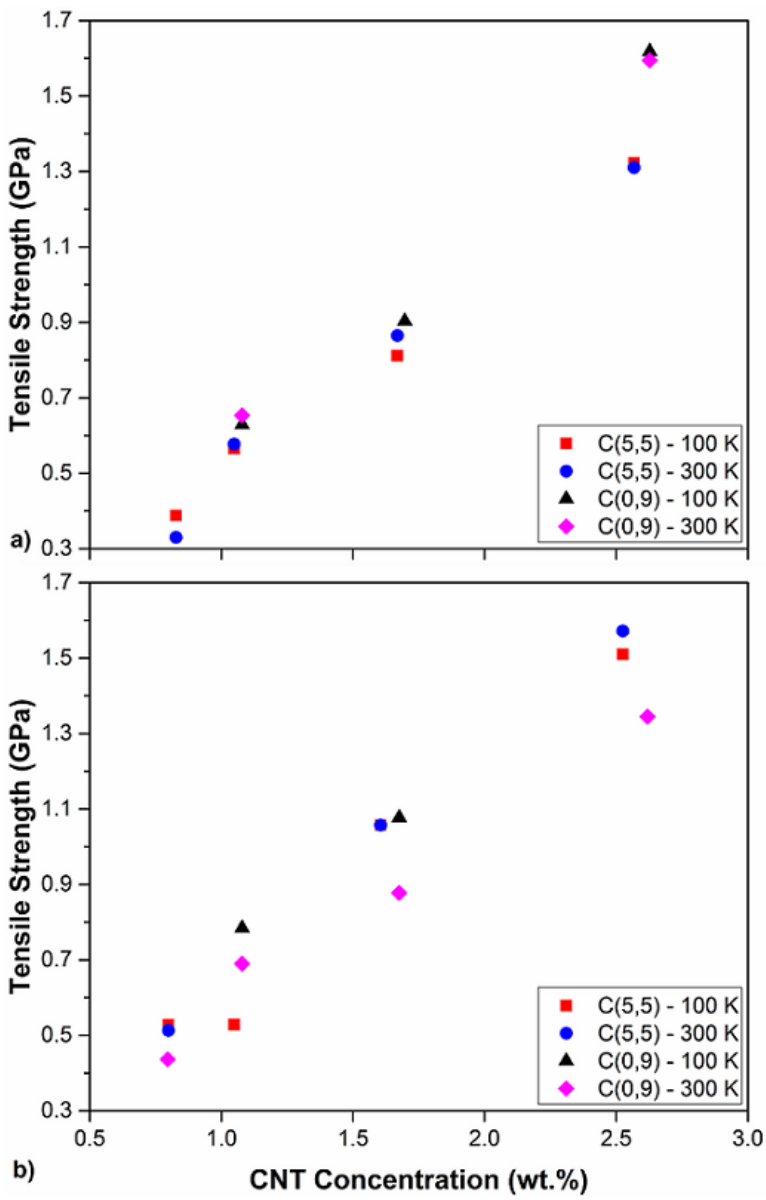

Figure 6.31. Influence of CNT concentration on the strength of CNT-filled a) LDPE and b) HDPE composites. Strain rate = 0.01/ps.

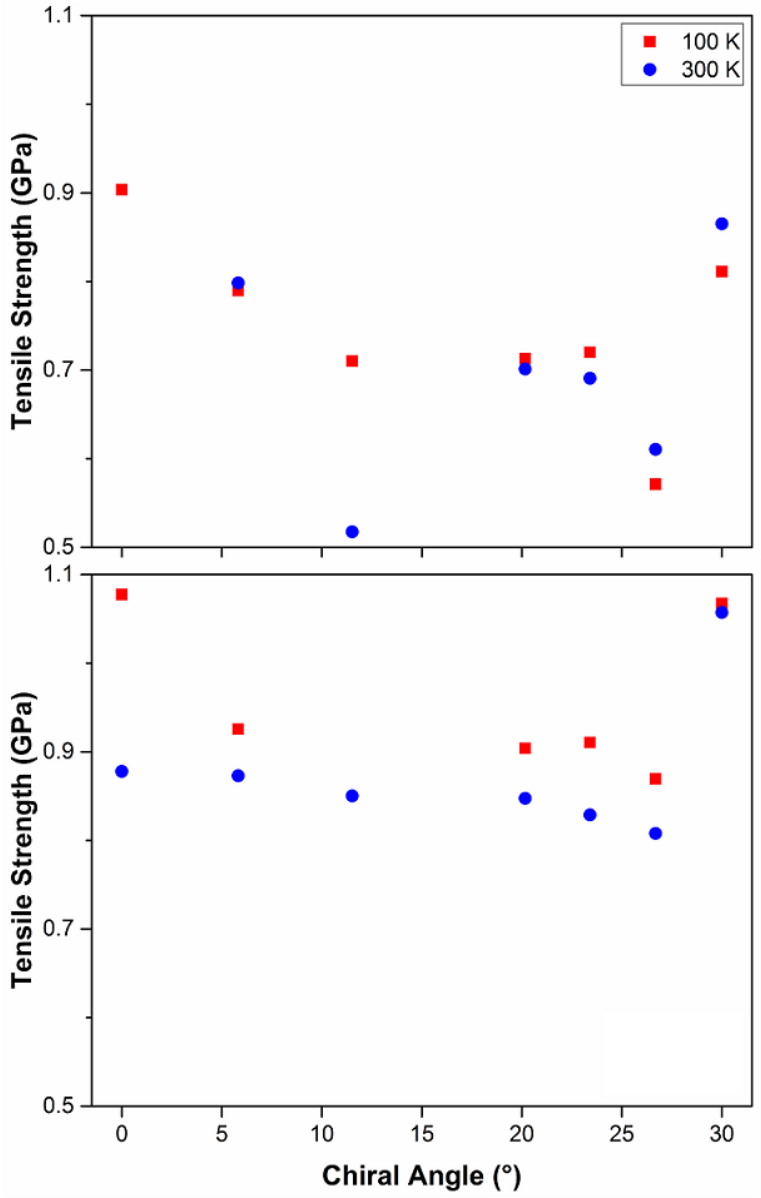

Figure 6.32. Influence of CNT chirality on the strength of CNT-filled PE composites. Strain rate = 0.01/ps.

6.4. MD simulation of polyvinyl chloride

This section presents fully-atomistic MD simulations on PVC.

6.4.1. Simulation models

Commercial PVC with the chemical formula $H_2C(H_2C{=}CHCl)_{n-2}CHCl$ contains approximately 10% crystallinity. This relatively low crystallinity is sufficient to have significant impact on the processing and properties of PVC, making it solid in room temperature (Gilbert 1994). However, the PVC commonly used in the geosynthetics industry is mixed with a plasticizer (PVC plastisol) and flows as a liquid in room temperature.

This section reports the MD simulations that were carried out in order to investigate the mechanical properties of PVC plastisol in both pristine form and when mixed with CNT. Three different tacticities for PVC were studied: isotactic, syndiotactic and atactic (Figure 6.33). Due to the computational cost involved, the total number of monomers in each PVC model was limited to 1,000. The protrusion of chains in Figure 6.33 is due to the periodic boundary conditions applied. Different combinations of tacticity, chain length and number of chains as listed in Table 6-7 were simulated in order to study their impacts on mechanical properties. Since amorphous PVC is liquid and shows no glass transition temperature (T_g) (described in detail later), it was assumed that its properties in room temperature would represent those of semicrystalline PVC above its T_g (353 K). Only the room temperature (conveniently 300 K) was considered. The simulation cells were orthogonal with lateral dimensions of 40.9 Å × 40.9 Å × 40.9 Å, giving a density of 1.523 g/cc. This density was also used by Hirvi and Pakkanen (2006) to study the hydrophobicity of PVC using MD. For computational efficiency, neighbor lists were built to keep track of nearby particles. The separation factor was set to 0.26/Å. The neighbor lists were updated every 10 integration time steps (every 5 fs), and the maximum number of neighbors for one atom was limited to 10,000.

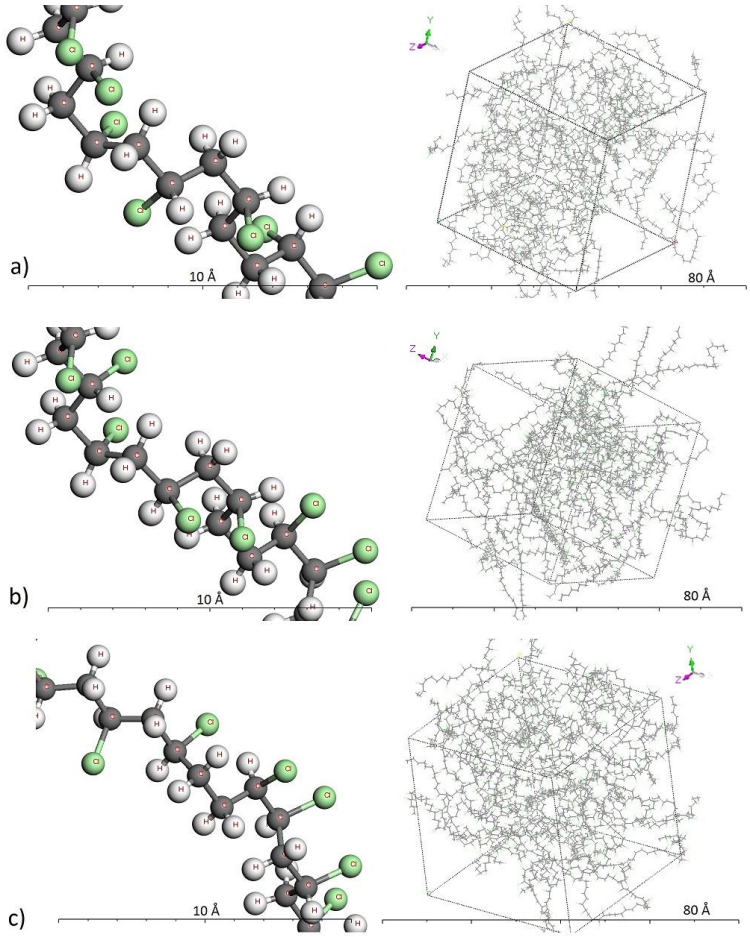

Figure 6.33. Single chain (left) and amorphous box (right) of a) isotactic (substituents on the same side of the chain), b) syndiotactic (substituents on alternating sides of the chain) and c) atactic (substituents placed randomly along the chain) PVC. Note: each box contains 30 PVC chains each having 33 monomers.

Table 6-7. Information germane to the PVC models studied

Model ID	Tacticity	Number of chains	Chain length (monomers)	Number of monomers
Iso-10-100	Isotactic	10	100	1,000
Iso-20-50		20	50	1,000
Iso-30-33		30	33	999
Syn-10-100	Syndiotactic	10	100	1,000
Syn-20-50		20	50	1,000
Syn-30-33		30	33	999
Atc-10-100	Atactic	10	100	1,000
Atc-20-50		20	50	1,000
Atc-30-33		30	33	999

6.4.1.1. Interatomic potential

The force field PCFF was used to define the interactions between the atoms in the models (i.e. C, H and Cl). PCFF is a member of a family of the CFF force fields (CFF91, PCFF, CFF and COMPASS) that have been parameterized against a wide range of experimental observables for polymers and organic compounds. PCFF is an extended version of CFF91 and was developed to cover organic polymers, (inorganic) metals and zeolites. It is useful for many materials including polymers and inorganic metals and has been adopted to study mechanical properties, compressibility and heat capacity (Sun *et al.* 1994).

6.4.1.2. Simulation sequence

The initial structure of each PVC model was subjected to an equilibration sequence as described below to relax any high energy configurations that would otherwise generate huge forces blowing the model components out of the simulation box. A time step of 0.5 fs (0.5×10^{-15} s) was used in all simulations. Each model was initially subjected to Langevin dynamics at 500 K and the constant NVE for 10 ps (20,000 time steps). The maximum distance an atom can move in one time step was limited to 0.05 Å. Subsequently, NPT (isothermal–isobaric) ensemble at 500 K and zero pressure was applied for 10 ps (20,000 time steps). The Nosé–Hoover thermostat and barostat were employed to control temperature and pressure. The entire collection of atoms was ensured not to drift or rotate during the simulation due to random perturbations.

The subsequent relaxation cooled the structure down to the desired temperature over a period of 12.5 ps (25,000 time steps) maintaining the pressure components at zero (cooling rate between successive temperatures was 1 K/ps). Volume change of the system Iso-10-

100 due to cooling down from 500 K to 100 K is shown in Figure 6.25. A glass transition temperature of 258 K, which is the temperature corresponding to the point of maximum curvature in the temperature-volumetric strain curve, is estimated for the system. The glass transition temperature corresponds to a distinct transition from a hard, glassy state to a soft, rubbery state. Two different temperatures of 100 K and 300 K as representative temperatures for each state were studied.

Following the cooling stage, the models were further relaxed for 10 ps (20,000 time steps) at the desired temperature using NPT ensemble. The energy history of the models was observed to ensure negligible energy drift at the end of each stage. In addition, their microstructures were frequently visualized in order to assure their appropriateness for the deformation stage. The corresponding statistics were collected at a frequency of 0.05 ps. An example of the history of the total energy and its kinetic and potential components is shown in Figure 6.35.

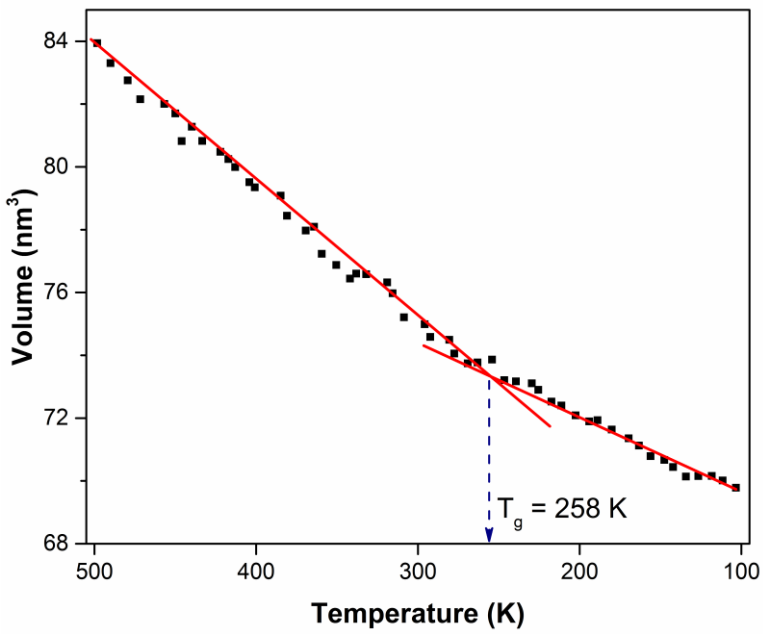

Figure 6.34. Volume change of the model Iso-10-100 as a function of temperature

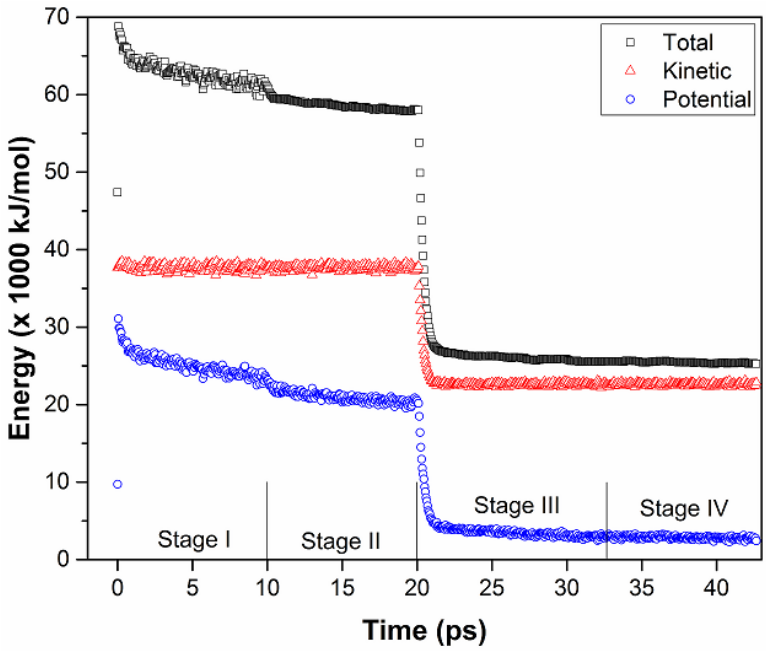

Figure 6.35. Evolution of the energy of the model Iso-10-100 during relaxation

Eventually, assuming the simulation box was isotropic due to the random distribution and orientation of constitutive chains, the box was subjected to uniaxial tensile deformation at a

strain rate of 0.001/ps. This was achieved by decoupling the boundary along the x axis from the NPT equations of motion and holding the pressure along the other directions at zero. The stress components were computed from the symmetric pressure tensor, which combines the stress components from kinetic energy tensor and the virial tensor. The contributions of bond, angle, dihedral and improper energies (collectively referred to as molecular energy) and those of the pairwise energy constituents (i.e. van der Waals, Coulombic, long-range kspace and long-range tail correction) to the total energy were also tracked as a function of strain.

6.4.2. Results and discussion

6.4.2.1. Stress-strain behavior

The stress-strain behavior of the model Iso-10-100 at 300 K and its corresponding microstructural evolution are shown in Figure 6.36 and Figure 6.37. Figure 6.36 indicates an initial linear portion followed by yielding at 4.8% strain. Further deformation of the model caused the stress to decline, indicating the strain softening behavior of the material up to 22% strain. As strain increases, the polymer chains are further aligned along the stretching direction, and the material undergoes strain hardening (Sarva and Boyce 2007). The stress increases almost linearly up to a large strain of 355% where failure occurs, showing the considerable ductility of the material.

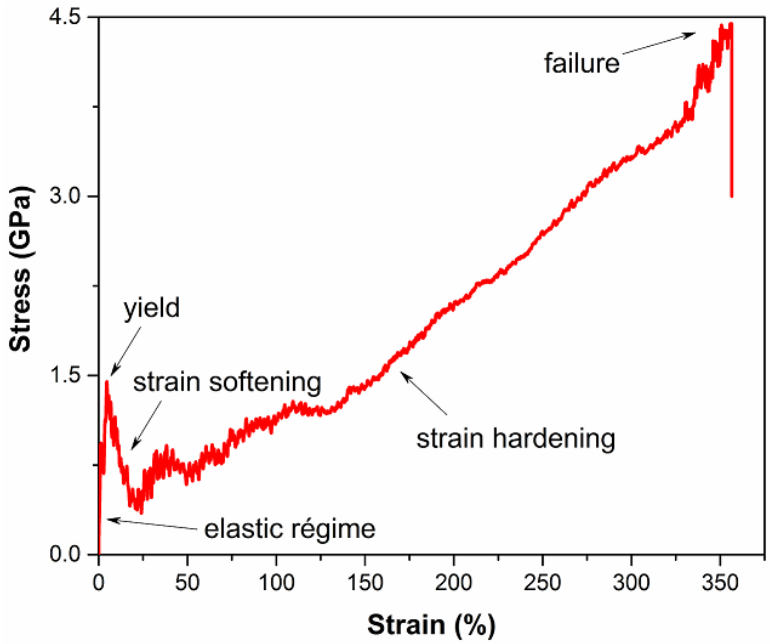

Figure 6.36. Stress-strain response of the model Iso-10-100 at 300 K in uniaxial tension

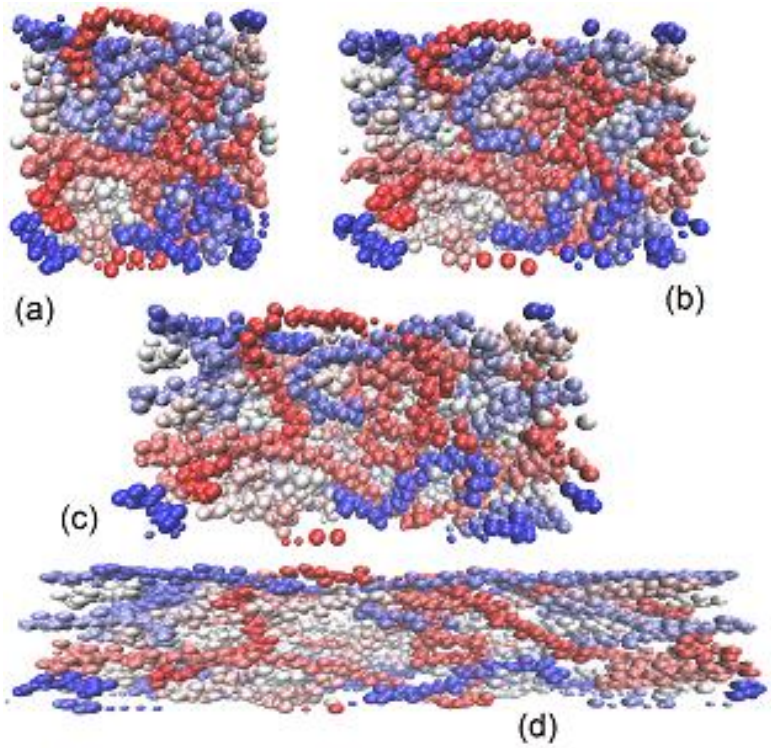

Figure 6.37. Microstructural evolution of the model Iso-10-100 at a) 0%, b) 50%, c) 100% and d) 200% strain. T = 300 K.

6.4.2.2. Influence of tacticity, temperature and chains size on stress-strain response

The stress-strain responses of the PVC models listed in Table 6-7 at two different temperatures of 100 K and 300 K are shown in Figures 6.38 to 6.40. Comparison of the results indicates that all the models exhibited elastic behaviors up to less than 7% strain and subsequently experience strain softening. The strain hardening behavior, however, is not consistently observed for all models; the models containing longer chains expectedly exhibited strain hardening. This behavior was more pronounced for the models simulated at the lower temperature (below the glass transition temperature).

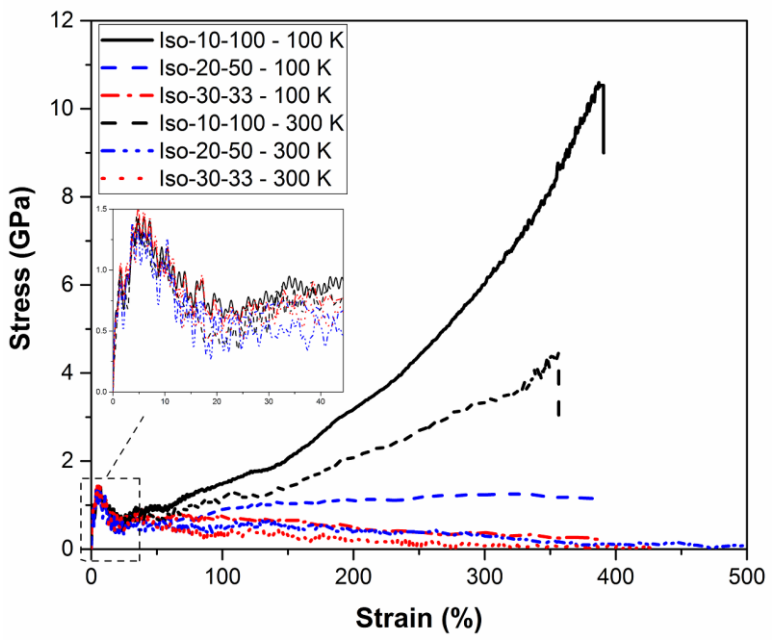

Figure 6.38. Stress-strain response of the isotactic PVC models at 100 K and 300 K

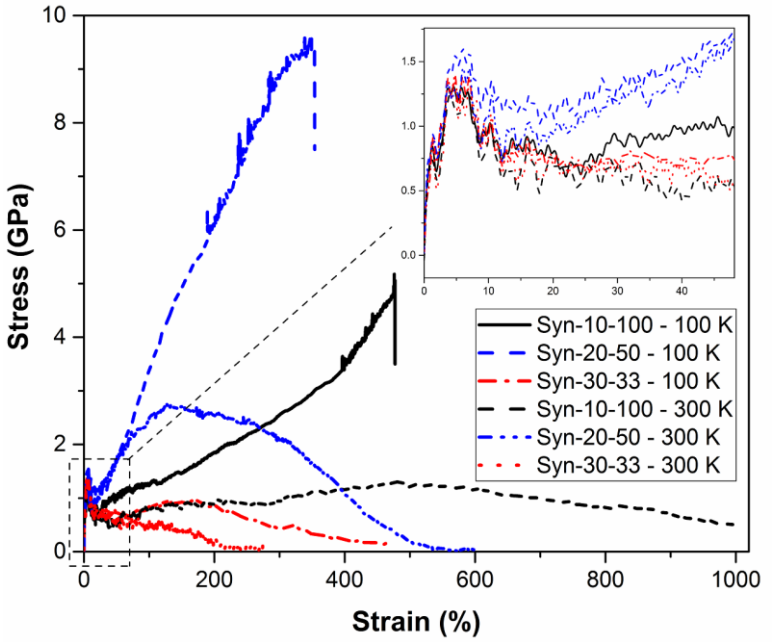

Figure 6.39. Stress-strain response of the syndiotactic PVC models at 100 K and 300 K

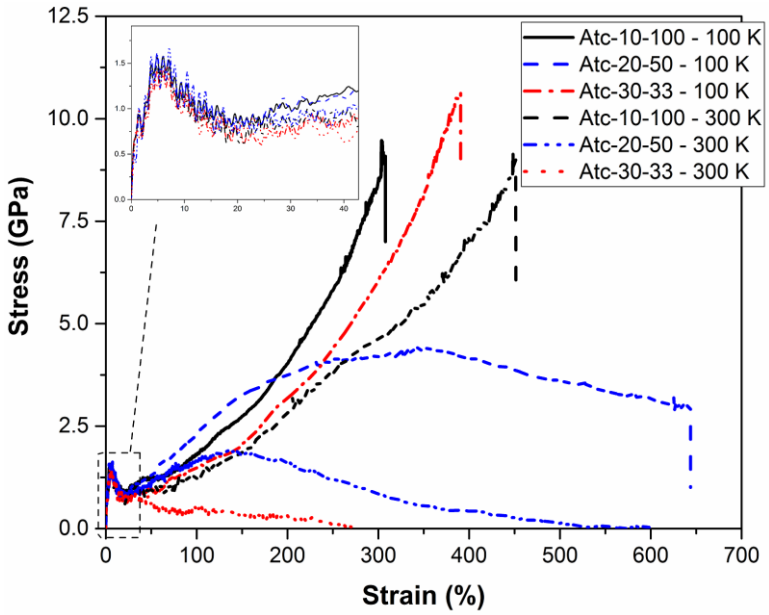

Figure 6.40. Stress-strain response of the atactic PVC models at 100 K and 300 K

With respect to the chain length and tacticity, the longest isotactic PVC had the highest strength among all the models. Reducing the chain size decreased the strength of isotactic models. This observation was not consistent across all tacticities. The strength of the longest syndiotactic PVC models (i.e. Syn-10-100) fell in between that of the other two models (i.e. Syn-20-50 and Syn-30-33). The lowest strength, however, was consistently linked to the models having the shortest chains. The failure of the atactic models to conform to this observation is ascribed to their configuration where substituents are placed randomly along the chain.

With regard to the temperature, the models simulated at 100 K showed considerably higher strengths. Consistently stronger performance of PVC at lower temperatures is possibly due to the fact that low temperatures obstruct the nucleation of discrete local failures within the its structure, thus enabling it to withstand larger loads before failure (Liu *et al.* 2007;

Dewapriya and Rajapakse 2014). In addition, a greater bond length at higher temperatures due to the thermal fluctuations arising from kinetic energy leads the bond to store higher potential energy. Therefore, the initial configuration of a PVC model stores less strain energy at lower temperatures. According to the total strain energy theory (Beltrami–Haigh's theory), a body subjected to a combined stress state fails when the total strain energy exceeds the total strain energy corresponding to simple tension. Therefore, the PVC models at lower temperatures can accommodate larger stresses before failure.

6.4.2.3. Poisson's ratio of PVC

The Poisson's ratio of the PVC models at different temperatures is summarized in Table 6-8. Results show that increasing temperature from 100 K to 300 K decreases the Poisson's ratio of all PVC models regardless of their tacticity. This observation could be interpreted by considering the mobility hindrance exerted by low temperatures which hampers the outward movement of polymer chains and aligns them in the loading direction. Based on the observations of Pandini and Pegoretti (2011), it is hypothesized that the Poisson's ratio of the polymer follows a sigmoidal behavior with an inflection point located in the proximity of the glass transition temperature of the polymer as temperature ascends from 100 K to 300 K.

Table 6-8. Poisson's ratio of the PVC models at different temperatures

Model ID	Temperature (K)	
	100	300
Iso-10-100	0.112	0.073
Iso-20-50	0.117	0.069
Iso-30-33	0.10`8	0.068
Syn-10-100	0.113	0.075
Syn-20-50	0.119	0.073
Syn-30-33	0.105	0.069
Atc-10-100	0.108	0.073
Atc-20-50	0.097	0.074
Atc-30-33	0.109	0.067

6.4.2.4. Internal energy evolution

Evolutions of the potential energy and its components (bonded and nonbonded interactions) for the model Iso-10-100 corresponding to the stress-strain behavior observed in Figure 6.36 is shown in Figure 6.41. The side-by-side comparison of the two figures indicates that only the angle energy of the model changed during the elastic régime. During the strain-softening régime, however, the energies associated with bonded interactions (i.e. bond, angle and dihedral) as well as the Coulombic interactions remained practically unchanged, and the energy evolution of the system was merely controlled by the van der Waals interactions. This observation held during the early stages of the strain-hardening régime until the stress in the system reached the maximum stress it had experienced before (i.e. yield stress). Beyond this point, the van der Waals energy plateaued to a value fairly equal to that of the dihedral energy, and the changes in the potential energy of the system was essentially governed by the bond and angle interactions. The slight increase in the energy associated with the dihedral interactions during strain-softening followed by its reduction throughout the strain-hardening régime could be due to the rotation of the *gauche* conformations to the lower energy *trans* conformations (Hossain *et al.* 2010).

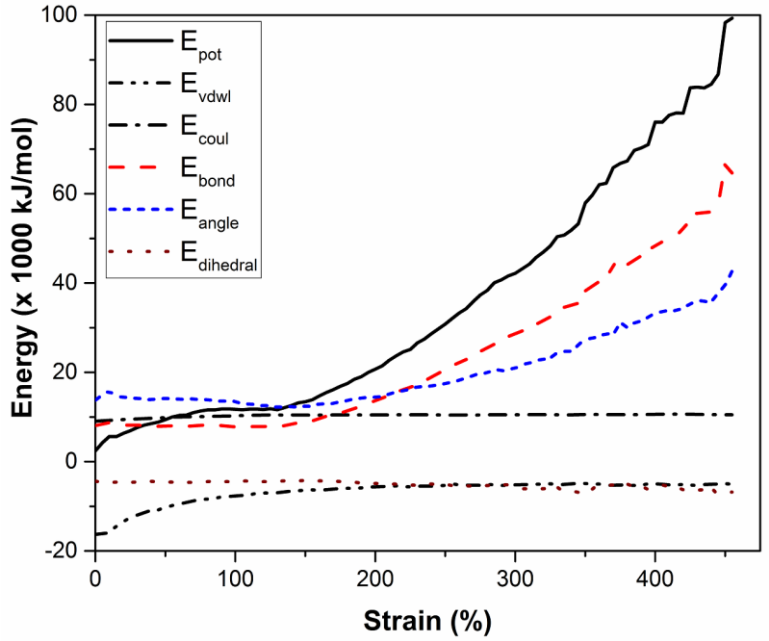

Figure 6.41. Evolutions of potential energy and its constituents for Iso-10-100 at 300 K

CHAPTER 7. CONCLUSIONS

7.1. Summary and conclusions

This study was focused on the development of sensor-enabled geogrids (SEGG) by means of laboratory experiments and molecular-scale simulations. Numerous laboratory tests were carried out in order to identify a range of formulations and production processes that would result in polymer nanocomposites with adequate mechanical and strain-sensitive electrical properties. Polyvinyl chloride (PVC) was selected for the tests as it is commonly used in the coating of woven and knitted geogrids. Two types of carbon black (CB) in powder form with measurably different structures (oil absorption numbers) as well as a multi-walled carbon nanotube (MWCNT) were used as conductive fillers. In-isolation monotonic tensile and cyclic loading tests together with electrical conductivity, stiffness and viscosity measurements were carried out on the CB-filled coating composites. Additional in-isolation and in-soil tests were performed on SEGG samples in order to investigate their mechanical and strain-sensitive electrical properties. In addition, similar in-isolation tests were carried out on MWCNT-filled PVC composite samples. During the course of the microscopy imaging of theses samples, a technique was developed for the multiscale characterization and dispersion assessment of CNT-filled composites using scanning electron microscopy (SEM), transmission electron microscopy (TEM) and laser scanning confocal microscopy (LSCM) techniques. The following conclusions were drawn from the laboratory experiments:

- For CB-filled PVC composites, the mechanical stirring method yielded higher quality samples with respect to the quality of dispersion and the magnitude and consistency of the measured tensoresistivity as compared to the sonication-based methods (Figures 3.9 and 3.10).

- The in-isolation monotonic tensoresistivity tests on coating specimens showed that both types of CB examined in this study exhibited significant strain sensitivity for detecting tensile strains in performance monitoring applications of geosynthetic structures. However, the specimens filled with the higher-structure CB showed a more consistent and reliable behavior in that their response was less sensitive to the strain rate and specimen width. In addition, the same specimens showed a smaller scatter in their measured tensoresistivity response as compared to those filled with a lower-structure carbon black. Additionally, the coating specimens filled with either of the CB types showed adequate tensile strength and ductility (Figures 3.19 and 3.20).

- The in-isolation cyclic tensoresistivity tests on coating specimens showed that the specimens filled with higher-structure CBs experience less damage upon cyclic deformation and show a higher degree of recoverability (i.e. less hysteresis) in tensoresistivity response. Prestraining of coating specimens improved the recoverability of their tensoresistivity response. Increasing the ratio (maximum prestrain:cyclic strain amplitude) resulted in a more consistent recoverability tensoresistivity response with cycle number (Section 3.2.3).

- The in-isolation and in-soil strain sensitivity tests on SEGG specimens showed that the gauge factors for the specimens tested in isolation were greater than those for otherwise

identical specimens that were tested at the same loading rate but subjected to confining pressure in a modified DST apparatus. This reduction in the gauge factor was attributed to the effect of confining pressure in bringing the CB particles and aggregates closer in the conductive network of the coating composite, thus enabling them to maintain their capability to transfer electrons up to larger strains. The results also showed that the specimens subjected to slower-rate tensile loads would exhibit greater strain sensitivities and lower tensile strength and failure strain (Section 3.3.3).

- The MWCNT/PVC composite samples mixed using an optimum combination of power and duration in the probe sonication method yielded the lowest percolation threshold with the highest overall electrical conductivity and statistical consistency among all of the methods examined. The curing (vulcanization) time required in compression molding was estimated using the Stokes-Einstein equation and experimentally validated through investigating the curing time vs. the electrical conductivity of the composite. The optimum curing time for compression molding of the resulting composite was found within the range between 10 and 15 minutes, beyond which the electrical conductivity of the composite did not improve.

- Mechanical response of the MWCNT/PVC composite samples was found to be linear at low strains leading to a strain hardening behavior at larger strains. It was found that on average, composite samples with 0.5 wt.% MWCNT concentration resulted in a 57% reduction in the ultimate (failure) strain and a five-fold increase in their tensile modulus when compared to otherwise identical pristine plastisol-plasticizer samples. The failure mechanism of the composite was microscopically observed using laser scanning confocal

microscopy to be initiated from inside the largest CNT bundles, followed by smaller bundles and debonding at CNT/polymer interfaces.

- The electrical conductivity of the MWCNT/PVC composite samples showed high sensitivity to the applied strain with a fairly low scatter.

With respect to numerical simulations, Monte Carlo (MC) simulations were carried out to study the influences of aspect ratio, distortion, effective electron transfer range and size on the predicted percolation behavior of CB- and CNT-filled composites. Numerous molecular dynamics (MD) simulations were also performed carried out to study the mechanical properties of graphene and single-walled CNTs (SWCNTs). They were also used to investigate the influence of polymer type, filler type and filler concentration on the mechanical properties of filled polyethylene and PVC composites.

- The MC simulation results consistently and expectedly showed that increasing the effective electron transfer range will facilitate the formation of a conductive network in a model, lowering its percolation threshold. It was also seen that mixing-induced distortion of CNTs tends to increase their percolation threshold, so does increasing the particle size.

- As an increasingly-popular filler in the nanocomposites development, graphene was simulated using MD in order to develop a failure criterion for it. To this end, a graphene sheet was biaxially loaded to failure at different temperatures using different sequences of loading in its zigzag and armchair principal directions. The predicted biaxial failure stresses in the two principal directions were then plotted normalized to their respective uniaxial ultimate strength values, and a bilinear failure envelope was fitted to the

corresponding data, resulting in a simple, temperature independent failure criterion expressed in Equation (6-7).

- A comprehensive series of MD simulations was also carried out in order to investigate the influence of chirality, size, aspect ratio and slenderness ratio on the tensile and compressive mechanical behavior of SWCNTs. The results of the compressive numerical experiments showed that the shortest SWCNTs exhibit a stable postbuckling behavior irrespective of the temperature applied. Also, the SWCNTs with a slenderness ratio of 10 showed temperature-dependency in their postbuckling behavior. This dependency was found to be more pronounced for slender CNTs (slenderness ratio ≥ 15) subjected to low strains. At larger strains, however, this distinction vanished where all CNTs exhibit similar postbuckling stress-strain responses. The onset of buckling was found to be inversely proportional to the slenderness of the tubes where shorter tubes buckled at relatively lower strains. In addition, it was seen that the elastic modulus at a given temperature is not considerably influenced by slenderness ratio and chirality. The results of the tensile experiments revealed a nonlinear elastic behavior for all CNTs. The failure modes that the fracture of zigzag CNTs were consistently found to occur perpendicularly to the loading direction, while diagonal fractures were observed for armchair and chiral CNTs. The results also indicate that the tensile strength and strain at failure steadily increased as the chiral angle increased from 0 for zigzag CNTs to 30° for armchair CNTs. In addition, larger CNTs were found to possess lower tensile strengths and fail at lower strains.

- MD simulations were also used to investigate the mechanical properties of PE, CNT-filled PE composites and PVC.

  The PE models showed typically three stages of deformation; elastic behavior up to the yield stress, post-yield strain softening and strain hardening.

  The strength of both LDPE and HDPE composites was found to improve linearly as a function of CNT concentration.

  All the studied PVC models exhibited elastic behavior up to less than 7% strain and subsequently experienced strain softening. The strain hardening behavior, however, was not consistently observed for all models; the models containing longer chains expectedly exhibited strain hardening. This behavior was more pronounced for the models simulated at the lower temperature (below the glass transition temperature).

7.2. Suggestions for further research

In the continuation of this study toward developing SEGG materials, it is recommended to

- design a durable, non-conductive yet UV-protective shield for SEGG samples in order to insulate them from the interference of surrounding environment to their measured electrical conductivity,

- manufacture prototype samples and test their performance in a pilot project (e.g. a SEGG-reinforced retaining wall),

- investigate the properties of interest (e.g. tensoresistive and mechanical) of nanocomposites made from graphene and the common polymers in the geosynthetics industry,
- use the microscopy technique developed in this study to correlate the microstructure of composites with their macroscopic properties, especially for autofluorescent polymers,
- study the tensoresistivity of CNT-filled composites under cyclic loading,
- revise the failure criterion developed for graphene to include the influence of defects (e.g. vacancy defects),
- select a proper representative for carbon black in the nanoscale (e.g. amorphous graphite) and run molecular dynamics simulations for its mechanical properties,
- construct and simulate larger fully-atomistic computational models for nanocomposites once currently-nonexistent computational resources become available, and
- create 3D models for filled composites and study their percolation threshold behavior and electrical properties under uncertainties using Monte Carlo simulations.

REFERENCES

Abbasi, S., Carreau, P. J., and Derdouri, A. (2010). "Flow induced orientation of multiwalled carbon nanotubes in polycarbonate nanocomposites: Rheology, conductivity and mechanical properties." *Polymer*, 51(4), 922-935.

Accorsi, J., and Romero, E. (1995). "Special carbon –blacks for plastics." *Plastic Engineering*, 51(4), 30-33.

Ahadi, E., and Konermann, L. (2012). "Modeling the behavior of coarse-grained polymer chains in charged water droplets: Implications for the mechanism of electrospray ionization." *The Journal of Physical Chemistry B*, 116(1), 104-112.

Ajayan, P. M., Schadler, L. S., Giannaris, C., and Rubio, A. (2000). "Single-walled carbon nanotube–polymer composites: Strength and weakness." *Advanced Materials*, 12(10), 750-753.

Aktan, A. E., Farhey, D. N., Helmicki, A. J., Brown, D. L., Hunt, V. J., Lee, K.-L., and Levi, A. (1997). "Structural identification for condition assessment: Experimental arts." *Journal of Structural Engineering*, 123(12), 1674-1684.

Al-Saleh, M. H., and Sundararaj, U. (2008). "Electromagnetic interference (emi) shielding effectiveness of pp/ps polymer blends containing high structure carbon black." *Macromolecular Materials and Engineering*, 293(7), 621-630.

Alamusi, Hu, N., Fukunaga, H., Atobe, S., Liu, Y., and Li, J. (2011). "Piezoresistive strain sensors made from carbon nanotubes based polymer nanocomposites." *Sensors (Basel, Switzerland)*, 11(11), 10691-10723.

Allaoui, A., Bai, S., Cheng, H. M., and Bai, J. B. (2002). "Mechanical and electrical properties of a mwnt/epoxy composite." *Composites Science and Technology*, 62(15), 1993-1998.

Anderson, T. W., and Darling, D. A. (1952). "Asymptotic theory of certain "goodness of fit" criteria based on stochastic processes." *The Annals of Mathematical Statistics*, 23(2), 193-212.

Andia, P. C., Costanzo, F., and Gray, G. L. (2006). "A classical mechanics approach to the determination of the stress–strain response of particle systems." *Modelling and Simulation in Materials Science and Engineering*, 14(4), 741.

Aneli, J. N., Zaikov, G. E., and Khananashvili, L. M. (1999). "Effects of mechanical deformations on the structurization and electric conductivity of electric conducting polymer composites." *Journal of Applied Polymer Science*, 74(3), 601-621.

Arash, B., Wang, Q., and Varadan, V. K. (2014). "Mechanical properties of carbon nanotube/polymer composites." *Scientific Reports*, 4.

ASTM D883 (2012). "Standard terminology relating to plastics." *Annual Book of ASTM Standards*, ASTM International, West Conshohocken, PA.

ASTM D1388 (2014). "Standard test method for stiffness of fabrics." *Annual Book of ASTM Standards*, ASTM International, West Conshohocken, PA.

ASTM D2383 (2014). "Standard practice for testing plasticizer compatibility in poly(vinyl chloride) (pvc) compounds under humid conditions." *Annual Book of ASTM Standards*, ASTM International, West Conshohocken, PA.

ASTM D2414 (2013). "Standard test method for carbon black—oil absorption number (oan)." *Annual Book of ASTM Standards*, ASTM International, West Conshohocken, PA.

ASTM D3039 (2014). "Standard test method for tensile properties of polymer matrix composite materials." *Annual Book of ASTM Standards*, ASTM International, West Conshohocken, PA.

ASTM D3080 (2011). "Standard test method for direct shear test of soils under consolidated drained conditions." *Annual Book of ASTM Standards*, ASTM International, West Conshohocken, PA.

ASTM D3291 (2011). "Standard practice for compatibility of plasticizers in poly(vinyl chloride) plastics under compression." *Annual Book of ASTM Standards*, ASTM International, West Conshohocken, PA.

ASTM D3849 (2014). "Standard test method for carbon black—morphological characterization of carbon black using lectron microscopy." *Annual Book of ASTM Standards*, ASTM International, West Conshohocken, PA.

ASTM D4496 (2013). "Standard test method for d-c resistance or conductance of moderately conductive materials." *Annual book of astm standards*, ASTM International, West Conshohocken, PA.

ASTM D5225 (2014). "Standard test method for measuring solution viscosity of polymers with a differential viscometer." *Annual Book of ASTM Standards*, ASTM International, West Conshohocken, PA.

ASTM D5832 (2014). "Standard test method for volatile matter content of activated carbon samples." *Annual Book of ASTM Standards*, ASTM International, West Conshohocken, PA.

ASTM D6556 (2014). "Standard test method for carbon black—total and external surface area by nitrogen adsorption." *Annual Book of ASTM Standards*, ASTM International, West Conshohocken, PA.

ASTM D6637 (2013). "Standard test method for determining tensile properties of geogrids by the single or multi-rib tensile method." *Annual book of astm standards*, ASTM International, West Conshohocken, PA.

Balberg, I., and Bozowski, S. (1982). "Percolation in a composite of random stick-like conducting particles." *Solid State Communications*, 44(4), 551-554.

Balberg, I., and Binenbaum, N. (1983). "Computer study of the percolation threshold in a two-dimensional anisotropic system of conducting sticks." *Physical Review B*, 28(7), 3799-3812.

Balberg, I., Anderson, C. H., Alexander, S., and Wagner, N. (1984). "Excluded volume and its relation to the onset of percolation." *Physical Review B*, 30(7), 3933-3943.

Balberg, I. (2002). "A comprehensive picture of the electrical phenomena in carbon black–polymer composites." *Carbon*, 40(2), 139-143.

Bandyopadhyay, A., Valavala, P. K., Clancy, T. C., Wise, K. E., and Odegard, G. M. (2011). "Molecular modeling of crosslinked epoxy polymers: The effect of crosslink density on thermomechanical properties." *Polymer*, 52(11), 2445-2452.

Bao, W. S., Meguid, S. A., Zhu, Z. H., and Meguid, M. J. (2011). "Modeling electrical conductivities of nanocomposites with aligned carbon nanotubes." *Nanotechnology*, 22(48), 485704.

Bao, W. S., Meguid, S. A., Zhu, Z. H., and Weng, G. J. (2012). "Tunneling resistance and its effect on the electrical conductivity of carbon nanotube nanocomposites." *Journal of Applied Physics*, 111(9), 093726-093726-093727.

Barber, A. H., Andrews, R., Schadler, L. S., and Wagner, H. D. (2005). "On the tensile strength distribution of multiwalled carbon nanotubes." *Applied Physics Letters*, 87(20), 203106.

Barrau, S., Demont, P., Perez, E., Peigney, A., Laurent, C., and Lacabanne, C. (2003). "Effect of palmitic acid on the electrical conductivity of carbon nanotubes-epoxy resin composites." *Macromolecules*, 36, 9678-9680.

Barry, D., and Hartigan, J. A. (1993). "A bayesian analysis for change point problems." *Journal of the American Statistical Association*, 88(421), 309-319.

Baschnagel, J., Binder, K., Doruker, P., Gusev, A. A., Hahn, O., Kremer, K., Mattice, W. L., Müller-Plathe, F., Murat, M., Paul, W., Santos, S., Suter, U. W., and Tries, V. (2000). "Bridging the gap between atomistic and coarse-grained models of polymers: Status and perspectives." *Viscoelasticity, atomistic models, statistical chemistry*, Springer Berlin Heidelberg, 41-156.

Bathurst, R. J., Walters, D., Vlachopoulos, N., Burgess, P., and Allen, T. M. (2000). "Full scale testing of geosynthetic reinforced walls." American Society of Civil Engineers, 201-217.

Bathurst, R. J., Allen, T. M., and Walters, D. L. (2002). "Short-term strain and deformation behavior of geosynthetic walls at working stress conditions." *Geosynthetics International*, 9(5-6), 451-482.

Bathurst, R. J., Allen, T. M., and Walters, D. L. (2005). "Reinforcement loads in geosynthetic walls and the case for a new working stress design method." *Geotextiles and Geomembranes*, 23(4), 287-322.

Bathurst, R. J., and Hatami, K. (2006). "Physical to computational modelling of reinforced soil walls under static loading." *Proc., International Conference on Physical Modeling in Geotechnics*Hong Kong, China, 3-17.

Bathurst, R. J., Vlachopoulos, N., Walters, D. L., Burgess, P. G., and Allen, T. M. (2006). "The influence of facing stiffness on the performance of two geosynthetic reinforced soil retaining walls." *Canadian Geotechnical Journal*, 43(12), 1225-1237.

Bauhofer, W., and Kovacs, J. Z. (2009). "A review and analysis of electrical percolation in carbon nanotube polymer composites." *Composites Science and Technology*, 69(10), 1486-1498.

Bautista-Quijano, J. R., Avilés, F., Aguilar, J. O., and Tapia, A. (2010). "Strain sensing capabilities of a piezoresistive mwcnt-polysulfone film." *Sensors and Actuators A: Physical*, 159(2), 135-140.

Belashi, A. (2011). "Percolation modeling in polymer nanocomposites." The University of Toledo.

Bellucci, S., Gaggiotti, G., Marchetti, M., Micciulla, F., Mucciato, R., and Regi, M. (2007). "Atomic force microscopy characterization of carbon nanotubes." *Journal of Physics: Conference Series*, 61(1), 99.

Benjamim, C. V. S., Bueno, B. S., and Zornberg, J. G. (2007). "Field monitoring evaluation of geotextile-reinforced soil-retaining walls." *Geosynthetics International*, 14(2), 100-118.

Berger, M. A., and McCullough, R. L. (1985). "Characterization and analysis of the electrical properties of a metal-filled polymer." *Composites Science and Technology*, 22(2), 81-106.

Bhattacharyya, A. R., Pötschke, P., Häußler, L., and Fischer, D. (2005). "Reactive compatibilization of melt mixed pa6/swnt composites: Mechanical properties and morphology." *Macromolecular Chemistry and Physics*, 206(20), 2084-2095.

Bigg, D. M. (1984). "An investigation of the effect of carbon black structure, polymer morphology, and processing history on the electrical conductivity of carbon-black-filled thermoplastics." *Journal of Rheology (1978-present)*, 28(5), 501-516.

Binnig, G., Rohrer, H., Gerber, C., and Weibel, E. (1982). "Surface studies by scanning tunneling microscopy." *Physical Review Letters*, 49(1), 57-61.

Binnig, G., Quate, C. F., and Gerber, C. (1986). "Atomic force microscope." *Physical Review Letters*, 56(9), 930-933.

Biscoe, J., and Warren, B. E. (1942). "An x-ray study of carbon black." *Journal of Applied Physics*, 13(6), 364-371.

Blase, X., Benedict, L. X., Shirley, E. L., and Louie, S. G. (1994). "Hybridization effects and metallicity in small radius carbon nanotubes." *Physical Review Letters*, 72(12), 1878-1881.

Blond, D., Barron, V., Ruether, M., Ryan, K. P., Nicolosi, V., Blau, W. J., and Coleman, J. N. (2006). "Enhancement of modulus, strength, and toughness in poly(methyl methacrylate)-based composites by the incorporation of poly(methyl methacrylate)-functionalized nanotubes." *Advanced Functional Materials*, 16(12), 1608-1614.

Böger, L., Wichmann, M. H. G., Meyer, L. O., and Schulte, K. (2008). "Load and health monitoring in glass fibre reinforced composites with an electrically conductive nanocomposite epoxy matrix." *Composites Science and Technology*, 68(7–8), 1886-1894.

Böhm, G. G. A., and Nguyen, M. N. (1995). "Flocculation of carbon black in filled rubber compounds. I. Flocculation occurring in unvulcanized compounds during annealing at elevated temperatures." *Journal of Applied Polymer Science*, 55(7), 1041-1050.

Bonessio, N., Lomiento, G., and Benzoni, G. (2012). "Damage identification procedure for seismically isolated bridges." *Structural Control and Health Monitoring*, 19(5), 565-578.

Bourrat, X. (1993). "Electrically conductive grades of carbon black: Structure and properties." *Carbon*, 31(2), 287-302.

Bowden, P. B., and Jukes, J. A. (1972). "The plastic flow of isotropic polymers." *Journal of Materials Science*, 7(1), 52-63.

Boyce, M. C., Parks, D. M., and Argon, A. S. (1989). "Plastic flow in oriented glassy polymers." *International Journal of Plasticity*, 5(6), 593-615.

Brenner, D. W. (1990). "Empirical potential for hydrocarbons for use in simulating the chemical vapor deposition of diamond films." *Physical Review B*, 42(15), 9458-9471.

Breton, Y., Désarmot, G., Salvetat, J. P., Delpeux, S., Sinturel, C., Béguin, F., and Bonnamy, S. (2004). "Mechanical properties of multiwall carbon nanotubes/epoxy composites: Influence of network morphology." *Carbon*, 42(5–6), 1027-1030.

Breuer, O., Tchoudakov, R., Narkis, M., and Siegmann, A. (1997). "Segregated structures in carbon black-containing immiscible polymer blends: Hips/lldpe systems." *Journal of Applied Polymer Science*, 64(6), 1097-1106.

Briançon, L., Nancey, A., Caquel, F., and Villard, P. (2004). "New technology for strain measurements in soil and the survey of reinforced earth constructions."Munich, Germany.

Broadbent, S. R., and Hammersley, J. M. (1957). "Percolation processes." *Mathematical Proceedings of the Cambridge Philosophical Society*, 53(03), 629-641.

Brown, D., and Clarke, J. H. R. (1991). "Molecular dynamics simulation of an amorphous polymer under tension. 1. Phenomenology." *Macromolecules*, 24(8), 2075-2082.

Broza, G., Piszczek, K., Schulte, K., and Sterzynski, T. (2007). "Nanocomposites of poly(vinyl chloride) with carbon nanotubes (cnt)." *Composites Science and Technology*, 67(5), 890-894.

Brunauer, S., Emmett, P. H., and Teller, E. (1938). "Adsorption of gases in multimolecular layers." *Journal of the American Chemical Society*, 60(2), 309-319.

Bryning, M. B., Milkie, D. E., Islam, M. F., Kikkawa, J. M., and Yodh, A. G. (2005). "Thermal conductivity and interfacial resistance in single-wall carbon nanotube epoxy composites." *Applied Physics Letters*, 87(16), 161909.

Bu, H., Chen, Y., Zou, M., Yi, H., Bi, K., and Ni, Z. (2009). "Atomistic simulations of mechanical properties of graphene nanoribbons." *Physics Letters A*, 373(37), 3359-3362.

Bulleit, W. M. (2008). "Uncertainty in structural engineering." *Practice Periodical on Structural Design and Construction*, 13(1), 24-30.

Bunde, A., and Dieterich, W. (2000). "Percolation in composites." *Journal of Electroceramics*, 5(2), 81-92.

Burkert, U., and Allinger, N. L. (1982). *Molecular mechanics*, American Chemical Society, Washington DC.

Cadek, M., Coleman, J. N., Barron, V., Hedicke, K., and Blau, W. J. (2002). "Morphological and mechanical properties of carbon-nanotube-reinforced semicrystalline and amorphous polymer composites." *Applied Physics Letters*, 81(27), 5123-5125.

Calleja, F. J. B., Bayer, R. K., and Ezquerra, T. A. (1988). "Electrical conductivity of polyethylene-carbon-fibre composites mixed with carbon black." *Journal of Materials Science*, 23(4), 1411-1415.

Calvert, P., Patra, P., Lo, T.-C., Chen, C. H., Sawhney, A., and Agrawal, A. (2007). "Piezoresistive sensors for smart textiles." *Proc., Electroactive Polymer Actuators and Devices (EAPAD)*San Diego, California, 65241I-65241 - 65241I-65248.

Campbell, E. R., Reisner, J. H., and Chung, K. T. (1983). "Charging phenomenon in conductor-insulator composites as displayed by the scanning electron microscope." *Journal of Applied Physics*, 54(2), 1133-1134.

Capaldi, F. M., Boyce, M. C., and Rutledge, G. C. (2002). "Enhanced mobility accompanies the active deformation of a glassy amorphous polymer." *Physical Review Letters*, 89(17), 175505.

Capaldi, F. M., Boyce, M. C., and Rutledge, G. C. (2004). "Molecular response of a glassy polymer to active deformation." *Polymer*, 45(4), 1391-1399.

Carey, B. J., Patra, P. K., Ci, L., Silva, G. G., and Ajayan, P. M. (2011). "Observation of dynamic strain hardening in polymer nanocomposites." *ACS Nano*, 5(4), 2715-2722.

Carmona, F., and Mouney, C. (1992). "Temperature-dependent resistivity and conduction mechanism in carbon particle-filled polymers." *Journal of Materials Science*, 27(5), 1322-1326.

Carrubba, P., Moraci, N., and Montanelli, F. (1999). "Instrumented soil reinforced retaining wall: Analysis of measurements." *Proc., Geosynthetics '99*Boston, MA.

Carrubba, P., Luchetta, F., Montanelli, F., and Moraci, N. (2000). "Instrumented reinforced wall: Measurements and fem results." American Society of Civil Engineers, 271-291.

Castillo, F. Y., Socher, R., Krause, B., Headrick, R., Grady, B. P., Prada-Silvy, R., and Pötschke, P. (2011). "Electrical, mechanical, and glass transition behavior of polycarbonate-based nanocomposites with different multi-walled carbon nanotubes." *Polymer*, 52(17), 3835-3845.

Celzard, A., McRae, E., Deleuze, C., Dufort, M., Furdin, G., and Marêché, J. F. (1996). "Critical concentration in percolating systems containing a high-aspect-ratio filler." *Physical Review B*, 53(10), 6209-6214.

Cembrola, R. J. (1982). "The relationship of carbon black dispersion to electrical resistivity and vulcanizate physical properties." *Polymer Engineering & Science*, 22(10), 601-609.

Chan, C.-M., Cheng, C.-L., and Yuen, M. M. F. (1997). "Electrical properties of polymer composites prepared by sintering a mixture of carbon black and ultra-high molecular weight polyethylene powder." *Polymer Engineering & Science*, 37(7), 1127-1136.

Chandra, N., Namilae, S., and Shet, C. (2004). "Local elastic properties of carbon nanotubes in the presence of stone-wales defects." *Physical Review B*, 69(9), 094101.

Cheaptubes (2015). "Carbon nanotube and graphene prices." <http://cheaptubes.com/carbon-nanotubes-prices.htm>. (June 26, 2015).

Cheung, D. L. G. (2002). "Structures and properties of liquid crystals and related molecules from computer simulation."Doctoral, Durham University.

Christensen, R. M. (2013). *The theory of materials failure*, Oxford University Press, Oxford, UK.

Chung, K. T. (1982). "Electrical permittivity and conductivity of carbon black-polyvinyl chloride composites." *Journal of Applied Physics*, 53(10), 6867.

Chung, K. T., Sabo, A., and Pica, A. P. (1982). "Electrical permittivity and conductivity of carbon black-polyvinyl chloride composites." *Journal of Applied Physics*, 53(10), 6867-6879.

Chung, K. T., Reisner, J. H., and Campbell, E. R. (1983). "Charging phenomena in the scanning electron microscopy of conductor-insulator composites: A tool for composite structural analysis." *Journal of Applied Physics*, 54(11), 6099-6112.

Clingerman, M. L., Weber, E. H., King, J. A., and Schulz, K. H. (2003). "Development of an additive equation for predicting the electrical conductivity of carbon-filled composites." *Journal of Applied Polymer Science*, 88(9), 2280-2299.

Coleman, J. N., Cadek, M., Blake, R., Nicolosi, V., Ryan, K. P., Belton, C., Fonseca, A., Nagy, J. B., Gun'ko, Y. K., and Blau, W. J. (2004). "High performance nanotube-reinforced plastics: Understanding the mechanism of strength increase." *Advanced Functional Materials*, 14(8), 791-798.

Cooper, C. A., Young, R. J., and Halsall, M. (2001). "Investigation into the deformation of carbon nanotubes and their composites through the use of raman spectroscopy." *Composites Part A: Applied Science and Manufacturing*, 32(3–4), 401-411.

Cormier, J., Rickman, J. M., and Delph, T. J. (2001). "Stress calculation in atomistic simulations of perfect and imperfect solids." *Journal of Applied Physics*, 89(1), 99-104.

Costa, P., Silva, J., Ansón-Casaos, A., Martinez, M. T., Abad, M. J., Viana, J., and Lanceros-Mendez, S. (2014). "Effect of carbon nanotube type and functionalization on the electrical, thermal, mechanical and electromechanical properties of carbon nanotube/styrene–butadiene–styrene composites for large strain sensor applications." *Composites Part B: Engineering*, 61, 136-146.

Costescu, B. I., Baldus, I. B., and Gräter, F. (2014). "Graphene mechanics: I. Efficient first principles based morse potential." *Physical chemistry chemical physics: PCCP*, 16(24), 12591-12598.

Cravanzola, S., Haznedar, G., Scarano, D., Zecchina, A., and Cesano, F. (2013). "Carbon-based piezoresistive polymer composites: Structure and electrical properties." *Carbon*, 62, 270-277.

CRN (2015). <http://www.crnano.org/basics.htm>.

Croitoru, M. D., Bertsche, G., Kern, D. P., Burkhardt, C., Bauerdick, S., Şahakalkan, S., and Roth, S. (2005). "Visualization and in situ contacting of carbon nanotubes in a scanning electron microscope." *Journal of Vacuum Science & Technology B*, 23(6), 2789-2792.

Cross, A., Haward, R. N., and Mills, N. J. (1979). "Post yield phenomena in tensile tests on poly(vinyl chloride)." *Polymer*, 20(3), 288-294.

Dani, A., and Ogale, A. A. (1996). "Electrical percolation behavior of short-fiber composites: Experimental characterization and modeling." *Composites Science and Technology*, 56(8), 911-920.

Dannenberg, E. M. (1952). "Carbon black dispersion and reinforcement." *Industrial & Engineering Chemistry*, 44(4), 813-818.

Das, N. C., Chaki, T. K., and Khastgir, D. (2002). "Effect of processing parameters, applied pressure and temperature on the electrical resistivity of rubber-based conductive composites." *Carbon*, 40(6), 807-816.

Dasenbrock, D., Abdoun, T., and Bennett, V. (2011). "Real-time structural health monitoring of landslides and geotechnical assets with shapeaccelarrays." *Proc., Geo-Frontiers*, American Society of Civil Engineers, Dallas, TX, 1585-1594.

Davis, G. T., and Eby, R. K. (1973). "Glass transition of polyethylene: Volume relaxation." *Journal of Applied Physics*, 44(10), 4274-4281.

de Gennes, P.-G. (1979). *Scaling concepts in polymer physics*, Cornell University Press, Ithaca, NY.

Demarchi, D., and Tagliaferro, A. (2015). *Carbon for sensing devices*, Springer International Publishing, Cham.

Demczyk, B. G., Wang, Y. M., Cumings, J., Hetman, M., Han, W., Zettl, A., and Ritchie, R. O. (2002). "Direct mechanical measurement of the tensile strength and elastic modulus of multiwalled carbon nanotubes." *Materials Science and Engineering: A*, 334(1–2), 173-178.

Depa, P. K., and Maranas, J. K. (2005). "Speed up of dynamic observables in coarse-grained molecular-dynamics simulations of unentangled polymers." *The Journal of Chemical Physics*, 123(9), 094901.

Depa, P. K., and Maranas, J. K. (2007). "Dynamic evolution in coarse-grained molecular dynamics simulations of polyethylene melts." *The Journal of Chemical Physics*, 126(5), 054903.

Dewapriya, M. a. N., Phani, A. S., and Rajapakse, R. K. N. D. (2013). "Influence of temperature and free edges on the mechanical properties of graphene." *Modelling and Simulation in Materials Science and Engineering*, 21(6), 065017.

Dewapriya, M. A. N., and Rajapakse, R. K. N. D. (2014). "Molecular dynamics simulations and continuum modeling of temperature and strain rate dependent fracture strength of graphene with vacancy defects." *Journal of Applied Mechanics*, 81(8), 081010-081010.

Dewapriya, M. A. N., Rajapakse, R. K. N. D., and Phani, A. S. (2014). "Atomistic and continuum modelling of temperature-dependent fracture of graphene." *International Journal of Fracture*, 187(2), 199-212.

Ding, T., Wang, L., and Wang, P. (2007). "Changes in electrical resistance of carbon-black-filled silicone rubber composite during compression." *Journal of Polymer Science Part B: Polymer Physics*, 45(19), 2700-2706.

Donnet, J.-B. (1994). "Fifty years of research and progress on carbon black." *Carbon*, 32(7), 1305-1310.

Doornik, J. A., and Hansen, H. (2008). "An omnibus test for univariate and multivariate normality*." *Oxford Bulletin of Economics and Statistics*, 70, 927-939.

Du, F., Scogna, R. C., Zhou, W., Brand, S., Fischer, J. E., and Winey, K. I. (2004). "Nanotube networks in polymer nanocomposites: Rheology and electrical conductivity." *Macromolecules*, 37(24), 9048-9055.

Dunn, W. L., and Shultis, J. K. (2011). *Exploring monte carlo methods*, Elsevier, Burlington, MA.

Dunnicliff, J. (1993). *Geotechnical instrumentation for monitoring field performance*, Wiley.

Eftekhari, M., Mohammadi, S., and Khoei, A. R. (2013). "Effect of defects on the local shell buckling and post-buckling behavior of single and multi-walled carbon nanotubes." *Computational Materials Science*, 79, 736-744.

Eftekhari, M., Hatefi Ardakani, S., and Mohammadi, S. (2014). "An xfem multiscale approach for fracture analysis of carbon nanotube reinforced concrete." *Theoretical and Applied Fracture Mechanics*, 72(0), 64-75.

Farrag, K., Oglesby, J., and Griffin, P. (1994). "Large strain measurements in geogrid reinforcement." *Transportation Research Record*(1439).

Farrag, K., Abu-Farsakh, M., and Morvant, M. (2004). "Stress and strain monitoring of reinforced soil test wall." *Transportation Research Record: Journal of the Transportation Research Board*, 1868, 89-99.

Farrar, C. R., and Worden, K. (2008). "An introduction to structural health monitoring." *Philosophical Transactions of the Royal Society of London A: Mathematical, Physical and Engineering Sciences*, 366(1870), 1591-1611.

Fathi, A. (2011). "Carbon black-filled polymers as geosynthetic sensors." The University of Oklahoma, Norman, OK.

Fathi, A., Hatami, K., and Grady, B. P. (2012). "Effect of carbon black structure on low-strain conductivity of polypropylene and low-density polyethylene composites." *Polymer Engineering & Science*, 52(3), 549-556.

Feller, J. F., Linossier, I., and Grohens, Y. (2002). "Conductive polymer composites: Comparative study of poly(ester)-short carbon fibres and poly(epoxy)-short carbon fibres mechanical and electrical properties." *Materials Letters*, 57(1), 64-71.

Feng, M. Q., Kim, J. M., and Xue, H. (1998). "Identification of a dynamic system using ambient vibration measurements." *Journal of Applied Mechanics*, 65(4), 1010-1021.

Fernández-Rossier, J., Palacios, J. J., and Brey, L. (2007). "Electronic structure of gated graphene and graphene ribbons." *Physical Review B*, 75(20), 205441.

Feynman, R. P. (1992). "There's plenty of room at the bottom [data storage]." *Journal of Microelectromechanical Systems*, 1(1), 60-66.

Fisher, M. E., and Essam, J. W. (1961). "Some cluster size and percolation problems." *Journal of Mathematical Physics*, 2(4), 609-619.

Fitzer, E., and Manocha, L. M. (1998). *Carbon reinforcements and carbon/carbon composites*, Springer, Germany.

Flandin, L., Chang, A., Nazarenko, S., Hiltner, A., and Baer, E. (2000). "Effect of strain on the properties of an ethylene–octene elastomer with conductive carbon fillers." *Journal of Applied Polymer Science*, 76(6), 894-905.

Flandin, L., Hiltner, A., and Baer, E. (2001). "Interrelationships between electrical and mechanical properties of a carbon black-filled ethylene–octene elastomer." *Polymer*, 42(2), 827-838.

Flory, P. J. (1953). *Principles of polymer chemistry*, Cornell University Press, Ithaca, NY.

Frankland, S. J. V., Harik, V. M., Odegard, G. M., Brenner, D. W., and Gates, T. S. (2003). "The stress–strain behavior of polymer–nanotube composites from molecular dynamics simulation." *Composites Science and Technology*, 63(11), 1655-1661.

Franklin, R. E. (1951). "Crystallite growth in graphitizing and non-graphitizing carbons." *Proceedings of the Royal Society of London. Series A. Mathematical and Physical Sciences*, 209(1097), 196-218.

Freed, K. F. (1985). "Polymers and random walks - renormalization group description and comparison with experiment." *Journal of Research of the National Bureau of Standards*, 90(6), 503.

Frømyr, T. R., Hansen, F. K., and Olsen, T. (2012). "The optimum dispersion of carbon nanotubes for epoxy nanocomposites: Evolution of the particle size distribution by ultrasonic treatment." *Journal of Nanotechnology*, 2012, e545930.

Fuechsle, M., Miwa, J. A., Mahapatra, S., Ryu, H., Lee, S., Warschkow, O., Hollenberg, L. C. L., Klimeck, G., and Simmons, M. Y. (2012). "A single-atom transistor." *Nature Nanotechnology*, 7(4), 242-246.

Fukunaga, H., Takimoto, J.-i., and Doi, M. (2002). "A coarse-graining procedure for flexible polymer chains with bonded and nonbonded interactions." *The Journal of Chemical Physics*, 116(18), 8183-8190.

Gao, G., Çagin, T., and Iii, W. A. G. (1998). "Energetics, structure, mechanical and vibrational properties of single-walled carbon nanotubes." *Nanotechnology*, 9(3), 184.

Gawlinski, E. T., and Stanley, H. E. (1981). "Continuum percolation in two dimensions: Monte carlo tests of scaling and universality for non-interacting discs." *Journal of Physics A: Mathematical and General*, 14(8), L291.

Geetha, S., Satheesh Kumar, K. K., Rao, C. R. K., Vijayan, M., and Trivedi, D. C. (2009). "Emi shielding: Methods and materials—a review." *Journal of Applied Polymer Science*, 112(4), 2073-2086.

Geim, A. K. (2009). "Graphene: Status and prospects." *Science*, 324(5934), 1530-1534.

Ghanem, R., and Ferro, G. (2006). "Health monitoring for strongly non-linear systems using the ensemble kalman filter." *Structural Control and Health Monitoring*, 13(1), 245-259.

Ghosh, A. K. (2009). *Introduction to measurements and instrumentation*, PHI Learning Pvt. Ltd., New Delhi, India.

Gilbert, M. (1994). "Crystallinity in poly(vinyl chloride)." *Journal of Macromolecular Science, Part C: Polymer Reviews*, 34(1), 77-135.

Gilles, C. (2006). "Distance between two lines in space."

Gingold, D. B., and Lobb, C. J. (1990). "Percolative conduction in three dimensions." *Physical Review B*, 42(13), 8220-8224.

Girifalco, L. A., Hodak, M., and Lee, R. S. (2000). "Carbon nanotubes, buckyballs, ropes, and a universal graphitic potential." *Physical Review B*, 62(19), 13104-13110.

Gnanendran, C. T., and Selvadurai, A. P. S. (2001). "Strain measurement and interpretation of stabilising force in geogrid reinforcement." *Geotextiles and Geomembranes*, 19(3), 177-194.

Gojny, F. H., Wichmann, M. H. G., Köpke, U., Fiedler, B., and Schulte, K. (2004). "Carbon nanotube-reinforced epoxy-composites: Enhanced stiffness and fracture toughness at low nanotube content." *Composites Science and Technology*, 64(15), 2363-2371.

Gojny, F. H., Wichmann, M. H. G., Fiedler, B., and Schulte, K. (2005). "Influence of different carbon nanotubes on the mechanical properties of epoxy matrix composites – a comparative study." *Composites Science and Technology*, 65(15–16), 2300-2313.

Göktürk, H. S., Fiske, T. J., and Kalyon, D. M. (1993). "Effects of particle shape and size distributions on the electrical and magnetic properties of nickel/polyethylene composites." *Journal of Applied Polymer Science*, 50(11), 1891-1901.

Good, R. J., and Hope, C. J. (1970). "New combining rule for intermolecular distances in intermolecular potential functions." *The Journal of Chemical Physics*, 53(2), 540-543.

Gorrasi, G., Romeo, V., Sannino, D., Sarno, M., Ciambelli, P., Vittoria, V., Vivo, B. D., and Tucci, V. (2007). "Carbon nanotube induced structural and physical property transitions of syndiotactic polypropylene." *Nanotechnology*, 18(27), 275703.

Govaert, L. E., Timmermans, P. H. M., and Brekelmans, W. A. M. (1999). "The influence of intrinsic strain softening on strain localization in polycarbonate: Modeling and experimental validation." *Journal of Engineering Materials and Technology*, 122(2), 177-185.

Grady, B. P. (2010). "Recent developments concerning the dispersion of carbon nanotubes in polymers." *Macromolecular Rapid Communications*, 31(3), 247-257.

Grady, B. P. (2011). *Carbon nanotube-polymer composites: Manufacture, properties, and applications*, John Wiley & Sons, Hoboken, NJ.

Griebel, M., and Hamaekers, J. (2005). "Molecular dynamics simulations of the elastic moduli of polymer–carbon nanotube composites." *Computer Methods in Applied Mechanics and Engineering*, 193(17–20), 1773-1788.

Griebel, M., Knapek, S., and Zumbusch, G. (2010). *Numerical simulation in molecular dynamics*, Springer-Verlag Berlin Heidelberg, New York, NY.

Grossiord, N., Wouters, M. E. L., Miltner, H. E., Lu, K., Loos, J., Mele, B. V., and Koning, C. E. (2010). "Isotactic polypropylene/carbon nanotube composites prepared by latex technology: Electrical conductivity study." *European Polymer Journal*, 46(9), 1833-1843.

Grujicic, M., Cao, G., and Roy, W. N. (2004). "A computational analysis of the percolation threshold and the electrical conductivity of carbon nanotubes filled polymeric materials." *Journal of Materials Science*, 39(14), 4441-4449.

Guo, J., Liu, Y., Prada-Silvy, R., Tan, Y., Azad, S., Krause, B., Pötschke, P., and Grady, B. P. (2014). "Aspect ratio effects of multi-walled carbon nanotubes on electrical, mechanical, and thermal properties of polycarbonate/mwcnt composites." *Journal of Polymer Science Part B: Polymer Physics*, 52(1), 73-83.

Guoquan, W., and Peng, Z. (2004). "Electrical conductivity of poly(vinyl chloride) plastisol–short carbon fiber composite." *Polymer Engineering & Science*, 37(1), 96-100.

Hadj-Hamou, T., Bakeer, R. M., and Gwyn, W. W. (1990). "Field performance of a geogrid-reinforced embankment." *Transportation Research Record*(1277).

Hadley, D. W. (1975). "Small strain elastic properties." *Structure and properties of oriented polymers*, I. M. Ward, ed., Springer Netherlands, 290-325.

Haghighatpanah, S., Bohlén, M., and Bolton, K. (2014). "Molecular level computational studies of polyethylene and polyacrylonitrile composites containing single walled carbon nanotubes: Effect of carboxylic acid functionalization on nanotube-polymer interfacial properties." *Frontiers in Chemistry*, 2.

Haile, J. M. (1997). *Molecular dynamics simulation: Elementary methods*, John Wiley & Sons, Inc., New York.

Haines, C. S., Lima, M. D., Li, N., Spinks, G. M., Foroughi, J., Madden, J. D. W., Kim, S. H., Fang, S., Andrade, M. J. d., Göktepe, F., Göktepe, Ö., Mirvakili, S. M., Naficy, S., Lepró, X., Oh, J., Kozlov, M. E., Kim, S. J., Xu, X., Swedlove, B. J., Wallace, G. G., and Baughman, R. H. (2014). "Artificial muscles from fishing line and sewing thread." *Science*, 343(6173), 868-872.

Haji Ali, F., and Tee, H. E. (1988). "Monitoring of reinforced slope. Reinforced soil and geotextiles."Bombay, India.

Halpin Affdl, J. C., and Kardos, J. L. (1976). "The halpin-tsai equations: A review." *Polymer Engineering & Science*, 16(5), 344-352.

Han, E. H. M., Leon, E. G., and Robert, J. M. S. (2000). "A multi-level finite element method for modeling rubber-toughened amorphous polymers." *Toughening of plastics*, American Chemical Society, 50-70.

Han, Z., and Fina, A. (2011). "Thermal conductivity of carbon nanotubes and their polymer nanocomposites: A review." *Progress in Polymer Science*, 36(7), 914-944.

Harmandaris, V. A., and Mavrantzas, V. G. (2004). "Molecular dynamics simulation of polymers." *Simulation methods for polymers*, M. Kotelyanskii, and D. N. Theodorou, eds., Macel Dekker, New York, NY.

Hatami, K., and Bathurst, R. J. (2005). "Development and verification of a numerical model for the analysis of geosynthetic-reinforced soil segmental walls under working stress conditions." *Canadian Geotechnical Journal*, 42(4), 1066-1085.

Hatami, K., Grady, B. P., and Ulmer, M. C. (2009). "Sensor-enabled geosynthetics: Use of conducting carbon networks as geosynthetic sensors." *Journal of Geotechnical and Geoenvironmental Engineering*, 135(7), 863-874.

Hatami, K., Grady, B., and Ulmer, M. (2011). "Closure to 'sensor-enabled geosynthetics: Use of conducting carbon networks as geosynthetic sensors' by kianoosh hatami, brian p. Grady, and matthew c. Ulmer." *Journal of Geotechnical and Geoenvironmental Engineering*, 137(4), 435-436.

Hatami, K., Hassanikhah, A., Yazdani, H., and Grady, B. (2014). "Tensoresistive pvc coating for sensor-enabled geogrids." *Journal of Nanomechanics and Micromechanics*, 4(4), A4013016.

Haward, R. N., and Thackray, G. (1968). "The use of a mathematical model to describe isothermal stress-strain curves in glassy thermoplastics." *Proceedings of the Royal Society of London A: Mathematical, Physical and Engineering Sciences*, 302(1471), 453-472.

Hera, A., and Hou, Z. (2004). "Application of wavelet approach for asce structural health monitoring benchmark studies." *Journal of Engineering Mechanics*, 130(1), 96-104.

Hernández, E., Goze, C., Bernier, P., and Rubio, A. (1998). "Elastic properties of c and ${b}_{\mathit{x}}{c}_{\mathit{y}}{n}_{\mathit{z}}$ composite nanotubes." *Physical Review Letters*, 80(20), 4502-4505.

Hilding, J., Grulke, E. A., George Zhang, Z., and Lockwood, F. (2003). "Dispersion of carbon nanotubes in liquids." *Journal of Dispersion Science and Technology*, 24(1), 1-41.

Hindermann-Bischoff, M., and Ehrburger-Dolle, F. (2001). "Electrical conductivity of carbon black–polyethylene composites: Experimental evidence of the change of cluster connectivity in the ptc effect." *Carbon*, 39(3), 375-382.

Hirvi, J. T., and Pakkanen, T. A. (2006). "Molecular dynamics simulations of water droplets on polymer surfaces." *The Journal of Chemical Physics*, 125(14), 144712.

Holtz, R. D. (2001). "Geosynthetics for soil reinforcement." *9th Spencer J. Buchanan Lecture*, Texas A & M University.

Hossain, D., Tschopp, M. A., Ward, D. K., Bouvard, J. L., Wang, P., and Horstemeyer, M. F. (2010). "Molecular dynamics simulations of deformation mechanisms of amorphous polyethylene." *Polymer*, 51(25), 6071-6083.

Hu, N., Karube, Y., Arai, M., Watanabe, T., Yan, C., Li, Y., Liu, Y., and Fukunaga, H. (2010). "Investigation on sensitivity of a polymer/carbon nanotube composite strain sensor." *Carbon*, 48(3), 680-687.

Huang, J.-C., Chuang, S.-F., Su, T.-Y., and Grossman, S. J. (1999). "The effects of plasticizers on carbon black-filled elastomers." *Journal of Polymer Engineering*, 19(1), 39-52.

Huang, J.-C. (2002). "Carbon black filled conducting polymers and polymer blends." *Advances in Polymer Technology*, 21(4), 299-313.

Huang, S., Qian, Y., Chen, J., Cai, Q., Wan, L., Wang, S., and Hu, W. (2008). "Identification of the structures of superlong oriented single-walled carbon nanotube arrays by electrodeposition of metal and raman spectroscopy." *Journal of the American Chemical Society*, 130(36), 11860-11861.

Huang, S., Liu, Z., Yin, C., Wang, Y., Gao, Y., Chen, C., and Yang, M. (2011). "Enhancement effect of filler network on isotactic polypropylene/carbon black composite melts." *Colloid and Polymer Science*, 289(15-16), 1673-1681.

Huang, Y. Y., Knowles, T. P. J., and Terentjev, E. M. (2009). "Strength of nanotubes, filaments, and nanowires from sonication-induced scission." *Advanced Materials*, 21(38-39), 3945-3948.

Huang, Y. Y., and Terentjev, E. M. (2012). "Dispersion of carbon nanotubes: Mixing, sonication, stabilization, and composite properties." *Polymers*, 4(1), 275.

Huston, D. (2010). *Structural sensing, health monitoring, and performance evaluation*, Taylor & Francis, Boca Raton, FL.

Iijima, S. (1991). "Helical microtubules of graphitic carbon." *Nature*, 354(6348), 56-58.

Islam, M. F., Rojas, E., Bergey, D. M., Johnson, A. T., and Yodh, A. G. (2003). "High weight fraction surfactant solubilization of single-wall carbon nanotubes in water." *Nano Letters*, 3(2), 269-273.

Ivakhnenko, V., and Eremin, Y. (2006). "Light scattering by needle-type and disk-type particles." *Journal of Quantitative Spectroscopy and Radiative Transfer*, 100(1–3), 165-172.

Jain, S. (1992). *Monte carlo simulations of disordered systems*, World Scientific, Singapore.

Jarque, C. M., and Bera, A. K. (1980). "Efficient tests for normality, homoscedasticity and serial independence of regression residuals." *Economics Letters*, 6(3), 255-259.

Jha, V., Thomas, A. G., Bennett, M., and Busfield, J. J. C. (2010). "Reversible electrical behavior with strain for a carbon black-filled rubber." *Journal of Applied Polymer Science*, 116(1), 541-546.

Jin, C., Lan, H., Peng, L., Suenaga, K., and Iijima, S. (2009). "Deriving carbon atomic chains from graphene." *Physical Review Letters*, 102(20), 205501.

Jing, X., Zhao, W., and Lan, L. (2000). "The effect of particle size on electric conducting percolation threshold in polymer/conducting particle composites." *Journal of Materials Science Letters*, 19(5), 377-379.

Jogi, B. F., Sawant, M., Kulkarni, M., and Brahmankar, P. K. (2012). "Dispersion and performance properties of carbon nanotubes (cnts) based polymer composites: A review." *Journal of Encapsulation and Adsorption Sciences*, 02(04), 69-78.

Jones, J. E. (1924). "On the determination of molecular fields. Ii. From the equation of state of a gas." *Proceedings of the Royal Society of London. Series A*, 106(738), 463-477.

Kang, I., Schulz, M. J., Kim, J. H., Shanov, V., and Shi, D. (2006). "A carbon nanotube strain sensor for structural health monitoring." *Smart Materials and Structures*, 15(3), 737.

Kato, H., and Miyashita, Y. (1990). "Qualification of the electrical conductivity of carbon black filled polymeric materials." *Proc., , Conference on Electrical Insulation and Dielectric Phenomena, 1990. Annual Report*, 417-424.

Kavassalis, T. A., and Sundararajan, P. R. (1993). "A molecular-dynamics study of polyethylene crystallization." *Macromolecules*, 26(16), 4144-4150.

Kawakatsu, T. (2004). *Statistical physics of polymers: An introduction*, Springer-Verlag Berlin Heidelberg, Germany.

Kay, D., Blond, E., and Mlynarek, J. (2004). "Geosynthetics durability: A polymer chemistry issue." *Proc., 57th Canadian Geotechnical Conference/5th Joint CGS/IAH Conference*Quebec City, Quebec, Canada, Session-4D. pp. 1-14.

Kearns, J. C., and Shambaugh, R. L. (2002). "Polypropylene fibers reinforced with carbon nanotubes." *Journal of Applied Polymer Science*, 86(8), 2079-2084.

Kee Paik, J. (2008). "Ultimate strength of perforated steel plates under combined biaxial compression and edge shear loads." *Thin-Walled Structures*, 46(2), 207-213.

Kerr, C. J., Huang, Y. Y., Marshall, J. E., and Terentjev, E. M. (2011). "Effect of filament aspect ratio on the dielectric response of multiwalled carbon nanotube composites." *Journal of Applied Physics*, 109(9), 094109.

Kharchenko, S. B., Douglas, J. F., Obrzut, J., Grulke, E. A., and Migler, K. B. (2004). "Flow-induced properties of nanotube-filled polymer materials." *Nature Materials*, 3(8), 564-568.

King, J. A., Morrison, F. A., Keith, J. M., Miller, M. G., Smith, R. C., Cruz, M., Neuhalfen, A. M., and Barton, R. L. (2006). "Electrical conductivity and rheology of carbon-filled liquid crystal polymer composites." *Journal of Applied Polymer Science*, 101(4), 2680-2688.

King, J. A., Johnson, B. A., Via, M. D., and Ciarkowski, C. J. (2009a). "Electrical conductivity of carbon-filled polypropylene-based resins." *Journal of Applied Polymer Science*, 112(1), 425-433.

King, J. A., Via, M. D., Keith, J. M., and Morrison, F. A. (2009b). "Effects of carbon fillers on rheology of polypropylene-based resins." *Journal of Composite Materials*, 43(25), 3073-3089.

Kirkpatrick, S. (1973). "Percolation and conduction." *Reviews of Modern Physics*, 45(4), 574-588.

Kis, A., and Zettl, A. (2008). *Nanomechanics of carbon nanotubes*.

Knite, M., Tupureina, V., Fuith, A., Zavickis, J., and Teteris, V. (2007). "Polyisoprene—multi-wall carbon nanotube composites for sensing strain." *Materials Science and Engineering: C*, 27(5–8), 1125-1128.

Koerner, R. M. (1996). "The state-of-the-practice regarding in-situ monitoring of geosynthetics."Maastricht, Netherlands, 71-86.

Koerner, R. M., and Hsuan, Y. G. (2001). "Geosynthetics: Characteristics and testing." *Geotechnical and geoenvironmental engineering handbook*, R. K. Rowe, ed., Springer US, 173-196.

Koerner, R. M. (2012). *Designing with geosynthetics - 6th edition vol. 1*, Xlibris, Corp.

Kolmogoroff, A. N. (1969). *The logarithmically normal law of distribution of dimensions of particles when broken into small parts*, NASA Publication.

Kolmogorov, A. N. (1933). "Sulla determinazione empirica di una legge di distribuzione." *Giornale dell' Istituto Italiano degli Attuari*, 4, 83-91.

Koncar, V., Cochrane, C., Lewandowski, M., Boussu, F., and Dufour, C. (2009). "Electro-conductive sensors and heating elements based on conductive polymer composites." *International Journal of Clothing Science and Technology*, 21(2/3), 82-92.

Kong, J., Soh, H. T., Cassell, A. M., Quate, C. F., and Dai, H. (1998). "Synthesis of individual single-walled carbon nanotubes on patterned silicon wafers." *Nature*, 395(6705), 878-881.

Konstantinova, E., Dantas, S. O., and Barone, P. M. V. B. (2006). "Electronic and elastic properties of two-dimensional carbon planes." *Physical Review B*, 74(3), 035417.

Koratkar, N. A. (2013). *Graphene in composite materials: Synthesis, characterization and applications*, DEStech Publications, Inc.

Kortschot, M. T., and Woodhams, R. T. (1988). "Computer simulation of the electrical conductivity of polymer composites containing metallic fillers." *Polymer Composites*, 9(1), 60-71.

Kost, J., Narkis, M., and Foux, A. (1984). "Resistivity behavior of carbon-black-filled silicone rubber in cyclic loading experiments." *Journal of Applied Polymer Science*, 29(12), 3937-3946.

Kovacs, J. Z., Andresen, K., Pauls, J. R., Garcia, C. P., Schossig, M., Schulte, K., and Bauhofer, W. (2007). "Analyzing the quality of carbon nanotube dispersions in polymers using scanning electron microscopy." *Carbon*, 45(6), 1279-1288.

Koval'chuk, A. A., Shchegolikhin, A. N., Shevchenko, V. G., Nedorezova, P. M., Klyamkina, A. N., and Aladyshev, A. M. (2008). "Synthesis and properties of polypropylene/multiwall carbon nanotube composites." *Macromolecules*, 41(9), 3149-3156.

Koziol, K., Vilatela, J., Moisala, A., Motta, M., Cunniff, P., Sennett, M., and Windle, A. (2007). "High-performance carbon nanotube fiber." *Science*, 318(5858), 1892-1895.

Ku-Herrera, J. J., and Avilés, F. (2012). "Cyclic tension and compression piezoresistivity of carbon nanotube/vinyl ester composites in the elastic and plastic regimes." *Carbon*, 50(7), 2592-2598.

Lahiff, E., Leahy, R., Coleman, J. N., and Blau, W. J. (2006). "Physical properties of novel free-standing polymer–nanotube thin films." *Carbon*, 44(8), 1525-1529.

Last, B. J., and Thouless, D. J. (1971). "Percolation theory and electrical conductivity." *Physical Review Letters*, 27(25), 1719-1721.

Laube, S., Monthey, S., and Wang, M. J. (2001). "Compounding with carbon black and oil." *Rubber technology: Compounding and testing for performance*, J. S. Dick, ed., Hanser Gardner Publications, Munich, Germany.

Lee, C., Wei, X., Kysar, J. W., and Hone, J. (2008). "Measurement of the elastic properties and intrinsic strength of monolayer graphene." *Science*, 321(5887), 385-388.

Levy, N., Burke, S. A., Meaker, K. L., Panlasigui, M., Zettl, A., Guinea, F., Neto, A. H. C., and Crommie, M. F. (2010). "Strain-induced pseudo–magnetic fields greater than 300 tesla in graphene nanobubbles." *Science*, 329(5991), 544-547.

Li, C., Thostenson, E. T., and Chou, T.-W. (2007a). "Dominant role of tunneling resistance in the electrical conductivity of carbon nanotube–based composites." *Applied Physics Letters*, 91(22), 223114.

Li, C., Thostenson, E. T., and Chou, T.-W. (2008). "Sensors and actuators based on carbon nanotubes and their composites: A review." *Composites Science and Technology*, 68(6), 1227-1249.

Li, J., Ma, P. C., Chow, W. S., To, C. K., Tang, B. Z., and Kim, J. K. (2007b). "Correlations between percolation threshold, dispersion state, and aspect ratio of carbon nanotubes." *Advanced Functional Materials*, 17(16), 3207-3215.

Li, J., Ballmer, S. G., Gillis, E. P., Fujii, S., Schmidt, M. J., Palazzolo, A. M. E., Lehmann, J. W., Morehouse, G. F., and Burke, M. D. (2015). "Synthesis of many different types of organic small molecules using one automated process." *Science*, 347(6227), 1221-1226.

Li, Q. W., Li, Y., Zhang, X. F., Chikkannanavar, S. B., Zhao, Y. H., Dangelewicz, A. M., Zheng, L. X., Doorn, S. K., Jia, Q. X., Peterson, D. E., Arendt, P. N., and Zhu, Y. T. (2007c). "Structure-dependent electrical properties of carbon nanotube fibers." *Advanced Materials*, 19(20), 3358-3363.

Li, W., Buschhorn, S. T., Schulte, K., and Bauhofer, W. (2011). "The imaging mechanism, imaging depth, and parameters influencing the visibility of carbon nanotubes in a polymer matrix using an sem." *Carbon*, 49(6), 1955-1964.

Li, W., and Bauhofer, W. (2014). "Visualization of cnts in polymer composites." *Polymer nanotube nanocomposites*, John Wiley & Sons, Inc., 405-428.

Li, W. Z., Xie, S. S., Qian, L. X., Chang, B. H., Zou, B. S., Zhou, W. Y., Zhao, R. A., and Wang, G. (1996). "Large-scale synthesis of aligned carbon nanotubes." *Science*, 274(5293), 1701-1703.

Li, Y., Lu, D., and Wong, C. P. (2010). "Isotropically conductive adhesives (icas)." *Electrical conductive adhesives with nanotechnologies*, Springer US, 121-225.

Lillehei, P. T., Kim, J.-W., Gibbons, L. J., and Park, C. (2009). "A quantitative assessment of carbon nanotube dispersion in polymer matrices." *Nanotechnology*, 20(32), 325708.

Ling, H. I., Mohri, Y., Leshchinsky, D., Burke, C., Matsushima, K., and Liu, H. (2005). "Large-scale shaking table tests on modular-block reinforced soil retaining walls." *Journal of Geotechnical and Geoenvironmental Engineering*, 131(4), 465-476.

Liu, C. (2011). *Foundations of mems*, Prentice Hall, Upper Saddle River, N.J.

Liu, F., Ming, P., and Li, J. (2007). "Ab initio calculation of ideal strength and phonon instability of graphene under tension." *Physical Review B*, 76(6), 064120.

Liu, F., Wang, H., Xue, L., Fan, L., and Zhu, Z. (2008). "Effect of microstructure on the mechanical properties of pan-based carbon fibers during high-temperature graphitization." *Journal of Materials Science*, 43(12), 4316-4322.

Liu, L., and Wagner, H. D. (2005). "Rubbery and glassy epoxy resins reinforced with carbon nanotubes." *Composites Science and Technology*, 65(11–12), 1861-1868.

Liu, T., Phang, I. Y., Shen, L., Chow, S. Y., and Zhang, W.-D. (2004). "Morphology and mechanical properties of multiwalled carbon nanotubes reinforced nylon-6 composites." *Macromolecules*, 37(19), 7214-7222.

Logakis, E., Pissis, P., Pospiech, D., Korwitz, A., Krause, B., Reuter, U., and Pötschke, P. (2010a). "Low electrical percolation threshold in poly(ethylene terephthalate)/multi-walled carbon nanotube nanocomposites." *European Polymer Journal*, 46(5), 928-936.

Logakis, E., Pollatos, E., Pandis, C., Peoglos, V., Zuburtikudis, I., Delides, C. G., Vatalis, A., Gjoka, M., Syskakis, E., Viras, K., and Pissis, P. (2010b). "Structure–property relationships in isotactic polypropylene/multi-walled carbon nanotubes nanocomposites." *Composites Science and Technology*, 70(2), 328-335.

Logakis, E., Pandis, C., Pissis, P., Pionteck, J., and Pötschke, P. (2011). "Highly conducting poly(methyl methacrylate)/carbon nanotubes composites: Investigation on their thermal,

dynamic-mechanical, electrical and dielectric properties." *Composites Science and Technology*, 71(6), 854-862.

Loos, J., Alexeev, A., Grossiord, N., Koning, C. E., and Regev, O. (2005). "Visualization of single-wall carbon nanotube (swnt) networks in conductive polystyrene nanocomposites by charge contrast imaging." *Ultramicroscopy*, 104(2), 160-167.

Lostumbo, J. M., and Artieres, O. (2011). "Geosynthetic enabled with fiber optic sensors for mse bridge abutment supporting shallow bridge foundation." American Society of Civil Engineers, 3497-3504.

Lourie, O., Cox, D. M., and Wagner, H. D. (1998). "Buckling and collapse of embedded carbon nanotubes." *Physical Review Letters*, 81(8), 1638-1641.

Lu, Q., Gao, W., and Huang, R. (2011). "Atomistic simulation and continuum modeling of graphene nanoribbons under uniaxial tension." *Modelling and Simulation in Materials Science and Engineering*, 19(5), 054006.

Lu, W., Chou, T.-W., and Thostenson, E. T. (2010). "A three-dimensional model of electrical percolation thresholds in carbon nanotube-based composites." *Applied Physics Letters*, 96(22), 223106.

Luheng, W., Tianhuai, D., and Peng, W. (2009). "Influence of carbon black concentration on piezoresistivity for carbon-black-filled silicone rubber composite." *Carbon*, 47(14), 3151-3157.

Luo, X., and Chung, D. D. L. (1999). "Electromagnetic interference shielding using continuous carbon-fiber carbon-matrix and polymer-matrix composites." *Composites Part B: Engineering*, 30(3), 227-231.

Lutsko, J. F. (1988). "Stress and elastic constants in anisotropic solids: Molecular dynamics techniques." *Journal of Applied Physics*, 64(3), 1152-1154.

Lynch, J. P., Loh, K. J., Hou, T. C., and Kotov, N. (2009). "Nanocomposite sensing skins for distributed structural sensing." *Nanotechnology in construction 3*, Z. Bittnar, P. J. M. Bartos, J. Němeček, V. Šmilauer, and J. Zeman, eds., Springer Berlin Heidelberg, 303-308.

Ma, H. M., and Gao, X. L. (2008). "A three-dimensional monte carlo model for electrically conductive polymer matrix composites filled with curved fibers." *Polymer*, 49(19), 4230-4238.

Ma, P.-C., Liu, M.-Y., Zhang, H., Wang, S.-Q., Wang, R., Wang, K., Wong, Y.-K., Tang, B.-Z., Hong, S.-H., Paik, K.-W., and Kim, J.-K. (2009). "Enhanced electrical conductivity of nanocomposites containing hybrid fillers of carbon nanotubes and carbon black." *ACS Applied Materials & Interfaces*, 1(5), 1090-1096.

Ma, Z., Merkus, H. G., de Smet, J. G. A. E., Heffels, C., and Scarlett, B. (2000). "New developments in particle characterization by laser diffraction: Size and shape." *Powder Technology*, 111(1–2), 66-78.

Mahmoud, W. E., El-Lawindy, A. M. Y., El Eraki, M. H., and Hassan, H. H. (2007). "Butadiene acrylonitrile rubber loaded fast extrusion furnace black as a compressive strain and pressure sensors." *Sensors and Actuators A: Physical*, 136(1), 229-233.

Mak, K. F., Sfeir, M. Y., Wu, Y., Lui, C. H., Misewich, J. A., and Heinz, T. F. (2008). "Measurement of the optical conductivity of graphene." *Physical Review Letters*, 101(19), 196405.

Mamunya, E. P., Davidenko, V. V., and Lebedev, E. V. (1996). "Effect of polymer-filler interface interactions on percolation conductivity of thermoplastics filled with carbon black." *Composite Interfaces*, 4(4), 169-176.

Mamunya, Y., Boudenne, A., Lebovka, N., Ibos, L., Candau, Y., and Lisunova, M. (2008). "Electrical and thermophysical behaviour of pvc-mwcnt nanocomposites." *Composites Science and Technology*, 68(9), 1981-1988.

Mamunya, Y. P., Levchenko, V. V., Rybak, A., Boiteux, G., Lebedev, E. V., Ulanski, J., and Seytre, G. (2010). "Electrical and thermomechanical properties of segregated nanocomposites based on pvc and multiwalled carbon nanotubes." *Journal of Non-Crystalline Solids*, 356(11–17), 635-641.

Mandal, A., and Singh, S. P. (2011). "Fiber pull-out strength of single-walled carbon nanotube reinforced polypropylene (pp) composite using molecular dynamics simulation."Denver, CO.

MarChem (2011). "Quality assurance report." MarChem Southeast, Inc., Adairsville, Georgia.

Marianetti, C., and Yevick, H. (2010). "Failure mechanisms of graphene under tension." *Physical Review Letters*, 105(24), 245502.

Marr, W. A. (2008). "Why performance monitoring?" *Proc., The first Pan American Geosynthetics Conference & Exhibition*Cancun, Mexico, 690-704.

Marsaglia, G., Zaman, A., and Wan Tsang, W. (1990). "Toward a universal random number generator." *Statistics & Probability Letters*, 9(1), 35-39.

Martin, C. A., Sandler, J. K. W., Shaffer, M. S. P., Schwarz, M. K., Bauhofer, W., Schulte, K., and Windle, A. H. (2004). "Formation of percolating networks in multi-wall carbon-nanotube–epoxy composites." *Composites Science and Technology*, 64(15), 2309-2316.

Maruthamuthu, M., Selvaraj, M., and Annadurai, S. (1993). "Electrical conductivity of modified poly(vinyl chloride)." *Bulletin of Materials Science*, 16(4), 273-286.

Masadome, T., Asano, Y., Imato, T., Ohkubo, S., Tobita, T., Tabei, H., Iwasaki, Y., Niwa, O., and Fushinuki, Y. (2002). "Preparation of refractive index matching polymer film alternative to oil for use in a portable surface-plasmon resonance phenomenon-based chemical sensor method." *Analytical and Bioanalytical Chemistry*, 373(4-5), 222-226.

Mather, P. J., and Thomas, K. M. (1997). "Carbon black/high density polyethylene conducting composite materials: Part ii the relationship between the positive temperature coefficient and the volume resistivity." *Journal of Materials Science*, 32(7), 1711-1715.

Mattoni, A., Ippolito, M., and Colombo, L. (2007). "Atomistic modeling of brittleness in covalent materials." *Physical Review B*, 76(22), 224103.

Mayo, S. L., Olafson, B. D., and Goddard, W. A. (1990). "Dreiding: A generic force field for molecular simulations." *Journal of Physical Chemistry*.

Medalia, A. I. (1986). "Electrical conduction in carbon black composites." *Rubber Chemistry and Technology*, 59(3), 432-454.

Medcoat (2015). "Dlc | medcoat." <http://www.medcoat.us/dlc-coatings/>. (June 25, 2015).

Meier, R. J., and Struik, L. C. E. (1998). "Atomistic modelling study of relaxation processes in polymers: The β-relaxation in polyvinylchloride." *Polymer*, 39(1), 31-38.

Metis Design (2015). "Structural health monitoring." *Metis Design*.

Mierczynska, A., Mayne-L'Hermite, M., Boiteux, G., and Jeszka, J. K. (2007). "Electrical and mechanical properties of carbon nanotube/ultrahigh-molecular-weight polyethylene composites prepared by a filler prelocalization method." *Journal of Applied Polymer Science*, 105(1), 158-168.

Mir, M., Hosseini, A., and Majzoobi, G. H. (2008). "A numerical study of vibrational properties of single-walled carbon nanotubes." *Computational Materials Science*, 43(3), 540-548.

Mironi-Harpaz, I., and Narkis, M. (2001). "Electrical behavior and structure of polypropylene/ultrahigh molecular weight polyethylene/carbon black immiscible blends." *Journal of Applied Polymer Science*, 81(1), 104-115.

Miyasaka, K., Watanabe, K., Jojima, E., Aida, H., Sumita, M., and Ishikawa, K. (1982). "Electrical conductivity of carbon-polymer composites as a function of carbon content." *Journal of Materials Science*, 17(6), 1610-1616.

Mukhopadhyay, K., Dwivedi, C. D., and Mathur, G. N. (2002). "Conversion of carbon nanotubes to carbon nanofibers by sonication." *Carbon*, 40(8), 1373-1376.

Munson-McGee, S. H. (1991). "Estimation of the critical concentration in an anisotropic percolation network." *Physical Review B*, 43(4), 3331-3336.

Musikding (2015). <http://www.musikding.de/Wire-potentiometer-100R-/-4W>. (2015).

Muster, J., Burghard, M., Roth, S., Duesberg, G. S., Hernández, E., and Rubio, A. (1998). "Scanning force microscopy characterization of individual carbon nanotubes on electrode arrays." *Journal of Vacuum Science & Technology B*, 16(5), 2796-2801.

Nakanishi, R., Kitaura, R., Warner, J. H., Yamamoto, Y., Arai, S., Miyata, Y., and Shinohara, H. (2013). "Thin single-wall bn-nanotubes formed inside carbon nanotubes." *Scientific Reports*, 3.

Nancey, A., Briançon, L., and Villard, P. (2004). "Geodetect: The first "intelligent" geosynthetic for the measurements of strain in soil and the survey of reinforced earth construction."London, UK.

Nancey, A., Voet, M., and Vlekken, J. (2005). "Geodetect: A new step for the use of giber optic bragg grating technology in soil engineering."Bruges, Belgium.

Nanni, F., Ruscito, G., Puglia, D., Terenzi, A., Kenny, J. M., and Gusmano, G. (2011). "Effect of carbon black nanoparticle intrinsic properties on the self-monitoring performance of glass fibre reinforced composite rods." *Composites Science and Technology*, 71(1), 1-8.

Narkis, M., Ram, A., and Stein, Z. (1981). "Electrical properties of carbon black filled crosslinked polyethylene." *Polymer Engineering & Science*, 21(16), 1049-1054.

Narkis, M., and Vaxman, A. (1984). "Resistivity behavior of filled electrically conductive crosslinked polyethylene." *Journal of Applied Polymer Science*, 29(5), 1639-1652.

Nat Nano (2006). "Nan'o·tech·nol'o·gy n." *Nature Nanotechnology*, 1(1), 8-10.

Néda, Z., Florian, R., and Brechet, Y. (1999). "Reconsideration of continuum percolation of isotropically oriented sticks in three dimensions." *Physical Review E*, 59(3), 3717-3719.

Ni, B., Sinnott, S. B., Mikulski, P. T., and Harrison, J. A. (2002). "Compression of carbon nanotubes filled with c60, ch4, or ne: Predictions from molecular dynamics simulations." *Physical Review Letters*, 88(20), 205505.

Nicodemo, L., Nicolais, L., Romeo, G., and Scafora, E. (1978). "Temperature effect on the electrical resistivity of metal/polymer composites." *Polymer Engineering & Science*, 18(4), 293-298.

Nishio, M., Mizutani, T., and Takeda, N. (2010). "Structural shape reconstruction with consideration of the reliability of distributed strain data from a brillouin-scattering-based optical fiber sensor." *Smart Materials and Structures*, 19(3), 035011.

Noguchi, T., Nagai, T., and Seto, J. e. (1986). "Melt viscosity and electrical conductivity of carbon black-pvc composite." *Journal of Applied Polymer Science*, 31(6), 1913-1924.

Novak, M. A., Surwade, S., Prokop, J., Bolotin, K., Hone, J., Brus, L., Nuckolls, C., and Liu, H. (2014). "Visualizing individual carbon nanotubes with optical microscopy." *Journal of the American Chemical Society*, 136(24), 8536-8539.

Novoselov, K. S., Geim, A. K., Morozov, S. V., Jiang, D., Zhang, Y., Dubonos, S. V., Grigorieva, I. V., and Firsov, A. A. (2004). "Electric field effect in atomically thin carbon films." *Science*, 306(5696), 666-669.

Ogale, A. A., and Wang, S. F. (1993). "Simulation of the percolation behavior of quasi- and transversely isotropic short-fiber composites with a continuum model." *Composites Science and Technology*, 46(4), 379-388.

Ogasawara, T., Ishida, Y., Ishikawa, T., and Yokota, R. (2004). "Characterization of multi-walled carbon nanotube/phenylethynyl terminated polyimide composites." *Composites Part A: Applied Science and Manufacturing*, 35(1), 67-74.

Okuhara, Y., Shin, S.-G., Matsubara, H., Yanagida, H., and Takeda, N. (2001). "Development of conductive frp containing carbon phase for self-diagnosis structures."Newport Beach, CA, 314-322.

Oliva-Avilés, A. I., Avilés, F., Seidel, G. D., and Sosa, V. (2013). "On the contribution of carbon nanotube deformation to piezoresistivity of carbon nanotube/polymer composites." *Composites Part B: Engineering*, 47, 200-206.

Oskouyi, A., Sundararaj, U., and Mertiny, P. (2014). "Tunneling conductivity and piezoresistivity of composites containing randomly dispersed conductive nano-platelets." *Materials*, 7(4), 2501.

Palacky, G. J. (1988). "Resistivity characteristics of geologic targets." *Electromagnetic methods in applied geophysics*, M. N. Nabighian, ed., SEG, Tulsa OK.

Pandini, S., and Pegoretti, A. (2011). "Time and temperature effects on poisson's ratio of poly(butylene terephthalate)." *eXPRESS Polymer Letters*, 5(8), 685-697.

Pant, P. V. K., Han, J., Smith, G. D., and Boyd, R. H. (1993). "A molecular dynamics simulation of polyethylene." *The Journal of Chemical Physics*, 99(1), 597-604.

Park, M., Kim, H., and Youngblood, J. P. (2008). "Strain-dependent electrical resistance of multi-walled carbon nanotube/polymer composite films." *Nanotechnology*, 19(5), 055705.

Parmar, K., Mahmoodi, M., Park, C., and Park, S. S. (2013). "Effect of cnt alignment on the strain sensing capability of carbon nanotube composites." *Smart Materials and Structures*, 22(7), 075006.

Patrick, S. (2005). *Practical guide to polyvinyl chloride*, Rapra Technology ltd., Shropshire, UK.

Paul, W., Yoon, D. Y., and Smith, G. D. (1995). "An optimized united atom model for simulations of polymethylene melts." *The Journal of Chemical Physics*, 103(4), 1702-1709.

Pawar, S. D., Murugavel, P., and Lal, D. M. (2009). "Effect of relative humidity and sea level pressure on electrical conductivity of air over indian ocean." *Journal of Geophysical Research: Atmospheres*, 114(D2), D02205.

Pearson, K. (1895). "Note on regression and inheritance in the case of two parents." *Proceedings of the Royal Society of London*, 58(347-352), 240-242.

Pei, H.-F., Teng, J., Yin, J.-H., and Chen, R. (2014). "A review of previous studies on the applications of optical fiber sensors in geotechnical health monitoring." *Measurement*, 58, 207-214.

Pei, Q. X., Zhang, Y. W., and Shenoy, V. B. (2010). "A molecular dynamics study of the mechanical properties of hydrogen functionalized graphene." *Carbon*, 48(3), 898-904.

Perriot, R., Gu, X., Lin, Y., Zhakhovsky, V. V., and Oleynik, I. I. (2013). "Screened environment-dependent reactive empirical bond-order potential for atomistic simulations of carbon materials." *Physical Review B*, 88(6), 064101.

Peters, J. E. (2009). "Thermal and electrical behavior of carbon nanotube composites." The University of Oklahoma, Norman, OK.

Peters, K. (2011). "Polymer optical fiber sensors—a review." *Smart Materials and Structures*, 20(1), 013002.

Petrović, Z. S., Martinović, B., Divjaković, V., and Budinski–Simendić, J. (1993). "Polypropylene–carbon black interaction in conductive composites." *Journal of Applied Polymer Science*, 49(9), 1659-1669.

Pham, G. T., Park, Y.-B., Liang, Z., Zhang, C., and Wang, B. (2008). "Processing and modeling of conductive thermoplastic/carbon nanotube films for strain sensing." *Composites Part B: Engineering*, 39(1), 209-216.

Physicsworld (2015). "Scientists delve deeper into carbon nanotubes - physicsworld.Com." <http://physicsworld.com/cws/article/news/2013/feb/19/scientists-delve-deeper-into-carbon-nanotubes>.

Pike, G. E., and Seager, C. H. (1974). "Percolation and conductivity: A computer study. I." *Physical Review B*, 10(4), 1421-1434.

Pinto, G., López-gonzález, C., and Jiménez-martín, A. (1999). "Polymer composites prepared by compression molding of a mixture of carbon black and nylon 6 powder." *Polymer Composites*, 20(6), 804-808.

Plimpton, S. (1995). "Fast parallel algorithms for short-range molecular dynamics." *Journal of Computational Physics*, 117(1), 1-19.

Plucknett, K. P., Pomfret, S. J., Normand, V., Ferdinando, D., Veerman, C., Frith, W. J., and Norton, I. T. (2001). "Dynamic experimentation on the confocal laser scanning microscope: Application to soft-solid, composite food materials." *J Microsc*, 201(Pt 2), 279-290.

Polley, M. H., and Boonstra, B. B. S. T. (1957). "Carbon blacks for highly conductive rubber." *Rubber Chemistry and Technology*, 30(1), 170-179.

Popplewell, L. M., Campanella, O. H., Sapru, V., and Peleg, M. (1989). "Theoretical comparison of two segregation indices for binary powder mixtures." *Powder Technology*, 58(1), 55-61.

Powell, K. L., Yeomans, J. A., and Smith, P. A. (1993). "Characterization of subsurface damage in ceramic-matrix composites by confocal scanning laser microscopy." *Journal of Microscopy*, 169(2), 189-195.

Powell, M. J. (1979). "Site percolation in randomly packed spheres." *Physical Review B*, 20(10), 4194-4198.

Probst, N. (1993). "Conducting carbon black." *Carbon black: Science and technology*, J.-B. Donnet, R. C. Bansal, and M.-J. Wang, eds., Marcel Dekker, New York, NY.

Pyshkina, O. A., Panova, T. V., Boeva, Z. A., Lezov, A. A., Polushina, G. E., Lezov, A. V., and Sergeyev, V. G. (2012). "Behavior of multiwalled carbon nanotubes functionalized with sulfo groups in aqueous salt solutions." *Nanotechnologies in Russia*, 7(11-12), 629-634.

Qian, D., Dickey, E. C., Andrews, R., and Rantell, T. (2000). "Load transfer and deformation mechanisms in carbon nanotube-polystyrene composites." *Applied Physics Letters*, 76(20), 2868-2870.

Rapaport, D. C. (2004). *The art of molecular dynamics simulation*, Cambridge University Press, Cambridge, UK.

Richeton, J., Ahzi, S., Vecchio, K. S., Jiang, F. C., and Adharapurapu, R. R. (2006). "Influence of temperature and strain rate on the mechanical behavior of three amorphous polymers: Characterization and modeling of the compressive yield stress." *International Journal of Solids and Structures*, 43(7–8), 2318-2335.

Risseeuw, P. A. (1984). "Long term behavior of heavy duty reinforcing mats/structural elements in earthworks." *Proc., Geotextile Technology Conference*London, UK.

Risseeuw, P. A., and Voskamp, W. (1984). "Reinforcing fabrics under embankments on soft subsoils, a calculation methods." *Proc., Construction Industry International*London, UK.

Rowe, R. K., and Mylleville, B. L. J. (1996). "A geogrid reinforced embarkment on peat over organic silt: A case history." *Canadian Geotechnical Journal*, 33(1), 106-122.

Rui, Y., Guo, J., Harwell, J., Nakanishi, T., Kotera, S., and Grady, B. P. (2014). "Electrical, mechanical, and crystallization properties of ethylene-tetrafluoroethylene

copolymer/multiwalled carbon nanotube composites." *Journal of Applied Polymer Science*, 131(22), n/a-n/a.

Saito, R., Fujita, M., Dresselhaus, G., and Dresselhaus, M. S. (1992). "Electronic structure of chiral graphene tubules." *Applied Physics Letters*, 60(18), 2204-2206.

Salvetat, J.-P., Kulik, A. J., Bonard, J.-M., Briggs, G. A. D., Stöckli, T., Méténier, K., Bonnamy, S., Béguin, F., Burnham, N. A., and Forró, L. (1999). "Elastic modulus of ordered and disordered multiwalled carbon nanotubes." *Advanced Materials*, 11(2), 161-165.

Sánchez-González, J., Macías-García, A., Alexandre-Franco, M. F., and Gómez-Serrano, V. (2005). "Electrical conductivity of carbon blacks under compression." *Carbon*, 43(4), 741-747.

Sandler, J. K. W., Pegel, S., Cadek, M., Gojny, F., van Es, M., Lohmar, J., Blau, W. J., Schulte, K., Windle, A. H., and Shaffer, M. S. P. (2004). "A comparative study of melt spun polyamide-12 fibres reinforced with carbon nanotubes and nanofibres." *Polymer*, 45(6), 2001-2015.

Sarva, S., and Boyce, M. (2007). "Mechanics of polycarbonate during high-rate tension." *Journal of Mechanics of Materials and Structures*, 2(10), 1853-1880.

Sarychev, A. K., and Brouers, F. (1994). "New scaling for ac properties of percolating composite materials." *Physical Review Letters*, 73(21), 2895-2898.

Schadler, L. S., Giannaris, S. C., and Ajayan, P. M. (1998). "Load transfer in carbon nanotube epoxy composites." *Applied Physics Letters*, 73(26), 3842-3844.

Scher, H., and Zallen, R. (1970). "Critical density in percolation processes." *The Journal of Chemical Physics*, 53(9), 3759-3761.

Schroder, D. K. (2006). *Semiconductor material and device characterization*, John Wiley & Sons.

Seager, C. H., and Pike, G. E. (1974). "Percolation and conductivity: A computer study. Ii." *Physical Review B*, 10(4), 1435-1446.

Seo, M.-K., and Park, S.-J. (2004). "Electrical resistivity and rheological behaviors of carbon nanotubes-filled polypropylene composites." *Chemical Physics Letters*, 395(1–3), 44-48.

Shanmugharaj, A. M., Bae, J. H., Lee, K. Y., Noh, W. H., Lee, S. H., and Ryu, S. H. (2007). "Physical and chemical characteristics of multiwalled carbon nanotubes functionalized with aminosilane and its influence on the properties of natural rubber composites." *Composites Science and Technology*, 67(9), 1813-1822.

Shapiro, S. S., and Wilk, M. B. (1965). "An analysis of variance test for normality (complete samples)." *Biometrika*, 52(3-4), 591-611.

Shenderova, O. A., Brenner, D. W., Omeltchenko, A., Su, X., and Yang, L. H. (2000). "Atomistic modeling of the fracture of polycrystalline diamond." *Physical Review B*, 61(6), 3877-3888.

Shi, J.-H., Yang, B.-X., Pramoda, K. P., and Goh, S. H. (2007). "Enhancement of the mechanical performance of poly(vinyl chloride) using poly(n-butyl methacrylate)-grafted multi-walled carbon nanotubes." *Nanotechnology*, 18(37), 375704.

Shinoda, M., and Bathurst, R. J. (2004). "Lateral and axial deformation of pp, hdpe and pet geogrids under tensile load." *Geotextiles and Geomembranes*, 22(4), 205-222.

Shokrieh, M. M., Saeedi, A., and Chitsazzadeh, M. (2013). "Mechanical properties of multi-walled carbon nanotube/polyester nanocomposites." *Journal of Nanostructure in Chemistry*, 3(1), 1-5.

Shrivastava, N. K., and Khatua, B. B. (2011). "Development of electrical conductivity with minimum possible percolation threshold in multi-wall carbon nanotube/polystyrene composites." *Carbon*, 49(13), 4571-4579.

Shukla, S. K. (2002). *Geosynthetics and their applications*, Thomas Telford.

Sichel, E. K., Gittleman, J. I., and Sheng, P. (1978). "Transport properties of the composite material carbon-poly(vinyl chloride)." *Physical Review B*, 18(10), 5712-5716.

Sichel, E. K., Gittleman, J. I., and Sheng, P. (1982). "Electrical properties of carbon-polymer composites." *Journal of Electronic Materials*, 11(4), 699-747.

Simac, M. R., Christopher, B. R., and Bonczkiewicz, C. (1990). "Instrumented field performance of a 6 m geogrid soil wall." CRC Press, Netherlands.

Simon, R. M. (1985). "Thermally and electrically conductive flake filled plastics." *Polymer News*, 11, 102-108.

Sluimer, G., and Risseeuw, P. A. (1982). "Strain gage technique for measuring deformations in geotextiles."Las Vegas, NV, 835-838.

Smirnov, N. V. (1933). "Estimate of deviation between empirical distribution functions in two independent samples." *Bulletin Moscow University*, 2, 3-16.

Smith, B. E., Yazdani, H., and Hatami, K. (2015). "Three-dimensional imaging and quantitative analysis of dispersion and mechanical failure in filled nanocomposites." *Composites Part A: Applied Science and Manufacturing*, 79, 23-29.

Socher, R., Krause, B., Hermasch, S., Wursche, R., and Pötschke, P. (2011). "Electrical and thermal properties of polyamide 12 composites with hybrid fillers systems of multiwalled carbon nanotubes and carbon black." *Composites Science and Technology*, 71(8), 1053-1059.

Song, H.-T., Dang, Z.-M., Lv, J., Yao, S.-H., Zha, J.-W., and Yin, Y. (2010). "Enhanced electrical properties in percolative low-density polyethylene/carbon nanotubes nanocomposites." *IEEE Transactions on Dielectrics and Electrical Insulation*, 17(3), 645-652.

Song, Y. S., and Youn, J. R. (2005). "Influence of dispersion states of carbon nanotubes on physical properties of epoxy nanocomposites." *Carbon*, 43(7), 1378-1385.

Sorensen, R. A., Liau, W. B., Kesner, L., and Boyd, R. H. (1988). "Prediction of polymer crystal structures and properties: Polyethylene and poly(oxymethylene)." *Macromolecules*, 21(1), 200-208.

Soule, D. E., and Nezbeda, C. W. (1968). "Direct basal-plane shear in single-crystal graphite." *Journal of Applied Physics*, 39(11), 5122-5139.

Špitalský, Z., Matějka, L., Šlouf, M., Konyushenko, E. N., Kovářová, J., Zemek, J., and Kotek, J. (2009). "Modification of carbon nanotubes and its effect on properties of carbon nanotube/epoxy nanocomposites." *Polymer Composites*, 30(10), 1378-1387.

Stamm, A. J. (1964). *Wood and cellulose science*, Ronald Press Co.

Stark, T. D., Choi, H., and Diebel, P. W. (2005). "Influence of plasticizer molecular weight on plasticizer retention in pvc geomembranes." *Geosynthetics International*, 12(2), 99-110.

Stauffer, D. (1987). *Introduction to percolation theory*, Taylor and Francis, Philadelphia.

Steinhauser, M. O., and Hiermaier, S. (2009). "A review of computational methods in materials science: Examples from shock-wave and polymer physics." *International Journal of Molecular Sciences*, 10(12), 5135-5216.

Stone, A. J. (1996). *The theory of intermolecular forces*, Oxford University Press, Oxford, UK.

Subramaniyan, A. K., and Sun, C. T. (2008). "Continuum interpretation of virial stress in molecular simulations." *International Journal of Solids and Structures*, 45(14–15), 4340-4346.

Sui, G., Zhong, W., Yang, X., and Zhao, S. (2007). "Processing and material characteristics of a carbon-nanotube-reinforced natural rubber." *Macromolecular Materials and Engineering*, 292(9), 1020-1026.

Sumita, M., Abe, H., Kayaki, H., and Miyasaka, K. (1986a). "Effect of melt viscosity and surface tension of polymers on the percolation threshold of conductive-particle-filled polymeric composites." *Journal of Macromolecular Science, Part B*, 25(1-2), 171-184.

Sumita, M., Asai, S., Miyadera, N., Jojima, E., and Miyasaka, K. (1986b). "Electrical conductivity of carbon black filled ethylene-vinyl acetate copolymer as a function of vinyl acetate content." *Colloid and Polymer Science*, 264(3), 212-217.

Sun, H., Mumby, S. J., Maple, J. R., and Hagler, A. T. (1994). "An ab initio cff93 all-atom force field for polycarbonates." *Journal of the American Chemical Society*, 116(7), 2978-2987.

Tang, W., Santare, M. H., and Advani, S. G. (2003). "Melt processing and mechanical property characterization of multi-walled carbon nanotube/high density polyethylene (mwnt/hdpe) composite films." *Carbon*, 41(14), 2779-2785.

Tang, Y. H., Witt, N., and Ye, L. (2012). "Conductive rubber nanocomposites as tensile and pressure sensors." *Applied Mechanics and Materials*, 217-219, 130-133.

Tchoudakov, R., Breuer, O., Narkis, M., and Siegmann, A. (1996). "Conductive polymer blends with low carbon black loading: Polypropylene/polyamide." *Polymer Engineering & Science*, 36(10), 1336-1346.

Terdalkar, S. S., Huang, S., Yuan, H., Rencis, J. J., Zhu, T., and Zhang, S. (2010). "Nanoscale fracture in graphene." *Chemical Physics Letters*, 494(4–6), 218-222.

Thess, A., Lee, R., Nikolaev, P., Dai, H., Petit, P., Robert, J., Xu, C., Lee, Y. H., Kim, S. G., Rinzler, A. G., Colbert, D. T., Scuseria, G. E., Tománek, D., Fischer, J. E., and Smalley, R. E. (1996). "Crystalline ropes of metallic carbon nanotubes." *Science*, 273(5274), 483-487.

Thostenson, E. T., and Chou, T.-W. (2003). "On the elastic properties of carbon nanotube-based composites: Modelling and characterization." *Journal of Physics D: Applied Physics*, 36(5), 573.

Titow, W. V. (1984). *Pvc technology*, Elsevier Applied Science Publishers, NY, USA.

Tjong, S. C., Liang, G. D., and Bao, S. P. (2007). "Electrical behavior of polypropylene/multiwalled carbon nanotube nanocomposites with low percolation threshold." *Scripta Materialia*, 57(6), 461-464.

Topsakal, M., and Ciraci, S. (2010). "Elastic and plastic deformation of graphene, silicene, and boron nitride honeycomb nanoribbons under uniaxial tension: A first-principles density-functional theory study." *Physical Review B*, 81(2), 024107.

Torquato, S. (2001). *Random heterogeneous materials: Microstructure and macroscopic properties*, Springer.

Toxvaerd, S. r. (1990). "Molecular dynamics calculation of the equation of state of alkanes." *The Journal of Chemical Physics*, 93(6), 4290-4295.

Treacy, M. M. J., Ebbesen, T. W., and Gibson, J. M. (1996). "Exceptionally high young's modulus observed for individual carbon nanotubes." *Nature*, 381(6584), 678-680.

Tsai, D. H. (1979). "The virial theorem and stress calculation in molecular dynamics." *The Journal of Chemical Physics*, 70(3), 1375-1382.

Tsvetkov, V. N. (1989). *Rigid-chain polymers: Hydrodynamic and optical properties in solution*, Springer, New York.

Tuleubekov, K., Volokh, K. Y., Stolarski, H., and Mogilevskaya, S. G. (2013). "Strength of graphene in biaxial tension." *European Journal of Mechanics - A/Solids*, 39, 291-297.

Ueda, N., and Taya, M. (1986). "Prediction of the electrical conductivity of two-dimensionally misoriented short fiber composites by a percolation model." *Journal of Applied Physics*, 60(1), 459-461.

Uhlherr, A., and Theodorou, D. N. (1998). "Hierarchical simulation approach to structure and dynamics of polymers." *Current Opinion in Solid State and Materials Science*, 3(6), 544-551.

USDOE (2005). *Fuel cell handbook*, University Press of Pacific, Honolulu Hawaii.

van Dommelen, L. (2003). "Physical interpretation of the virial stress." *Physical Interpretation of the Virial Stress*.

van Melick, H. G. H., Govaert, L. E., and Meijer, H. E. H. (2003). "On the origin of strain hardening in glassy polymers." *Polymer*, 44(8), 2493-2502.

Varadan, V. K. (2003). "Nanotechnology: Mems and nems and their applications to smart systems and devices." 20-43.

Viswanadham, B. V. S., and König, D. (2004). "Studies on scaling and instrumentation of a geogrid." *Geotextiles and Geomembranes*, 22(5), 307-328.

Volokh, K. Y. (2012). "On the strength of graphene." *Journal of Applied Mechanics*, 79(6), 064501-064501.

Wanatowski, D., and Chu, J. (2006). "Stress-strain behavior of a granular fill measured by a new plane-strain apparatus." *Geotechnical Testing Journal*, 29(2), 12621.

Wang, C. M., Chowdhury, A. N. R., Koh, S. J. A., and Zhang, Y. Y. (2014). "Molecular dynamics simulation and continuum shell model for buckling analysis of carbon nanotubes." *Modeling of carbon nanotubes, graphene and their composites*, K. I. Tserpes, and N. Silvestre, eds., Springer International Publishing, 239-273.

Wang, P., and Ding, T. (2010). "Creep of electrical resistance under uniaxial pressures for carbon black–silicone rubber composite." *Journal of Materials Science*, 45(13), 3595-3601.

Wang, S., Yang, B., Yuan, J., Si, Y., and Chen, H. (2015). "Large-scale molecular simulations on the mechanical response and failure behavior of a defective graphene: Cases of 5–8–5 defects." *Scientific Reports*, 5, 14957.

Wang, S. F., and Ogale, A. A. (1993). "Continuum space simulation and experimental characterization of electrical percolation behavior of particulate composites." *Composites Science and Technology*, 46(2), 93-103.

Wang, Y., Zhang, L., Fan, Y., Jiang, D., and An, L. (2009a). "Stress-dependent piezoresistivity of tunneling-percolation systems." *Journal of Materials Science*, 44(11), 2814-2819.

Wang, Y. Q., Sutton, M. A., Bruck, H. A., and Schreier, H. W. (2009b). "Quantitative error assessment in pattern matching: Effects of intensity pattern noise, interpolation, strain and image contrast on motion measurements." *Strain*, 45(2), 160-178.

Warren, B. E. (1934). "X-ray diffraction study of carbon black." *The Journal of Chemical Physics*, 2(9), 551-555.

Warren, K. A., Christopher, B., and Howard, I. L. (2010). "Geosynthetic strain gage installation procedures and alternative strain measurement methods for roadway applications." *Geosynthetics International*, 17(6), 403-430.

Washburn, E. W. (1921). "The dynamics of capillary flow." *Physical Review*, 17(3), 273-283.

Watts, G. R. A., Brady, K. C., and Greene, M. J. (1998). *The creep of geosynthetics*, Thomas Telford, London, UK.

WenXing, B., ChangChun, Z., and WanZhao, C. (2004). "Simulation of young's modulus of single-walled carbon nanotubes by molecular dynamics." *Physica B: Condensed Matter*, 352(1–4), 156-163.

Whitney, W., and Andrews, R. D. (1967). "Yielding of glassy polymers: Volume effects." *Journal of Polymer Science Part C: Polymer Symposia*, 16(5), 2981-2990.

Whittaker, A. G. (1978). "The controversial carbon solid–liquid–vapour triple point." *Nature*, 276(5689), 695-696.

Wichmann, M. H. G., Buschhorn, S. T., Gehrmann, J., and Schulte, K. (2009). "Piezoresistive response of epoxy composites with carbon nanoparticles under tensile load." *Physical Review B*, 80(24), 245437.

Wilder, J. W. G., Venema, L. C., Rinzler, A. G., Smalley, R. E., and Dekker, C. (1998). "Electronic structure of atomically resolved carbon nanotubes." *Nature*, 391(6662), 59-62.

Wilson, S. M., and Bacic, A. (2012). "Preparation of plant cells for transmission electron microscopy to optimize immunogold labeling of carbohydrate and protein epitopes." *Nature Protocols*, 7(9), 1716-1727.

Wu (1982). *Polymer interface and adhesion*, CRC Press.

Wu, H., Feng, L., Jiang, A., and Zhang, B. (2011). "Effect of the processing of injection-molded, carbon black-filled polymer composites on resistivity." *Polymer Journal*, 43(11), 930-936.

Wu, P. D., and van der Giessen, E. (1993). "On improved network models for rubber elasticity and their applications to orientation hardening in glassy polymers." *Journal of the Mechanics and Physics of Solids*, 41(3), 427-456.

Xia, H., Wang, Q., and Qiu, G. (2003). "Polymer-encapsulated carbon nanotubes prepared through ultrasonically initiated in situ emulsion polymerization." *Chemistry of Materials*, 15(20), 3879-3886.

Xia, W., and Thorpe, M. F. (1988). "Percolation properties of random ellipses." *Physical Review A*, 38(5), 2650-2656.

Xiao, H., Li, H., and Ou, J. (2010). "Modeling of piezoresistivity of carbon black filled cement-based composites under multi-axial strain." *Sensors and Actuators A: Physical*, 160(1–2), 87-93.

Xiao, K. Q., Zhang, L. C., and Zarudi, I. (2007). "Mechanical and rheological properties of carbon nanotube-reinforced polyethylene composites." *Composites Science and Technology*, 67(2), 177-182.

Xiao, S., and Hou, W. (2006). "Studies of size effects on carbon nanotubes' mechanical properties by using different potential functions." *Fullerenes, Nanotubes and Carbon Nanostructures*, 14(1), 9-16.

Xu, L., Wei, N., and Zheng, Y. (2013). "Mechanical properties of highly defective graphene: From brittle rupture to ductile fracture." *Nanotechnology*, 24(50), 505703.

Yacubowicz, J., Narkis, M., and Benguigui, L. (1990). "Electrical and dielectric properties of segregated carbon black–polyethylene systems." *Polymer Engineering & Science*, 30(8), 459-468.

Yamaguchi, K., Busfield, J. J. C., and Thomas, A. G. (2003). "Electrical and mechanical behavior of filled elastomers. I. The effect of strain." *Journal of Polymer Science Part B: Polymer Physics*, 41(17), 2079-2089.

Yang, L., Ge, Y., Zhu, Q., Zhang, C., Wang, Z., and Liu, P. (2012). "Experimental and numerical studies on the sensitivity of carbon fibre/silicone rubber composite sensors." *Smart Materials and Structures*, 21(3), 035011.

Yazdani, H., Hatami, K., Khosravi, E., Harper, K., and Grady, B. P. (2014). "Strain-sensitive conductivity of carbon black-filled pvc composites subjected to cyclic loading." *Carbon*, 79, 393-405.

Yazdani, H., and Hatami, K. (2015). "Failure criterion for graphene in biaxial loading—a molecular dynamics study." *Modelling and Simulation in Materials Science and Engineering*, 23(6), 065004.

Yazdani, H., Smith, B., and Hatami, K. (2015a). "Multiscale 3d dispersion characterization of carbon nanotube-filled polymer composites using microscopic imaging and data mining." *Carbon nanotechnology*, W. I. Milne, M. Cole, and S. Mitura, eds., One Central Press, Manchester, UK.

Yazdani, H., Smith, B., and Hatami, K. (2015b). "Multi-walled carbon nanotube-filled polyvinyl chloride composites: Influence of processing methods on dispersion quality, electrical conductivity and mechanical properties." *Composites Part A: Applied Science and Manufacturing*, Under revision after the first round review.

Yazdani, H., Smith, B., and Hatami, K. (2015c). "Electrical conductivity and mechanical performance of multi-walled carbon nanotube-filled polyvinyl chloride composites subjected to tensile load." *Composites Part A: Applied Science and Manufacturing*, Under Review.

Yazdani, H., Hatami, K., and Grady, B. P. (2016). "Sensor-enabled geogrids for performance monitoring of reinforced soil structures." *ASTM Journal of Testing and Evaluation*, 44(1).

Yee, C. (2001). "Fiber-optic strain gauges."

Yi, J. Y., and Choi, G. M. (1999). "Percolation behavior of conductor-insulator composites with varying aspect ratio of conductive fiber." *Journal of Electroceramics*, 3(4), 361-369.

Yoon, D. Y., Smith, G. D., and Matsuda, T. (1993). "A comparison of a united atom and an explicit atom model in simulations of polymethylene." *The Journal of Chemical Physics*, 98(12), 10037-10043.

Yu, M.-F., Lourie, O., Dyer, M. J., Moloni, K., Kelly, T. F., and Ruoff, R. S. (2000). "Strength and breaking mechanism of multiwalled carbon nanotubes under tensile load." *Science*, 287(5453), 637-640.

Yu, M., Dyer, M. J., Skidmore, G. D., Rohrs, H. W., Lu, X., Ausman, K. D., Ehr, J. R. V., and Ruoff, R. S. (1999). "Three-dimensional manipulation of carbon nanotubes under a scanning electron microscope." *Nanotechnology*, 10(3), 244.

Yu, Y., Song, S., Bu, Z., Gu, X., Song, G., and Sun, L. (2013). "Influence of filler waviness and aspect ratio on the percolation threshold of carbon nanomaterials reinforced polymer nanocomposites." *Journal of Materials Science*, 48(17), 5727-5732.

Yui, H., Wu, G., Sano, H., Sumita, M., and Kino, K. (2006). "Morphology and electrical conductivity of injection-molded polypropylene/carbon black composites with addition of high-density polyethylene." *Polymer*, 47(10), 3599-3608.

Zandiatashbar, A., Lee, G.-H., An, S. J., Lee, S., Mathew, N., Terrones, M., Hayashi, T., Picu, C. R., Hone, J., and Koratkar, N. (2014). "Effect of defects on the intrinsic strength and stiffness of graphene." *Nature Communications*, 5.

Zhang, B., Mei, L., and Xiao, H. (2012). "Nanofracture in graphene under complex mechanical stresses." *Applied Physics Letters*, 101(12), 121915.

Zhang, H., Zhou, T., Xie, G., Cao, J., and Yang, Z. (2014). "Thermal transport in folded zigzag and armchair graphene nanoribbons." *Applied Physics Letters*, 104(24), 241908.

Zhang, Q., Rastogi, S., Chen, D., Lippits, D., and Lemstra, P. J. (2006). "Low percolation threshold in single-walled carbon nanotube/high density polyethylene composites prepared by melt processing technique." *Carbon*, 44(4), 778-785.

Zhang, R., Baxendale, M., and Peijs, T. (2007a). "Universal resistivity–strain dependence of carbon nanotube/polymer composites." *Physical Review B*, 76(19), 195433.

Zhang, R., Deng, H., Valenca, R., Jin, J., Fu, Q., Bilotti, E., and Peijs, T. (2013a). "Strain sensing behaviour of elastomeric composite films containing carbon nanotubes under cyclic loading." *Composites Science and Technology*, 74, 1-5.

Zhang, R., Zhang, Y., Zhang, Q., Xie, H., Wang, H., Nie, J., Wen, Q., and Wei, F. (2013b). "Optical visualization of individual ultralong carbon nanotubes by chemical vapour deposition of titanium dioxide nanoparticles." *Nature Communications*, 4, 1727.

Zhang, W., Dehghani-Sanij, A. A., and Blackburn, R. S. (2007b). "Carbon based conductive polymer composites." *Journal of Materials Science*, 42(10), 3408-3418.

Zhao, D., Lei, Q., Qin, C., and Bai, X. (2006). "Melt process and performance of multi-walled carbon nanotubes reinforced ldpe composites." *Pigment & Resin Technology*, 35(6), 341-345.

Zhao, H., Min, K., and Aluru, N. R. (2009). "Size and chirality dependent elastic properties of graphene nanoribbons under uniaxial tension." *Nano Letters*, 9(8), 3012-3015.

Zhao, H., and Aluru, N. R. (2010). "Temperature and strain-rate dependent fracture strength of graphene." *Journal of Applied Physics*, 108(6), 064321.

Zhao, J., Dai, K., Liu, C., Zheng, G., Wang, B., Liu, C., Chen, J., and Shen, C. (2013). "A comparison between strain sensing behaviors of carbon black/polypropylene and carbon nanotubes/polypropylene electrically conductive composites." *Composites Part A: Applied Science and Manufacturing*, 48, 129-136.

Zhao, M., Ming, B., Kim, J.-W., Gibbons, L. J., Gu, X., Nguyen, T., Park, C., Lillehei, P. T., Villarrubia, J. S., Vladár, A. E., and Liddle, J. A. (2015). "New insights into subsurface imaging of carbon nanotubes in polymer composites via scanning electron microscopy." *Nanotechnology*, 26(8), 085703.

Zheng, S., Deng, J., Yang, L., Ren, D., Huang, S., Yang, W., Liu, Z., and Yang, M. (2014). "Investigation on the piezoresistive behavior of high-density polyethylene/carbon black films in the elastic and plastic regimes." *Composites Science and Technology*, 97, 34-40.

Zhou, M. (2003). "A new look at the atomic level virial stress: On continuum-molecular system equivalence." *Proceedings of the Royal Society of London A: Mathematical, Physical and Engineering Sciences*, 459(2037), 2347-2392.

Zhu, B.-K., Xie, S.-H., Xu, Z.-K., and Xu, Y.-Y. (2006). "Preparation and properties of the polyimide/multi-walled carbon nanotubes (mwnts) nanocomposites." *Composites Science and Technology*, 66(3–4), 548-554.

Zhu, R., Pan, E., and Roy, A. K. (2007). "Molecular dynamics study of the stress–strain behavior of carbon-nanotube reinforced epon 862 composites." *Materials Science and Engineering: A*, 447(1–2), 51-57.

APPENDIX A: PUBLLICATIONS AND PRESENTATIONS FROM THIS STUDY

Peer-reviewed Book Chapters

Yazdani H., Smith B. and Hatami K., "Multiscale 3D dispersion characterization of carbon nanotube-filled polymer composites using microscopic imaging and data mining." in *Carbon Nanotubes*, W.I. Milne (ed.), One Central Press, Manchester, UK. (in press)

Peer-reviewed Journal Papers

Published/Under Review

Yazdani H., Smith B. and Hatami K., "Electrical conductivity and mechanical performance of multi-walled carbon nanotube-filled polyvinyl chloride composites subjected to tensile load." *Journal of Applied Polymer Science*. (under review)

Yazdani H., Smith B. and Hatami K., "Multi-walled carbon nanotube-filled polyvinyl chloride composites: influence of processing methods on dispersion quality, electrical conductivity and mechanical properties." *Composites Part A: Applied Science and Manufacturing*. (in press)

Yazdani H., Hatami K. and Grady B.P., (2016). "Sensor-enabled Geogrids for Performance Monitoring of Reinforced Soil Structures." *ASTM Journal of Testing and Evaluation*, 44 (1).

Smith B., **Yazdani H.** and Hatami K., (2015). "Three-dimensional Imaging and Quantitative Analysis of Dispersion and Mechanical Failure in Filled Nanocomposites." *Composites Part A: Applied Science and Manufacturing*, 79, 23–29.

Yazdani H. and Hatami K., (2015). "Failure Criterion for Graphene in Biaxial Loading – a Molecular Dynamics Study." *Modelling and Simulation in Materials Science and Engineering*, 23 (6), 065004.

Yazdani H., Hatami K., Khosravi E., Harper K. and Grady B.P., (2014). "Strain-sensitive Conductivity of Carbon Black-filled PVC Composites Subjected to Cyclic Loading. " *Carbon*, 79, 393–405.

Hatami K., Hassanikhah A., **Yazdani H.** and Grady B.P., (2014). "Tensoresistive PVC Coating for Sensor-enabled Geogrids." Invited Paper. *ASCE Journal of Nanomechanics and Micromechanics*, A4013016.

Pending Submissions

Yazdani H. and Hatami K., "Recent Advances in Sensor-enabled Geosynthetics."

Yazdani H. and Hatami K., "Tensile and Compressive Properties of Single-walled Carbon Nanotubes – a Molecular Dynamics Study."

Yazdani H. and Hatami K., "Failure Criterion for Defective Graphene."

Conference Papers

Yazdani H. and Hatami K., "Sensor-Enabled Geogrids for Stabilization and Instrumentation of Earth Structures." abstract accepted for the *5th International Symposium on Life -Cycle Civil Engineering, IALCCE2016*, Delft, The Netherlands.

Yazdani H., Hatami K., Hawa T. and Grady B.P., (2013). "Atomic-Scale Simulation of Sensor-Enabled Geosynthetics for Health Monitoring of Reinforced Soil Slopes and Embankments." *ASCE Geo-Congress*, San Diego, 1529–1535.

Yazdani H., Hatami K., Hawa T. and Grady B.P., (2012). "Molecular Dynamics Simulation of Sensor-Enabled Geosynthetics." *The 15th Nanotechnology Conference*, Santa Clara, US, Paper No. 918.

Professional Presentations

Yazdani H., (2014). "High-performance Computing in Materials Science and Engineering." *The 10th Annual Conference in Computer Science*, Norman, OK.

Yazdani H., (2014). "Sensor-enabled Geosynthetics; where Cutting-edge Science Meets Transportation Infrastructure." *Oklahoma Department of Transportation (ODOT) Research Day*, OKC, OK.

Yazdani H., (2014). "Recent Advances in Sensor-enabled Geosynthetics." *Research Day*, National Weather Center, Norman, OK.

Hassanikhah A., **Yazdani H.**, Harper K., Hatami K. and Grady B.P., (2013). "Sensor-enabled geogrids for stabilization and instrumentation of transportation infrastructure." *Oklahoma Department of Transportation (ODOT) Research Day*, OKC, OK.

Hatami K., Hassanikhah A., **Yazdani H.** and Grady B.P., (2012). "Developing Sensor-enabled Geosynthetics using Conducting Carbon Networks: A Proof-of-Concept Study." *The NSF CMMI Engineering Research and Innovation Conference*, Boston, Massachusetts.

Yazdani H., (2012). "Molecular Dynamics Simulation of Sensor-enabled Geosynthetics." *USUCGER 1st Early Career Geotechnical Engineering Conference*, Boston, Massachusetts.

Yazdani H., (2012). "Molecular Dynamics Simulation of Sensor-enabled Geosynthetics." *Oklahoma Department of Transportation (ODOT) Research Day*, OKC, OK.

Yazdani H., (2011). "Application of Molecular-scale Simulations in Civil Engineering." *Oklahoma Department of Transportation (ODOT) Research Day*, OKC, OK.

Yazdani H., (2011). "Molecular-scale Simulations in Civil Engineering." *Research Day of the OU Supercomputing Center for Education & Research (OSCER)*, National Weather Center, Norman, OK.

Reports

Hatami K. and **Yazdani H.**, (2013). "Fabrication, Cyclic Loading and In-soil Performance of Sensor-Enabled Geosynthetics." *Vice President for Research,* The University of Oklahoma.